Durham E-Theses

Theoretical Studies of dilute Bose-Einstein condensates in a double-well potential

Sakellari, Eleni

Theoretical Studies of dilute Bose-Einstein condensates in a double-well potential

Eleni Sakellari

A thesis submitted in partial fulfilment
of the requirements for the degree of
Doctor of Philosophy

The University of Durham
Department of Physics
2004

Theoretical Studies of dilute Bose-Einstein condensates in a double-well potential

Eleni Sakellari

Abstract

In this Thesis we apply the Gross-Pitaevskii equation (GPE) to describe properties of a dilute, near zero temperature Bose gas for various confining geometries. We start by reviewing some basic information about the density, the chemical potential and elementary excitations of a dilute atomic condensate confined in a single harmonic trap for a Bose condensate with repulsive and attractive interactions and we also discuss the stability in the case of attractive interactions. We extend our study to a one and three dimensional double-well trap. We investigate the eigenenergy levels and show that the nonlinearity leads to triangular structures which appear either in the ground or excited states for the case of a Bose condensate with attractive or repulsive interactions respectively. We apply the eigenenergy level picture to analyse Josephson effects induced when the barrier is moved at a constant velocity across the trapping potential or by the application of a time-dependent potential gradient. The GPE simulations are compared to the predictions of a nonlinear two-state model. Above a critical velocity there is a transition to a superposition of ground and excited states which leads to sudden changes in the population difference. The direction of Josephson flow depends critically on the initial state of the system and we discuss the feasibility of experimental control of the atomic flow using phase-imprinting. The stability of a low temperature Bose-Einstein condensate with attractive interactions in one and three dimensional double-well potentials is discussed. The condensate is shown to collapse at a critical potential gradient which corresponds to a critical number of atoms in one of the two wells. Finally we investigate the stability and tunnelling effects in a multi-well system.

Contents

List of Figures

Declaration

I confirm that no part of the material offered has previously been submitted by me for a degree in this or in any other University. If material has been generated through joint work, my independent contribution has been clearly indicated. In all other cases material from the work of others has been acknowledged and quotations and paraphrases suitability indicated.

Eleni Sakellari

Durham, 2nd July 2004

Acknowledgements

I would like to thank all the people who have contributed to my research. I am particularly thankful to Charles Adams, my supervisor, for his advice, enthusiasm and support. It is a pleasure to thank the following people: Niels Kylstra, for useful discussions and for providing me with analytical results, Mark Leadbeater for significant contributions to many codes I developed and to Nick Proukakis for his guidance in many projects and for extensive reading and comments on the Thesis. Last but not least, I would like to thank Thomas Winiecki for helping me getting started with programming and Ciprian Chirila, Carolyn McCoey and Nick Parker, my officemates, for many exciting discussions.

Chapter 1

Introduction

In nature there are two fundamental types of particles, fermions and bosons. Fermions have half-integral spin and obey Fermi-Dirac statistics while bosons have integral spin and obey Bose-Einstein statistics. A gas of fermions can have at most one particle in each quantum state, whereas bosons can all occupy the same state. For bosons, below a certain temperature the atomic de Broglie waves of neighbouring atoms start overlapping and a macroscopic number of bosons tend to occupy the lowest-energy state of the system. At this temperature they form a Bose-Einstein condensate and they can be described by one and the same single particle wave-function. This temperature is given by the condition $n\lambda_{dB}^3 = 2.612$, where n is the number density and $\lambda_{dB} = \sqrt{\hbar^2/2k_BmT}$ is the de Broglie wavelength [1, 2, 3, 4, 5, 6].

A possible manifestation of Bose-Einstein condensate was first proposed in the 1930's after liquid helium was found to behave as a superfluid below a temperature of 2.18 K. The analogy between liquid ^{4}He and an ideal Bose-Einstein gas was first considered by London (1938) [7]. The ^{4}He atom is composed of an even number of elementary particles and according to the above the system should obey Bose-Einstein statistics. He suggested that the sharp peak in the heat capacity known as the λ-transition could be understood as an analogue of the transition which occurs in an ideal Bose gas at low temperatures. The fact that no λ-transition has been found in ^{3}He supports London's viewpoint. Soon thereafter Tisza suggested that the anomalous flow behaviour seen below the λ-point (in the so called He-II phase)

could be qualitatively understood in terms of a "two fluid" model in which the condensate behaves completely without friction, while the rest behaves like an ordinary liquid [2, 5]. Although BEC is related to superfluidity in helium, the interactions between the atoms are so strong that the process of condensation cannot be clearly identified. Therefore due to strong interactions the fraction of the condensate is small ($\sim 8\%$) thus it is difficult to develop a complete theoretical description of this system. The process of BEC has also been identified in other many-body systems, such as excitons in semiconductors [8, 9], in neutron stars [10] and the Cooper pairs in superconductors [11] and in ^{3}He [12].

1.1 Alkali gases

A breakthrough in the study of BEC came with the experimental realisation of dilute, weakly-interacting alkali gases. The first observations were made in 1995 in a remarkable set of experiments on vapours of ^{87}Rb [13] and ^{23}Na [14]. Atoms confined in magneto-optical traps were cooled down by laser and evaporative cooling techniques to temperatures of order of 100 nanokelvin, suffeciently cold to observe BEC. The first evidence for condensation emerged from the free expansion of the condensate after switching off the confining trap: a sharp peak in the velocity distribution appeared below a critical temperature. In the same year, first signatures of BEC in ^{7}Li were also reported [15].

BEC in alkali gases is new fast evolving field. By 2004 BEC has been realized in ^{1}H [16], ^{85}Rb [17], metastable ^{4}He [18, 19], ^{41}K [20], ^{133}Cs [21] and ^{174}Yb [22]. The use of Feshbach resonances [23, 24, 25] has led to the condensation of diatomic molecules of ^{6}Li [26, 27] and ^{40}K [28]. We have already mentioned that fermions cannot occupy the same physical state - the exact opposite of what happens in a BEC. When two fermionic atoms join to form molecules, they become composite bosons, which can gather in the quantum state of lowest energy.

Typical temperatures for BEC are of orders of $1 - 100$ nanokelvin and the record low is ~ 500 picokelvin [29] at densities between 10^{10} to 10^{14} cm^3. In contrast, the

temperatures that quantum mechanical effects are important for superfluid helium are of order of K and the density is $\sim 10^{22}$ cm^{-3}. The number of atoms in the condensate varies from the order of millions to just few hundred. By varying the confining potential, the shape of the condensate may be spherical with a diameter of few decades μm, "pancake"-shaped or "cigar"-shaped with 15μm in diameter and up to 5mm length. Because the densities are extremely small (100,000 smaller than air) and the temperatures are extremely low, three-body collisions are rare events and the lifetime of the metastable gas is of the order of seconds.

Alkali gases constitute an ideal system to study BEC. Their optical transitions can be excited by available lasers and have favourable internal energy-level structure for cooling. Moreover the densities of such systems are sufficiently low so their dilute nature allows one to describe the interparticle interactions with a single parameter, the s-wave scattering length. In addition magnetic-field Feshbach resonances [23, 24, 25] play an important role to control not only the strength of interparticle interactions but also whether they are effectively repulsive or attractive. The behaviour of dilute Bose gases such as the static and dynamical properties can be studied within the theory of weakly interacting bosons pioneerd by Bogoliubov and developed by Gross and Pitaevskii. The so-called Gross-Pitaevskii equation (GPE) provides the main theoretical tool for the study of atomic condensates (see following Section and Chapter 2). Despite being weakly interacting, at such low temperatures, the interactions in such systems still play an important role in various properties.

The combination of experimental and theoretical "accessibility" in ultra-cold gases has created great interest in investigating quantum phenomena. A major reason is that almost all atoms $\sim 90\%$ occupy the same quantum state which is characterized by a complex order parameter which in terms of quantum mechanics is characterized by an amplitude and a phase. Therefore these systems are ideal for studies of properties that reveal its coherent nature. The existence of a common phase is relevant for the motion of the cloud since the superfluid velocity is proportional to the gradient of the phase.

In superconductors the (relative) phase has been observed through the Josephson

effect [30, 31] and in superfluids through the irrotationality of the flow. In BECs it can be measured through interference phenomena. The simplest example is the interference between two independent condensates which is clear evidence for coherence in such systems [32]. Two separated BECs where produced in a double-well potential by splitting a magnetic trap in half with a laser beam. After switching off the trap, the two independent condensates expanded and overlapped. Interference patterns in the overlapping region have been observed providing clear evidence for the coherence properties of a many-atom ground state with a second one. The relative phase between two trapped condensates in different hyperfine states and its subsequent dynamical evolution have been also observed in a two-component condensate [33]. Tunnelling effects in macroscopic systems are a manifestation of macroscopic quantum phase coherence and in the next section we review tunnelling experiments.

1.2 Quantum tunnelling of macroscopic systems

A Superconducting state is described by a complex order parameter that can be considered as a wavefunction of a macroscopic number of electrons that "condensate" in the same quantum state. In this sense, the superconducting state can be regarded as a macroscopic quantum state that possesses a quantum phase common to all particles. Phase coherence can be demonstrated through the Josephson effect [30, 31]. Josephson [30] predicted that if two superconductors are separated by a weak link, then the wavefunctions describing the two systems overlap, resulting in current flow through the junction. The current I is related to the phase difference ϕ by the equation

$$I = I_0 \sin \phi \,, \tag{1.1}$$

where I_0 is the critical current of the link, that is the maximum current allowed to flow through the junction. The phase difference can be varied by the application of

a chemical potential difference $\Delta\mu$ according to the equation

$$\partial\Delta\phi/\partial t = -\Delta\mu/\hbar \qquad (1.2)$$

where $\hbar$ is Planck's constant divided by 2π. The above equations (the dc and ac Josephson relations) for the current and relative phase, are also applicable for any two weakly coupled, phase coherent systems [30, 34, 35] and in the context of superconducting Josephson junctions (SJJs) will be derived in the following Sections. In addition, if a π phase difference is maintained across the link, so-called π-junction [36], Eq. (1.1) shows that the current obtains negative values [37], i.e. the current flow in the opposite direction to expected.

Long after the observation of Josephson effects in superconductors, analogue effects in superfluid helium were also observed. Josephson effects were first observed in ^{3}He-B [38, 39] and finally, almost four decades after Josephson's original paper, similar effects were also discovered in ^{4}He [40]. The weak link which separates two helium reservoirs was made using an array of 100 nm diameter apertures near the superfluid transition temperature T_λ. The difficulty in observing Josephson effects in helium was mainly because the weak link has to be made comparable to the healing length ξ of the superfluid (the minimum length over which the wavefunction can change) and takes the values 65 nm and 0.1 nm for ^{3}He and ^{4}He respectively. At temperatures of the order of T_λ, superfluid Josephson oscillations were observed where the flow of mass current across the weak link obeys Eqs. (1.1) and (1.2), with $\Delta\mu = M\Delta P/\rho$, where ρ is the liquid density, ΔP the pressure difference between the two helium reservoirs and M the particle mass. In addition, ^{3}He exhibits π-states with phase difference of π across the weak link [41], which are the superfluid analogue of a superconducting π junction.

The coherent properties of atomic BECs have been demonstrated by experiments in one [42, 43, 44, 45] and three dimensional [46] optical lattices through the formation of interference peaks when the lattice was turned off. Optical lattices are periodic potential structures created by the interference of laser beams. The potential is deep enough that atoms become trapped in the "egg-carton" like potential wells

but shallow enough that phase coherence between separated condensates allows the population to tunnel between wells. By increasing the lattice depth, the tunnelling is suppressed and the atoms are confined in the lattice minima resulting in loss of superfluidity and phase coherence. This is known as the Mott Insulator phase and the transition from a superfluid to Mott Insulator phase has been demonstrated in a recent experiment [46]. In the superfluid state the number of atoms in each well can vary whereas the phase is exactly the same in each well. In contrast, in the Mott-Insulator phase, the atoms are localised at each lattice sites with an exactly defined number, and the phase changes randomly from one well to the next. Experiments with neutral atoms in optical lattices have attracted interest in realizing a quantum computer [47].

Josephson effects in BECs have been demonstrated in one dimensional lattice. In [42] coherent matter wave emission was explored when atoms were released from a vertical array. Neglecting atomic interactions, the combination of optical plus gravitational potential leads to periodic time-dependent atom current with frequency determined by the gravitational potential difference between neighbouring sites. This effect is analogous to the ac Josephson effects in SJJs where the frequency is determined by the chemical potential difference between two superconducting reservoirs. More recent studies have measured the Josephson critical current in a linear chain of condensates produced in an optical lattice by observing the small amplitude atomic oscillations when the centre of the harmonic potential is suddenly displaced along the optical axis [43]. However if the displacement is bigger than a critical value the phase coherence and superfluidity of the BEC are destroyed [44].

Double-well systems provide simple models for understanding Bosonic Josephson junctions (BJJs). The aim of this Thesis is to explore Josephson effects in a double-well potential. The motivation arises from the expectation of new dynamical regimes not accessible in superconducting/superfluid systems. In particular we find new effects due to the interparticle interactions which are sensitive to the choice of the initial conditions.

Magnetic [32, 48] and optical [49, 50] double-well potentials have been created in recent experiments and a proposal for a magnetic double-well has also been reported [51]. These experiments are related with the so-called "external" Josephson effect in which two macroscopic states are spatially separated [2]. However up to now the experimental realization of the Josephson effects in a double-well potential is not possible due to the small critical current which is unobservable in current experimental set ups.

Another type of weak link was realized in JILA [52] which is related with the "internal" Josephson effect in which two states differ in an internal quantum number [2]. In Ref. [52] ^{87}Rb atoms in two different hyperfine states were confined in the same magnetic trap. The system is driven by a weak field which couples the two internal states and transfers population back and forth between condensates. As a consequence Josephson-like oscillations in the relative population are observed which depend on the initial relative populations and phase. An analogue of this effect was observed in the 1970s with the ^{3}He-A [53].

Considerable theoretical work based on mean-field theory has been performed on BECs in a double-well potential [52, 54, 55, 56, 57, 58, 59, 60, 61]. Mean-field theory provides an accurate description of the evolution of the macroscopic wavefunction and the corresponding nonlinear dynamics at low temperatures. A simplified two-state model can be developed using the ansatz that the order parameter may be written in terms of a superposition of two wavefunctions on each well [62, 63, 64, 65, 66, 67, 68, 69, 70, 71, 72, 73]. The dynamics is described in terms of two variables; the phase difference between two condensates and the relative population difference which is the BEC analogue of the current in SJJs. These variables obey a set of two coupled nonlinear equations which are the generalization of Eqs. (1.1) and (1.2) for the current and the relative phase in SJJs.

In the following sections we shall give a brief review of the Gross-Pitaevskii equation and introduce the Josephson equations in the context of SJJs.

1.3 Bose-Einstein Condensates

1.3.1 The non-interacting case

We consider a system of N non-interacting *spinless* bosons, each of mass m confined by an external potential $V_{\text{trap}}(r)$. The many-body Hamiltonian is the sum of single-particle Hamiltonians [1, 5],

$$\widehat{H} = \sum_{i=1}^{N} \widehat{h}_i, \tag{1.3}$$

where $\widehat{h}_i$ is the Hamiltonian of the ith particle with spatial coordinate r_i is given by,

$$\widehat{h}_i = -\frac{\hbar^2}{2m} \nabla_{r_i}^2 + V_{\text{trap}}(r_i) \ . \tag{1.4}$$

In second quantisation and using the basis of single-particle creation $\widehat{a}_\ell^\dagger$ and annilation $\widehat{a}_m$ operators, the many-body Hamiltonian, Eq. (1.3), of the system is given by,

$$\widehat{H} = \sum_{\ell m} \epsilon_{\ell m} \widehat{a}_\ell^\dagger \widehat{a}_m \ , \tag{1.5}$$

where

$$\epsilon_{\ell m} = \int \mathrm{d}^3 r \, \psi_\ell^*(r_i) \widehat{h}_i \psi_m(r_i) \tag{1.6}$$

is the single-particle energy expanded in the trap eigenstates $\psi_{\ell m}(r)$. The single-particle creation and annihilation operators satisfy the commutation relations [5],

$$\left[\widehat{a}_\ell, \widehat{a}_m^\dagger\right] = \delta_{\ell m}, \quad \left[\widehat{a}_\ell, \widehat{a}_m\right] = 0 \quad \text{and} \quad \left[\widehat{a}_\ell^\dagger, \widehat{a}_m^\dagger\right] = 0 \ . \tag{1.7}$$

The equivalent form of the many-body Hamiltonian, Eq. (1.5), in terms of the quantum field creation $\widehat{\psi}^\dagger(r)$ and annihilation $\widehat{\psi}(r)$ operators is given by [5],

$$\widehat{H} = \int \mathrm{d}^3 r \, \widehat{\psi}^\dagger(r) \left[-\frac{\hbar^2}{2m} \nabla^2 + V_{\text{trap}}(r)\right] \widehat{\psi}(r) \ , \tag{1.8}$$

where the field operators in the basis of single-particle creation and annihilation operators [5] can be written as,

$$\widehat{\psi}^{\dagger}\left(\boldsymbol{r}\right) = \sum_{\ell} \psi_{\ell}\left(\boldsymbol{r}\right)\widehat{a}_{\ell}^{\dagger}, \tag{1.9}$$

and

$$\widehat{\psi}\left(\boldsymbol{r}\right) = \sum_{\ell} \psi_{\ell}\left(\boldsymbol{r}\right)\widehat{a}_{\ell}. \tag{1.10}$$

The field creation and annihilation operators satisfy the bosonic commutation relations [5],

$$\left[\widehat{\psi}\left(\boldsymbol{r}\right),\widehat{\psi}^{\dagger}\left(\boldsymbol{r}'\right)\right] = \delta\left(\boldsymbol{r}-\boldsymbol{r}'\right), \quad \left[\widehat{\psi}\left(\boldsymbol{r}\right),\widehat{\psi}\left(\boldsymbol{r}'\right)\right] = 0, \quad \left[\widehat{\psi}^{\dagger}\left(\boldsymbol{r}\right),\widehat{\psi}^{\dagger}\left(\boldsymbol{r}'\right)\right] = 0. \tag{1.11}$$

For an ideal Bose gas, BEC occurs when all atoms occupy the same single-particle ground state. Then the total wavefunction for the ground state of the Hamiltonian Eq. (1.8) for non-interacting particles is just the product of these single-particle ground state wavefunctions which are given by the solution of the linear Schrödinger equation, i.e.,

$$\psi\left(\boldsymbol{r}_{1},..,\boldsymbol{r}_{N}\right) = \prod_{i} \psi_{0}\left(\boldsymbol{r}_{i}\right). \tag{1.12}$$

The total number of atoms N in the grand-canonical ensemble and using Bose statistics is given by the sum over the eigenstates of single-particle Hamiltonians $\widehat{h}_{i}$ [5]

$$N = \sum_{n_{x},n_{y},n_{z}} \frac{1}{\exp\left[\beta\left(\epsilon_{n_{x},n_{y},n_{z}}-\mu\right)\right]-1}, \tag{1.13}$$

where μ is the chemical potential and $\beta = (k_{B}T)^{-1}$. The confining potential for alkali atoms at low energies is given by

$$V_{\text{trap}}\left(\boldsymbol{r}\right) = \frac{m}{2}\left(\omega_{x}^{2}x^{2}+\omega_{y}^{2}y^{2}+\omega_{z}^{2}z^{2}\right). \tag{1.14}$$

The thermodynamic limit in the case of harmonic trapping is defined by setting $N \to \infty$ and $\omega_0 \to 0$, with the combination $N\omega_0^3$ kept fixed where $\omega_0 = (\omega_x \omega_y \omega_z)^{1/3}$ is the geometric average of trap frequencies. The eigenvalues of these single-particle Hamiltonians have the form

$$\epsilon_{n_x n_y n_z} = \left(n_x + \frac{1}{2}\right)\hbar\omega_x + \left(n_y + \frac{1}{2}\right)\hbar\omega_y + \left(n_z + \frac{1}{2}\right)\hbar\omega_z . \tag{1.15}$$

The population of the ground state N_0 becomes macroscopic, of the order of N, when the chemical potential μ becomes equal to the energy of the lowest state $\epsilon_{000} = (3/2)\hbar\overline{\omega}$, where $\overline{\omega} = (\omega_x + \omega_y + \omega_z)/3$ is the arithmetic average of the trapping frequencies.

Using the condition that the excitation energies are much larger than the level spacing of the trapping potential one can replace the sum by an integral over eigenstates of the single-particle Hamiltonian. This semi-classical approximation is valid when $k_B T \gg \hbar\omega_{ho}$.

If we separate the number of particles in the ground state N_0 from the rest of the integral one can find the number of particles in the excited states

$$N - N_0 = \int_0^\infty \frac{dn_x dn_y dn_z}{\exp\left[\beta\hbar\left(\omega_x n_x + \omega_y n_y + \omega_z n_z\right)\right] - 1} . \tag{1.16}$$

The above integral can be evaluated if we make a change of variables $\beta\hbar\omega_x n_x = x$, etc, giving

$$N - N_0 = \zeta(3)\left(\frac{k_B T}{\hbar\omega_{ho}}\right)^3 , \tag{1.17}$$

where $\zeta(x) \equiv 1 + 2^{-x} + 3^{-x} + 4^{-x} + \ldots$ is the Riemann ζ function yielding results such as $\zeta(3) = 1.202$, $\zeta(3/2) = 2.612$, etc. We can also calculate the transition temperature T_c^0, for non-interacting bosons, by setting $N_0 \to 0$ at the transition. One finds that

$$k_B T_c^0 = \hbar\omega_0\left(\frac{N}{\zeta(3)}\right)^{1/3} . \tag{1.18}$$

Inserting the above expression for the transition temperature into Eq. (1.17) one finds the T dependence of the condensate fraction for $T < T_c^0$,

$$\frac{N_0}{N} = 1 - \left(\frac{T}{T_c^0}\right)^3 . \tag{1.19}$$

The above results for the transition temperature and the condensate fraction can be compared with those for an ideal, i.e. non-interacting, homogeneous gas in three dimensions. In this case the many-body Hamiltonian is given by

$$H = \int \mathrm{d}^3 r \; \hat{\psi}^\dagger(r) \left[-\frac{\hbar^2}{2m}\nabla^2\right] \hat{\psi}(r) , \tag{1.20}$$

while the eigenvalues of the eigenstates of single-particle Hamiltonians in free space are given by $\epsilon = p^2/2m$.

Applying the same method we used for trapped bosons, one finds

$$k_B T_c^0 = \frac{2\pi\hbar^2}{m} \left(\frac{N}{V\zeta(3/2)}\right)^{2/3} = 3.313 \, \frac{\hbar^2}{m} \left(\frac{N}{V}\right)^{2/3} , \tag{1.21}$$

for the transition temperature, and

$$\frac{N_0}{N} = 1 - \left(\frac{T}{T_c^0}\right)^{3/2} , \tag{1.22}$$

for the condensate fraction. Comparing Eqs. (1.16) and (1.19) we note that the trapping potential affects the transition temperature and the number of particles in the condensate. We also see that for the same total number of atoms, the number of atoms in the ground state is larger in the case of a confined system than a free system. This can be explained using statistical mechanics and the energy density of states (see for example Huang [5]).

1.3.2 The interacting case

a. Mean-field theory

In this subsection, we consider the general case of N *spinless* bosons that are interacting with a potential $U(r - r')$. The many-body Hamiltonian is given by the same equation as Eq. (1.8) if we add an extra term due to the interactions. Thus using again second quantisation and the basis of field operators the total Hamiltonian can be written in the form

$$\widehat{H} = \int d^3 r \, \widehat{\psi}^\dagger(r) \left[-\frac{\hbar^2}{2m} \nabla^2 + V_{\text{trap}}(r) \right] \widehat{\psi}(r) +$$
$$\frac{1}{2} \int d^3 r d^3 r' \, \widehat{\psi}^\dagger(r) \widehat{\psi}^\dagger(r') U(r - r') \widehat{\psi}(r') \widehat{\psi}(r) \ . \tag{1.23}$$

The last term represents the effects of two-body interatomic interactions (neglecting 3-body interactions as the system is dilute). Using the same analysis as in the previous subsection, the field operators satisfy the commutation relations, Eq. (1.11), and we can expand them in the basis of single-particle creation and annihilation operators, Eqs. (1.9) and (1.10). The ground-state wave function is again the product of N single-particle wavefunctions which are now given by the solution of a nonlinear Schrödinger-type equation.

Bogoliubov was the first to describe a dilute Bose gas in terms of mean field theory [1]. In the case of weak interactions BEC occurs when a macroscopic number of atoms N_0 occupies the same single-particle wavefunction and the ratio $(N - N_0)/N \ll 1$ in the thermodynamic limit $N \to \infty$. In this case, $N_0 + 1 \simeq N_0$ and the operators $\widehat{a}_0$ and $\widehat{a}_0^+$ can be treated as real numbers: $\widehat{a}_0 = \widehat{a}_0^+ = \sqrt{N_0}$, and the field operator can be decomposed in

$$\widehat{\psi}(r) = \psi_0 + \widehat{\psi}'(r) = \sqrt{\frac{N_0}{V}} + \widehat{\psi}'(r) \ , \tag{1.24}$$

where $\widehat{\psi}'(r) \ll \sqrt{\frac{N_0}{V}}$ is called quantum depletion. Treating the depletion as a small perturbation, Bogoliubov built the "first-order" theory of uniform Bose gases.

b. The Gross-Pitaevskii equation

The Bogoliubov theory can also be applied for nonuniform and time-dependent

configurations [1]. In this case the field operator can be decomposed as

$$\hat{\Psi}(r,t) = \psi(r,t) + \hat{\Psi}'(r,t) \ ,$$

(1.25)

where $\psi(r,t)$ is a classical field defined as the expectation value of the field operator, $\psi(r,t) = \left\langle \hat{\Psi}(r,t) \right\rangle$. It has a well-defined phase and its modulus gives the density of the condensate $n_0 = |\psi(r,t)|^2$. It is often called the wave function of the condensate and it characterises the off-diagonal behaviour of the one-particle density matrix

$$\rho(r',r,t) = \left\langle \psi^*(r',t)\,\psi(r,t) \right\rangle \ ,$$

(1.26)

which is different from zero for macroscopic distances $|r - r'|$ of the order of the size of the sample (long-range order).

In order to derive the equation of the condensate wavefunction $\psi(r,t)$ we use the time evolution for the field operator $\hat{\Psi}(r,t)$ in the Heisenberg picture with the many-body Hamiltonian, Eq. (1.23). This yields,

$$
\begin{aligned}
i\hbar\frac{\partial}{\partial t}\hat{\Psi}(r,t) &= \left[\hat{\Psi}(r,t),\hat{H}\right] \\
&= \left[-\frac{\hbar^2\nabla^2}{2m} + V_{\text{trap}}(r)\right]\hat{\Psi}(r,t) + \\
&\quad \left[\int \mathrm{d}^3r'\,\hat{\Psi}^\dagger(r',t)\,U(r-r')\,\hat{\Psi}(r',t)\right]\hat{\Psi}(r,t) \ .
\end{aligned}
$$

(1.27)

We also make some additional approximations [1]: (a) For $T = 0$ and for weakly interacting systems we can replace $\hat{\Psi}(r,t)$ with the classical field $\psi(r,t)$. (b) At low temperatures the condensates are dilute (interparticle spacing $n^{1/3}$ far exceeds the range of interactions which is determined by the s-wave scattering length, a, $na^3 \ll 1$) and the interatomic collisions are described in the limit of s-wave scattering. With this approximation we can replace $U(r - r')$ with an effective interaction $g\delta(r - r')$ where g is a coupling constant given by the equation

$$g = \frac{4\pi\hbar^2 a}{m}$$

(1.28)

which characterises the strength of interparticle interactions. The value of g can be either zero, positive or negative according to the sign of the scattering length a. For $g = 0$ we recover the ideal, non-interacting limit. Positive (negative) values of a correspond to effective repulsive (attractive) interactions respectively. With this approximation for the interatomic potential and by substitution in the equation of motion Eq. (1.27) for the wavefunction $\psi(r, t)$, one finds

$$i\hbar\frac{\partial}{\partial t}\psi(r,t) = \left(-\frac{\hbar^2\nabla^2}{2m} + V_{\text{trap}}(r) + \mathcal{N}g\left|\psi(r,t)\right|^2\right)\psi(r,t) , \qquad (1.29)$$

where m is the atomic mass, $\mathcal{N}$ is the number of atoms in the condensate, g is the self-interaction constant and $V_{\text{trap}}(r)$ is the total confining potential. In the most common case of a three dimensional magnetic trap V_{trap} has the form,

$$V_{\text{trap}}(r) = \frac{1}{2}m\left(\omega_\perp^2(x^2 + y^2) + \omega_\parallel^2 z^2\right) = \frac{1}{2}m\omega_\perp^2\left(x^2 + y^2 + \lambda^2 z^2\right) , \qquad (1.30)$$

where $\omega_\perp$ and $\omega_\parallel$ are the transverse and the axial trap frequencies respectively and $\lambda \equiv \omega_\parallel/\omega_\perp$ is called the asymmetry parameter. If $\lambda = 1$ the trap is spherical, whereas if $\lambda < 1$ the trap is "cigar-shaped" and for $\lambda > 1$ the trap is "pancake-like". The condensate wavefunction is normalised to unity that is,

$$\int_{-\infty}^{+\infty} \left|\psi(r,t)\right|^2 d^3r = 1 . \qquad (1.31)$$

Eq. (1.29) is called the Gross-Pitaevskii equation (GPE). It has the form of a nonlinear Schrödinger equation. The GPE can be used to describe the behaviour of dilute Bose gases at low temperatures, where the depletion of the condensate is negligible. At finite temperatures not all the atoms are in the condensate and the GPE can also be generalized to include thermally excited particles [74].

1.4 Superconductors

Superconductivity is the ability of certain materials to conduct electric current with practically zero resistance a phenomenon which is analogous to the superflow of He

II through narrow channels. Analogous to helium, metals become superconductors below a critical temperature T_c. The transition to superconductivity is marked by a sharp discontinuity in the specific heat, contrasts to the λ anomaly in helium.

Superconductivity was first observed in 1911 by H. K. Onnes, a Dutch physicist who observed that mercury displayed no electrical resistance when cooled to 4 K, the temperature of liquid He. Since then superconductivity has been achieved at higher temperatures, although the achievement of superconductivity at room temperatures remains an open question.

The microscopic theory that describes superconductivity was developed by Bardeen, Cooper and Schrieffer and is known as BCS theory [11]. It's based on s-wave pairing of two electrons which form Cooper pairs in which the centre-of-mass momentum is zero. The attractive interaction between electrons is via the metallic lattice: if an electron travels through the lattice, it couples to the positive ions, emitting a phonon. If a pair of electrons travels through the lattice, then one electron can emit a phonon which is absorbed by another. It is found that the interaction involving the exchange of a phonon is negative then the force between the electrons is attractive. As the electrostatic (Coulomb) interaction between a pair of electrons is always repulsive, a material only becomes superconducting if the net force is attractive. At zero temperature the ground state of the material is described by the BCS ground state which is formed by Cooper pairs and is separated by an energy gap Δ from the Fermi energy of the normal metal.

Consider two superconductors separated by a thin insulating material which are close enough that one affects the other. In this case the tunnelling of Cooper pairs produces "supercurrent" from one superconductor to the other. The weak link is a junction referred to as "Josephson junction" and the tunnelling is known as Josephson tunnelling. There is also single electron, "normal tunnelling", in parallel with the Josephson current but this normal tunnelling is very small compared to the Josephson current. The Josephson effect and Josephson junctions have many practical applications and perhaps the most well known devices which utilize the Josephson effect, are superconducting quantum interference devices (SQUID's). Because of

its importance we summarize in the next Section the basic equations that describe Josephson tunnelling based on a "two-level" picture and on the resistively shunted junction (RSJ) model. The derivation and notation follow that in [31].

1.5 Josephson Equations

1.5.1 Two-level model

Let us consider the system superconductor-barrier-superconunctor. Below a critical temperature T_c a macroscopically large number of Cooper pairs condensate into the ground state. We denote by $\Psi_L(\Psi_R)$ the pair wavefunction for the left (right) superconductor so that $|\Psi|^2$ represents the actual Cooper pair density ρ. Thus,

$$|\Psi_L|^2 = \rho_L, \quad \text{and} \quad |\Psi_R|^2 = \rho_R . \tag{1.32}$$

We assume weak coupling between the two superconductors due to finite overlap of the wavefunctions $\Psi_{L,R}$. In the basis of $|\Psi_L\rangle$, $|\Psi_R\rangle$ a vector that describes the system is of the form,

$$|\psi\rangle = c_L|\Psi_L\rangle + c_R|\Psi_R\rangle , \tag{1.33}$$

where $c_{L,R}$ describe the amplitudes to find a particle in the left/right state respectively. The time evolution is described by the Schrödinger equation,

$$i\hbar\partial_t|\psi\rangle = H|\psi\rangle = (H_L + H_T + H_R)|\psi\rangle , \tag{1.34}$$

where,

$$H_L = E_L|\Psi_L\rangle\langle\Psi_L| \quad \text{and} \quad H_R = E_R|\Psi_R\rangle\langle\Psi_R| \tag{1.35}$$

are the two Hamiltonians relative to the unperturbed states $|\Psi_L\rangle$ and $|\Psi_R\rangle$ with $E_{L,R}$ the ground state energies of the two superconductors and

$$H_T = K\left[|\Psi_L\rangle\langle\Psi_R| + |\Psi_R\rangle\langle\Psi_L|\right] \tag{1.36}$$

is the tunnelling Hamiltonian between the two states with K the coupling constant. Substituting Eq. (1.30) into (1.31) we find,

$$i\hbar \dot{c}_L = E_L c_L + K c_R \, , \tag{1.37}$$

$$i\hbar \dot{c}_R = E_R c_R + K c_L \, . \tag{1.38}$$

For two isolated superconductors, the energy terms are $E_L = 2\mu_L$ and $E_R = 2\mu_R$ with μ_L and μ_R are the chemical potentials. With a dc voltage across the junction, the chemical potentials are shifted thus creating an energy difference $E_L - E_R = 2eV$. Redefining the zero energy to be halfway between the two values on the left and on the right we obtain,

$$i\hbar \frac{\partial c_L}{\partial t} = eV c_L + K c_R \, , \tag{1.39}$$

$$i\hbar \frac{\partial c_R}{\partial t} = -eV c_R + K c_L \, . \tag{1.40}$$

The amplitudes $c_{L,R}$ can be written in terms of the density ρ and the phase ϕ,

$$c_L = \sqrt{\rho_L}\exp(i\phi_L) \quad \text{and} \quad c_R = \sqrt{\rho_R}\exp(i\phi_R) \, . \tag{1.41}$$

Separating the real and imaginary parts in Eq. (1.40) we obtain,

$$\frac{\partial \rho_L}{\partial t} = \frac{2}{\hbar} K \sqrt{\rho_L \rho_R} \sin\phi \, , \tag{1.42}$$

$$\frac{\partial \rho_R}{\partial t} = -\frac{2}{\hbar} K \sqrt{\rho_L \rho_R} \sin\phi \tag{1.43}$$

and

$$\frac{\partial \phi_L}{\partial t} = \frac{K}{\hbar} \sqrt{\frac{\rho_L}{\rho_R}} \cos\phi + \frac{eV}{\hbar} \, , \tag{1.44}$$

$$\frac{\partial \phi_R}{\partial t} = \frac{K}{\hbar} \sqrt{\frac{\rho_L}{\rho_R}} \cos\phi - \frac{eV}{\hbar} \, . \tag{1.45}$$

respectively, where we have defined

$$\phi = \phi_L - \phi_R \tag{1.46}$$

as the phase difference across the junction. The pair current density I is given by

$$I \equiv \frac{\partial \rho_L}{\partial t} = -\frac{\partial \rho_R}{\partial t} \qquad (1.47)$$

thus using the above equations we take

$$I = \frac{2K}{\hbar} \sqrt{\rho_L \rho_R} \sin \phi \; . \qquad (1.48)$$

If we now assume $\rho_L = \rho_R = \rho$ Eq. (1.48) gives

$$I = I_0 \sin \phi \; , \qquad (1.49)$$

where $I_0 = 2K\rho/\hbar$. From Eq. (1.45) it follows,

$$\frac{\partial \phi}{\partial t} = \frac{2eV}{\hbar} \; . \qquad (1.50)$$

Equations (1.49) and (1.50) describe the Josephson effects in SJJ. We can define two cases. If $V = 0$, ϕ is constant but not necessarily zero so a finite current flows across the junction with zero potential until a critical value I_0. However if we apply a static voltage, $V \neq 0$ then

$$\phi = \phi_0 + \frac{2eV}{\hbar}t \quad \text{and} \quad I = I_0 \sin\left(\phi_0 + \frac{2eV}{\hbar}t\right) \qquad (1.51)$$

which corresponds to an ac Josephson effect. Thus in this case we have a current across the junction which varies with time, with frequency $\omega = 2eV/\hbar$. One possibility to observe the effect is to expose the Josephson junction to electromagnetic radiation of frequency ω' which leads to steps in the $V - I$ characteristics of the junction. The steps occur at voltages, $V_n = n\hbar\omega'/2eV$, where n is an integer which identifies a constant voltage step in the $V - I$ characteristics.

1.5.2 Resistively Shunted Junction model

Superconducting Josephson Junctions (SJJ) are usually modelled by the resistibly shunted junction (RSJ) model. The weak link is represented by the equivalent

circuit of Fig. 1.1. The RSJ model assumes that each junction is equivalent to an ideal junction with capacitance and quasiparticle conductance in parallel with a Josephson element. The circuit is current biased with a dc current I and an ac component of amplitude I_1. We can apply the Kirchhoff's current law to derive the
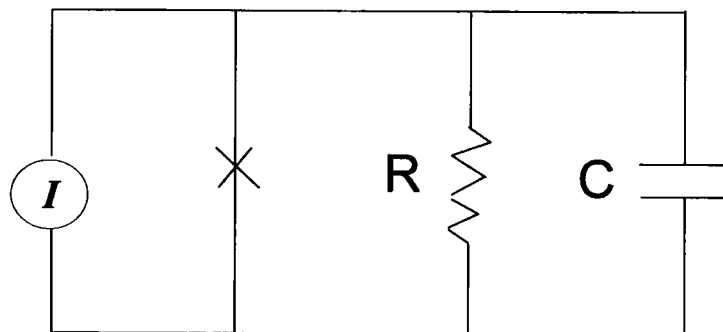
Figure 1.1: Circuit diagram for a Josephson junction. The × represents an ideal junction.

equations for the circuit,

$$I = C\frac{dV}{dt} + GV + I_1 \sin\phi \quad \text{with} \quad G = 1/R, \tag{1.52}$$

where the first term describes the displacement current through the capacitor C, GV is the current through the resistor R, and $I_1 \sin\phi$ is the Josephson supercurrent. The voltage $V(t)$ is related to the phase difference $\phi(t)$, by Eq. (1.50). Substituting into Eq. (1.52), we obtain,

$$I = \frac{\hbar}{2e}C\frac{d^2\phi}{dt^2} + \frac{\hbar}{2e}\frac{1}{R}\frac{d\phi}{dt} + I_1 \sin\phi \ . \tag{1.53}$$

We can define for convenience dimensionless variables,

$$t' = \omega_I t \quad \text{and} \quad \beta_I = \frac{1}{\omega_I}\frac{1}{RC} \ , \tag{1.54}$$

where $\omega_I = \sqrt{2eI_1/\hbar C}$ is the plasma frequency, yielding,

$$a = \frac{d^2\phi}{dt'} + \beta_I\frac{d\phi}{dt'} + \sin\phi \ , \tag{1.55}$$

where $a = I/I_1$ is the normalized current. Eq. (1.55) is not analytically solvable except in the case in which the second derivative term is neglected. In other cases solutions can be obtained numerically or by using mechanical models such as a single *rigid* pendulum of mass m and length ℓ, where θ is the angle from the vertical, shown in Fig. 1.2. In this case using Classical Mechanics the equation of motion describing
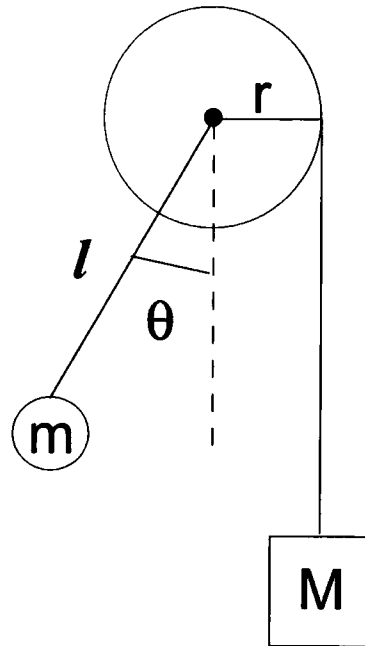
Figure 1.2: Single pendulum of mass m, length ℓ, and θ is the angle from the vertical.

the pendulum is,

$$\tau_o = M_I \frac{d^2\theta}{dt^2} \quad \text{or} \quad Mrg - mg\ell\sin\theta - D_t\frac{d\theta}{dt} = M_I\frac{d^2\theta}{dt^2}, \tag{1.56}$$

where M_I is the moment of inertia and τ_o is the total torque which has three terms: the first term is the applied torque τ_a, the second term represents the torque due to gravity and the last term is the opposing torque due to friction with D_t the damping coefficient. Eq. (1.56) becomes,

$$\tau_a = M_I\frac{d^2\theta}{dt^2} + D_t\frac{d\theta}{dt} + mg\ell\sin\theta . \tag{1.57}$$

Introducing the parameters,

$$\tau = \omega_M t, \quad \beta_m = \frac{D_t}{\sqrt{M_I mg\ell}} \quad \text{and} \quad \omega_M = (mg\ell/M_I)^{1/2} \,, \tag{1.58}$$

Eq. (1.57), becomes,

$$\frac{\tau_a}{mg\ell} = \frac{d^2\theta}{d\tau^2} + \beta_M \frac{d\theta}{d\tau} + \sin\theta \,. \tag{1.59}$$

There are close analogies with Eq. (1.55) that describes the Josephson weak link as shown below:

$$
\begin{aligned}
I \ (\text{external current}) \quad &\rightarrow \quad \tau_a \quad (\text{applied torque}) \\
C \quad (\text{capacitor}) \quad &\rightarrow \quad M_I \quad (\text{moment of inertia}) \\
1/R \quad (\text{resistor}) \quad &\rightarrow \quad D_t \quad (\text{damping coefficient}) \\
I_o \ (\text{maximum current}) \quad &\rightarrow \quad mg\ell \quad (\text{maximum torque due to gravity}) \\
\phi \quad (\text{phase difference}) \quad &\rightarrow \quad \theta \quad (\text{angle from the vertical}) \,.
\end{aligned}
$$

The mechanical analogue of a *rigid* pendulum has been successfully used to describe SJJs and in the following Chapters we shall see how this model is modified to describe BJJs as well (see Chapter 4).

1.6   Plan of Thesis

In this thesis we shall investigate Josephson effects in dilute, weakly interacting, low temperature alkali gases confined in a double-well potential within the Gross-Pitaevskii mean-field theory.

In Chapter 2, we review stationary solutions to the GPE for different single-harmonic trap geometries and values of the nonlinear parameter. We introduce the Thomas-Fermi approximation and study dynamical properties of the condensate such as collective excitations. In Chapter 3, we expand our previous knowledge of a BEC

in a single harmonic trap to a double-well potential and study eigenenergy states by numerical solution of the GPE and the two-state model. In Chapter 4 we begin our study of Josephson dynamics in a double-well potential by considering solutions from the two-state model for the ground and first excited states that have equal populations at the centre of the trap. In Chapters 5 and 6 we go beyond the two-state model by considering full integration of the GPE to study the dynamics for ground and first excited states respectively. In Chapter 7, we study properties of a BEC with attractive interactions in both a single trap and a double-well potential. In the latter case, the dynamical properties of such system are examined in Chapter 8 and we extend our studies to a multi-well system. The Conclusions summarise the main results.

Several topics discussed in this thesis have been published in the following papers:

- *Josephson spectroscopy of a dilute Bose-Einstein condensate in a double-well potential*, E. Sakellari, M. Leadbeater, N. J. Kylstra and C. S. Adams, Phys. Rev. A. **66**, 033612 (2002).

- *Josephson tunnelling of a phase imprinted Bose-Einstein condensate in a time-dependent double-well potential*, E. Sakellari, N. P. Proukakis, M. Leadbeater and C. S. Adams, New J. Phys. **6**, 42 (2004).

- *Tunnelling induced collapse of an atomic Bose-Einstein condensate in a double-well potential*, E. Sakellari, N. P. Proukakis and C. S. Adams, submitted

Chapter 2

Numerical solutions of the Gross-Pitaevskii equation

We present numerical solutions of the stationary Gross-Pitaevskii equation, GPE, for positive and negative scattering lengths. We begin by expressing GPE in dimensionless units and define the energy functional. We show how to reduce the three dimensional GPE to a one dimensional equation. We present numerical results in one and three dimensions in the case of a spherical and a cylindrical trap and consider the Thomas-Fermi limit. Finally we study collective excitations and compare the numerical results with analytical solutions, providing a stringent test of our numerical methods.

2.1   Introduction

At low temperatures, the behaviour of a Bose-Einstein condensate is accurately described by a nonlinear Schrödinger equation known as the Gross-Pitaevskii equation, (GPE), [1, 2]

$$i\hbar\frac{\partial}{\partial t}\psi\left(\boldsymbol{r},t\right) = \left(-\frac{\hbar^2\nabla^2}{2m} + V_{\text{trap}}\left(\boldsymbol{r}\right) + \mathcal{N}g\left|\psi\left(\boldsymbol{r},t\right)\right|^2\right)\psi\left(\boldsymbol{r},t\right)\ , \qquad (2.1)$$

where $g = 4\pi\hbar^2 a/m$ is the usual three-dimensional scattering amplitude, defined in terms of the *s*-wave scattering length a, and $\mathcal{N}$ is the total number of atoms

(mass m). The function $\psi(r,t)$ is an order parameter and can be regarded as the wavefunction of the single-particle state into which condensation occurs. $V_{\text{trap}}(r)$ represents the total confining potential. Large stable condensates can be produced for positive values of the scattering length which correspond to repulsive interactions. On the other hand, spatially confined condensates with negative values of the scattering length become unstable against collapse if the number of atoms in the condensate increases above a critical value [1, 15, 75, 76, 77, 78, 79]. Although at low temperatures the atomic clouds realized in experiments are dilute, the effects of interactions are important and determine the shape, energy and elementary excitations of the condensate cloud.

GPE has been successfully applied to the dilute, near zero temperature Bose gas. Numerical solution of the GPE (2.1), has been obtained by several authors see for example [1, 75, 80, 81, 82, 83]. Solutions of the GPE provide information about the density, chemical potential and the evolution of the condensate. Early experimental studies also confirmed that the GPE is accurate in the low temperature limit [84, 85].

It is convenient to work in dimensionless units. Therefore we begin this Chapter in Section 2.2 by rescaling the GPE (2.1), and the nonlinearity g in dimensionless units and discuss typical numbers of atoms in the condensate $\mathcal{N}$. In Section 2.3 we introduce the three dimensional energy functional. In Section 2.4 we show how to reduce the three dimensional GPE to an effective one dimensional equation in the limit of tight transverse confinement. We present numerical solutions in one and three dimensions in Sections 2.5 and 2.6 respectively. We consider both cases of repulsive and attractive interactions. We then discuss in Section 2.7 the so-called Thomas-Fermi approximation, where the ground state can be calculated analytically. Finally, in Section 2.8 we discuss the dynamic behaviour of the condensate by studying the collective modes.

2.2 Harmonic Oscillator Units

For harmonically confined gases we use the so-called harmonic oscillator units (h.o.u.). The distance unit that is associated with the size of the confining potential is the oscillator length $a_\perp = \sqrt{\hbar/m\omega_\perp}$ in the transverse direction(s) and $a_\parallel = \sqrt{\hbar/m\omega_\parallel}$ in the z-direction, which denote the size of the noninteracting ground state wavefunction in a harmonic oscillator potential with transverse and longitudinal confining frequencies $\omega_\perp$ and $\omega_\parallel$, respectively. Using the above lengths the spatial transformation to the harmonic oscillator units becomes,

$$r_i' = a_\perp^{-1} r_i \; , \tag{2.2}$$

where the index $i = 1, 2, 3$ denotes the three space coordinates x, y, z. Similarly, time and energy are defined in terms of the transverse trap frequency,

$$t' = \omega_\perp t \; , \tag{2.3}$$

and

$$E' = (\hbar\omega_\perp)^{-1} E \; . \tag{2.4}$$

With these transformations the normalisation condition for the condensate wavefunction $\psi(r, t)$, becomes,

$$\int_{-\infty}^{+\infty} |\psi(r, t)|^2 \, d^3r = \int_{-\infty}^{+\infty} |\psi'(r', t')|^2 \, d^3r' = 1 \tag{2.5}$$

where,

$$\psi'(r', t') = a_\perp^{-3/2} \psi(r, t) \, , \tag{2.6}$$

is the wavefunction in h.o.u. Applying all the above transformations, we obtain the following dimensionless GPE from Eq. (2.1) (primes henceforth neglected for

convenience),

$$i\frac{\partial}{\partial t}\psi(\boldsymbol{r},t) = \left[-\frac{1}{2}\nabla^2 + V(\boldsymbol{r}) + g_{3D}|\psi(\boldsymbol{r},t)|^2\right]\psi(\boldsymbol{r},t) \tag{2.7}$$

where, $V(\boldsymbol{r})$ represents the total confining potential and

$$g_{3D} = \frac{\mathcal{N}g}{a_\perp^3 \hbar\omega_\perp} = \frac{4\pi\mathcal{N}a}{a_\perp} \tag{2.8}$$

is the three dimensional nonlinearity in h.o.u. The ratio $g_{3D}/4\pi$ introduces an important parameter $\mathcal{N}a/a_\perp$ which characterizes the effects of the interparticle interactions E_{int}, on the zero point kinetic energy, E_{kin} of the condensate at $T \sim 0$. It is obtained by evaluating the ratio E_{int}/E_{kin}: The interaction term is given by $g\mathcal{N}\bar{n}$, where $\bar{n} = \mathcal{N}/a_0^3$ is the average density of the gas, thus $E_{int} \sim \mathcal{N}^2|a|/a_0^3$. Moreover the kinetic term is of the order of $\mathcal{N}\hbar\omega_0$ or equivalently $E_{kin} \sim \mathcal{N}a_0^{-2}$. Taking the ratio E_{int}/E_{kin} we find Eq. (2.8). The importance of this parameter will be emphasised throughout the Thesis.

In order to derive stationary solutions of Eq. (2.7) we use the transformation $\psi(\boldsymbol{r},t) = \exp(-i\mu t)\Psi(\boldsymbol{r})$ and we obtain the three dimensional time-independent GPE,

$$\mu\Psi(\boldsymbol{r}) = \left[-\frac{1}{2}\nabla^2 + V(\boldsymbol{r}) + g_{3D}|\Psi(\boldsymbol{r})|^2\right]\Psi(\boldsymbol{r}) , \tag{2.9}$$

where μ is the dimensionless chemical potential of the three dimensional system. Rearranging the terms in the equation for g_{3D}, Eq. (2.8), one finds the following expression for the number of particles in the condensate $\mathcal{N}$,

$$\mathcal{N} = \frac{g_{3D}}{4\pi}\frac{a_\perp}{a} = \frac{g_{3D}}{4\pi a}\sqrt{\frac{\hbar}{m\omega_\perp}} = \frac{1}{4\pi a}\sqrt{\frac{\hbar}{m}}\frac{g_{3D}}{\sqrt{\omega_\perp}} . \tag{2.10}$$

We can also find an expression to introduce the asymmetry parameter λ via $\omega_\perp = \omega_\parallel/\lambda$. It is clear from Eq. (2.10) that for a given type of atoms, large number of condensate atoms $\mathcal{N}$ can be obtained by increasing the nonlinearity g_{3D} and for small frequencies $\omega_\perp$ and $\omega_\parallel$ and large values of λ. Eq. (2.10) shows that $\mathcal{N}$ is inversely proportional to the mass m and the s-wave scattering length a, therefore for

given transverse trap frequency and nonlinearity, larger values of $\mathcal{N}$ can be obtained with lighter atoms. In Tables 2.1 and 2.2 we give typical values of the number of particles in the condensate $\mathcal{N}$ in the case of positive and negative scattering length respectively for a given choice of the nonlinearity g_{3D}.

Elements	scattering length (nm)	mass (10^{-27}Kg)	$(1/4\pi|a|)\sqrt{\hbar/m}$	$\mathcal{N}$
^{1}H	1.40	1.661	14300.12	11×10^6
^{4}He	16.00	6.644	626.11	3500
^{23}Na	2.79	38.203	1502.23	8500
^{41}K	3.44	68.101	910.09	5106
^{87}Rb	5.77	144.507	215.34	1200
^{133}Cs	23.28	220.913	74.52	420
^{174}Yb	6.00	289.014	0.25	2

Table 2.1: Atom number $\mathcal{N}$ corresponding to a dimensionless nonlinear coefficient $g_{3D} = 10\pi$ and $\omega_\perp = 10\pi$ for various atomic species.

Elements	scattering length (nm)	mass (10^{-27}Kg)	$(1/4\pi|a|)\sqrt{\hbar/m}$	$\mathcal{N}$
^{7}Li	-1.45	11.627	5231.23	1470
^{85}Rb	-19.52	141.185	108.91	30

Table 2.2: Same as Table 2.1 but now we consider $g_{3D} = 0.5\pi$ for the elements with negative scattering length.

2.3 Energy functional

The three dimensional energy functional in h.o.u. is defined by,

$$
\begin{aligned}
E[\Psi] &= \int d\mathbf{r} \left[\frac{1}{2}|\nabla\Psi(\mathbf{r})|^2 + V_{\text{trap}}(\mathbf{r})|\Psi(\mathbf{r})|^2 + \frac{1}{2}g_{3D}|\Psi(\mathbf{r})|^4 \right] \\
&= E_{\text{kin}} + E_{\text{pot}} + E_{\text{int}} .
\end{aligned}
\tag{2.11}
$$

The first term represents the mean kinetic energy of the condensate E_{kin}, the second term is the mean potential energy E_{pot} and the last term is the mean-field interaction energy E_{int}. In case of a harmonic trap (Eq. (1.30)), E_{pot} represents the harmonic

oscillator energy E_{ho} and has the form,

$$E_{\text{ho}} = \frac{1}{2}\left(x^2 + y^2 + \lambda^2 z^2\right) . \tag{2.12}$$

Comparison of Eqs. (2.9) and (2.11) yields,

$$\mu = E + \frac{1}{2}g_{3D}\int d\mathbf{r}|\Psi|^4 , \tag{2.13}$$

therefore in the interacting case, $g_{3D} \neq 0$, the chemical potential is not equal to the mean energy per particle [2, 86, 87].

2.4   Reduction from three to one dimensions

Recently there has been an interest in studying theoretically the properties of quasi-one dimensional trapped atomic gases, see e.g. [88, 89, 90, 91]. Moreover one dimensional Bose systems have also been prepared experimentally showing the transition from three to one dimensional behaviour [92, 93, 94, 95]. These are systems which can be reached by applying a strong confinement in the transverse, x-y plane such that all thermal and interatomic induced excitations are suppressed. The condition that the one dimensional limit is reached is $\mu < \hbar\omega_\perp$ and $k_BT \ll \hbar\omega_\perp$ where μ is the three dimensional chemical potential and $\omega_\perp$ is the frequency of the transverse confinement. In this limit the BEC can be described by a one-dimensional Bose gas in the axial, z-direction. Let us consider a weakly interacting BEC in a cigar-shaped condensate, $\lambda < 1$. The total wavefunction of the condensate is $\psi(x,y,z,t) = \phi(x,y)\Phi(z,t)$ where $\phi(x,y)$ is normalised to unity. In the case of weakly interacting BECs we can assume a Gaussian ansatz for the $\phi(x,y)$ wavefunction,

$$\phi(x,y) = \frac{1}{\sqrt{\pi}}\exp[-(x^2+y^2)/2] . \tag{2.14}$$

Substituting the above expression in the three dimensional energy functional (Eq. (2.11)), in the presence of a harmonic trap (Eq. (1.30)), and integrating the two transverse

degrees of freedom we obtain the one dimensional energy functional, (see Appendix B for analytical derivation),

$$E_{1D}[\Phi] = \int dz \left[\tfrac{1}{2}|\nabla\Phi|^2 + (V(z) + 1)|\Phi|^2 + \tfrac{1}{2}g_{1D}|\Phi|^4 \right] \ . \tag{2.15}$$

In the above equation the constant 1, in units of $\hbar\omega_\perp$, corresponds to the zero-point energy in the transverse directions and g_{1D} is the one-dimensional nonlinear parameter, given by [86, 87],

$$g_{1D} = g_{3D} \int dx dy |\phi(x,y)|^4 = \frac{g_{3D}}{2\pi} \ . \tag{2.16}$$

The reduced one dimensional GPE is obtained by using a variational method,

$$i\partial_t \Phi = \frac{\delta E_{1D}}{\delta \Phi^*} \ , \tag{2.17}$$

and has the form,

$$i\partial_t \Phi(z,t) = \left(-\frac{1}{2}\frac{\partial^2}{\partial z^2} + (V(z) + 1) + g_{1D}|\Phi(z,t)|^2 \right) \Phi(z,t) \ , \tag{2.18}$$

where $\Phi(z,t)$ is normalized to unity, g_{1D} is the one dimensional self-interaction parameter and $V(z)$ is the confining potential in the axial direction. We can replace $\Phi = \psi \exp(-it)$ which drops the constant 1 and obtain the one dimensional time-dependent GPE,

$$i\partial_t \psi(z,t) = \left(-\frac{1}{2}\frac{\partial^2}{\partial z^2} + V(z) + g_{1D}|\psi(z,t)|^2 \right) \psi(z,t) \ , \tag{2.19}$$

with the normalization condition for the wavefunction,

$$\int_{-\infty}^{+\infty} |\psi(z,t)|^2 dz = 1 \ . \tag{2.20}$$

To find stationary time-independent solutions of Eq. (2.19) we make the substitution $\psi(z,t) = \exp(-i\mu_{1D}t)\Psi(z)$ for the condensate wave function in one dimension,

where μ_{1D} is the one dimensional chemical potential. Applying the above transformation to Eq. (2.19) we find the following time-independent equation for $\Psi(z)$ in one dimension,

$$\mu_{1D}\Psi(z) = \left(-\frac{1}{2}\frac{\partial^2}{\partial z^2} + V(z) + g_{1D}|\Psi(z)|^2\right)\Psi(z) . \tag{2.21}$$

We stress that $\Phi(z,t) = \exp(-i\mu_{3D}t)\Psi(z)$ thus combining the above transformations for the wavefunction $\Phi(z,t)$, we obtain $\mu_{3D} = \mu_{1D} + 1$. For a weakly interacting and elongated BEC, we expect the three and one dimensional results to be in good agreement which shows the one-dimensional behaviour of a BEC confined in a cigar-shaped trap. The agreement becomes worse in the Thomas-Fermi (TF) limit which will be discussed in the following sections. For more details on the comparison of three and one dimensional results see Chapters 3 and 6.

2.5 One dimensional solutions of the GPE

We calculate numerically the time-independent solutions of Eq. (2.21). In the case of a harmonic trap in the axial direction, the one dimensional time-independent Eq. (2.21) becomes,

$$\mu_{1D}\Psi(z) = \left(-\frac{1}{2}\frac{\partial^2}{\partial z^2} + \frac{1}{2}z^2 + g_{1D}|\Psi(z)|^2\right)\Psi(z) , \tag{2.22}$$

where the wavefunction satisfies the normalization condition Eq. (2.20) and $g_{1D} = 2\mathcal{N}a/a_\perp$ is a dimensionless coefficient that characterises the strength of interparticle interactions.

For strong repulsive interactions, the interactions dominate and we can drop the kinetic term in Eq. (2.22). This is called the Thomas-Fermi (TF) limit and the density profile takes the parabolic form,

$$|\Psi(z)|^2 = \frac{\mu_{1D} - V(z)}{g_{1D}} . \tag{2.23}$$

Substituting Eq. (2.23) into Eq. (2.20) one obtains an expression for the chemical potential in one dimension in the TF-limit which has the form,

$$\mu_{TF}^{1D} = \frac{1}{2}\left(\frac{3g_{1D}}{2}\right)^{2/3} . \tag{2.24}$$

We solve numerically the one dimensional GPE (2.21), for various values of the one dimensional nonlinear parameter g_{1D} using Newton's method [96]. As an initial wavefunction we consider the normalised nth order wavefunctions of the linear Schrödinger equation in the presence of a harmonic trap,

$$\Psi_n(z) = \left(\frac{1}{\pi^{1/2}2^n n!}\right)^{1/2} H_n(z)e^{-z^2/2} , \tag{2.25}$$

where $H_n(z)$ are the nth order Hermite polynomials.

In Fig. 2.1 we plot density profiles for the three lowest energy states for positive values of g_{1D} [97]. We note that in all cases the density profiles tend to spread out when $g_{1D} > 0$ increases. Moreover the distance from the origin to the density distributions changes very little as $g_{1D} > 0$ increases for the first excited states, Fig. 2.1(b), whereas for the second excited states, the distance of the second node approaches a fixed separation increasing g_{1D}, as shown in Fig. 2.1(c). In Fig. 2.2 we plot the chemical potential as a function of the nonlinear constant $g_{1D} > 0$ for the ground and the first two excited states. We also plot the TF limit for the one dimensional chemical potential given by Eq. (2.24). We note that for large nonlinearities g_{1D} the ground state approaches the TF limit. In Fig. 2.3(a) we plot density profiles for the ground state in the case of negative scattering length. We note that in contrast to repulsive interactions, attractive interactions, $g_{1D} < 0$ increase the central density. In Fig. 2.3(b) we plot the ground state eigenenergy μ, as a function of the nonlinear constant g_{1D}. Fig. 2.3(b) shows that values of μ can be found for all the values of g_{1D} (both positive and negative). For further details about the one dimensional solutions of the GPE in the case of attractive interactions see Chapter 7 and Appendix C.
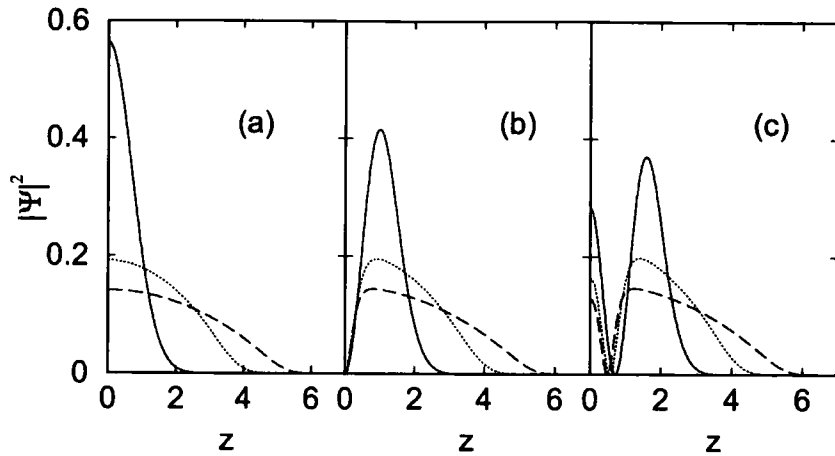
Figure 2.1: Condensate density $|\Psi|^2$, against the position z, for (a) the ground, (b) first and (c) second excited states for positive values of the nonlinear constant g_{1D} =: 0, (solid), 40, (dotted) and 100 (dashed) lines.
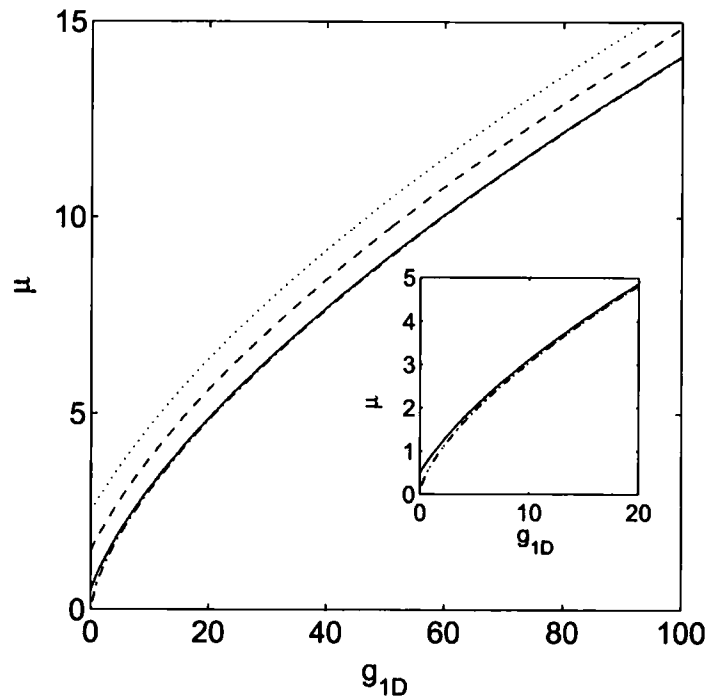
Figure 2.2: Chemical potential μ, for the ground state, (solid), the first, (dashed) and the second (dotted lines) excited states for positive values of the nonlinear constant g_{1D}. The chemical potential for the TF-limit, Eq. (2.24), is also plotted as dashed-dotted line. Inset the chemical potential for the ground (solid) and the TF-limit (dashed-dotted) lines.
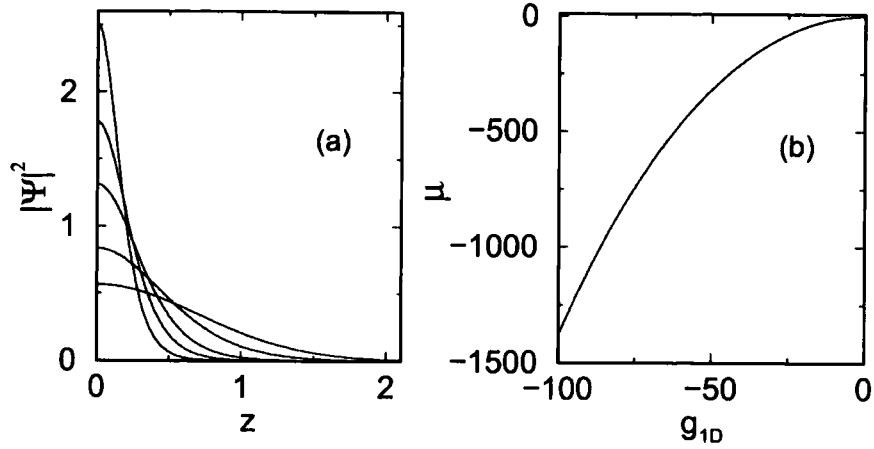
Figure 2.3: (a) Density profiles, $|\Psi|^2$, as a function of the position z, for various values of the nonlinear constant $g_{1D} = -10, -7, -5, -2.5, 0$ (in terms of increasing width). (b) Eigenenergy value, μ, for the ground state as a function of the nonlinear constant g_{1D}.

2.6 Three dimensional solutions of the GPE

We solve the three dimensional time-independent GPE (2.9) in an anisotropic axially symmetric trap. We calculate relevant quantities such as the condensate wavefuction at $T = 0$ and chemical potential of the condensate [1, 75, 81, 82], vortex states [81, 82, 98] and we finally discuss the behaviour of elementary excitations [1, 99, 100, 101].

2.6.1 Basic Equations

Let us consider an axially symmetric trap of the form,

$$V_{\text{trap}}(r) = \frac{1}{2}\left(r_\perp^2 + \lambda^2 z^2\right) , \qquad (2.26)$$

with $r_\perp^2 = x^2 + y^2$. The three dimensional time-independent GPE (2.9) in the presence of an axially symmetric trap, Eq. (2.26) has the form,

$$\mu\Psi(r) = \left[-\tfrac{1}{2}\nabla^2_{r_\perp,\phi,z} + \tfrac{1}{2}\left(r_\perp^2 + \lambda^2 z^2\right) + g_{3D}|\Psi(r)|^2\right]\Psi(r) , \qquad (2.27)$$

where μ is the chemical potential of the full three dimensional system, $\nabla^2_{r_\perp,\phi,z}$ is the Laplacian in cylindrical coordinates [6],

$$\nabla^2_{r_\perp,\phi,z} = \frac{1}{r_\perp} \frac{\partial}{\partial r_\perp} \left(r_\perp \frac{\partial}{\partial r_\perp} \right) + \frac{1}{r_\perp^2} \frac{\partial^2}{\partial \phi^2} + \frac{\partial^2}{\partial z^2} , \qquad (2.28)$$

$\lambda = \omega_z/\omega_\perp$ is the asymmetry parameter, $\Psi(r)$ is the condensate wavefunction normalised to unity (Eq. 2.5) and g_{3D} defined in Eq. (2.8), is the three dimensional nonlinear coefficient. The most general solution of Eq. (2.27) can be written as

$$\Psi(r) = \Psi'(r) \exp(iS(r)) , \qquad (2.29)$$

where $|\Psi'(r)|^2 = \rho(r)$ is the number density while $S(r)$ is the phase. If the solution is axially symmetric, for example a vortex state, then $S(r) = \kappa\phi$, where ϕ is the azimuthal angle around the vortex axis, and κ is the quantum of circulation. The velocity field is given by $v = (\hbar/m)\nabla S$, therefore if $\kappa \neq 0$ one has vortex states with tangential velocity

$$v = \frac{\hbar}{mr_\perp}\kappa \qquad (2.30)$$

and angular momentum along the z-axis $\kappa\hbar$. Using transformation Eq. (2.29), the expression of the nonlinearity given by Eq. (2.8) and substituting in Eq. (2.27) one finds, (neglecting the primes),

$$\mu\Psi(r) = \left[-\frac{1}{2}\nabla^2_{r_\perp,z} + U_{\text{eff}}(r) + g_{3D}|\Psi(r)|^2 \right] \Psi(r) , \qquad (2.31)$$

where,

$$U_{\text{eff}}(r) = \frac{\kappa^2}{2r^2} + \frac{1}{2}\left(r_\perp^2 + \lambda^2 z^2 \right) , \qquad (2.32)$$

which differs from Eq. (2.27) because of the centrifugal term. Due to this term, solutions of Eq. (2.31) for $\kappa \neq 0$ have to vanish on the z-axis within a core of radius the healing length ξ [102] and ensures that the kinetic energy remains finite as $r_\perp^2 \rightarrow 0$.

2.6.2 Ground state solutions

We solve numerically Eq. (2.31) in the presence of the potential Eq. (2.32) for $\kappa = 0$ and for various values of the nonlinearity g_{3D} using the Crank-Nicholson method [96]. As initial wavefunction we consider the normalised wavefunctions of the linear Schrödinger equation in the presence of a harmonic trap,

$$\Psi(\mathbf{r}) = \frac{1}{(2\pi)^{3/4}} \exp\left(-(r_\perp^2 + z^2)/4\right) . \tag{2.33}$$

In Fig. 2.4 we show typical density plots in the r and the z direction, for positive values of the three dimensional nonlinear constant g_{3D} and for different geometries. As in the one-dimensional case, we note that repulsive interactions decrease the central density and the condensate spreads out increasing g_{3D}. Moreover Fig. 2.4 shows that the trap geometry modifies the density profiles with a tighter potential resulting in higher central density. Thus although the size of the condensate is almost the same in the r-direction, Figs. 2.4(a)-(c), stronger confining potential in the z-direction, $(\lambda > 1)$, results in smaller spatial extension along that axis, Fig. 2.4(f). In Fig. 2.5 we plot the chemical potential for positive values of g_{3D} for different geometries. We note that for $\lambda = 1$ and for $g_{3D} = 0$, $\mu = 1.5$ which is the exact solution in the non-interacting limit.

In Fig. 2.6 we plot the stationary solutions of Eq. (2.31) for a range of values of $g_{3D} < 0$, and $\lambda^2 = 1/8, 1, 8$. Apart from the same effects in the density profiles due to the confining potential as in the case of repulsive interactions, (Fig. 2.4), there are interesting effects arising from the attractive nonlinearity. Comparing with Fig. 2.4 we note that an attractive (repulsive) interaction increases (decreases) the central density which is similar to the one dimensional case. In addition, the spatial extension of the system decreases, increasing the interaction energy and eventually tends to zero. Thus in the case of a three dimensional Bose gas confined in a trap, increasing the number of atoms in the condensate, above a critical number $\mathcal{N}_{cr}$, can cause the collapse of the gas [1, 15, 75, 76, 77, 78, 79]. The study of collapse is an important feature in the case of Bose gases interacting with attractive forces and
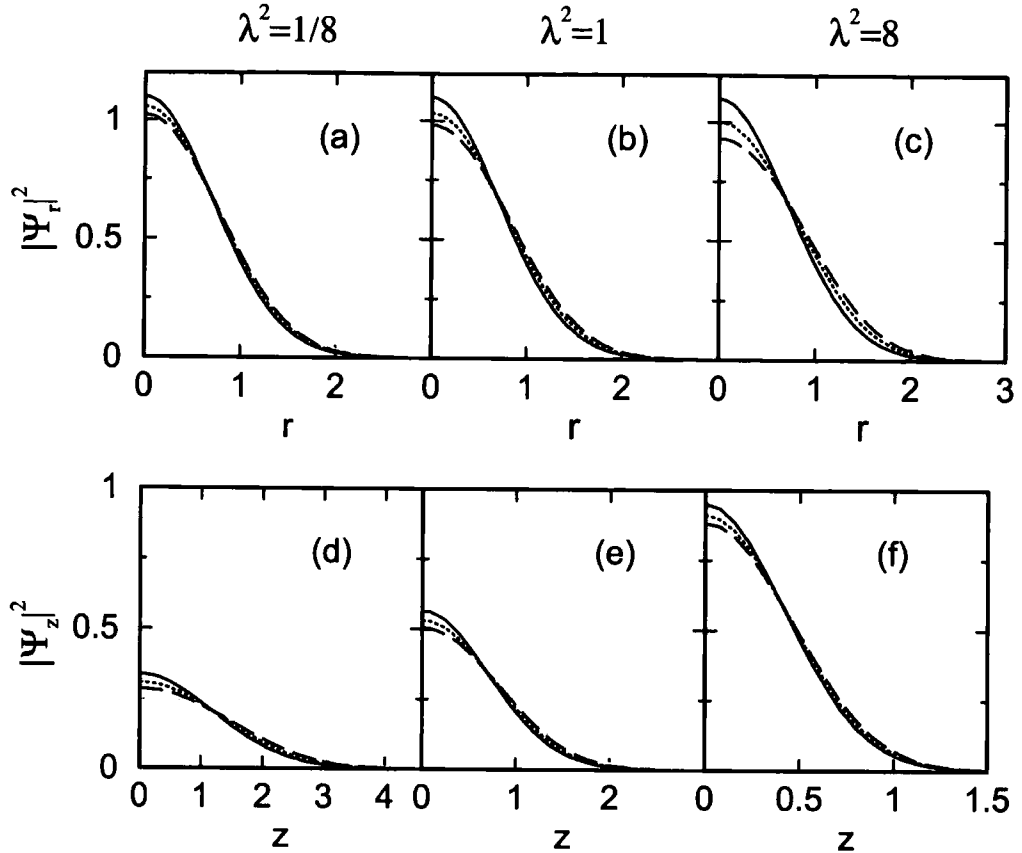
Figure 2.4: Condensate densities along the r-axis (upper row) and along the z-axis (lower row) for (a) and (d) $\lambda^2 = 1/8$, (b) and (e) $\lambda = 1$ and finally (c) and (f) $\lambda^2 = 8$. Black solid lines correspond to the non-interacting case, dotted, long-dashed and grey lines correspond to $g_{3D} = 5, 10$ and 20 respectively.

will be discussed in more details in Chapters 7 and 8 and Appendix C.

2.6.3 Vortex states

In the previous subsection we showed how vortex states can be obtained from the GPE (2.27). Quantised vortices have been the object of both theoretical (see for example an excellent review [98] and references therein) and experimental work [103, 104, 105, 106, 107, 108]. Here we consider states having a vortex line along the z-axis and we solve the time-independent GPE (2.31) states with $\kappa \neq 0$ using the Crank-Nicholson method [96]. For weak interactions the vortex condensate
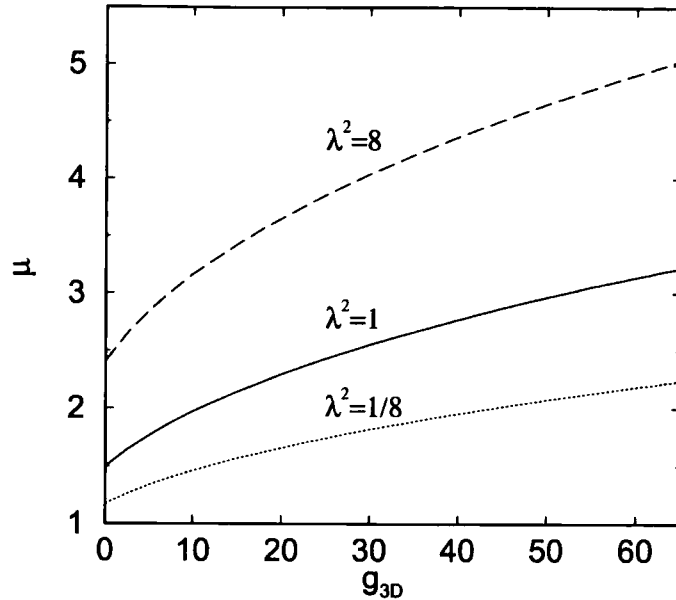
Figure 2.5: Chemical potential μ, for the ground state for positive values of the nonlinear constant g_{3D} for $\lambda^2 =:$ 8 (dashed), 1, (solid) and 1/8 (dotted) lines.

wavefunction is well approximated by [81, 109],

$$\Psi_\kappa \propto r_\perp^\kappa \exp\left(-(r_\perp^2 + z^2)/4\right) . \tag{2.34}$$

In Fig. 2.7 we plot typical condensate densities for states with vorticity, $\kappa = 1$ and $\kappa = 2$, for positive values of the nonlinear constant g_{3D} and for $\lambda = 1$. These states correspond to atoms flowing around the z-axis with angular momentum $\hbar$ and $2\hbar$. We note that the density at the centre of the vortex core is zero and that the vortex core radius remains constant for increasing g_{3D}. In Fig. 2.8 we plot density profiles in the rz plane for $\kappa = 1$ and $\kappa = 2$ vortex states, Fig. 2.8(b) and (c) respectively for a value of nonlinearity $g_{3D} = 71$. In Fig. 2.8(a) we also plot the $\kappa = 0$ ground state. From Fig. 2.8 we notice that due to the centrifugal term, i.e. first term in Eq. (2.32), atoms are pushed away from the z-axis forming a toroidal cloud [81].
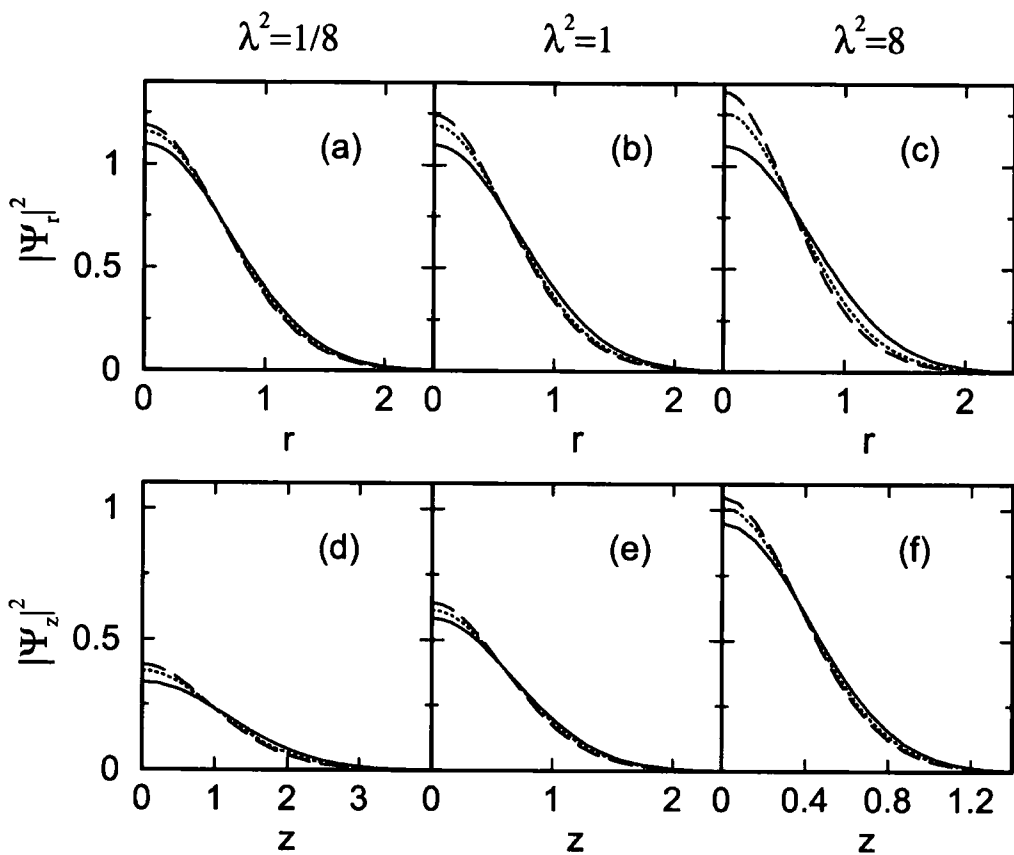
Figure 2.6: Same as Fig. 2.4 but now $g_{3D} =:$ 0, (solid), -2.5, (dotted) and -3.5 (dashed) lines.
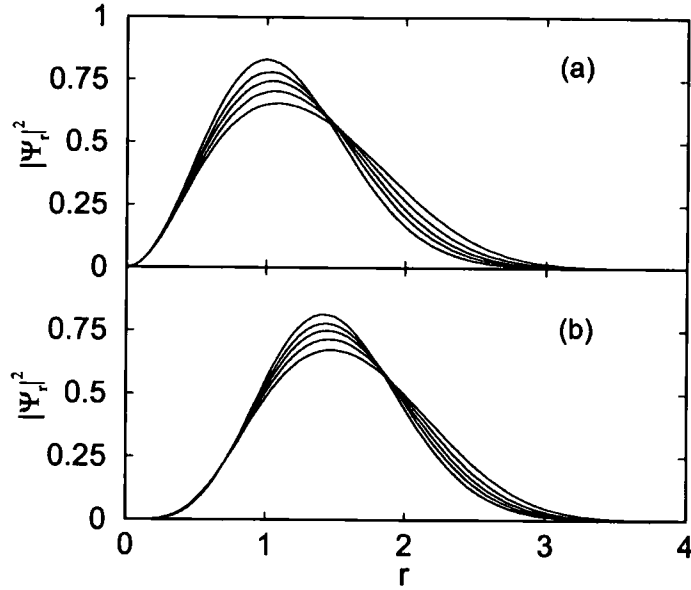
Figure 2.7: Condensate densities for states with vortices in a spherical trap, $\lambda = 1$ for (a) $\kappa = 1$ and (b) $\kappa = 2$. Solid lines correspond to $g_{3D} = 0, 10, 20, 35$ and 60 in order of increasing width.

2.7 Thomas-Fermi limit

In the case of an assembly of atoms interacting with repulsive forces, solutions of the GPE (2.31) in the large interacting limit take a rather simple form [1].

In the previous subsections we found that for repulsive interactions, increasing g_{3D}, the wavefunction spreads out and for large interactions the density becomes approximately parabolic. This can be shown by neglecting the kinetic energy term in the GPE (2.31) giving

$$\mu \Psi \left(r \right) = \left(U_{\text{eff}} \left(r \right) + g_{3D} |\Psi(r)|^2 \right) \Psi(r) , \qquad (2.35)$$

which has the solution

$$|\Psi(r)|^2 = \left[\frac{\mu - U_{\text{eff}}(r)}{g_{3D}} \right] \qquad (2.36)$$

for $|r| < |r_c|$ where r_c is given by the solution of $\mu = U_{\text{eff}}(r)$ and is zero elsewhere.
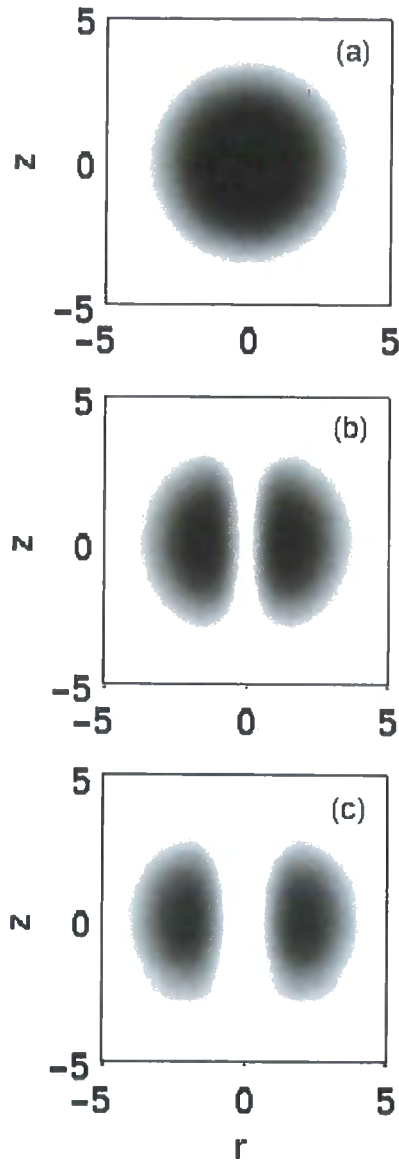
Figure 2.8: Density plots in the rz plane for the condensate wavefunction for (a) the ground $\kappa = 0$ and (b) and (c) vortex states with $\kappa = 1$ and 2 respectively. In all cases $g_{3D} = 71$.

From Eq. (2.36) and using the normalisation condition Eq. (2.5) for the condensate wavefunction one finds the value of μ for the ground state, $\kappa = 0$, as a function of the nonlinear constant g_{3D},

$$2\mu_{TF}^{3D} = \left(\frac{15 g_{3D} \lambda}{4\pi}\right)^{2/5} \tag{2.37}$$

in harmonic oscillator units.

In Fig. 2.9 we plot the chemical potential μ obtained by solving numerically Eq. (2.31) for $\lambda = 1$, $\kappa = 0$, (dot-dashed line), and $\kappa = 1$ (dotted line). Fig. 2.9 shows that for large values of g_{3D} the chemical potential μ approaches the TF value Eq. (2.37) for the ground state, whereas the first excited (vortex) state is constantly shifted by κ (in h.o.u.) compared to the TF solution, Eq. (2.37). For large g_{3D} the energy is given by $\mu = 1 + \frac{1}{2}\lambda + \kappa$ [81] using the dimensionless units and the notation of the previous subsection.
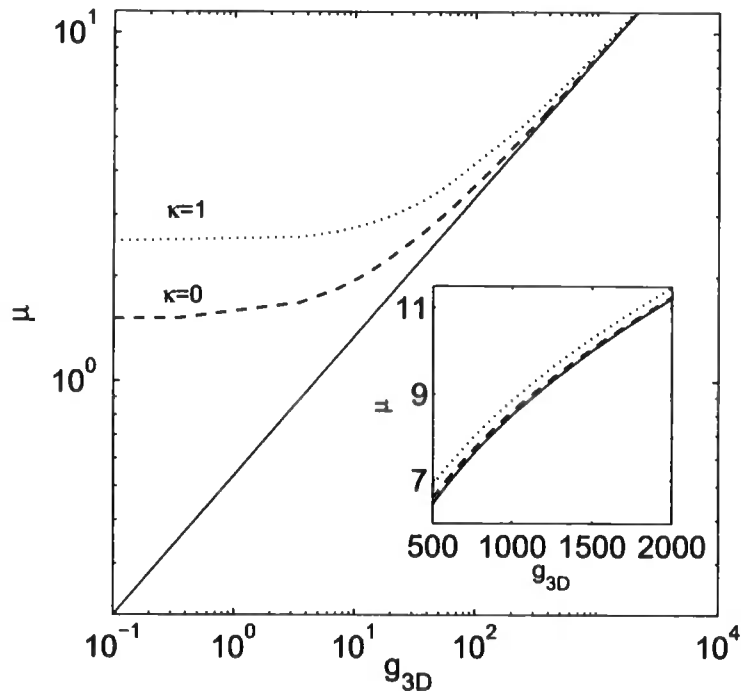
Figure 2.9: Chemical potential for the ground, $\kappa = 0$, (dot-dashed) and the first excited, $\kappa = 1$, state (dotted) line. The TF limit, μ_{TF}^{3D}, (Eq. (2.37)) is also plotted as solid line. Inset we plot the chemical potential for large g_{3D}.

2.8 Dynamic Properties of trapped Bose-Einstein Condensates

Our aim in this section is to discuss the behaviour of the elementary excitations of the ground state and a single vortex line along the symmetry axis of an axially symmetric trap, Eq. (2.26). For a spherical trap the solutions are characterized by the quantum numbers n, ℓ, m, where n corresponds to the number of radial modes and ℓ is the total angular momentum and m its z component. For axially symmetric traps m is still a good quantum number and we can find the dispersion law for particular cases. Stringari [99] proved that the dispersion law for $\ell = 2$ and $m = 0$ is given by [99]

$$\omega^2 \left(m = 0 \right) = \omega_\perp^2 \left(2 + \frac{3}{2}\lambda^2 \mp \frac{1}{2}\sqrt{9\lambda^4 - 16\lambda^2 + 16} \right) , \qquad (2.38)$$

where $\lambda = \omega_z/\omega_\perp$ is the asymmetry parameter. When $\lambda \to 1$ the above equation gives, $\omega_- \left(m = 0 \right) = \sqrt{2}\omega_\perp$ and $\omega_+ \left(m = 0 \right) = \sqrt{5}\omega_\perp$ which correspond to the hydrodynamic predictions for the quadrupole $(n = 0, \ell = 2)$ and monopole $(n = 1, \ell = 0)$ frequencies in a spherical trap [99]. When $\lambda \ll 1$ (cigar-type geometry) the two frequencies become $\sqrt{\frac{5}{2}}\,\omega_z$ and $2\omega_\perp$. In the opposite limit $\lambda \gg 1$ (pancake-type geometry) the two solutions are $\sqrt{\frac{10}{3}}\,\omega_\perp$ and $\sqrt{3}\omega_z$.

We compare the above analytical results by solving the GPE (2.27) numerically using the Crank-Nicholson method [96] and a potential of the form Eq. (2.32) with $\lambda = 1$. We study the collective oscillations along the axial direction of a condensate without a vortex $\kappa = 0$ [84, 99] and in the presence of a vortex line along the axial direction, $\kappa = 1$ [100, 101]. We study the response of the condensate by a small increase of λ at $t = 0$. We determine the quadrupole and monopole modes along the axial direction by calculating the following integrals [110],

$$q_z = \int \left(3z^2 - r^2 \right) |\Psi(r)|^2 2\pi r_\perp \mathrm{d}r_\perp \mathrm{d}z \qquad (2.39)$$

and

$$m = \int r|\Psi(r)|^2 2\pi r_\perp \mathrm{d}r_\perp \mathrm{d}z \tag{2.40}$$

where $r^2 = r_\perp^2 + z^2$.
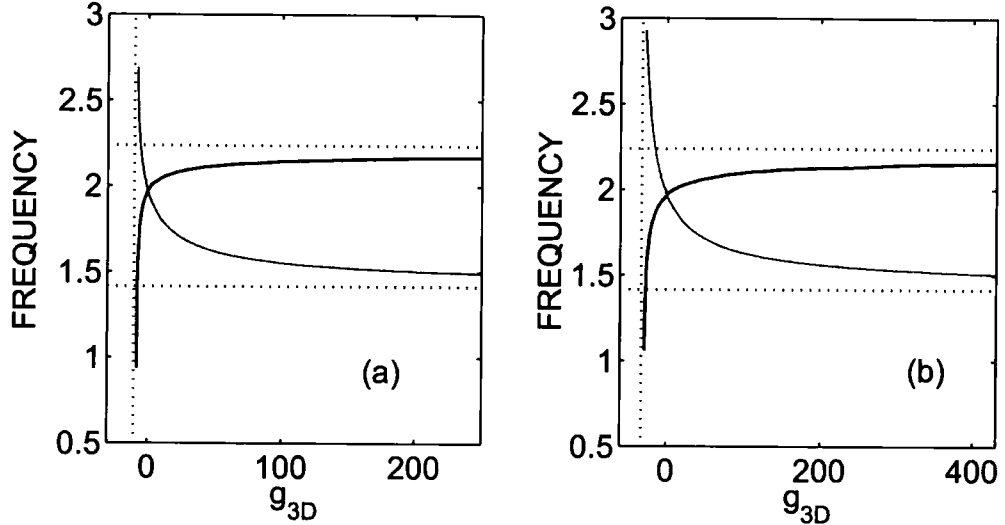
Figure 2.10: Monopole (grey) and quadrupole (black line) frequencies obtained from the numerical solution of the GPE (2.27) for an isotropic trap, $\lambda = 1$. (a) shows the case with no vortex $\kappa = 0$ and (b) shows the two modes in the case of a vortex line along the z-axis, $\kappa = 1$.

In Fig. 2.10 we show the behaviour of these modes as a function of the nonlinear constant g_{3D}, without a vortex, (Fig. 2.10(a)), and with a vortex, (Fig. 2.10(b)). We observe that for large nonlinearities (TF-limit), the solutions for the two modes approach the asymptotic results $\sqrt{2}$ and $\sqrt{5}$ for the quadrupole and monopole frequencies respectively. We observe that for the noninteracting limit ($g_{3D} = 0$) one recovers the harmonic oscillator prediction $\omega = 2\omega_\perp$ [99] while for large g_{3D} the two frequencies in the presence of a vortex are shifted compared to the $\kappa = 0$ case [101]. Both figures show a cut-off in the frequencies for negative values of g_{3D}, which coincides with the instability mentioned in Section 2.6. However, comparing the two graphs, Fig. 2.10(a) and (b), we observe that the $\kappa = 1$ state is more stable than the state without a vortex. For more details about this instability see Chapters 7 and 8 and Appendix C.

In this Chapter we reviewed some basic properties that describe a dilute BEC confined in a single harmonic trap by numerical solution of the GPE. In the following Chapters we apply this knowledge to describe the behaviour of BECs confined in a double-well potential.

Chapter 3

Eigenenergy levels of a BEC in double-well potential

We study the eigenenergy levels of a dilute BEC with repulsive interactions, confined in a double-well potential. By solving the time-independent GPE in one and three dimensions, we show that the nonlinearity leads to the appearance of loop structures in the higher energy levels. We show that the eigenenergies can be reproduced by the two-state model and we compare the model curves with the exact solutions of the GPE.

3.1   Introduction

The creation of superconducting [111] and superfluid [112] weak links has led to the experimental observation of Josephson effects [30], arising as a result of macroscopic quantum phase coherence. Josephson weak links are typically created by connecting two initially independent systems (superconductors / superfluids) via a barrier with dimensions of the order of the system healing length. Such junctions lead to a variety of interesting phenomena [31], including dc- and ac-Josephson effects. Observations in superconductors preceded those in superfluids, due to the much larger healing lengths, thus enabling easier fabrication of weak links. Evidence for Josephson-like effects has been observed in ^{4}He weak links [40], and unequivocally demonstrated for weakly-coupled ^{3}He systems [113]. The recent achievement of dilute trapped

atomic Bose-Einstein condensation (BEC) [13, 14, 15, 16, 17, 18, 19, 20, 21, 22] gives rise to a new system for studying Josephson effects in neutral quantum fluids, with the creation of atomic BEC Josephson junction arrays, in which the harmonically trapped atoms are additionally confined by an optical lattice potential, generated by far-detuned laser beams. Phase coherence in different wells is observed by interference experiments of condensates released from the lattice [42]. In addition, Josephson effects [43] and the control of tunnelling rate have been demonstrated [46]. Although experiments (and theoretical analysis) of such systems are well underway, deeper insight into the diverse range of Josephson phenomena can be obtained by looking at the simplest single junction, double-well system which is the main subject of this Thesis. This system has already received considerable theoretical attention, with treatments based on zero temperature mean field theory [52, 54, 55, 56, 57, 58, 59, 60, 61] and a two-state approximation [62, 63, 64, 65, 66, 67, 68, 69, 70, 71, 72, 73].

In this Chapter, we begin our studies of dilute BECs in a double-well potential, by exploring the eigenenergy structure of such system. In Section 3.2, we present the model we use to obtain the eigenenergy curves and states based on numerical solution of the GPE and on the two-state model approximation [62, 63, 64, 65, 66, 67, 68, 69, 70, 71, 72, 73]. Next, in Section 3.3, we calculate numerically the eigenenergies of an one dimensional double-well potential as a function of the barrier position and we compare the results with the two-state model solutions in Section 3.4. In Section 3.5 we study three dimensional solutions of the GPE and finally in Section 3.6 we compare to the one dimensional results. In both limits, in the vicinity of a level crossing the nonlinearity leads to triangular structures in the eigenenergy curves [114]. Similar structures have been shown to occur in a nonlinear Landau-Zener model [115], and near the zone boundary in optical lattices [116, 117, 118].

3.2 Description of the Model

3.2.1 GPE solutions

First we present the eigenenergies of the double-well potential, based on numerical solution of the GPE. We begin by considering a one-dimensional model described by the GPE,

$$i\frac{\partial}{\partial t}\psi(z,t) = -\frac{1}{2}\nabla^2\psi(z,t) + V_{z_0}(z)\psi(z,t) + g_{1D}|\psi(z,t)|^2\psi(z,t) \ . \tag{3.1}$$

Here $g_{1D} = 2\mathcal{N}a/a_\perp$ is the one dimensional nonlinear parameter, defined in terms of the s-wave scattering length a, $\mathcal{N}$ is the total number of atoms with mass m and $a_\perp = \sqrt{\hbar/m\omega_\perp}$ is the harmonic oscillator length in the transverse direction(s). We have concentrated on a system confined by the potential

$$V_{z_0}(z) = \tfrac{1}{2}z^2 + h\,\exp[-(z - z_0)^2] \ , \tag{3.2}$$

describing a harmonic trap with a Gaussian potential barrier with height h, unit width, displaced by a distance z_0 from the centre of the trap. For $z_0 = 0$ the double-well is symmetric whereas for $z_0 > 0$, the double-well is asymmetric and the right well obtains higher potential energy. This model facilitates an exploration of a wide range of values of the nonlinearity, g_{1D}, barrier height, h, (considered in this Chapter) and barrier velocity, $v = z_0/t$ (discussed in following Chapters).

The above one dimensional model can be generalized to three dimensions. In the latter case, the asymmetry was induced by an additional linear potential of gradient δ pivoted at the centre of a harmonic trap. However as it will be verified in later Sections, the results obtained by this three dimensional model are similar to those described in the one dimensional case. The three dimensional model is described by the following dimensionless GPE, describing the evolution of the condensate wavefunction (normalised to unity)

$$i\frac{\partial}{\partial t}\psi(\boldsymbol{r},t) = \left[-\frac{1}{2}\left(\frac{\partial^2}{\partial x^2} + \frac{\partial^2}{\partial y^2} + \frac{\partial^2}{\partial z^2}\right) + V(\boldsymbol{r}) + g_{3D}|\psi(\boldsymbol{r},t)|^2\right]\psi(\boldsymbol{r},t) \ , \tag{3.3}$$

where the atom-atom interaction is parametrized by $g_{3D} = g/(a_\perp^3 \hbar \omega_\perp)$, where $g = 4\mathcal{N}\pi\hbar^2 a/m$ is the usual three-dimensional scattering amplitude, and the three dimensional confining potential has the form,

$$V(\mathbf{r}) = \tfrac{1}{2}\left[(x^2 + y^2) + \lambda^2 z^2\right] + h\exp\left[-(z/w)^2\right] + \delta z \ . \tag{3.4}$$

The first term describes a cylindrically symmetric harmonic potential, with a trap aspect ratio $\lambda = \omega_\parallel / \omega_\perp$: the trap is spherical for $\lambda = 1$, "cigar-shaped" for $\lambda < 1$ and "pancake-like" for $\lambda > 1$. The second term describes a Gaussian potential of height h generated by a blue detuned light sheet of beam waist w in the z direction located at $z = 0$. In Eq. (3.4), the contribution δz corresponds to an additional linear potential of gradient δ pivoted at the centre of the trap. For $\delta > 0$ considered throughout this Thesis, the right well obtains higher potential energy and the trap centre is additionally shifted into the $z > 0$ region; however this shift is negligible for the parameters studied throughout this work, and will be henceforth ignored.

We work in the dimensionless units, discussed in Chapter 2, and distance, time and energy are measured in terms of the harmonic oscillator units (h.o.u.), $(\hbar/m\omega_\perp)^{1/2}$, $\omega_\perp^{-1}$ and $\hbar\omega_\perp$, respectively, where $\omega_\perp$ is the harmonic trap frequency in the transverse direction(s) and m is the atomic mass. Time-independent states of the form, $\psi(\mathbf{r}, t) = e^{-i\mu t}\Psi(\mathbf{r})$, where μ is the chemical potential (of the one and three dimensional system respectively), are found by numerical solution of the GPE using the Newton code [96] for solving nonlinear equations, described in Appendix A. As an initial guess we begin with a known solution, e.g. the harmonic oscillator ground state with no barrier and no interactions and then slowly increase the barrier height and the interaction parameter. To find the first excited state one may begin with the ground state solution for the symmetric double-well and change the parity.

In Fig. 3.1 we show the density profiles for the ground state for increasing barrier height. As h is increased, the ground state spreads as the barrier pushes atoms from the centre of the trap. Eventually, the ground state becomes double peaked.
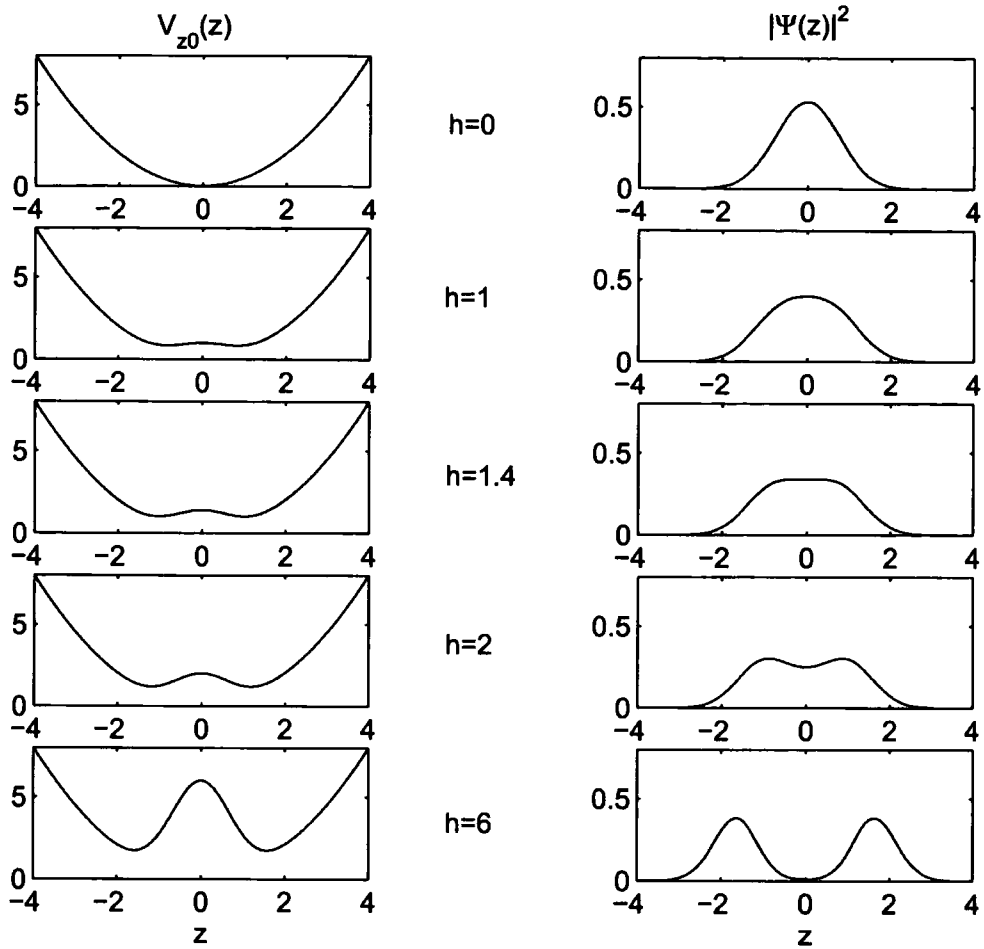
Figure 3.1: Schematic of the potential, V_{z0}, along the z-direction for different values of h, (left column) and the corresponding density profiles for the ground state (right column).

Fig. 3.2 shows the eigenenergy curves for the case of noninteracting and interacting Bose gas with $a > 0$. Our studies explicitly consider the $z_0 > 0$ limit, however, for completeness, we also plot the $z_0 < 0$ solutions, which are produced by projecting the $z_0 > 0$ values about the origin (centre of the barrier). This fact has also been explicitly verified by calculations. For the noninteracting limit there are only two levels and, for $z_0 = 0$, the eigenstates are a symmetric ground state Ψ_g, and an antisymmetric first excited state with equal population in both wells and a phase difference π across the trap centre, which we shall henceforth refer to as Ψ_e. However

sufficiently large positive nonlinearity leads to the appearance of loop structure in the eigenenergy levels for the excited states. The two lower energy eigenstates are a symmetric ground state Ψ_g with equal population in both wells, whereas the first excited state is split into three sublevels which correspond to a lower energy antisymmetric Ψ_e state and two higher energy "self-trapped" states [60, 63, 64, 65], with most of the population in either the left or right well, see Fig. 3.2.
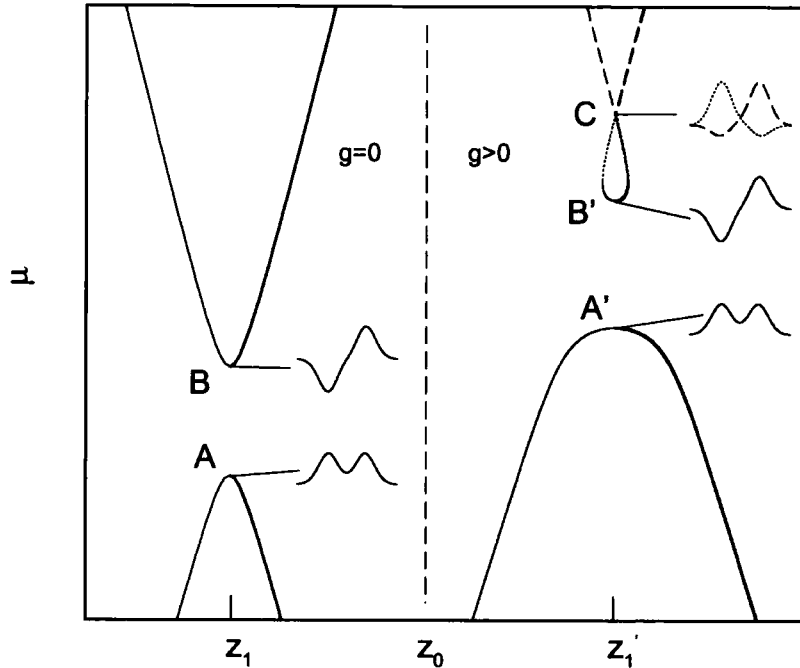
Figure 3.2: Lowest eigenenergy levels of a dilute BEC in a double-well potential for noninteracting gas ($g = 0$) and a gas with repulsive interactions, ($g > 0$) as a function of the barrier displacement z_0. Bold lines correspond to stationary solutions of Eq. (3.1) and black lines are the symmetric projections for $z_0 < z_1$ ($z_0 < z_1'$). The wavefunctions at the centre of the barrier z_1 and z_1' for each case, are also shown.

3.2.2 Two-state model approximation

In the following we present a different method to calculate the eigenstates based on a two-state model approximation [62, 63, 64, 65, 66, 67, 68, 69, 70, 71, 72, 73]. We consider the one dimensional limit; however similar results apply to the three dimensional limit by applying the substitutions $z \to r$ and $g_{1D} \to g_{3D}$. The two-state model is applicable when the barrier displacement is small, so that to a good

approximation the shape of the two wells does not change, while the minima of the wells are simply shifted by an amount proportional to the displacement. We write the general solution of the wavefunction $\psi(z,t)$ as a superposition of the states $\Psi_L(z)$, $\Psi_R(z)$ localised in the left and right well with complex time-dependent coefficients, $c_L(t)$ and $c_R(t)$. Thus the wavefunction is of the form,

$$\psi(z,t) = c_L(t)\Psi_L(z) + c_R(t)\Psi_R(z) \ . \tag{3.5}$$

The wavefunctions Ψ_i (here $i = L, R$ denotes the left, right well), are eigenfunctions of the time-independent GPEs

$$\mu\Psi_i = -\frac{1}{2}\nabla^2\Psi_i + V_i\Psi_i + g_{1D}|\Psi_i|^2\Psi_i \ , \tag{3.6}$$

with normalization condition $\langle\Psi_L|\Psi_R\rangle \simeq 0$ and $\langle\Psi_L|\Psi_L\rangle = \langle\Psi_R|\Psi_R\rangle = 1$. The potentials V_L and V_R are single-well potentials displaced to the left and to the right of $z = 0$, respectively, with $V_L(z) = V_R(-z)$ so that $\Psi_L(z) = \Psi_R(-z)$. The time-dependent coefficients are expressed in terms of the population of the particles and the phase on the left and right well as,

$$c_i(t) = \sqrt{N_i}\exp(i\theta_i(t)) \ , \tag{3.7}$$

with $N_L + N_R = N = 1$. Substituting Eq. (3.5) into Eq. (3.1), multiplying by Ψ_i and integrating over spatial coordinates we obtain the coupled equations for the amplitudes,

$$
\begin{aligned}
i\dot{c}_L(t) &= \left[E_L + E_{C_L}N_L(t)\right]c_L(t) - \\
&\quad \left[E_J + U_L N_L(t) + U_R N_R(t)\right]c_R(t) \ , \tag{3.8} \\
i\dot{c}_R(t) &= \left[E_R + E_{C_R}N_R(t)\right]c_R(t) - \\
&\quad \left[E_J + U_L N_L(t) + U_R N_R(t)\right]c_L(t) \ . \tag{3.9}
\end{aligned}
$$

In the above equations, E_i is the zero-point energy in well i,

$$E_i = \int dz(|\nabla\Psi_i(z)|^2 + V(z)|\Psi_i(z)|^2) \ , \tag{3.10}$$

$E_{C_i}N_i(t)$ is the self-interaction energy of each well, with

$$E_{C_L} = g_{1D} \int dz |\Psi_L(z)|^4 = g_{1D} \int dz |\Psi_R(z)|^4 = E_{C_R} = E_C \ , \qquad (3.11)$$

E_J represents the Josephson coupling energy between the two separated condensates due to tunnelling through the barrier,

$$E_J = \int dz [\nabla \Psi_L(z) \nabla \Psi_R(z) + \Psi_L(z) V(z) \Psi_R(z)] \ , \qquad (3.12)$$

and $U_L N_L + U_R N_R$ represents the contribution of the mean-field theory due to the coupling and contains terms of fourth order in the localised wavefunctions $\Psi_i(z)$, with,

$$U_i = g_{1D} \int dz \Psi_i(z)^2 \Psi_L(z) \Psi_R(z) \ . \qquad (3.13)$$

For most cases the last two terms in Eqs. (3.8) and (3.9) can be neglected, and one yields the following equations for the two-state model,

$$i\dot{c}_L(t) = (E_L + E_C N_L(t))c_L(t) - E_J c_R(t) \ , \qquad (3.14)$$

$$i\dot{c}_R(t) = (E_R + E_C N_R(t))c_R(t) - E_J c_L(t) \ . \qquad (3.15)$$

The above system can be written in a matrix equation,

$$i\dot{C} = H \cdot C \ , \qquad (3.16)$$

where C is the column vector,

$$\begin{pmatrix} c_L(t) \\ c_R(t) \end{pmatrix} \qquad (3.17)$$

and H is the nonlinear Hamiltonian matrix,

$$H = \begin{pmatrix} E_L + E_C N_L & -E_J \\ -E_J & E_R + E_C N_R \end{pmatrix} \ . \qquad (3.18)$$

Recalling that the two mode wavefunctions in each well satisfy $\langle\Psi_L|V_{z_0=0}|\Psi_L\rangle =$ $\langle\Psi_R|V_{z_0=0}|\Psi_R\rangle$ and redefining the zero of energy at half the eigenenergy difference between the states Ψ_g and Ψ_e, the Hamiltonian and therefore Eqs. (3.14) and (3.15) become,

$$H = \frac{1}{2}\begin{pmatrix} -\Delta + E_C N & -E_J \\ -E_J & \Delta - E_C N \end{pmatrix} ,$$

(3.19)

and

$$i\dot{c}_L(t) = (-\Delta/2 + E_C/2N)\, c_L(t) - E_J/2c_R(t) ,$$

(3.20)

$$i\dot{c}_R(t) = (\Delta/2 - E_C/2N)\, c_R(t) - E_J/2c_L(t) .$$

(3.21)

In the above Hamiltonian, $N = (N_L - N_R)$ is the population difference between the left and right well, and E_C and E_J are the self-interaction and the Josephson energies defined in Eq. (3.11) and Eq. (3.12) respectively. We define the shift in the zero-point energies in each well due to the displacement of the barrier to be

$$\frac{1}{2}\Delta = \langle\Psi_L|(V_{z_0=0} - V_{z_0})|\Psi_L\rangle = \langle\Psi_R|(V_{z_0} - V_{z_0=0})|\Psi_R\rangle .$$

(3.22)

Linearizing yields,

$$\frac{1}{2}\Delta \simeq z_0\langle\Psi_L|\left(\frac{dV_{z_0}}{dz_0}\right)_{z_0=0}|\Psi_L\rangle = -\alpha z_0 ,$$

(3.23)

where $\alpha < 0$ is the rate of change of the eigenenergy with z_0 for the self-trapping state, or the ground state with $z_0 > z_c$. For small g_{1D} and high barriers, such that $E_C \gg E_J$, one finds $\alpha \sim -E_C/2z_c$.

The eigenenergies of the system are found by substituting $i\dot{c}(t) = \mu c(t)$ in the expressions for the time-derivatives in Eqs. (3.20) and (3.21). We obtain the following system of equations,

$$\mu c_L(t) = (-\Delta/2 + E_C N/2)c_L(t) - (E_J/2)c_R(t)$$

(3.24)

$$\mu c_R(t) = -(E_J/2)c_L(t) + (\Delta/2 - E_C N/2)c_R(t) .$$

(3.25)

Substituting the expression of $c_i(t)$ from Eq. (3.7) we have,

$$(-\Delta/2 + E_C N/2 - \mu)\sqrt{N_L}\exp(i\theta_L) \; - \; (E_J/2)\sqrt{N_R}\exp(i\theta_R) \;\; = \;\; 0 \quad (3.26)$$

$$-(E_J/2)\sqrt{N_L}\exp(i\theta_L) \; + \; (\Delta/2 - E_C N/2 - \mu)\sqrt{N_R}\exp(i\theta_R) \;\; = \;\; 0 \,. \; (3.27)$$

By multiplying Eq. (3.24) with $\sqrt{N_L}\exp(-i\theta_L)$ and Eq. (3.25) with $\sqrt{N_R}\exp(-i\theta_R)$, defining the phase difference $\theta(t) = \theta_L(t) - \theta_R(t)$ and rearranging, one finds,

$$(-\Delta/2 + E_C N/2 - \mu)N_L \; - \; (E_J/2)\sqrt{N_L N_R}\exp(-i\theta) \;\; = \;\; 0 \quad (3.28)$$

$$-(E_J/2)\sqrt{N_L N_R}\exp(i\theta) \; + \; (\Delta/2 - E_C N/2 - \mu)N_R \;\; = \;\; 0 \,. \quad (3.29)$$

Adding and subtracting we obtain,

$$(-\Delta/2)N + (E_C/2)N^2 - \mu - E_J\sqrt{N_L N_R}\cos(\theta) \;\; = \;\; 0 \quad (3.30)$$

$$(-\Delta/2) + (E_C/2)N + \mu N - iE_J\sqrt{N_L N_R}\sin(\theta) \;\; = \;\; 0 \,, \quad (3.31)$$

where we have used $N_L + N_R = 1$ and $N_L - N_R = N$. Equating the real and imaginary parts in Eq. (3.31) we obtain the population difference N between the left and the right wells and the phase difference θ via,

$$N = \frac{\Delta}{(E_C - 2\mu)} \quad (3.32)$$

and

$$\sin\theta = 0 \rightarrow \theta = k\pi \rightarrow \theta = 0 \,. \quad (3.33)$$

We can find the equation for the eigenvalues μ if we make the final substitutions in Eq. (3.30) for the phase $\theta = 0$, the population difference N, Eq. (3.32), and $N_L N_R = (1 - N^2)/4$. The latter expression is obtained by taking the difference between the square of the equations $N_L + N_R = 1$ and $N_L - N_R = N$. Thus the eigenstates are given by,

$$\mu^4 - E_C\mu^3 + \frac{1}{4}(E_C^2 - E_J^2 - \Delta^2)\mu^2 + \frac{1}{4}E_C E_J^2\mu - \frac{1}{16}E_C^2 E_J^2 = 0 \,. \quad (3.34)$$

An important feature of the above equation is that there are four real roots when the coefficient of the quadratic term $(E_C^2 - E_J^2 - \Delta^2)$ is positive and only two when it is negative. For a symmetric double-well $(\Delta = 0)$, the additional roots appear at the critical point where the self-interaction energy satisfies $E_C = E_J$. For $E_C > E_J$, the eigenenergies of the stationary states are $\pm E_J/2$ and $E_C/2$, with the latter being doubly degenerate. The additional roots disappear if the displacement of the barrier is such that $|\Delta| = |2\alpha z_0| > \sqrt{E_C^2 - E_J^2}$.
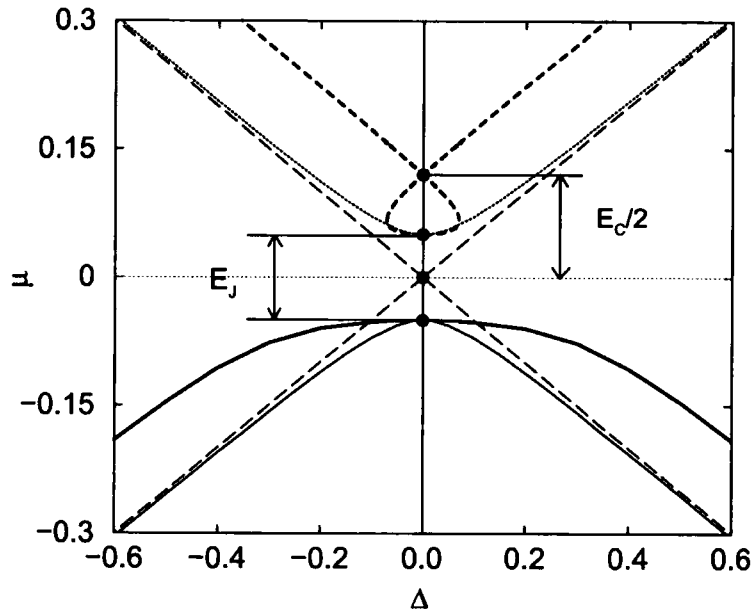
Figure 3.3: Schematic representation of the energy splittings E_J and E_C for the two-state model. Eigenenergies μ for the double-well potential as a function of Δ, for the ground and the first excited states for $E_C \neq 0$, (thick black) lines and $E_C = 0$, (thin black) lines are also shown as solid and dashed lines respectively. The asymptotes (long dashed lines) correspond to the limit that $E_J = E_C = 0$, yielding $\mu = \pm|\Delta|/2$. Dotted horizontal line corresponds to the zero energy of the two-state model.

This behaviour is illustrated in Fig. 3.3, where we plot numerical solutions of Eq. (3.34) for the eigenstates μ (indicated by bold black lines) as a function of Δ for $E_J = 0.1 \ \hbar\omega_\perp$ and $E_C = 0.24 \ \hbar\omega_\perp$. However we can find simple analytical solutions in the noninteracting limit, by setting $E_C = 0$ in Eq. (3.34), yielding,

$$\mu^4 - \frac{1}{4}(E_J^2 + \Delta^2)\mu^2 = 0 \quad \text{or} \quad \mu_\pm = \frac{1}{2}\sqrt{E_J^2 + \Delta^2} \ . \tag{3.35}$$

The above solutions are also shown in Fig. 3.3 as black lines. For large Δ the eigenenergies approach an asymptotic value corresponding to the limit $E_J = 0$, and become a linear function of Δ, resulting $\mu_\pm = |\Delta|/2$, represented by long-dashed lines in Fig. 3.3.
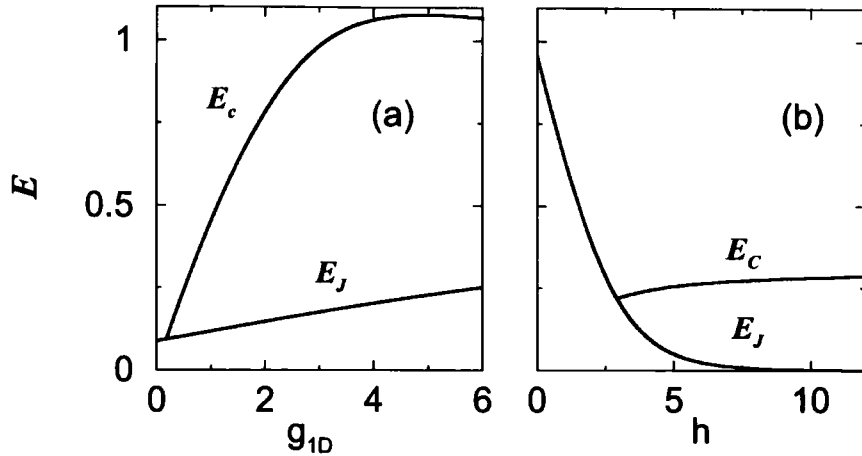
Figure 3.4: The dependence of the self-interaction energy, E_C, and the Josephson energy, E_J, (a) on the nonlinear parameter, g (with $h = 4\ \hbar\omega_\perp$), and (b) on the barrier height, h ($\hbar\omega_\perp$) (with $g_{1D} = 0.5$).

To apply the two-state model one needs to known the value of E_J, E_C and α for any particular barrier height or nonlinearity. In Fig. 3.4 we show how the energy splittings vary with the nonlinearity and the barrier height. The critical point, $E_C = E_J$, appears as either a critical nonlinearity or a critical height depending on which parameter is varied. We note that for large nonlinearity, the existence of the second excited state, e_2, effectively puts an upper limit on the value of E_C.

Next we give more details how the nonlinearity and the barrier height modify the eigenenergy levels by solving the GPE in one dimension.

3.3 Eigenenergies of a double-well potential in one dimension

In Fig. 3.5 we show the eigenenergies for the case of high barrier ($\mu \ll h$) of the ground level g and the first and second excited levels, e_1 and e_2, as a function of

the barrier position z_0 with $g_{1D} = 0.5$ and $h = 12$ $\hbar\omega_\perp$. A triangular structure appears in the upper levels at each level crossing. For states g and e_1 this structure is essentially the same as that discussed by Wu and Niu in the context of a nonlinear two-state model [115].
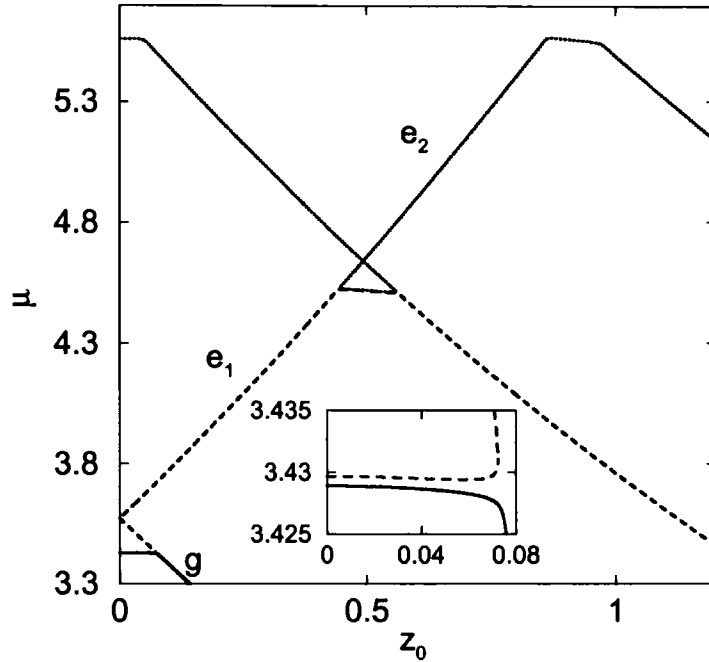
Figure 3.5: The energy eigenvalue, μ, as a function of the barrier displacement, z_0, for the ground state g, and the first two excited states, e_1 and e_2 with $h = 12$ $\hbar\omega_\perp$ and $g_{1D} = 0.5$. In the vicinity of the level crossing the upper level is split into three states that form a triangular structure. The ground-excited state splitting is shown inset.

For small z_0 the energy of the ground state is almost independent of the barrier position. This is because the transfer of atoms through the barrier exactly compensates for the change in potential energy. However, this cannot continue when all the atoms reach one side and the energy becomes strongly position dependent again at the critical displacement, z_c ($z_c = 0.07$ $a_\perp$ for the parameters in Fig. 3.3). At $z_0 \sim 0.5$ $a_\perp$ there is a second level crossing where it becomes energetically favourable for the first excited state e_1 to move from the upper to the lower well. In this region the energy level structure is similar to that at $z_0 = 0$, where the ground state population moves from the upper to the lower well.
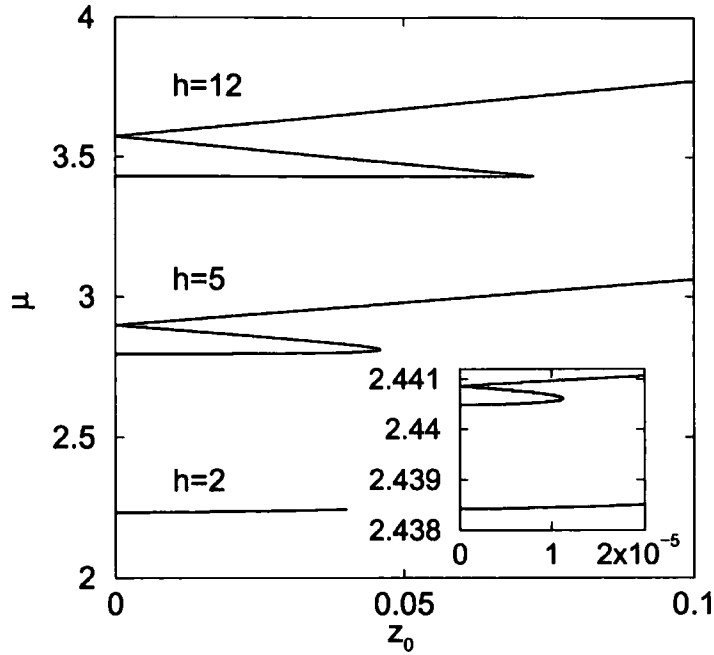
Figure 3.6: The energy eigenvalue, μ, as a function of the barrier displacement, z_0, for e_1 with $g_{1D} = 0.5$ and barrier heights $h = 2, 5$, and 12 $\hbar\omega_\perp$. The energy curves for $h = 2.91$ $\hbar\omega_\perp$ and $h = 2.92$ $\hbar\omega_\perp$ are shown inset. The loop structure appears at $h = 2.916$ $\hbar\omega_\perp$.

The energy splitting between the ground and lowest excited state is extremely small for $h = 12$ $\hbar\omega_\perp$, see Fig. 3.5(inset). Lower barriers ($\mu \sim h$) result in larger energy splittings, and therefore from an experimental viewpoint are more interesting, making them more robust to coupling due to external (e.g. thermal [68, 71, 73, 123]) perturbations. In Fig. 3.6 we illustrate how the triangular structures evolve as a function of barrier height with $g_{1D} = 0.5$. The appearance of the loop structure, which coincides with the threshold for self-trapping, occurs at critical height $h = 2.916$ $\hbar\omega_\perp$ (see Section 3.6). The structure becomes more triangular as h increases.

In Fig. 3.7 we show the eigenenergies for $h = 4$ $\hbar\omega_\perp$ with two different values of nonlinearity g. In Fig. 3.7(a) $g_{1D} = 0.5$, and the loop structure appears for the first but not the second excited state. The appearance of a loop structure results in the breakdown of adiabatic following of an eigenenergy curve [115]. In the following Chapters, we will see that this breakdown is associated with a discontinuity in the
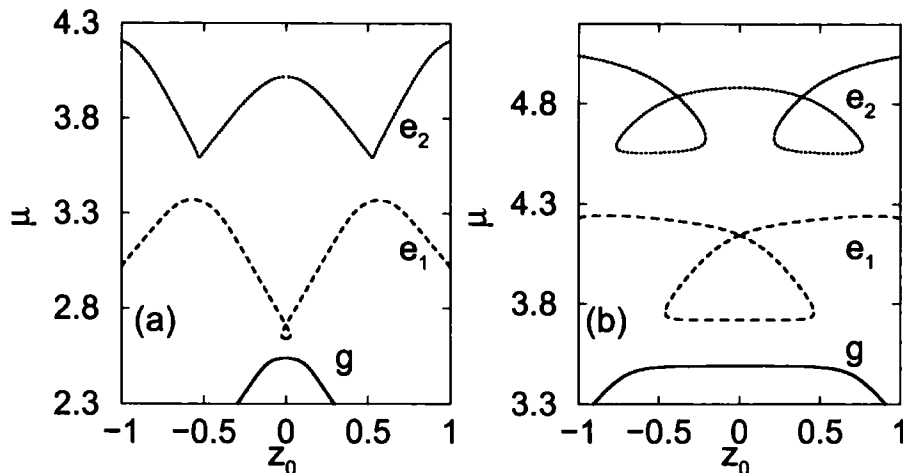
Figure 3.7: The energy eigenvalue, μ, as a function of the barrier displacement, z_0, for the ground state g, and the first two excited states, e_1 and e_2 with $h = 4\ \hbar\omega_\perp$ and (a) $g_{1D} = 0.5$ and (b) $g_{1D} = 5$.

population difference between the two wells. Finally in Fig. 3.7(b), we illustrate the effect of increasing the nonlinear parameter to $g_{1D} = 5$. In this case the energy splittings are a significant fraction of the harmonic oscillator energy level spacing and the critical displacement coincides with the position of the crossings between states e_1 and e_2.

3.4 Comparison to the two-state model

In this section we compare the eigenenergies with those determined from the numerical solution of the one-dimensional GPE. The energy curves are parametrised by three numbers: the splitting between the two lower levels, which is equal to E_J; the energy of the self-trapping states, $E_C/2$; and the energy gradient α. Fig. 3.8 shows a comparison between the exact eigenenergies and the model curves for $h = 4\ \hbar\omega_\perp$, $g_{1D} = 0.5$. The values of E_C, E_J, and α are taken from the exact solutions. The energy gradient is matched to that of the self-trapping states at $z_0 = 0$ ($\alpha = 3.187\ \hbar\omega_\perp/a_\perp$). This value gives the best agreement when comparing population dynamics (see Chapter 5). However, due to the slight curvature of the eigenenergy curves a smaller value ($\alpha = 2.663\ \hbar\omega_\perp/a_\perp$) gives a better fit

to the triangular structure. The agreement between the two-state model and the exact eigenenergies becomes less good at higher nonlinearities as the influence of higher-lying states increases.
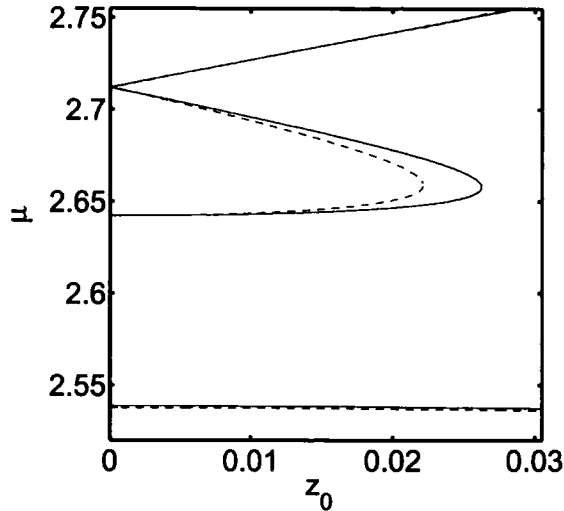
Figure 3.8: Comparison between the exact (solid) and the two-state model (dashed) eigenenergies, μ, as a function of the barrier displacement, z_0, for $h = 4$ $\hbar\omega_\perp$ and $g_{1D} = 0.5$.

3.5   Eigenenergies of a double-well potential in three dimensions

By solving the three dimensional time-independent GPE (3.3), with a confining potential of the form Eq. (3.4) we obtain an eigenenergy structure similar to the one dimensional case. Note that in the three dimensional case we use a potential gradient rather than a barrier displacement to create the asymmetry, but the end result is essentially the same. Sufficiently large repulsive interactions lead to the appearance of a loop structure in the first excited state, shown in Fig. 3.9(b). For completeness the corresponding wavefunctions for the ground g and the first excited state e_1 are shown in Fig. 3.9(c) and they have similar form to the one dimensional states shown in Fig. 3.2.

In Fig. 3.10 we present the eigenenergy curves for the same nonlinearity, $g_{3D} = 10\pi$
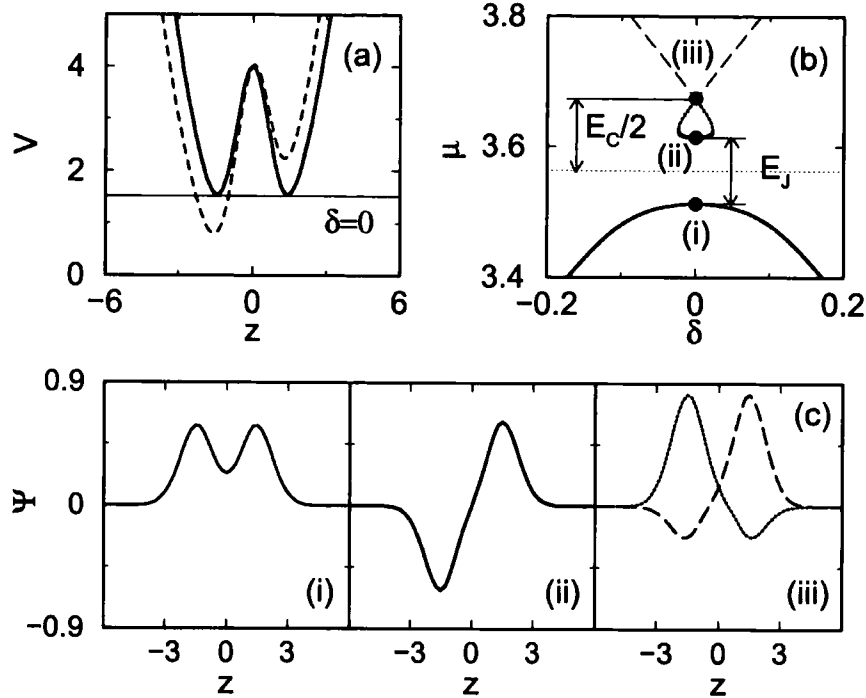
Figure 3.9: Double well potential with corresponding eigenenergies and eigenstates.
(a) Schematic geometry of the total confining potential in the axial direction for
a Gaussian barrier (height $h = 4 \, \hbar\omega_\perp$, waist $w = a_\perp$) located at the centre of the
trap. Plotted are the symmetric ($\delta = 0$, solid line) and asymmetric ($\delta = 0.5 \, \hbar\omega_\perp/a_\perp$,
dashed line) cases. (b) Eigenenergies for the double-well as a function of the potential
gradient δ indicating the self-interaction energy, E_C, and the Josephson coupling
energy, E_J. The horizontal dotted grey line corresponds to the zero energy of the
two-state model. The parameters used here are $g_{3D} = \pi$ and spherical trap geometry
($\lambda = 1$) corresponding to $E_C = 0.220 \, \hbar\omega_\perp$ and $E_J = 0.102 \, \hbar\omega_\perp$. (c) Eigenstates at
the centre of the trap: (i) ground state (lower solid line), (ii) anti-symmetric first-
excited state with equal population in both wells (thick solid line), (iii) first excited
state with unequal populations, having more population in left well (dotted), or in
right well (dashed).

and different geometries. The parameters λ, h have been chosen such as to match the

central density. We note that loop structure is independent of the trap geometry, it

appears also for a "pancake" trap and that increasing $\lambda > 1$ results in bigger energy

splittings.

An interesting subject is to investigate which type of geometry is favourable for

observing Josephson effects. It is proved in [57] that this condition is best satisfied
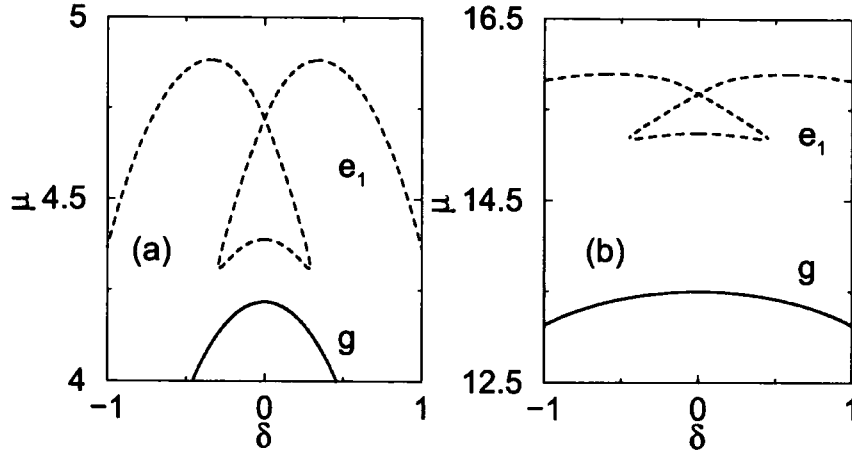
Figure 3.10: The energy eigenvalue, μ, as a function of the potential gradient δ, for the ground, g, and the first excited state, e_1 for $g_{3D} = 10\pi$ and (a) spherical ($\lambda = 1$) and $h = 4\,\hbar\omega_\perp$ and (b) "pancake" ($\lambda = \sqrt{8}$) trap and $h = 15\,\hbar\omega_\perp$. For the (b) case the energy splittings are larger thus the experimental observation of the Josephson effects are more feasible in the case of "pancake" geometry.

for a "pancake" trap which increases the weak link area between the two weakly coupled Bose-Einstein condensates and therefore the Josephson tunnelling. For the value of nonlinearity chosen in Fig. 3.8, $g_{3D} = 10\pi$ and for a typical frequency $\omega_\perp = 2\pi \times 5$ Hz, substituting in Eq. (2.10), (see Chapter 2), yields $\mathcal{N} = 3500$ for ^{23}Na and $\mathcal{N} = 1200$ for ^{87}Rb which is independent of the asymmetry parameter λ. Although $\mathcal{N}$ is the same for both spherical and "pancake" geometries, the latter is preferable for observing Josephson effects due to the larger energy splittings.

3.6 Comparison to the one dimensional results

The reduction from three to one dimension is not straightforward due to the non-linear term of the GPE. By using a variational method the one dimensional time-independent GPE is obtained by integrating the two transverse degrees of freedom in the energy functional (see Chapter 2). By using a Gaussian ansatz, we have found that the nonlinearity in one dimension is given by the equation $g_{1D} = g_{3D}/(2\pi)$ that matches the one and three dimensional axial density profiles. In Fig. 3.11 we show for comparison the eigenenergy curves for the ground g and the first two excited states

e_1 and e_2 as a function of the potential gradient δ with $h = 4\ \hbar\omega_\perp$ in one (light grey) and three dimensional (black) lines for a spherical trap, with (a) $g_{1D} = 0.5$ and $g_{3D} = \pi$ and (b) $g_{1D} = 5$ and $g_{3D} = 10\pi$. In plotting the eigenenergies, we have used the equation $\mu_{3D} = \mu_{1D} + 1$ that relates the chemical potential in one and three dimensions (see Chapter 2). We observe that the three dimensional GPE agrees with one dimensional equation in the limit of weak interactions. However, as expected, for large nonlinearities the Gaussian approximation for the transverse wavefunction fails.
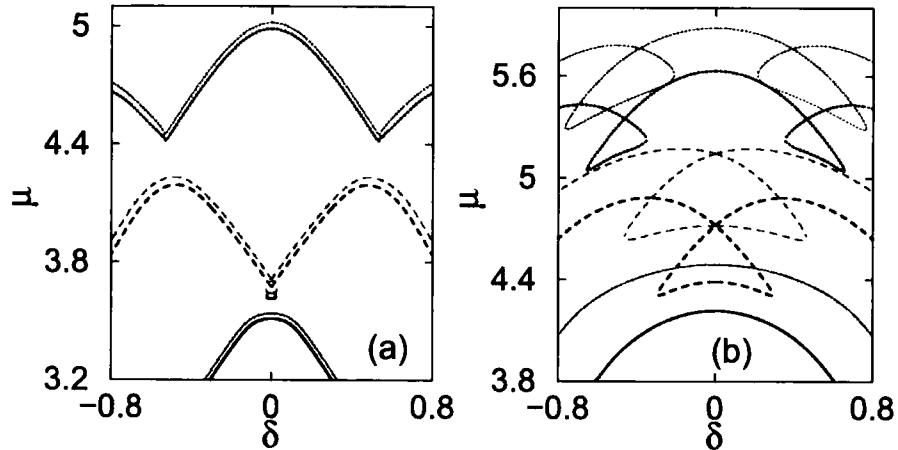
Figure 3.11: The energy eigenvalue, μ, as a function of the potential gradient δ, for the ground state g and the first two excited states, e_1 (dashed) and e_2 (dotted) lines in one (light grey) and three dimensions (black) lines, with $h = 4\ \hbar\omega_\perp$ and (a) $g_{1D} = 0.5$ and $g_{3D} = \pi$ and (b) $g_{1D} = 5$ and $g_{3D} = 10\pi$. In both cases in three dimensions, we assume a spherical trap, $\lambda = 1$.

In the following Chapter, we study the two-state model in more detail to investigate the tunnelling dynamics of initial states that have zero and π phase. These states correspond to the ground (Ψ_g) and the first excited (Ψ_e) states respectively.

Chapter 4

Josephson dynamics within the two-state model

We study the tunnelling dynamics of atoms through a barrier between two weakly coupled Bose-Einstein condensates in a double-well potential. The dynamics is described in terms of a two-state model and reveals a variety of interesting phenomena, including macroscopic quantum self-trapping where the average population imbalance is nonzero and π-phase oscillations where the mean value of the phase across the junction is π.

4.1 Introduction

In this Chapter we continue our study of an atomic BEC formed in a double-well potential by considering the tunnelling dynamics. We assume that the two traps are weakly connected and the lowest states are well separated from higher lying states even in the presence of many-body interactions. Under these assumptions, the dynamics of the system is described by means of a two-mode equations of motion for the population and the phase difference across the junction [60, 62, 63, 64, 65, 66, 67, 68, 69, 70, 71, 72, 73]. Recently, interesting effects including dc- and ac-Josephson effects in bosonic Josephson junctions, (BJJs), have been extensively studied [58, 60, 64, 65]. Moreover macroscopic quantum self-trapping (MQST) [64, 65, 66] and π oscillations [64, 65, 66, 67] have also been reported in such systems. MQST arises

from the nonlinear interatomic interaction and is a kind of self-locked population imbalance between two BECs. Atomic BJJs also exhibit π-oscillations where the mean value of the phase difference across the junction is π. These modes have been also observed in two weakly linked ^{3}He-B reservoirs [41].

The tunnelling between two weakly coupled BJJs, is analogous to the Josephson effect in Superconductors (SJJs), [30]. In the latter case, the presence of an external circuit results in zero Cooper-pair population imbalance (if the materials are the same) and the tunnelling arises from the relative phase difference of the macroscopic wavefunctions between the two Superconductors. Moreover, SJJs are described in terms of a *rigid* pendulum (see Introduction) whereas BJJs, are generally discussed in terms of a *nonrigid* pendulum and the tunnelling is a result of oscillatory exchange of neutral atoms between the two separated traps (see Section 4.3).

The two-mode or BJJ equations are also applicable to describe internal Josephson effects such as population transfer between different hyperfine states by variable external fields [52] and Bloch band tunnelling [56]. The internal Josephson effect in ^{3}He-A weak links, is described by equations analogous to the BJJ equations with the weak coupling provided by the dipole interaction of spin up and spin down and the *rigid* two-state equations describe the rate of change between spin-up and spin-down [53].

This Chapter is organised as follows. In Section 4.2 we begin the study of Josephson dynamics in BJJs, by considering the dynamics of a single particle in a double-well potential. Section 4.3 introduces the two-state model, BJJ equations and generalises the previous picture of single-particle tunnelling for the case of macroscopically occupied state. We solve the BJJs for the case of a symmetric and asymmetric trap and discuss different regimes.

4.2 Evolution of a wave packet

Before studying the two-state model, we review the basic theory of evolution of a wavepacket (see any standard textbook of quantum mechanics, e.g. [6]). We
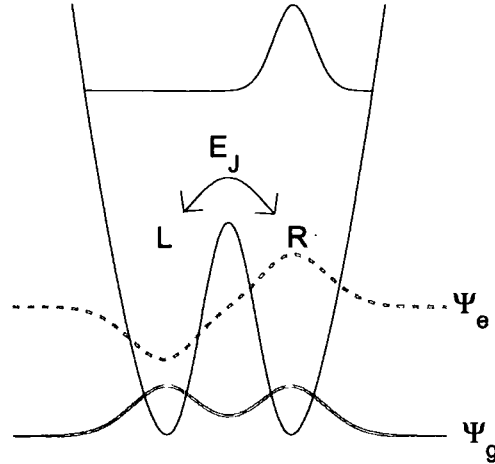
Figure 4.1: Eigenstates Ψ_g (solid grey) and Ψ_e (dashed grey lines) in the double-well potential. We also show a state that has most particles in the right well.

consider the problem in one dimension but it is also applicable in three dimensions. Let us first consider an eigenstate, the ground, Ψ_g or the first excited state Ψ_e in a double-well potential that have equal population in the left and right well (solid and dashed grey lines in Fig. 4.1 respectively). If a system is initially prepared in one of its eigenstates, it will remain in the same state in the absence of external perturbations. However, time evolution will rise when a system is initially prepared in any other state, e.g. a superposition state that is localised in the right well (black line in Fig. 4.1). This state can be represented in the basis of the eigenstates of the system by,

$$\Psi(z, t = 0) = \frac{1}{\sqrt{2}}(\Psi_g(z) + \Psi_e(z)) , \tag{4.1}$$

and the evolution of the wavefunction is simply,

$$\Psi(z, t) = \frac{1}{\sqrt{2}}(\exp(-iE_g t/\hbar)\Psi_g(z) + \exp(-iE_e t/\hbar)\Psi_e(z)) , \tag{4.2}$$

where $E_{g,e}$ are the eigenenergies of the corresponding eigenstates $\Psi_{g,e}$, which for simplicity we assume real functions. The shape of the wave packet is given by the

probability density,

$$P(z,t) = |\Psi(z,t)|^2 = \frac{1}{2}\Psi_g^2(z) + \frac{1}{2}\Psi_e^2(z) + \Psi_g(z)\Psi_e(z)\cos(\omega t) , \qquad (4.3)$$

where $\Psi_i^2(z)$, $i = g, e$, are the probability density amplitudes in the ground or first excited state and $\omega = (E_e - E_g)/\hbar$ is the frequency, corresponding to a transition between the ground and first excited states. The last term in Eq. (4.3) describes the interference between the two states Ψ_g and Ψ_e and produces density oscillations as shown in Fig. 4.2. The quantum interference between the two states induces oscillations between the two wells in a periodic manner, and we can have more particles on the left or right well, depending on which point of the cycle we are in. At the middle point of each cycle, the population is equal in both wells (bold black lines).
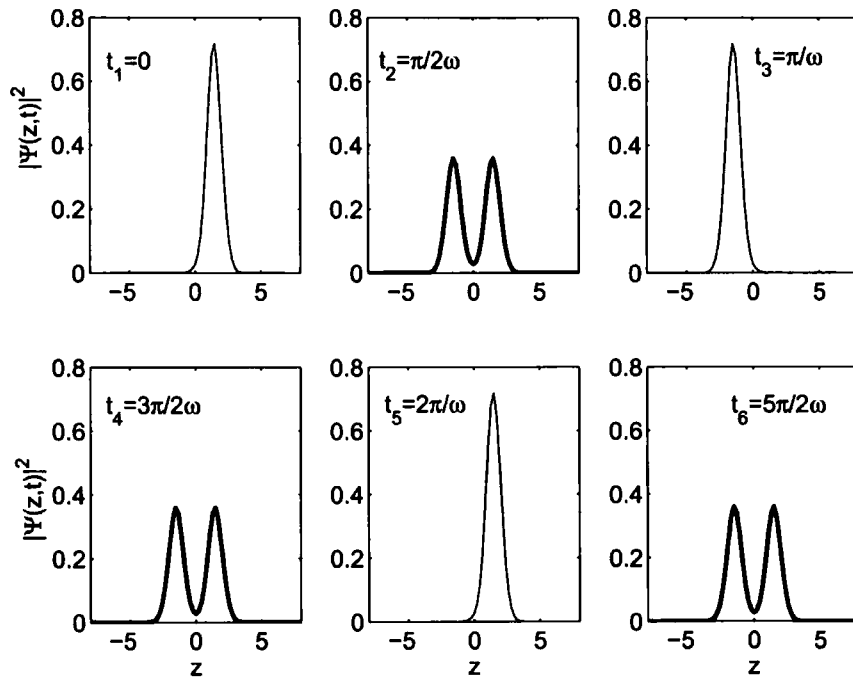
Figure 4.2: Coherent density oscillations of a wavefunction obtained by interference of the ground and first excited states in a double-well potential. The period of the motion is $2\pi/\omega$.

In the following Section we generalize the above picture of single-particle wavefunction evolution, to study the tunnelling dynamics between macroscopic wavefunctions for the cases of both ideal and interacting Bose gases. We present results for the evolution of the phase and fractional population difference between two separated BECs in a double-well potential. Next we present the two-state model.

4.3   Two-state model

The description of the GPE dynamics for a BEC in a double-well trap reduces to a nonlinear, two-mode equations for the time dependent amplitudes $c_{L,R}(t) = \sqrt{(N_{L,R}(t))}\exp(i\theta_{L,R}(t))$, where $N_{L,R}$ and $\theta_{L,R}$ are the populations and phases of the condensate in the left (L) or right (R) well respectively.

We can derive the equations for the population difference N and the relative phase θ by substituting $c_i = \sqrt{N_i}\exp(-i\theta_i)$ into Eq. (3.20) and Eq. (3.21),

$$iN_L^{-1/2}\dot{N}_L/2\exp\left(i\theta_L\right) + i\sqrt{N_L}i\dot{\theta}_L\exp\left(i\theta_L\right) = (-\Delta/2 + E_C N/2)\sqrt{N_L}\exp\left(i\theta_L\right) - (E_J/2)\sqrt{N_R}\exp\left(i\theta_R\right) \quad (4.4)$$

$$iN_R^{-1/2}\dot{N}_R/2\exp\left(i\theta_R\right) + i\sqrt{N_R}i\dot{\theta}_R\exp\left(i\theta_R\right) = (\Delta/2 - E_C N/2)\sqrt{N_R}\exp\left(i\theta_R\right) - (E_J/2)\sqrt{N_L}\exp\left(i\theta_L\right) . \quad (4.5)$$

Multiplying Eqs. (4.4) and (4.5) by $\exp(-i\theta_L)$ and $\exp(-i\theta_R)$ respectively and rearranging the terms we obtain,

$$iN_L^{-1/2}\dot{N}_L - 2\sqrt{N_L}\dot{\theta}_L = (-\Delta + E_C N)\sqrt{N_L} - E_J\sqrt{N_R}\exp\left(-i\theta\right) \quad (4.6)$$

$$iN_R^{-1/2}\dot{N}_R - 2\sqrt{N_R}\dot{\theta}_R = (\Delta - E_C N)\sqrt{N_R} - E_J\sqrt{N_L}\exp\left(i\theta\right) , \quad (4.7)$$

where $\theta = \theta_L - \theta_R$. We can obtain the equations of motion for the phase θ_i and the population N_i of the condensate in each well i by equating the real and imaginary parts in the above equations. Eq. (4.6) gives,

$$\dot{\theta}_L = -(-\Delta/2 + E_C N/2) + (E_J/2)\sqrt{N_R/N_L}\cos\theta \quad (4.8)$$

$$\dot{N}_L = E_J \sqrt{N_L N_R} \sin \theta , \tag{4.9}$$

and Eq. (4.7),

$$\dot{\theta}_R = -(\Delta/2 - E_C N/2) + (E_J/2)\sqrt{N_L/N_R} \cos \theta \tag{4.10}$$

$$\dot{N}_R = -E_J \sqrt{N_L N_R} \sin \theta . \tag{4.11}$$

Thus we obtain the following two coupled systems for θ_i,

$$\dot{\theta}_L = -(-\Delta/2 + E_C N/2) + (E_J/2)\sqrt{N_R/N_L} \cos \theta \tag{4.12}$$

$$\dot{\theta}_R = -(\Delta/2 - E_C N/2) + (E_J/2)\sqrt{N_L/N_R} \cos \theta , \tag{4.13}$$

and for the populations N_i,

$$\dot{N}_L = E_J \sqrt{N_L N_R} \sin \theta \tag{4.14}$$

$$\dot{N}_R = -E_J \sqrt{N_L N_R} \sin \theta . \tag{4.15}$$

Subtracting the above equations so that to create the differences $\dot{N} = \dot{N}_L - \dot{N}_R$ and $\dot{\theta} = \dot{\theta}_L - \dot{\theta}_R$ we obtain,

$$\dot{N} = 2E_J \sqrt{N_L N_R} \sin \theta \tag{4.16}$$

$$\dot{\theta} = \Delta - E_C N + (E_J/2)\left(\sqrt{N_R/N_L} - \sqrt{N_L/N_R}\right) \cos \theta , \tag{4.17}$$

or

$$\dot{N} = E_J \sqrt{1 - N^2} \sin \theta \tag{4.18}$$

$$\dot{\theta} = \Delta - E_C N + \frac{E_J N}{\sqrt{1 - N^2}} \cos \theta , \tag{4.19}$$

where we have used the equation $N_L N_R = (1 - N^2)/4$.

The equations of motion can also be derived from the Hamiltonian formalism,

$$\dot{N} = -\frac{\partial H}{\partial \theta} \tag{4.20}$$

$$\dot{\theta} = \frac{\partial H}{\partial N} \tag{4.21}$$

where H is the Hamiltonian of the system,

$$H = \frac{-1}{2} E_C N^2 + \Delta N + E_J \sqrt{1 - N^2} \cos\theta \,, \qquad (4.22)$$

and N is the momentum for the generalized coordinate θ.

Eqs. (4.18) and (4.19), describe Josephson effects between two BJJs with fractional population difference N and relative phase θ. In order to apply the above equations one needs to know the parameters $E_C, E_J, \Delta = \alpha z_0$, where α is a numerical factor, obtained by numerical solution of the time-independent GPE. The corresponding evolution is characterized by the ratio $\Lambda = E_C/E_J$, of the self-interaction to the Josephson coupling energy. For $\Lambda > 1$ the behaviour is similar to SJJ and for $\Lambda < 1$ Rabi oscillations are observed. The condition $\Lambda_C = 1$ marks the transition from interaction-dominated to tunnelling-dominated regime. However for the parameters used throughout this Thesis, the Rabi oscillation regime is not attainable.

Moreover Eqs. (4.18) and (4.19), are the analog of Eqs. (1.49) and (1.50) for SJJ. However there are some differences between the two systems. BJJ is described by a *nonrigid* pendulum of length $\sqrt{1 - N^2}$ dependent on the momentum N whereas SJJ is described by a *rigid* pendulum of length I_0. Moreover in the SJJ $N = 0$ due to the presence of an external circuit in contrast to the BJJ where $N \neq 0$ due to density oscillations. The latter leads to interesting phenomena unique in BJJs which will be presented in the next Sections.

4.3.1 Symmetric double-well

For a symmetric double-well, $\Delta = 0$, the equations of motion, Eqs. (4.18) and (4.19), become,

$$\dot{N} = E_J \sqrt{1 - N^2} \sin\theta \,, \qquad (4.23)$$

$$\dot{\theta} = -N E_C - \frac{E_J N}{\sqrt{1 - N^2}} \cos\theta \,. \qquad (4.24)$$

For the noninteracting Bose gases ($E_C = 0$) the eigenstates at $z_0 = 0$ are a symmetric ground state Ψ_g and an antisymmetric first excited state, Ψ_e, (see Fig. 4.1). Within the two-state model these states are described with the initial conditions $N(0) = 0$ and $\theta(0) = 0$ and $N(0) = 0$ and $\theta(0) = \pi$ respectively. In this case the properties of the system are time-independent, since both of them are eigenstates. However, if we start with an initial population imbalance, the system will yield Rabi-oscillations with frequency $\Omega = E_J$. This picture is the generalization of a single-particle dynamics for the case of many-atom BEC state and has been discussed in [119].

4.3.2 Interacting limit

We now focus on the more interesting case of interacting atoms ($E_C \neq 0$). As before we are interested in the dynamical properties of the system such as the evolution of the population and the phase difference across the junction. Our studies reveal that new interesting phenomena arise due to the nonlinearity and the choice of the initial conditions $N(0)$ and $\theta(0)$. We consider two different cases where the time-averaged phase difference across the junction is zero and π. In the former case the oscillations are called zero phase oscillations whereas in the latter case, they are conventially referred to as π-oscillations as discussed in the context of BJJ by Smerzi [64, 65, 66, 67]. Now we will discuss each mode separately.

Zero phase oscillations

In Fig. 4.3 we show the evolution of the population difference for increasing values of $N(0)$ for $\theta(0) = 0$. If the system is initially in a state that is not an eigenstate of the symmetric double-well, for example in a state that has $N(0) \neq 0$, then the system yields Josephson oscillations between the wells with complete exchange of atoms. The amplitude of these oscillations (i) increases for $N(0) < N_c$, (Figs. 4.3(a) and (b)), (ii) reaches a critical value at $N(0) = N_c$, (Fig. 4.3(c)) and (iii) then decreases again for $N(0) > N_c$, (Fig. 4.3(d)) with the oscillations trapped in one well. In the latter case the populations become macroscopically self-trapped, (MQST), with
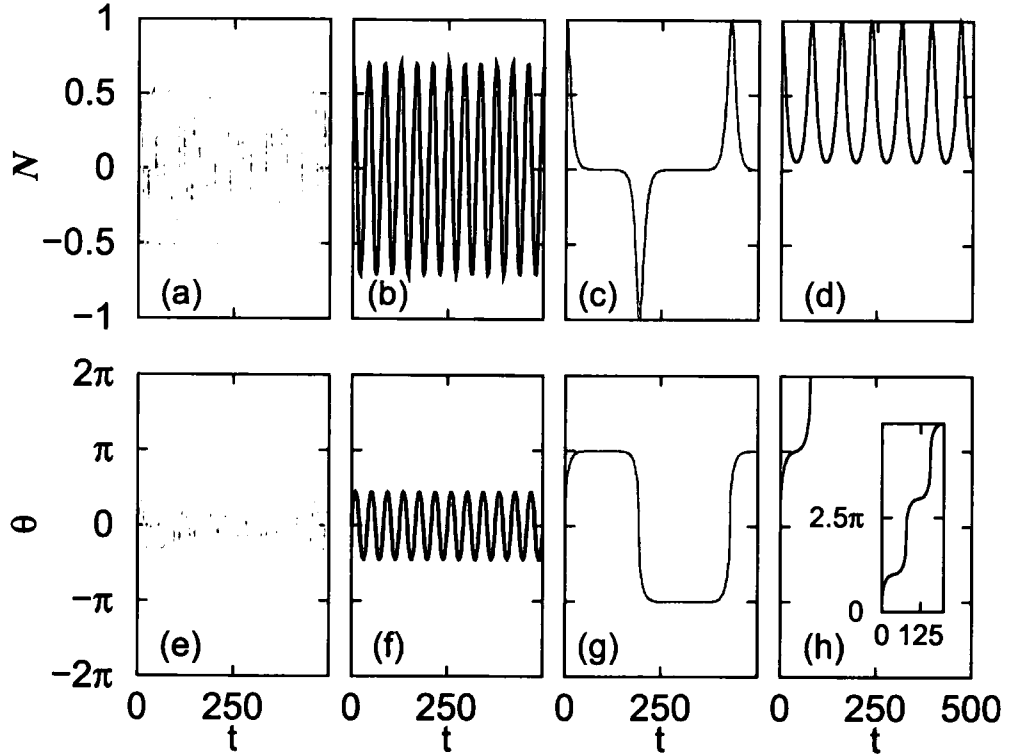
Figure 4.3: (a)-(d) The fractional population difference, N, and (e)-(h) the corresponding phase difference, θ, as a function of time $(\omega_\perp^{-1})$ for $E_J = 0.1\hbar\omega_\perp$, $E_C = 0.22\hbar\omega_\perp$ and $\theta(0) = 0$ in a symmetric trap ($\Delta = 0$). In (a) and (e) $N(0) = 0.5$, (b) and (f) $N(0) = 0.7$, (c) and (g) $N(0) = N_c = 0.99585919488$ and finally (d) and (h) $N(0) = 0.996$. The phase difference θ as a function of time is plotted inset in (h).

$\langle N(t) \rangle \neq 0$. Thus even though there is an initial population imbalance $N(0)$, there is a small periodic transfer of atoms between the two wells while the majority of atoms remains trapped in one well. For $\theta(0) = 0$ MQST occurs if $N(0) > N_c$ whereas for $\theta(0) = \pi$ it occurs when $N(0) < N_c$, as we shall see next. Finally by looking at the evolution of the phase difference, we observe oscillations with a time-average value of $\langle \theta(t) \rangle = 0$ that increasing $N(0) < N_c$, become nonsinusoidal (Figs. 4.3(e)-(g)). For $N(0) > N_c$, (Fig. 4.3(h)), the phase difference oscillates around a nonzero value, running phase mode, which corresponds to the MQST regime.

The behaviour of the zero phase modes can be also represented using a phase portrait

(θ, N) of the variables θ and N, shown in Fig. 4.4(a). The trajectories correspond to the values of $N(0)$ used in Fig. 4.3 with $\theta(0) = 0$. We see that for $N(0) <$ N_c the trajectories are closed loops that enclose the origin, and that for $N(0) >$ N_c the trajectories are unbounded. This transition is represented by a grey line which acts as a separatrix between symmetric and nonsymmetric oscillations of the population imbalance N. In the classical picture of *nonrigid* pendulum, it represents the transition of oscillatory to rotational motion.
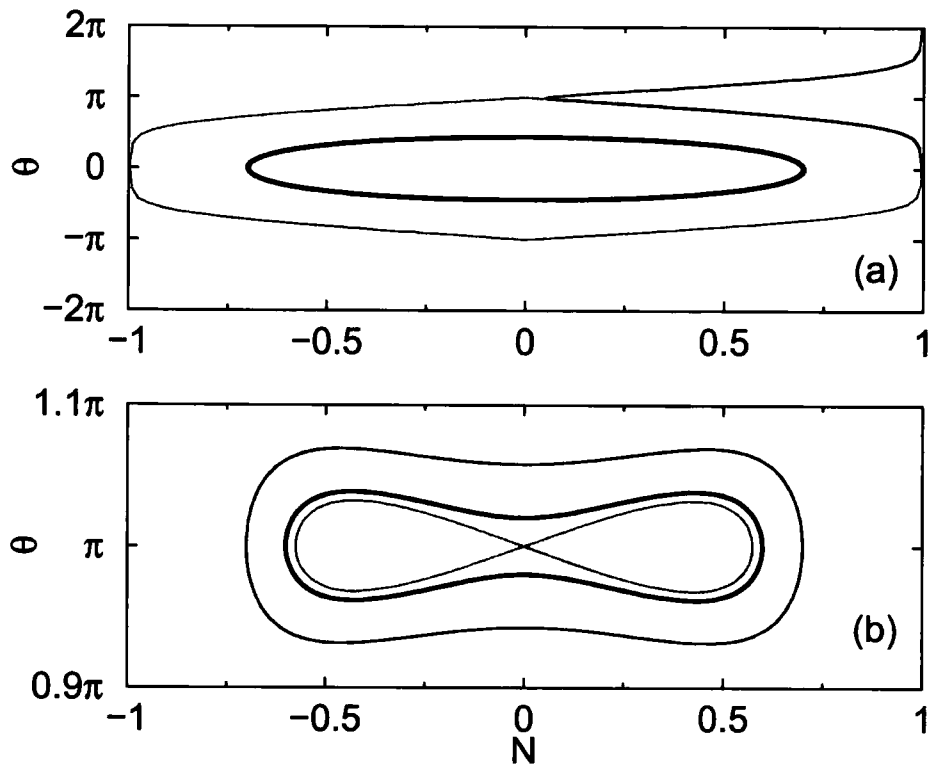
Figure 4.4: Phase as a function of N for (a) the case of Figs. 4.3 and (b) 4.5. In (a) $\theta(0) = 0$ and $N(0) := 0.5$,(light grey), 0.7, (bold black), 0.99585919488 (dark grey) and 0.996 (black) lines. In (b) $\theta(0) = \pi$ and $N(0) := 0.5$,(light grey), 0.5749595734, (dark grey), 0.6 (bold black) and 0.7 (black) lines.

π-oscillations

For the initial condition $\theta(0) = \pi$ one finds oscillations with $\langle\theta(t)\rangle = \pi$ [64, 65, 66, 67]. For our study we plot the evolution of $N(t)$ and $\theta(t)$ for fixed $\theta(0) = \pi$ and

various values of $N(0)$. Figs. 4.5(a)-(d) show Josephson oscillations with increasing amplitude. For $N(0) < N_c$ (Fig. 4.5(a)) there is a transition to the MQST regime with the oscillations are trapped in one well whereas for $N(0) > N_c$ (Figs. 4.5(c) and (d)) the evolution of the population difference oscillates around a zero value $(\langle N(t) \rangle = 0)$. The transition from the MQST regime to Josephson oscillations is marked from a value of $N(0) = N_c$ (Fig. 4.5(b)) for which the Josephson oscillations are frozen initially and appear again for later times.
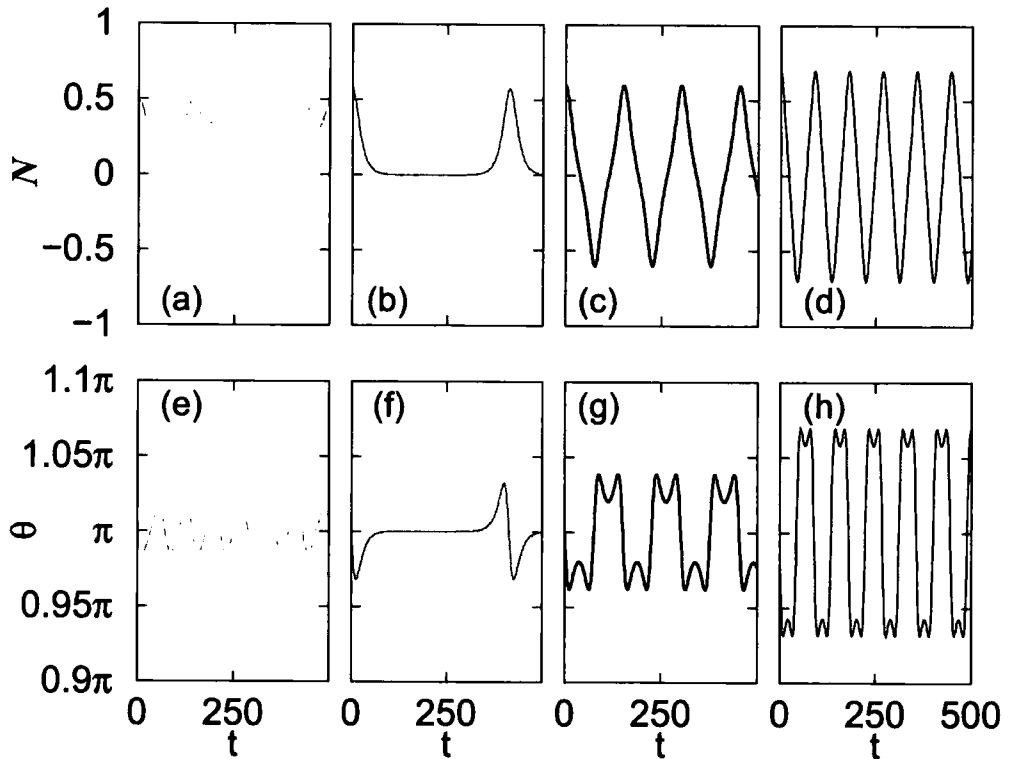
Figure 4.5: (a)-(d) The population difference, N, and (e)-(h) the corresponding phase difference, θ, as a function of time $(\omega_\perp^{-1})$ for $E_J = 0.2\hbar\omega_\perp$, $E_C = 0.22\hbar\omega_\perp$ and $\theta(0) = \pi$ in a symmetric trap $(\Delta = 0)$. In (a) and (e) $N(0) = 0.5$, (b) and (f) $N(0) = N_c = 0.5749595734$, (c) and (g) $N(0) = 0.6$ and finally (d) and (h) $N(0) = 0.7$.

By looking at the phase profiles as a function of time in Figs. 4.5(e)-(h) we observe that the phase oscillates around a mean value $\langle\theta(t)\rangle = \pi$ and that increasing $N(0)$ these oscillations become nonsinusoidal. In Fig. 4.4(b) we plot the phase portrait, (θ, N), of the variable θ as a function of N for the case of π-modes. The trajectories

are closed loops for all values of $N(0) > N_c$ and for $N(0) < N_c$ do not enclose the origin. For $N(0) = N_c$, grey loop in Fig. 4.4(b), the trajectory crosses the origin and is the separatrix of the MQST and symmetric regimes.
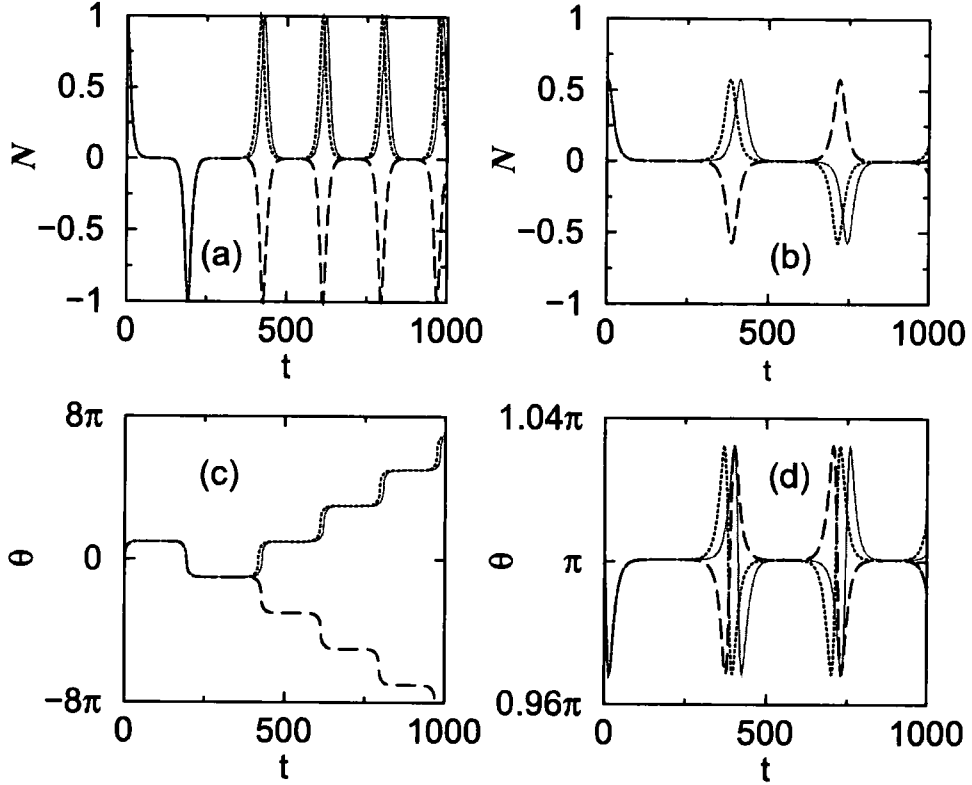
Figure 4.6: The sensitivity of evolution of the population difference (a)-(b) and the phase difference θ across the junction in the initial conditions $N(0)$ and $\theta(0)$ for a symmetric ($\Delta = 0$) double-well. In (a) and (c) $E_J = 0.1\hbar\omega_\perp$, $E_C = 0.22\hbar\omega_\perp$, $\theta(0) = 0$ and $N(0) := 0.99585919487$ (dotted black), 0.99585919488 (grey) and 0.99585919489 (dashed black) lines. In (b) and (d) $E_J = 0.2\hbar\omega_\perp$, $E_C = 0.22\hbar\omega_\perp$, $\theta(0) = \pi$ and $N(0) := 0.5749595733$ (dotted black), 0.5749595734 (grey) and 0.5749595735 (dashed black) lines.

Finally we point out that the value of N_c, for both the zero and π-phase modes, depends critically on the initial conditions. Fig. 4.6 shows that even a small change in the initial condition for $N(0)$, occuring in the tenth decimal place, changes the corresponding evolution of the parameters N, θ. We emphasize that, in both cases, one could not manage to lock the fractional population difference at $N(t) = 0$ for a long time interval as the sensitivity in $N(0)$ is extremely high, see Fig. 4.6.

4.3.3   Asymmetric double-well

We continue our study of the Josephson dynamics in an asymmetric double-well ($\Delta \neq 0$). The asymmetry is induced by a barrier that moves away from the origin with a constant velocity v. We solve the full set of Eqs. (4.18) and (4.19), using $\Delta = -2\alpha z_0 = -2\alpha v t$. In Fig. 4.7 we show the Josephson dynamics of a system with initial conditions $N(0) = 0$ and $\theta(0) = 0$ (Figs. 4.7(a) and 4.7(b)) and π, (Figs. 4.7(c) and 4.7(d)) for various values of velocities for the low (left) and high barrier limit (right column). These initial conditions correspond to the ground, Ψ_g, and first excited, Ψ_e, state with equal population in both wells. For Ψ_g, the asymmetry induces a Josephson current to the left (lower potential energy region), whereas for Ψ_e flow occurs to the right (higher potential energy). Moreover the evolution of the population difference for Ψ_e initial state, Figs. 4.7(c) and 4.7(d) predicts that the atoms remain in the upper (right) well (MQST).

MQST regime

We attempt to find the condition for MQST in the case of an asymmetric trap for zero- and π-phase modes. We study the dynamical properties of the system with a fixed population asymmetry $N(0)$ for various values of the potential gradient Δ.

a. zero phase modes

Firstly let us consider the case of $\theta(0) = 0$ shown in Fig. 4.8. Fig. 4.8(a) shows that there is a range of values $\Delta < \Delta_c$ for which $\langle N(t) \rangle < N(0) \neq 0$ whereas for $\Delta > \Delta_c$, the evolution of $N(t)$ is trapped in the left (lower well), with amplitudes that vary between $N(0)$ and $N_{max} = 1$. In the case of an asymmetric well the latter condition corresponds to the MQST regime. At $\Delta = \Delta_c = 0.177\hbar\omega_\perp$ the average population difference is $\langle N(t) \rangle = N(0)$ with $N(0)$ a stationary value of the two-state model. Fig. 4.8(b) displays the corresponding $\theta(t)$. For $\Delta \leq \Delta_c$, the time average value of the phase across the junction equals zero, $\langle \theta(t) \rangle = 0$, whereas for $\Delta > \Delta_c$, $\langle \theta(t) \rangle \neq 0$ corresponding to the running-phase MQST regime.

The dynamics can also be represented in terms of phase portraits (θ, N) shown in
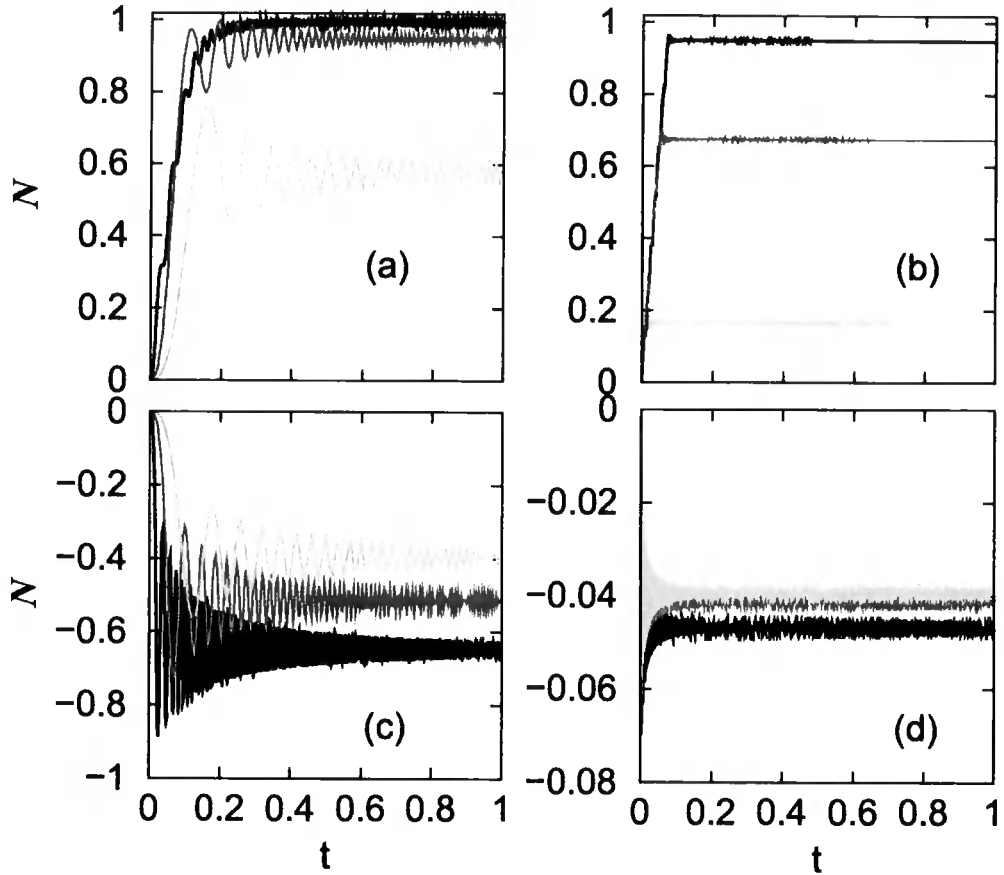
Figure 4.7: Evolution of fractional population N as a function of barrier displacement z_0, for a system initially prepared in the ground Ψ_g, ($N(0) = 0$ and $\theta(0) = 0$), Figs. (a) and (b) and the first excited state Ψ_e state, ($N(0) = 0$ and $\theta(0) = \pi$) Figs. (c) and (d). The barrier is moved from the centre towards the right well at constant speed $v(a_\perp\omega_\perp) =: 1 \times 10^{-3}$, (black), 4×10^{-3}, (brown) and 1×10^{-2} (grey lines) in (a) and (c) and 2×10^{-5}, (black), 3.4×10^{-5}, (brown) and 4×10^{-5} (grey lines) in (b) and (d). The parameters for the two-state model used here are:(a) and (c) $E_J = 0.1\hbar\omega_\perp$, $E_C = 0.24\hbar\omega_\perp$ and $2\alpha = 3.187\hbar\omega_\perp/a_\perp$ and (b) and (d) $E_J = 0.0007\hbar\omega_\perp$, $E_C = 0.287\hbar\omega_\perp$ and $2\alpha = 3.964\hbar\omega_\perp/a_\perp$.

Fig. 4.8(c). For $\Delta < \Delta_c$ the trajectories are closed and increasing Δ, the trajectory area decreases while for $\Delta = \Delta_c$ it shrinks to a point at $\langle N(t) \rangle = N(0)$. For $\Delta > \Delta_c$ the trajectories are reflected along the $\langle N(t) \rangle = N(0)$ vertical axis, and for further increase of Δ the trajectories are unbounded (MQST regime). The critical value Δ_c
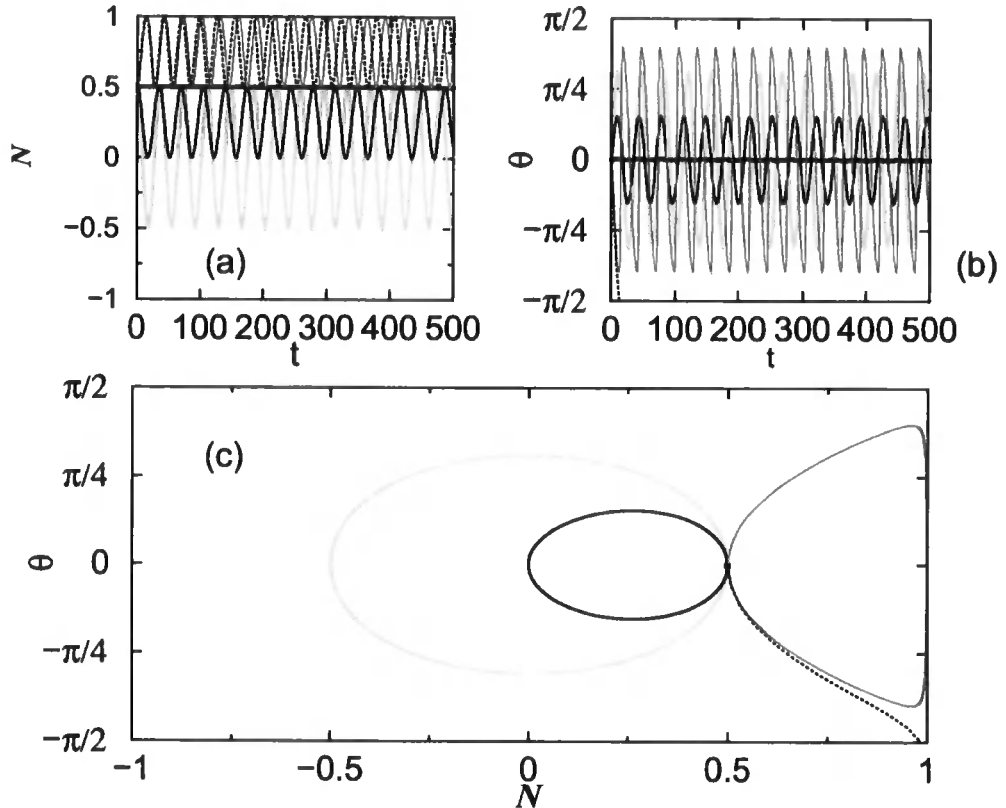
Figure 4.8: Evolution of (a) the population imbalance N and (b) the phase difference across the junction θ for different values of the potential gradient Δ. (c) Corresponding phase portrait (θ, N) for a system with $\theta(0) = 0$ and $N(0) = 0.5$. The values of the potential gradient are $\Delta(\hbar\omega_\perp) =: 0$ (light grey), 0.0867 (black), 0.177 (bold black), 0.344 (dark grey) and 0.357 (dotted black) lines. Other parameters for the two-state model are $E_J = 0.1\hbar\omega_\perp$ and $E_C = 0.24\hbar\omega_\perp$.

can be obtained by the two-state model Eqs. (4.18) and (4.19), by setting $\theta = \pi$ which gives,

$$\Delta_c = \left(E_C + \frac{E_J}{\sqrt{1 - N_c^2}} \right) N_c \,, \tag{4.25}$$

where $N_c = N(0)$. In the mechanical model of a *nonrigid* pendulum this corresponds

to the condition that the pendulum has enough energy to go over the top. Substituting the values $E_J = 0.1\hbar\omega_\perp$ and $E_C = 0.24\hbar\omega_\perp$ (see Fig. 4.8) we find $\Delta_c = 0.177\hbar\omega_\perp$ which is in excellent agreement with the two-state model prediction.

b. π phase modes

We now study the critical condition for MQST in the case of π modes, shown in Fig. 4.9. As in the previous case we firstly present the evolution of $N(t)$ in Fig. 4.9(a).
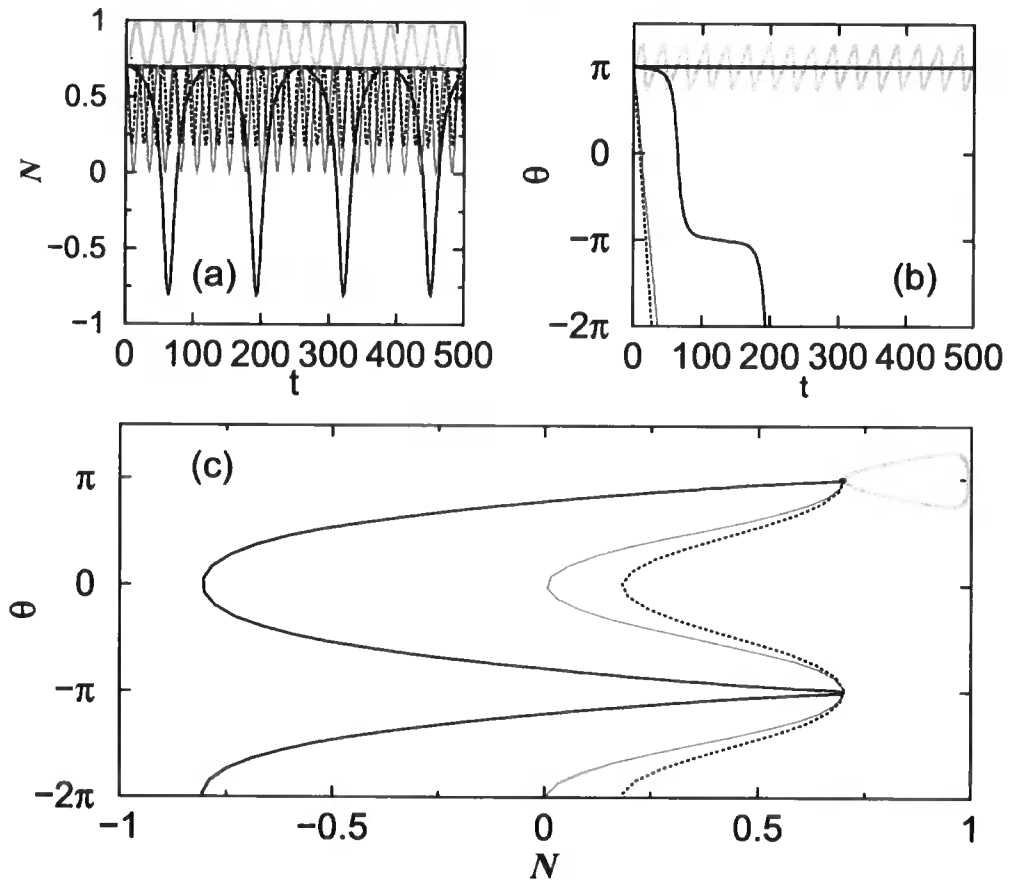
Figure 4.9: Evolution of (a) the population imbalance N and (b) the phase difference across the junction θ for different values of the potential gradient Δ. The phase portrait (θ, N) is also plotted in (c) for a system with $\theta(0) = \pi$ and $N(0) = 0.7$. The values of the potential gradient are $\Delta(\hbar\omega_\perp) =: 0$ (light grey), 0.070 (bold black), 0.072 (black), 0.332 (dark grey) and 0.352 (dotted black) lines. Other parameters as Fig. 4.8.

For $\Delta < \Delta_c$, the average value of the population difference is trapped in the lower

(left) well and oscillates between $N(0)$ and $N_{max} = 1$. In agreement with the case of zero phase modes, at $\Delta = \Delta_c = 0.070\hbar\omega_\perp$ the average population difference is $\langle N(t) \rangle = N(0)$ with $N(0)$ a stationary value of the two-state model whereas for larger values of $\Delta > \Delta_c$ the oscillations of $N(t)$ are nonsinusoidal with $\langle N(t) \rangle \neq 0$. We also study the evolution of $\theta(t)$ in Fig. 4.9(b). For $\Delta \leq \Delta_c$, $\langle \theta(t) \rangle = \pi$ whereas for $\Delta > \Delta_c$, $\langle \theta \rangle \neq 0$. Finally in Fig. 4.9(c) we present the phase portraits (θ, N). For $\Delta < \Delta_c$ the trajectories are closed. For increasing Δ the trajectory area decreases and at $\Delta = \Delta_c$ it shrinks to a point at $\langle N(t) \rangle = N(0)$. For $\Delta > \Delta_c$ the trajectories are reflected about the $\langle N(t) \rangle = N(0)$ vertical axis and are unbounded.

In the case of π-phase modes, the critical value Δ_c can be also obtained by the two-state model Eqs. (4.18) and (4.19), by setting $\theta = 0$ which gives,

$$\Delta_c = \left(E_C - \frac{E_J}{\sqrt{1 - N_c^2}} \right) N_c \,, \tag{4.26}$$

where $N_c = N(0)$. In the mechanical model of a *nonrigid* pendulum this corresponds to the condition that the pendulum reaches the equilibrium ($\theta = 0$). Substituting the values $E_J = 0.1\hbar\omega_\perp$ and $E_C = 0.24\hbar\omega_\perp$ (see Fig. 4.8) we find $\Delta_c = 0.070\hbar\omega_\perp$ which is in excellent agreement with the two-state model prediction.

In this Chapter we presented the Josephson dynamics of states with initial phase zero or π and various initial population difference $N(0)$ in a symmetric and asymmetric double-well potential within the two-state model. In the following, we continue our studies on the Josephson dynamics of a system with repulsive interactions initially prepared in the Ψ_g (Chapter 5) and Ψ_e (Chapter 6) states by considering the full numerical solution of the GPE and we compare our results to the two-state model.

Chapter 5

Josephson tunnelling of a dilute BEC initially prepared in the ground state

We investigate the Josephson dynamics of a dilute Bose-Einstein condensate initially prepared in the ground state in a one dimensional asymmetric double-well potential. The asymmetry is induced by a Gaussian barrier that moves uniformly through the condensate at a constant velocity. Above a critical velocity there is a transition to an ac current. We study the tunnelling dynamics by considering transitions between eigenstates and we show that in the regime of greatest interest for experiments, i.e., where the energy splittings are large, the influence of higher-lying states cannot be ignored.

5.1 Introduction

The experimental realization of atomic Bose-Einstein condensation (BEC) [13, 14, 15, 16, 17, 18, 19, 20, 21, 22] gives rise to a new system for studying Josephson effects consisting of two weakly interacting BECs. Such systems can be produced in a double-well trap with the two independent condensates coupled by quantum tunnelling. The weak link is provided by a barrier moving with constant velocity across the trap. If the velocity is small there is no potential difference across the

junction which is the analogue of the dc current in SJJs. At a critical velocity there is a sharp transition between the dc and ac regimes and the fractional population difference remains constant, apart from a decaying oscillatory component.

In the previous Chapter we studied Josephson effects in BJJs within the two-state model which is based on the approximation that the wavefunction is given by a superposition of two time-independent wavefunctions of the left and right well. However our analysis in this Chapter goes beyond the two-state model to investigate numerical solutions of the GPE which is a powerful tool to describe the behaviour of dilute, near zero temperature condensates. Our main motivation is to find new effects not present in the two-state model as well as to check its limitations. Our studies of the Josephson dynamics are based by considering transitions between eigenstates of a double-well potential. Here we limit our discussion to the dynamics of a BEC initially prepared in the ground state, and in the following Chapter we consider the Josephson dynamics of phase-imprinted states.

This Chapter is organised as follows. In Section 5.2, we calculate the fractional population difference of the lowest three eigenstates in an asymmetric double-well potential. In Section 5.3, we consider the time-independent evolution as the barrier is moved at a constant velocity from the centre outwards and in Section 5.4, we discuss the critical velocity for the transition between dc and ac current. In Section 5.5, we study the Josephson dynamics for the case of asymmetric initial conditions. We close this Chapter, by discussing typical experimental parameters in Section 5.6.

5.2 General discussion on the eigenstate fractional population difference

We present typical plots of the fractional population difference N, for the ground and the first two excited states which correspond to the eigenenergy levels shown in Chapter 3. Our results are based on varying the nonlinearity at fixed barrier height, but it should be noted that similar results will be obtained in the opposite limit of variable barrier height at fixed nonlinearity. Our study is based on numerical

solutions of the time-independent GPE (3.1), using the Newton method presented in Appendix A. Our studies explicitly consider the $z_0 > 0$ limit, however, for completeness, we also plot the $z_0 < 0$ values, which which are produced by projecting the $z_0 > 0$ solutions about the origin. This fact has also been explicitly verified by calculations.

Fig. 5.1 shows the fractional population difference for the ground state. In Fig. 5.1(a) typical eigenenergy levels for various nonlinearites are plotted. We observe that for positive nonlinearity there is only one eigenenergy level for the ground state at $z_0 > 0$ thus there is only one curve for the fractional population difference at $z_0 > 0$. Fig. 5.1(b) shows the effect of the nonlinearity on the fractional population difference. As the nonlinearity is increased, the crossover region in which the population is transferred from right to left well becomes smoother. The corresponding wavefunctions for the case g_{1D} are plotted in Fig. 5.1(c) at points (i)-(iv). This demonstrates that the initially symmetric population distribution for the ground state becomes asymmetric with increasing z_0, with the population gradually transferred to the left well.

We also consider the fractional population difference for the excited states, shown in Fig. 5.2. Fig. 5.2(a) shows the eigenenergy levels for the first excited eigenstate for small (grey) and large (black lines) nonlinearities. The corresponding fractional population differences are shown in Figs. 5.2(i)-(iii). For $g_{1D} = 0$ there is no loop structure and the fractional population difference is single valued (zero at $z_0 = 0$), as shown in Fig. 5.2(i). However, for sufficiently large nonlinearities, loop structure appears in the eigenenergy levels which is related to the existence of "self-trapped" states that have nonzero fractional population difference at $z_0 = 0$ (see discussion in Chapter 3). Therefore the first excited state is degenerate at the origin and the fractional population difference acquires three values at $z_0 = 0$, shown in Figs. 5.2(ii) and (iii). These values correspond to: a state with the population balanced in both wells at the centre of the trap, thus $(N(0) = 0)$; and two other nonzero values that correspond to "self-trapped" states that have most particles trapped on the left $(N(0) > 0)$ and right well $(N(0) < 0)$, see also the wavefunctions plotted in Fig. 3.2.
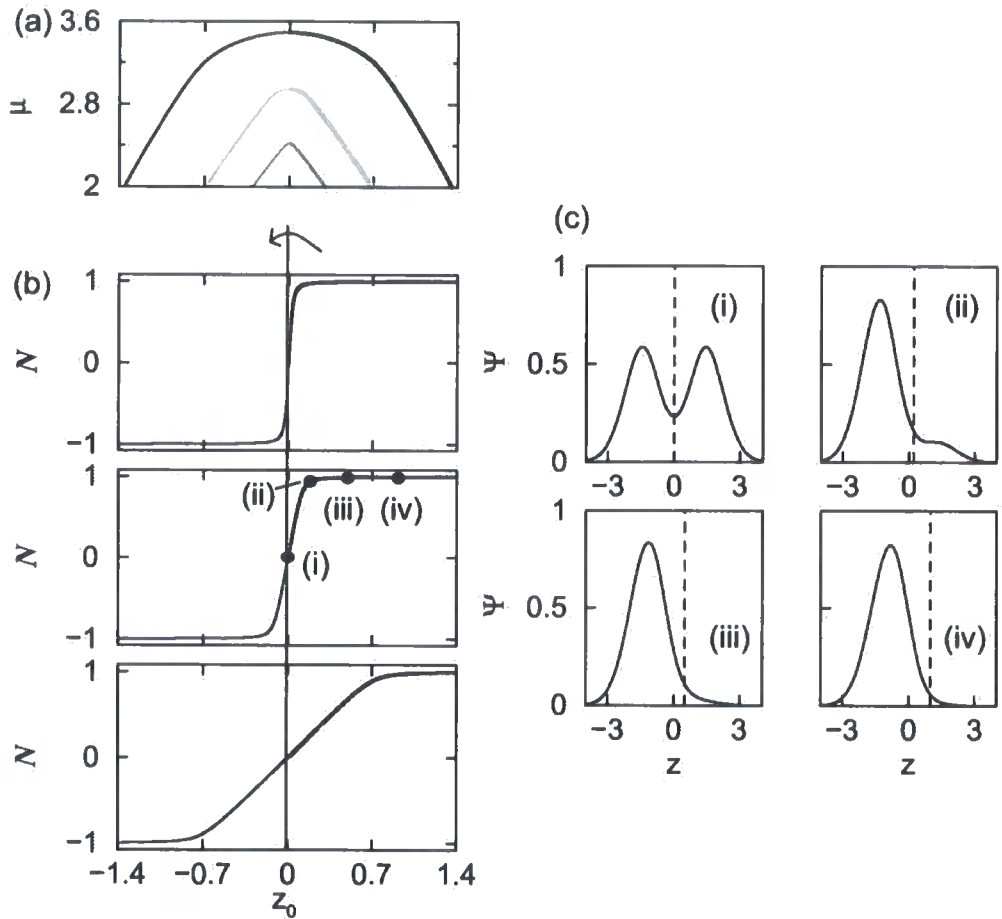
Figure 5.1: (a) The eigenenergies μ as a function of the barrier displacement z_0 for
the the ground eigenstate g for barrier height $h = 4\ \hbar\omega_\perp$ and $g_{1D} := 0$, (dark grey),
0.5, (light grey) and 5 (black lines). The eigenenergies for $g_{1D} = 0.5$ have been
shifted along the μ-axis by $+0.3\ \hbar\omega_\perp$. (b) The corresponding population difference
N for $g_{1D} = 0, 0.5, 5$ (from top to bottom). (c) Plots of the ground eigenstates for
the case of $g_{1D} = 0.5$ at various positions of the barrier displacement, z_0 indicated
by dashed lines. From (i)-(iv) $z_0\ (a_\perp) = 0, 0.2, 0.5, 0.9$.

In all cases (i)-(iii), the fractional population difference oscillates as a function of the barrier displacement with zeroes at the level crossings ($z_0 = 0$ with the ground state and $z_0 \sim 0.5$ $a_\perp$ with the second excited state, see for example the eigenstates in Fig. 5.2(a)).

Finally we consider the second excited state, e_2. An example of the eigenlevel structure for small (grey) and large (black lines) nonlinearities is shown in Fig. 5.2(b). The corresponding fractional population difference for the second excited eigenstates are shown in Figs. 5.2(iv)-(vi). As before, sufficiently large nonlinearities lead to the appearance of loop structure in the eigenlevels (see for example black line in Fig. 5.2(b)). In addition, the fractional population difference oscillates as a function of z_0 and is symmetric around the $z_0 = 0$ axis with $N(0) = 0$. However, there are two extra zero values of the fractional population difference which correspond to the level crossings with the first at $z_0 \sim 0.5$ $a_\perp$ and the third $z_0 \sim 0.9$ $a_\perp$ excited states, (see for example grey line in Fig. 5.2(b)). Moreover, Fig. 5.2(v) shows that the derivative dN/dz_0 diverges for $g_{1D} = 0.5$ at $z_0 \sim 0.5$ $a_\perp$ which is related to a cusp-like structure in the eigenenergy curve at that point. Figs. 5.2(i)-(vi) show that increasing the interactions, the fractional population difference curves undergo a shearing along the z_0 axis.

We further comment on the "self-trapped" states appearing in the loop structure. In Fig. 5.3, we show the population difference of the "self-trapping" state. A population asymmetry appears at the critical point, $E_C = E_J$, corresponding to the critical barrier height, $h = 2.916$ $\hbar\omega_\perp$ for $g_{1D} = 0.5$ (see also Chapter 3). The asymmetry increases with increasing barrier height. As a function of the nonlinearity, the "self-trapping" population first increases, then saturates, and finally decreases at large g_{1D} due to the influence of e_2.

We now apply the eigenstate level picture to analyse the population dynamics when the barrier is moved uniformly through the condensate at velocity v. The time-dependent GPE (3.1), is integrated using a Crank-Nicholson algorithm and the time evolution analysed in terms of transitions between eigenstates.
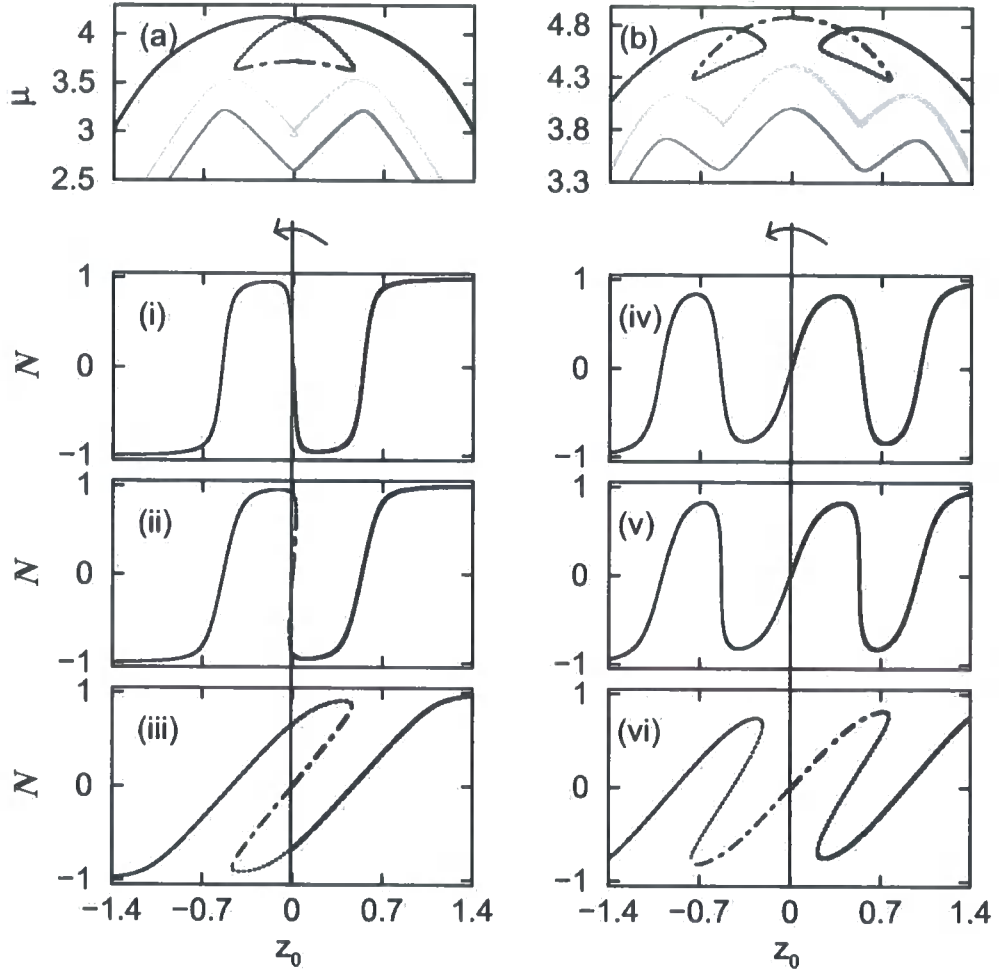
Figure 5.2: The eigenenergies μ for (a) the first and (b) the second excited states for large (black) and low interactions (grey) lines as a function of the barrier displacement z_0 for $g_{1D} := 0$, (dark grey), 0.5, (light grey) and 5 (black). The eigenenergies for $g_{1D} = 0$ and 0.5 have been shifted along the μ-axis by $+0.1 \ \hbar\omega_\perp$ and $+0.3 \ \hbar\omega_\perp$ respectively. The fractional population difference N for the first (i)-(iii) and (iv)-(vi) the second excited state respectively as a function of z_0 for $h = 4 \ \hbar\omega_\perp$. In (i) and (iv) $g_{1D} = 0$, (ii) and (v) $g_{1D} = 0.5$ and finally (iii) and (vi) $g_{1D} = 5$. Bold lines correspond to stationary solutions of Eq. (3.1) and black lines are the symmetric projections in the $-z_0$-axis.
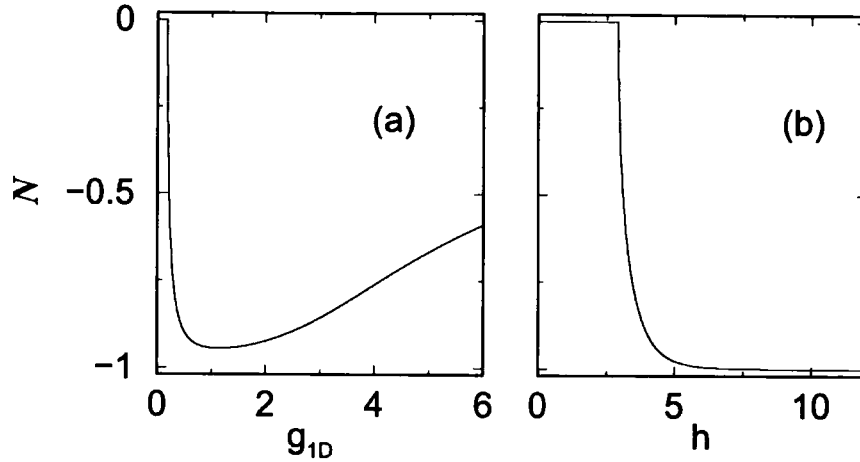
Figure 5.3: The population asymmetry of the self-trapping state as a function of the self-interaction parameter, g_{1D} (with $h = 4\ \hbar\omega_\perp$), and the barrier height, h (with $g_{1D} = 0.5$).

5.3 Symmetric initial condition

We consider first the case where the barrier is moved from the centre towards the right at different velocities. We show both the eigenstate fractional population differences $(N = N_L - N_R)$ and the calculated evolution of the population difference for $g_{1D} = 0.5$. This is shown in Figs. 5.4(a) and (b) for both low $(\mu \sim h)$ and high barriers $(\mu \ll h)$, respectively. In both cases, for low velocities, the evolution is adiabatic, and the time-dependent solution follows the ground state population difference curve resulting in a dc tunnelling current. Above a critical velocity v_c, there is a transition to a superposition of ground and excited states such that the fractional population difference remains constant, apart from a decaying oscillatory component. Subsequently, the excited state component encounters a level crossing with higher-lying states which leads to further 'steps' in the fractional population difference or resonances in the tunnelling current. For example, for the velocity $v = 0.01\ a_\perp\omega_\perp$ shown in Fig. 5.4(a), the time-dependent evolution follows the first excited state, whereas in Fig. 5.4(b) for $v = 4\times10^{-5}\ a_\perp\omega_\perp$ the speed is just below the critical velocity for the transition from the second to the third excited states leading to a large tunnelling current as the object moves past $z_0 \sim 0.9\ a_\perp$. Compared to the

solutions of the two state-model shown in Figs. 4.7(a) and (b), we note that for slow velocities $v < v_c$, both methods give similar results. However for large velocities the two-state model does not predict the additional steps in the population dynamics. The break down of the two-state model occurs mainly due to the influence of higher-lying states.
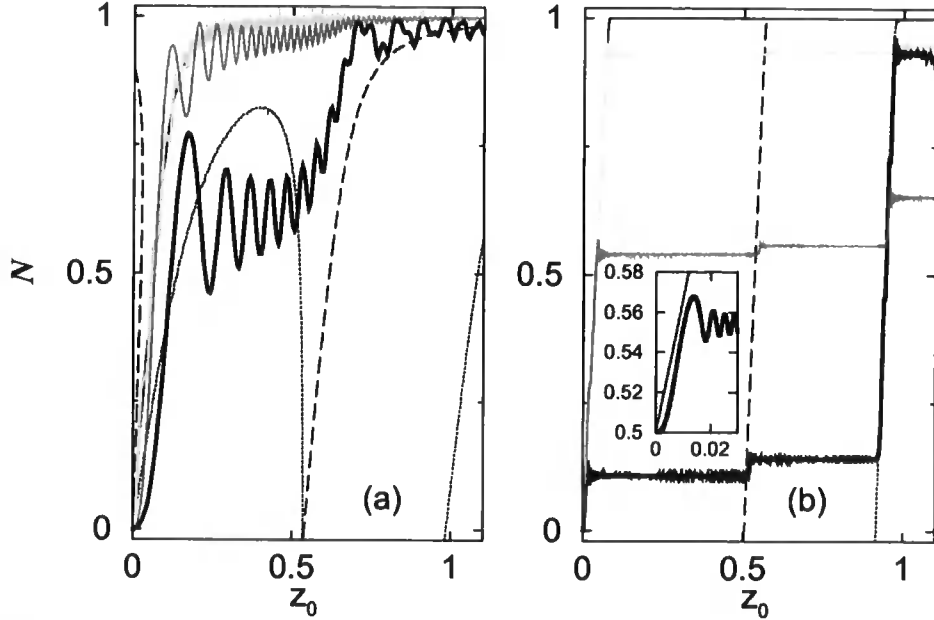
Figure 5.4: The fractional population difference, N, as a function of the barrier displacement, z_0, for the eigenstates g, e_1 and e_2 with $g_{1D} = 0.5$ and (a) $h = 4\ \hbar\omega_\perp$ and (b) $h = 12\ \hbar\omega_\perp$. The fractional population difference as the barrier is moved from the centre towards the right at speeds: (a) $v\ (a_\perp\omega_\perp) = 0.001, 0.004, 0.01$ and (b) $v(\times 10^{-5}\ a_\perp\omega_\perp) = 2, 3.4, 4$ are plotted as grey, brown and thick black line respectively. An expanded view of the short-time evolution of the case $v = 4 \times 10^{-5}\ a_\perp\omega_\perp$ is shown inset (b). The corresponding population differences N for eigenstates g, e_1, and e_2 are indicated by the solid, dashed and dotted lines in both cases.

5.4   Critical velocity

Following previous calculations, we plot the fractional population difference as a function of the barrier speed in Fig. 5.5. For comparison we also plot the prediction of the two-state model. For $v < v_c$ the fractional population difference increases
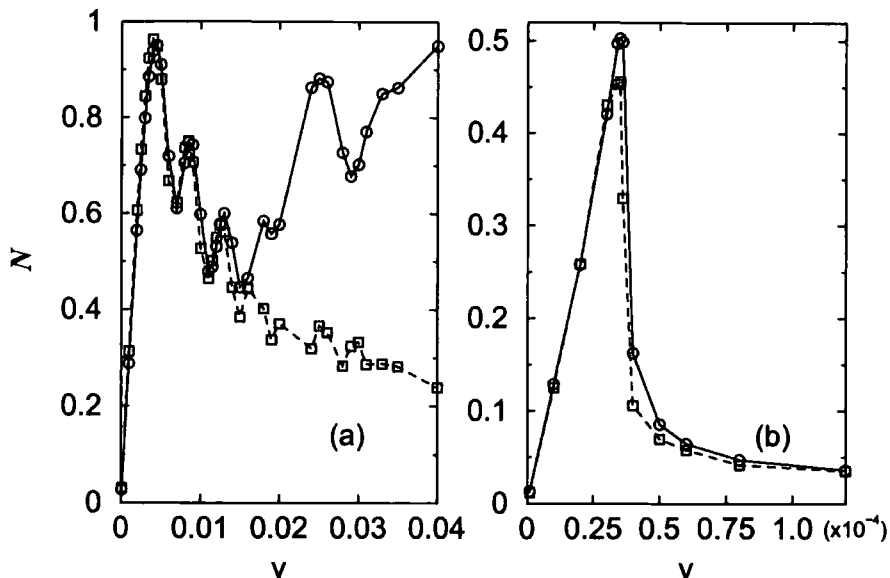
Figure 5.5: The fractional population difference as a function of the barrier speed v obtained from the GPE (solid line) and the two-state model (dashed line) for $g_{1D} = 0.5$ and (a) $h = 4\ \hbar\omega_\perp$ and (b) $h = 12\ \hbar\omega_\perp$. The barrier is moved from the centre outwards for a time (a) $t = 30\ \omega_\perp^{-1}$ and (b) $t = 1000\ \omega_\perp^{-1}$. For $v = v_c$ there is a large step in the fractional population difference which corresponds to the critical velocity for the transition from a dc to an ac-current. In (a) $v_c = 0.005\ a_\perp\omega_\perp$ and (b) $v_c = 0.000035\ a_\perp\omega_\perp$ which are in good agreement with previous calculations. In (a) for $v > 0.017\ a_\perp\omega_\perp$ the second level crossing is reached leading to a departure between the GP simulation and the prediction of the two-state model whereas in (b) we are below the second level crossing for the range of velocities chosen. Other parameters as in Fig. 4.7.

such that the chemical potential difference is kept zero, corresponding to a dc-current. However, above $v = v_c$ there is a large drop in the fractional population difference corresponding to the transition to an ac Josephson regime. Moreover Fig. 5.5 shows that except for large displacements, i.e., large velocity in Fig. 5.5(a), the two-state approximation reproduces the GP solution extremely well. The two-state approximation works so well because if the barrier is displaced by less than its width, then apart from a shift in the potential and energy of the minima, the shape of the potential on either side of the barrier does not change significantly. Consequently, the parameters E_C and E_J derived from the symmetric wave functions are also accurate for the asymmetric well. However, when the barrier reaches a position

corresponding to a level crossing between excited states, the two-state model ceases to be a good approximation because it does not include the effects of higher lying states. For the parameters in Fig. 5.5(a) the second level crossing at $z_0 \sim 0.5\ a_\perp$ is reached when $v > 0.017\ a_\perp \omega_\perp$, see Fig. 3.7(a).

Apart from the eigenenergy level picture, the dynamics of BJJ can be also described in terms of the motion of a particle moving in a "washboard" potential. Differentiating Eqs. (4.18) and (4.19) and substituting for $\dot{N}$ and $\dot{\theta}$ gives

$$\ddot{\theta} = \dot{\Delta} - \frac{E_J(E_C - N\Delta)}{\sqrt{1 - N^2}} \sin\theta - \frac{E_J^2(1 + N^2)}{2(1 - N^2)} \sin 2\theta \ . \tag{5.1}$$

If N is roughly constant, this equation may be re-written as $\ddot{\theta} = -\partial_\theta U$, where $U(\theta)$ describes a "tilted-washboard" potential,

$$U(\theta) = 1 - \dot{\Delta}\theta - \frac{E_J E_C}{\sqrt{1 - N^2}} \cos\theta - \frac{1}{4}E_J^2 \frac{1 + N^2}{1 - N^2} \cos 2\theta - \frac{E_J N\Delta}{\sqrt{1 - N^2}} \cos\theta \ . \tag{5.2}$$

For $N \approx 0$ at $t = 0$ and using $\Delta = -2\alpha z_0 = -2\alpha v t$, the above equation is reduced to,

$$U(\theta) = 1 - 2\alpha v\theta - \frac{E_J E_C}{\sqrt{1 - N^2}} \cos\theta - \frac{1}{4}E_J^2 \frac{1 + N^2}{1 - N^2} \cos 2\theta - \frac{E_J N 2\alpha v t}{\sqrt{1 - N^2}} \cos\theta \ , \tag{5.3}$$

which is plotted in Fig. 5.6 for different velocities and for the case of low and high barrier heights. We observe that there is a critical velocity v_c, such that for $v < v_c$ the particle is trapped at the minima of the potential $U(\theta)$ which corresponds to a dc-Josephson current. However for $v > v_c$, the minima of the potential $U(\theta)$ disappear, and the particle runs down the washboard potential, corresponding to an ac-Josephson current. The critical velocity, v_c, is determined by setting the minimum gradient of $U(\theta)$ equal to zero yielding,

$$v_c = -\frac{E_J E_C}{2\alpha} - \frac{E_J^2}{4\alpha} \ . \tag{5.4}$$

For $g_{1D} = 0.5$ and $h = 4\ \hbar\omega_\perp$, GP calculations yield $E_J = 0.1\ \hbar\omega_\perp$, $E_C = 0.24\ \hbar\omega_\perp$ and $2\alpha = 3.187\ \hbar\omega_\perp/a_\perp$, thus the above equation gives $v_c = 0.008\ a_\perp\omega_\perp$. However
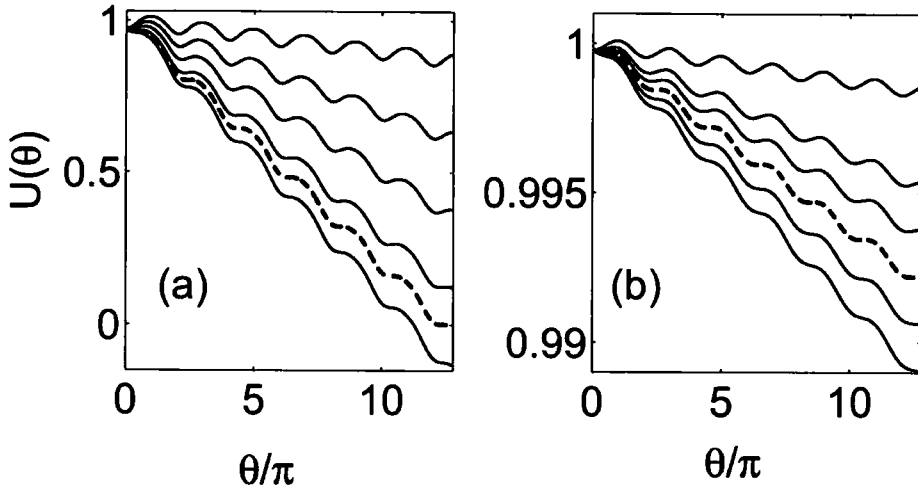
Figure 5.6: Plots of the washboard potential as a function of θ/π for different velocities v, for $g_{1D} = 0.5$ and (a) $h = 4 \ \hbar\omega_\perp$ and (b) $h = 12 \ \hbar\omega_\perp$. For $v = v_c$ the washboard potential has no bound states (dashed lines). For the parameters used here, Eq. (5.4) gives $v_c = 0.008 \ a_\perp\omega_\perp$ in (a) and $5 \times 10^{-5} \ a_\perp\omega_\perp$ in (b). In (a) $v(\times10^{-3} \ a_\perp\omega_\perp) := 1, 3, 5, 7, 8, 9$ whereas in (b) $v(\times10^{-5} \ a_\perp\omega_\perp) := 1, 3, 4, 5, 7, 9$.

for $E_C \gg E_J$, one can use the linear approximation, $\alpha = -E_C/2z_c$, where z_c is the critical displacement, which yields $v_c \sim E_J z_c$. Taking the values for $g_{1D} = 0.5$ and $h = 12 \ \hbar\omega_\perp$, $E_J = 7 \times 10^{-4} \ \hbar\omega_\perp$ and $z_c = 0.07 \ a_\perp$, gives $v_c \sim 5 \times 10^{-5} \ a_\perp\omega_\perp$. According to Eqs. (4.18) and (4.19) the maximum fractional population difference occurs at approximately $v_c/\sqrt{2} = 0.005 \ a_\perp\omega_\perp$ and $3.4 \times 10^{-5} \ a_\perp\omega_\perp$, for the case of Fig. 5.4(a) and (b) respectively, which are in excellent agreement with the values determined by numerical integration of the GPE.

5.5 Asymmetric initial condition

As stated above, the small critical velocity for high barriers (typically less than a μm/s) makes experimental verification challenging. Although higher critical velocities are obtained for lower barriers, the transition between the dc and ac regime becomes less sharp. This problem can be partially circumvented by noting that one can induce larger population changes by starting with an asymmetric well and moving the barrier back through the origin. This is illustrated in Fig. 5.7 with a

lower barrier height, $h = 4\ \hbar\omega_\perp$. Again for low barrier speeds the population follows the ground state distribution, whereas for faster speeds a transition to an oscillatory current is observed. The critical velocity is a factor of 200 times larger than for $h = 12\ \hbar\omega_\perp$.
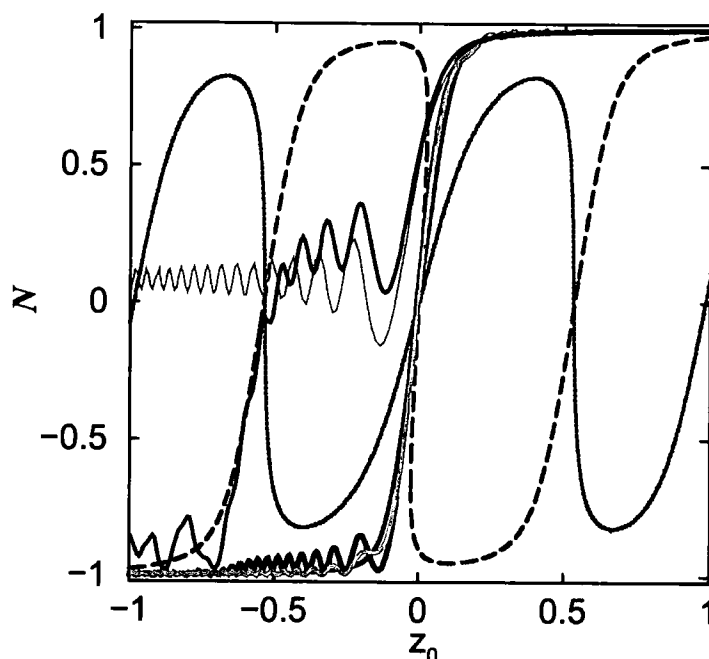
Figure 5.7: The fractional population difference, N, obtained from numerical solution of the GPE, (black) and the two-state model (brown) as a function of the barrier displacement, z_0, as the barrier is moved from $z_0 = a_\perp$ towards the left at a constant speed $v = 0.007\ a_\perp\omega_\perp$ (thick) and $0.015\ a_\perp\omega_\perp$ (light) for $h = 4\ \hbar\omega_\perp$ and $g_{1D} = 0.5$. The corresponding population differences for eigenstates g, e_1, and e_2 are indicated by the solid, dashed and dotted lines.

For $z_0 < -0.6\ a_\perp$ the fractional population difference follows that of the excited state, e_1, therefore to observe a large population difference, it is important to stop the motion before the barrier reaches $z_0 \sim -0.4\ a_\perp$. This restricts the evolution to short times or low velocities.

For small velocities the two-state model gives similar results to the GP solutions apart from a smaller amplitude in the oscillatory current. However for larger velocities the two-state description is insufficient to completely describe the tunnelling dynamics because it does not include the effects of higher lying states. Therefore

a full numerical solution of the GPE is needed to accurately describe the dynamics for $z_0 < -0.5\ a_\perp$.

In Fig. 5.8 we show the fractional population difference as a function of the barrier velocity for an asymmetric initial state. Comparison with Fig. 5.5 illustrates that a larger fractional population difference and a better demarcation of the critical velocity is obtained by moving the barrier from the edge of the condensate inwards (asymmetric initial condition). However, it is not straightforward to predict the critical velocity for the asymmetric initial condition because the relative importance of the coefficients in Eq. (5.1) depends on the instantaneous value of $N(t)$. For the parameters chosen in Fig. 5.8(a), the numerical results indicate that the critical velocity is similar to that for a symmetric initial state, however it is reduced from the symmetric one by a factor of three, shown in Fig. 5.8(b). Finally, in both cases, the two-state model gives similar predictions.
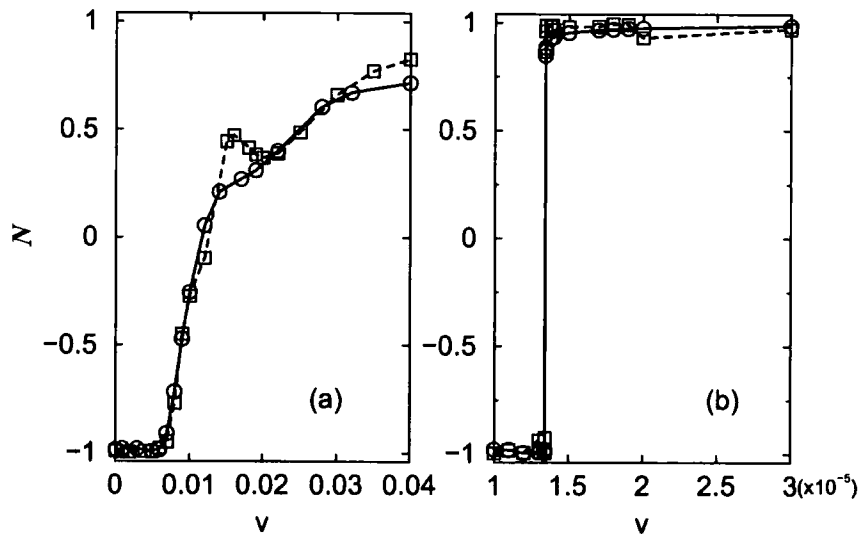
Figure 5.8: The fractional population difference as a function of the barrier speed v obtained from the GPE (solid line) and the two-state model (dashed line) for $g_{1D} = 0.5$ and (a) $h = 4\ \hbar\omega_\perp$ and (b) $h = 12\ \hbar\omega_\perp$ for an asymmetric initial condition. The barrier is moved from (a) $z_0 = 0.95\ a_\perp$ and (b) $0.6\ a_\perp$ and stopped at $z_0 = -0.3\ a_\perp$ and $-0.2\ a_\perp$ respectively. In (a) $v_c = 0.0075\ a_\perp\omega_\perp$ similar with the critical velocity obtained using a symmetric initial condition and (b) $v_c = 0.00001345\ a_\perp\omega_\perp$ which is approximately three times smaller than the corresponding one for the symmetric initial state. Other parameters as in Fig. 4.7.

Finally, we consider the interesting case where the influence of higher-lying states severely limits the applicability of the two-state model. In Fig. 5.9 we show the population change as a barrier with height $h = 4\ \hbar\omega_\perp$ is moved through the centre of a condensate with $g_{1D} = 5$. For these parameters the critical velocity is sufficiently high that the level crossing to a higher-lying state is reached before the transition to the ac regime is completed. However, a large fractional population difference for different barrier velocities can still be observed if the motion is halted when the barrier reaches $z_0 \sim -0.5\ a_\perp$.
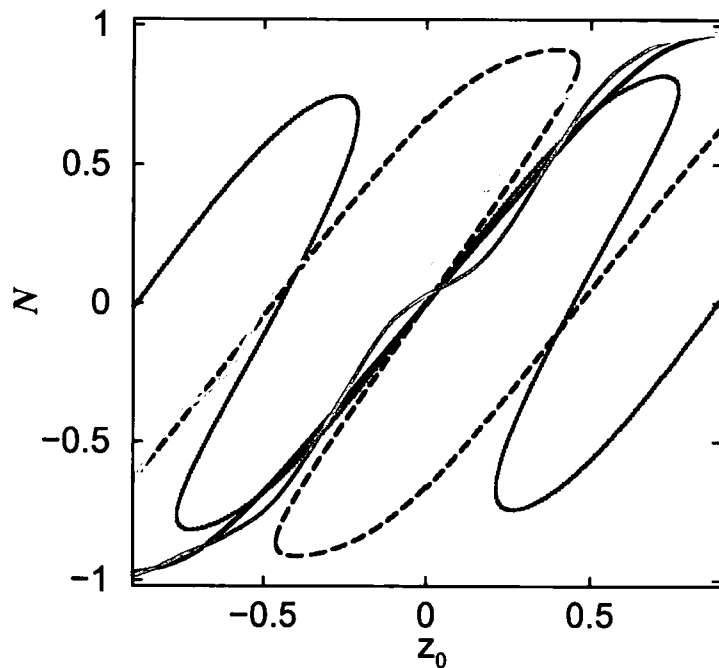
Figure 5.9: The fractional population difference, N, as a function of the barrier displacement, z_0, as the barrier is moved from $z_0 = 0.9\ a_\perp$ towards the left at speed $v\ (a_\perp\omega_\perp) = 0.05$ (light grey) and 0.08 (brown) for $h = 4\ \hbar\omega_\perp$ and $g_{1D} = 5$. The corresponding population difference for eigenstates g, e_1, and e_2 are indicated by the solid, dashed and dotted lines.

5.6 Experimental realization

The large critical velocity, $v_c \sim 0.08\ a_\perp\omega_\perp$, offers the best potential for the experimental observation of dc tunnelling currents. For example, taking a sodium

condensate with $g_{1D} = 5$, trap frequency of 20 Hz, equation,

$$\mathcal{N} = \frac{g_{1D} a_\perp}{2a} = \frac{g_{1D}}{2a} \sqrt{\frac{\hbar}{m\omega_\perp}} \tag{5.5}$$

yields $\mathcal{N} = 4000$ atoms. The dark and light grey curves in Fig. 5.9 correspond to a barrier formed by a blue detuned laser sheet with waist 5 μm, moved by 2.5 μm in 80 ms and 50 ms, respectively. For these parameters, a model involving higher-lying excited states is essential to give a clear picture of the Josephson population dynamics.

We have studied the Josephson dynamics for a system initially prepared in the ground state and we have compared our results with the two-state model. In the following Chapter we study the tunnelling dynamics of a phase imprinted condensate.

Chapter 6

Josephson tunnelling of phase-imprinted BECs

We discuss the feasibility of experimental control of the flow direction of atomic Bose-Einstein condensates in a double-well potential using phase-imprinting. The flow is induced by the application of a time-dependent potential gradient, providing a clear signature of macroscopic quantum tunnelling in atomic condensates. By studying both initial state preparation and subsequent tunnelling dynamics we find the parameters to optimise the phase induced Josephson current. We find that the effect is largest for condensates of up to a few thousand atoms and is only weakly-dependent on trap geometry.

6.1 Introduction

In this Chapter, we investigate the Josephson dynamics for a phase-imprinted atomic condensate in a double-well potential under the influence of a time-dependent potential gradient. We focus on the sensitivity of the Josephson flow direction to the initial state preparation. In particular, preparation in the odd parity energy eigenstate combined with the application of the potential gradient leads to a flow towards a region of higher potential energy providing a clear signature of Josephson tunnelling. Flow reversal in context of the Josephson effect is well known. For example in a superconducting π-junction [36], the addition of a macroscopic phase

difference $\phi = \pi$ across the superconducting weak link leads to reversal of the sign of the current [37, 120, 121]. Also a related effect has been predicted for condensates in optical lattices as a result of the renormalization of the mass in the lattice, based on Bloch wave analysis [122]. The superfluid analogue of a supeconducting π-junction is a metastable π-state, recently observed in ^{3}He weak links [41]. Atomic BEC junctions behave similarly to those of ^{3}He-B. Thus, although superconducting Josephson junctions can be mapped onto a *rigid* pendulum, atomic condensate tunnel junctions map onto a *nonrigid* pendulum [64, 65, 66], thus exhibiting richer oscillation modes. For example, π oscillations arise in such systems [64, 65, 66, 67]. For an atomic condensate in a double-well potential, π oscillation modes can be produced by imprinting a phase shift of π between the two wells. We study how these modes behave under the action of an external potential difference.

This Chapter is structured as follows. In Section 6.2 we discuss the dynamics associated with particular initial states, including the π oscillation modes, under the addition of a time-dependent potential gradient. Under the action of a gradient, states with initial phase difference π across them exhibit tunnelling to the upper well, providing a clear manifestation of Josephson effects. In Section 6.3 we compare the one and three dimensional results, whereas in section 6.4 we give an explanation in terms of a first-order time-dependent perturbation theory. Finally in Section 6.5 we discuss the possibility of experimental observation of this phenomenon in current BEC set-ups.

6.2 Tunnelling Dynamics under a time-dependent magnetic field gradient

In the previous Chapter we studied the tunnelling dynamics of BEC initially prepared in the Ψ_g state in a one dimensional double-well potential, by considering a barrier that moves with a constant velocity along the trap. In this Chapter we study the tunnelling dynamics in three dimensional double-well induced by a time-dependent potential gradient which increases linearly. The potential gradient is applied at $t = 0$, i.e., $\delta = Rt$ for $t > 0$, (dashed line in Fig. 3.9(a) showing the right

well with higher potential energy than the left). Fig. 6.1 shows that the evolution of the fractional population difference for the ground state Ψ_g (grey line) is similar to the one studied in the previous Chapter. We also show the tunnelling of the excited state Ψ_e (black line) with initial phase π. We note that the direction of the initial flow depends on the initial phase difference.
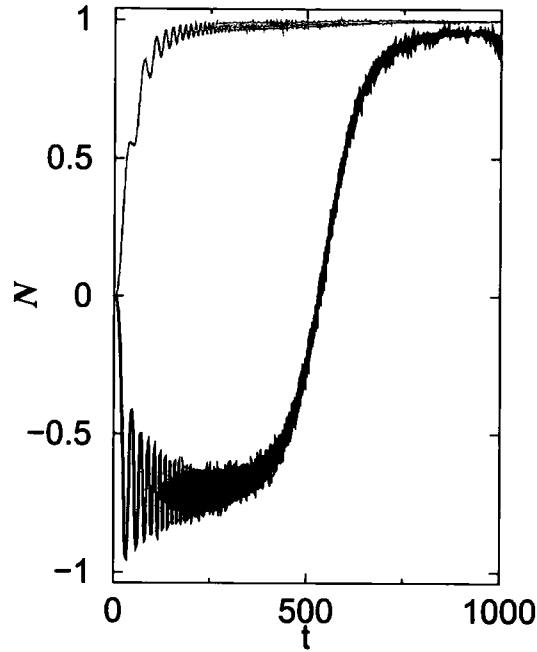
Figure 6.1: Evolution of fractional population difference N as a function of time $(\omega_\perp^{-1})$, for a system initially prepared in Ψ_g (grey) and Ψ_e (black lines) states based obtained from the numerical solution of the GPE (3.3). The tunnelling is induced by a time-dependent potential gradient $\delta = Rt$ which increases at constant rate $R = 10^{-3}$ ($\hbar\omega_\perp^2/a_\perp$). Other parameters used here: $h = 4\ \hbar\omega_\perp$, $\lambda = 1$, $g_{3D} = \pi$.

The main theme of this Chapter is to investigate the tunnelling of states with initial phase $\phi = 0$ and π whose symmetry is broken by the addition of a time-dependent potential gradient. We also study the tunnelling dynamics in a symmetric double-well potential ($\delta = 0$) which are well known in terms of the two-state coupled Eqs. (4.18) and (4.19) (see Chapter 4).

If a system is initially prepared in one of its eigenstates, Ψ_g or Ψ_e, it will remain in that same state and there is no tunnelling current. This is shown in Fig. 6.2(a),
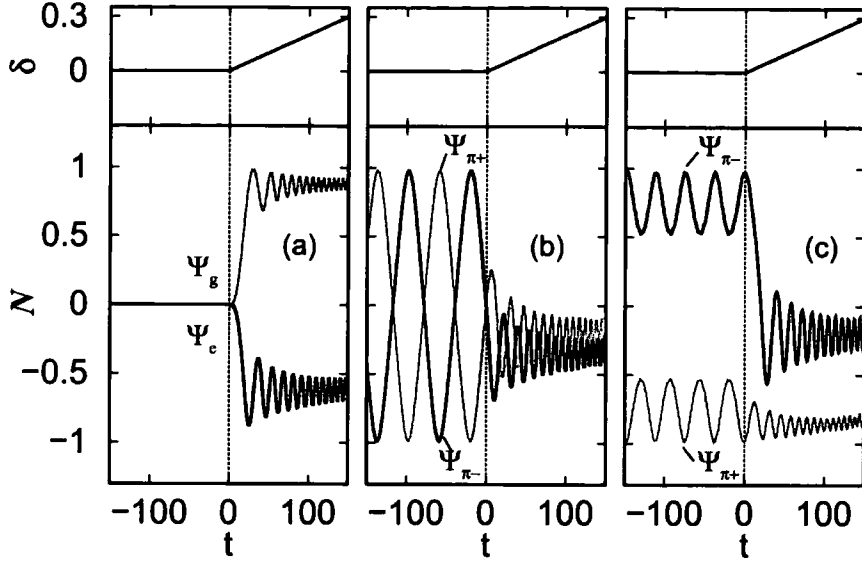
Figure 6.2: Evolution of fractional population difference N as a function of time (calculated using the GPE) without ($t < 0$) and with ($t > 0$) a potential gradient $\delta = Rt$ (shown at the top of each figure) for different initial states: (a) a pure ground Ψ_g or first excited Ψ_e state with equal populations in both wells. In this case, tunnelling only arises due to the additional external potential; (b) the superposition states $\Psi_{\pi\pm}$ for $g_{3D} = \pi/2$, corresponding to the regime $\Lambda < \Lambda_c$ ($E_C = 0.123\ \hbar\omega_\perp$ and $E_J = 0.095\ \hbar\omega_\perp$), showing maximum amplitude π-oscillations for $t < 0$: and (c) the superposition states $\Psi_{\pi\pm}$ for $g_{3D} = \pi$, corresponding to $\Lambda > \Lambda_c$ ($E_C = 0.220\ \hbar\omega_\perp$ and $E_J = 0.102\ \hbar\omega_\perp$). Note that in (b) and (c) we have shifted the time origin by a quarter of an oscillation period such that $N = 0$ at $t = 0$. The other parameters used here are $\lambda = 1$, $h = 4\ \hbar\omega_\perp$, $R = 2 \times 10^{-3}\ (\hbar\omega_\perp^2/a_\perp)$.

where we plot the fractional relative population, N as a function of time with $\delta = 0$ for $t < 0$. However, if the system is prepared in a superposition of Ψ_g or Ψ_e with a π phase difference, i.e.,

$$\Psi_{\pi\pm} = \frac{1}{\sqrt{2}}(\Psi_g \pm \Psi_e)\ , \tag{6.1}$$

the population tunnels back and forth (see Fig. 6.2(b) and (c)) and the relative phase between the two wells oscillates around a mean value of π (π-oscillations [64, 65, 66, 67]). The amplitude of the π-oscillations depends on the ratio $\Lambda = E_C/E_J$ [2, 55, 57, 65, 66, 67]. By solving the two-state coupled Eqs. (4.18) and (4.19) with initial conditions $N(0) = 0.994$ (determined from the GP solution for $\psi_{\pi-}$) and

$\phi(0) = \pi$, we find a critical ratio, $\Lambda_c \sim 1.80$ (see Fig. 6.3). For $\Lambda < \Lambda_c$, (Figs. 6.3(a) and (b)), the population oscillates between $\pm N(0)$, as in Fig. 6.2(b)($t < 0$), whereas for $\Lambda > \Lambda_c$, (Fig. 6.3(d)), the oscillations in N are suppressed, as in Fig. 6.2(c) ($t < 0$). For $\Lambda = \Lambda_c$, (Fig. 6.3(c)), the oscillations are frozen initially and appear again for later times.
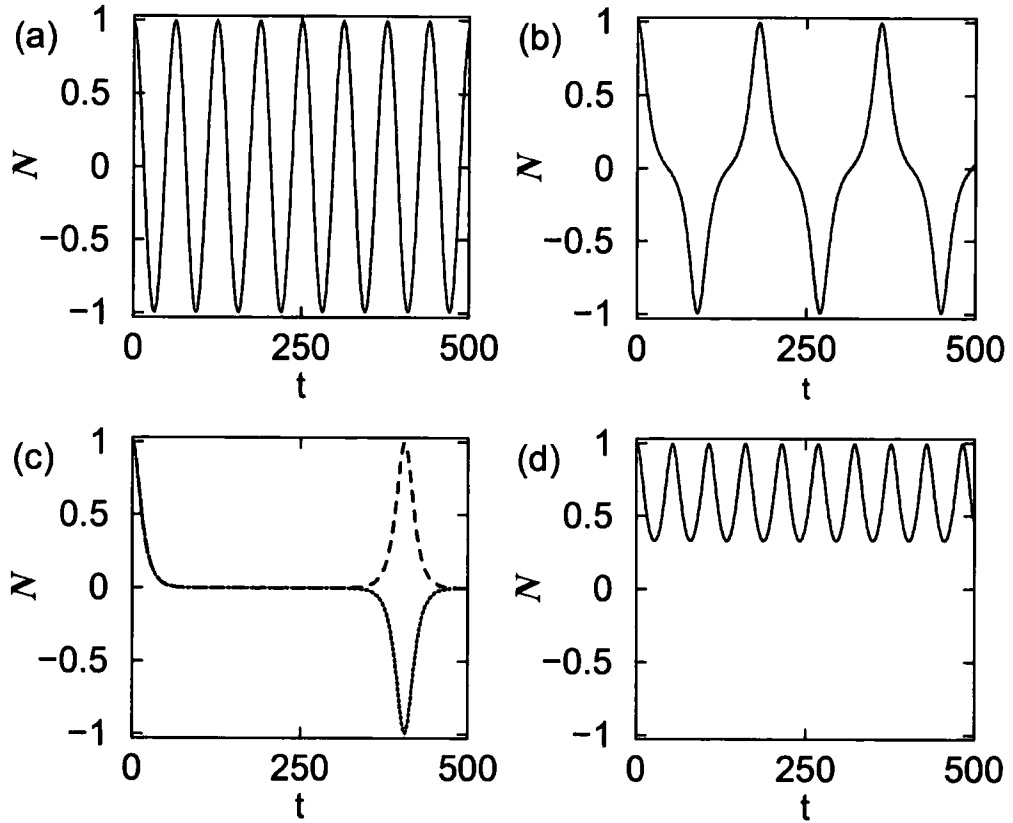
Figure 6.3: Evolution of fractional population difference N as a function of time, calculated using the two-state coupled Eqs. (4.18) and (4.19), with initial conditions $N(0) = 0.994$ and $\phi(0) = \pi$ in a symmetric double-well trap ($\delta = 0$). Λ takes the values: (a) 0, (b) 1.8, (c) 1.80407218718131001 (dashed) with $N > 0$ and 1.8080407218718131010 (dotted) with $N < 0$ and finally (d) 1.9.

The effect of introducing an asymmetry depends sensitively on the initial state. For Ψ_g, the potential gradient induces a Josephson current to the left (lower potential energy region), whereas for Ψ_e flow occurs to the right (higher potential energy) (Fig. 6.2(a)). The situation is more complex for superposition states, such as $\Psi_{\pi\pm}$.

For $\Lambda < \Lambda_c$, if the potential gradient is turned on rapidly (compared to the period of the π-oscillations), the oscillations in N are suppressed tending towards a mean N close to its initial value, Fig. 6.2(b). For $\Lambda > \Lambda_c$, the induced flow is very different for $\Psi_{\pi+}$ and $\Psi_{\pi-}$. For $\Psi_{\pi+}$ most of the population remains "self-trapped" in the higher energy well, whereas for $\Psi_{\pi-}$ a large fraction of the population flows from the lower to the upper well. In this regime, the experimental preparation of $\Psi_{\pi\pm}$ from the ground state is more difficult as it requires a transfer of population in addition to imprinting a phase diference of π. However, as we will see in Section 6.5, straightforward phase-imprinting can generate a superposition that contains a large fraction of $\Psi_{\pi\pm}$.
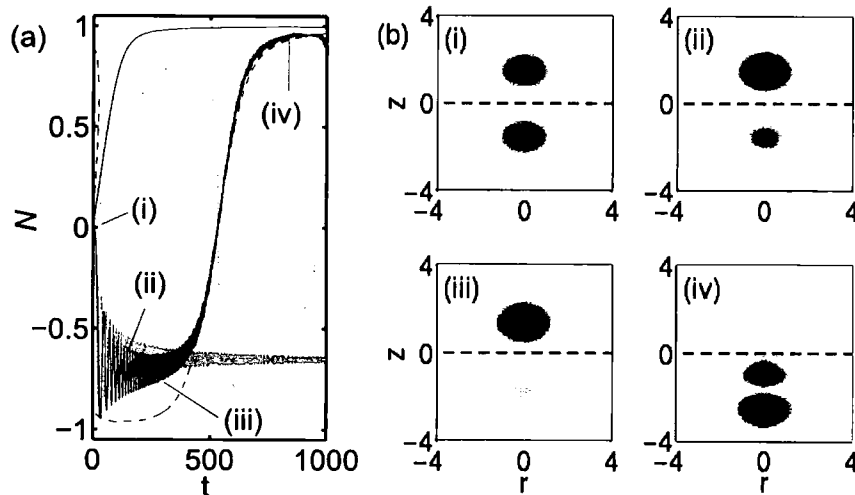
Figure 6.4: (a) Evolution of fractional population difference N as a function of time, for a system initially prepared in state Ψ_e based on the GPE (black line) and the two-state model, Eqs. (4.18) and (4.19) (grey line) with initial condition $N(0) = 0$ and $\phi(0) = \pi$ and parameters $E_J = 0.10\ \hbar\omega_\perp$, $E_C = 0.22\ \hbar\omega_\perp$ and $2a = 3.77\ \hbar\omega_\perp/a_\perp$ (obtained from the numerical solution of the GPE). The fractional population differences for the eigenstates are also plotted for the ground (solid line), first excited (dashed line) and second excited states (dotted line). (b) Snapshots of the evolution of the density distribution for case (a) when (i) $t = 0$, (ii) 100, (iii) 300 and (iv) 800 in units of $(\omega_\perp^{-1})$. Other parameters same as Fig. 6.1.

The tunnelling behaviour of different initial states such as Ψ_g and Ψ_e under a potential gradient can be explained in terms of the time-independent solutions (see Chapter 3). These can be plotted as a function of time via their dependence on the

time-dependent potential gradient $\delta = Rt$. The time evolution and the corresponding time-independent population difference for state Ψ_e is shown in Fig. 6.4(a), from which it is found that, for slow velocities, the system follows the eigenstate almost adiabatically. The initial dynamics discussed above is also well described by the two-state model [62, 63, 64, 65, 66, 67, 68, 69, 70, 71, 72, 73] (grey line in Fig. 6.4(a)). However, for larger gradients the full potential GP calculation predicts that the atoms return to the lower (or left) potential well, whereas the two-state model suggests they remain in the upper (right) well. This breakdown of the two-state model occurs because it does not take higher lying modes into consideration [60] (see also discussion in Chapter 5). This is an important consideration for any experimental demonstration of macroscopic flow to the higher well. The tunnelling dynamics of Ψ_e state is also illustrated by the density snapshots in Fig. 6.4(b). The population of both wells is initially equal ($t = 0$). As the gradient is increased population starts being transferred towards the right ($z > 0$), upper well. Increasing the asymmetry beyond a threshold value leads the population to be once again transferred to the left ($z < 0$), lower well. Eventually, a transition to the second excited state occurs at large potential gradients.

The flow towards the right (higher) potential well shown in Fig. 6.4(b) provides a clear macroscopic demonstration of quantum tunnelling. To consider whether this effect is observable in current experimental set-ups, we have studied the effect of varying the nonlinearity, trap geometry, and the time dependence of the ramp.

6.2.1 Dependence on nonlinearity

We now discuss the dependence of the flow on the nonlinearity for fixed trap geometry. Figs. 6.5(a)-(c) show the evolution of the fractional population difference for identical trap geometry, rate and different nonlinearities. The corresponding evolution for the eigenstate population difference is also shown as dashed lines. We observe that for the same trap geometry, increasing the nonlinearity causes a reduction in the amount of initial flow to the upper well. For the parameters chosen in Fig. 6.5, with a nonlinearity ten times bigger (i.e. $g_{3D} = 10\pi$), leads to a reduction

of the average population imbalance induced by the applied potential gradient of slightly more than a factor of 2. This restricts the observation of the phenomenon for small nonlinearities, corresponding to no more than few thousands atoms (see Section 6.5 for experimental estimates). The effect of interactions have also been considered in [56], with the effective interaction also modified by atom losses [72].
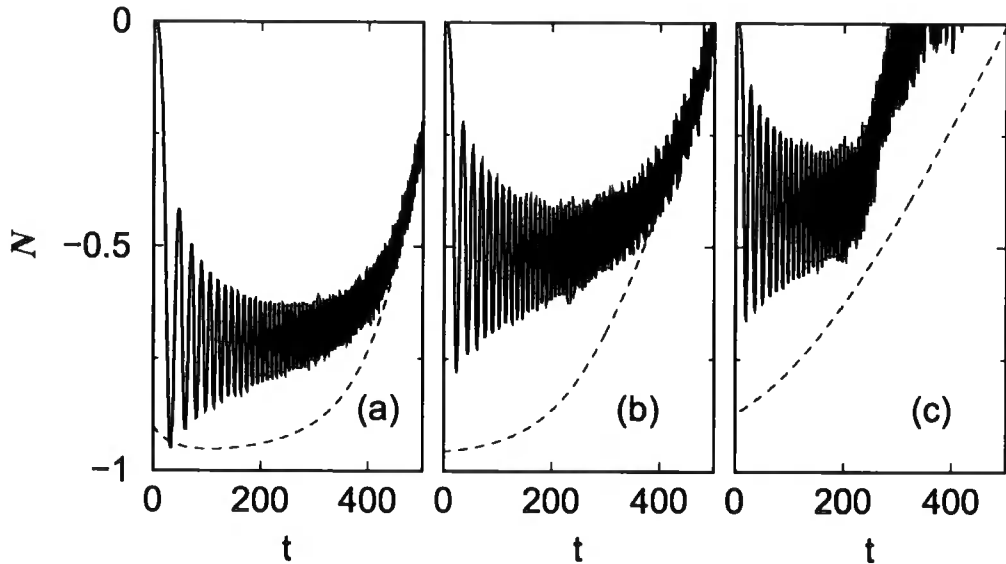
Figure 6.5: Evolution of fractional population difference N as a function of time $(\omega_\perp^{-1})$ for identical trap configurations ($\lambda = 1$, $h = 4$ $\hbar\omega_\perp$ and $R = 10^{-3}$ $(\hbar\omega_\perp^2/a_\perp)$) and increasing nonlinearity (a) $g_{3D} = \pi$, (b) 4π and (c) 10π. Dashed lines indicate corresponding eigenstate populations for the first excited state.

6.2.2   Dependence on trap geometry

Tunnelling has been predicted to be enhanced for 'pancake' traps ($\lambda > 1$) [57], with such traps leading to a slightly increased current flow. Furthermore, such geometries feature enhanced energy splitting between ground and first excited state, (see Chapter 3), thus making them more robust to coupling due to external (e.g. thermal [68, 73, 71, 123]) perturbations. However, the suppression of tunnelling induced by increased nonlinearities cannot be compensated by changing the geometry, as shown in Fig. 6.6 for trap aspect ratios in the range 1 to $\sqrt{8}$. In plotting this figure, the barrier height h has been increased for larger λ, such that the peak density in the

trap centre remains essentially unchanged (see Fig. 6.7).
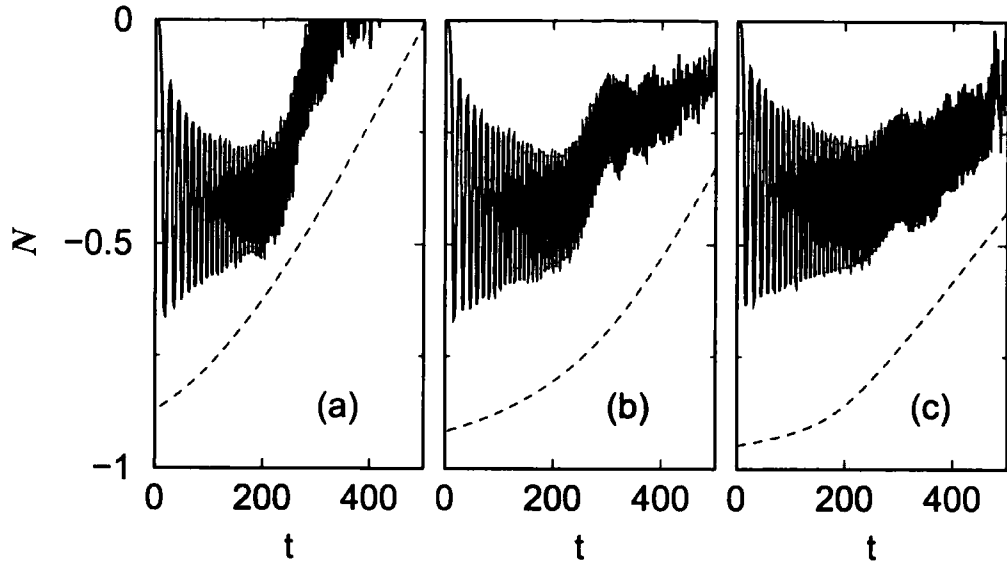
Figure 6.6: Dependence of fractional population difference dynamics on trap geometry. Plotted is the evolution of N as a function of time $(\omega_\perp^{-1})$ for $R = 10^{-3}$ $(\hbar\omega_\perp^2/a_\perp)$ (black), $g_{3D} = 10\pi$ and different trap aspect ratios: (a) cylindrically-symmetric trap $\lambda = 1$ ($h = 4$ $\hbar\omega_\perp$) (same as Fig. 6.1), (b) 'pancake'-like trap with $\lambda = \sqrt{2}$ ($h = 6$ $\hbar\omega_\perp$) and (c) $\lambda = \sqrt{8}$ ($h = 15$ $\hbar\omega_\perp$), respectively.
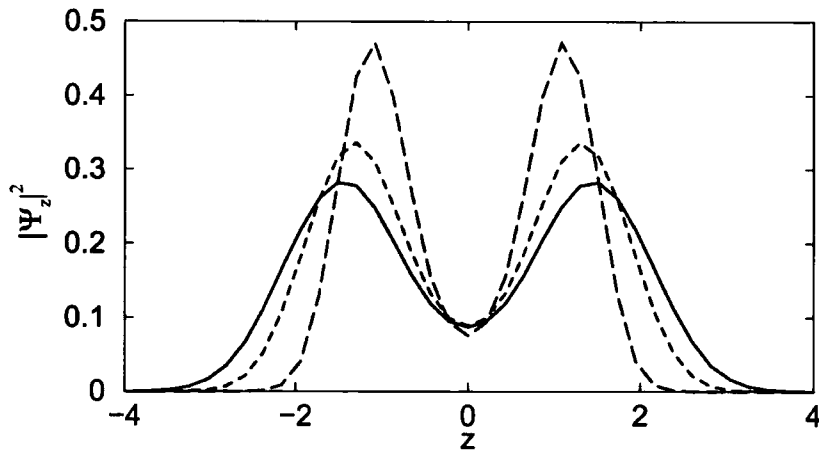
Figure 6.7: Density distributions $|\Psi_z|^2$ along the z-axis for the Ψ_g for fixed $g_{3D} = 10\pi$ and different geometries: solid corresponds to the geometry shown in Fig. 6.6(a), dashed to the one in Fig. 6.6(b) and finally long dashed to the one in Fig. 6.6(c).

6.2.3   Dependence on the rate

We should further comment on the extent to which the above findings depend on the rate R with which the linear potential gradient $\delta = Rt$ is applied. In Fig. 6.8 we plot the population difference N for fixed geometry and nonlinearity, but for two different rates at which the potential gradient is increased. We observe that when R is increased by a factor of 10 then the maximum flow to the right well is reduced by roughly a factor of 2. Also flow to higher potential region can only be observed for approximately one tenth of the time, unless the gradient is ramped up to a particular value and subsequently kept constant which is also shown in Fig. 6.8. We see that in both cases, the population remains trapped in the right or upper well, i.e. MQST occurs to a state with higher potential energy. In this regime, where the gradient does not exceed the value at which the flow is reversed, the two-state model predicts the behaviour correctly.
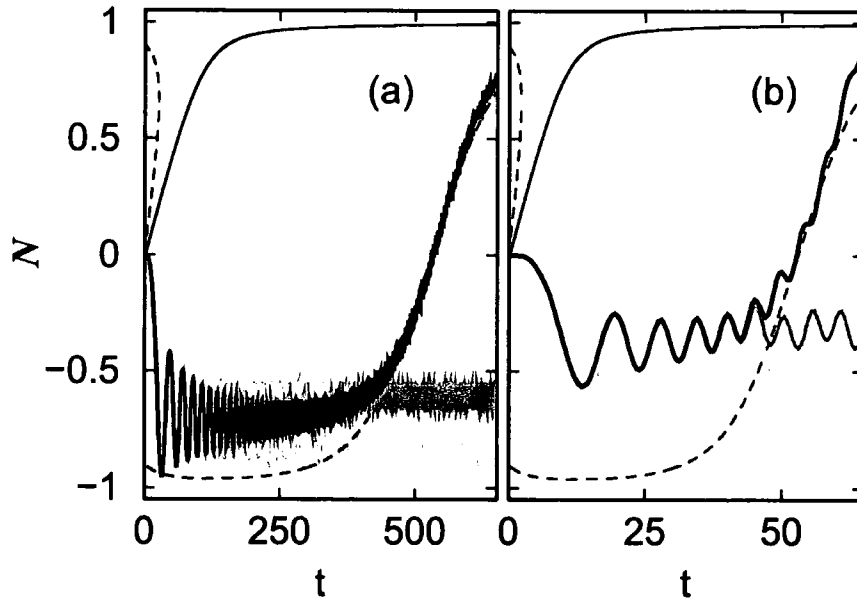
Figure 6.8: Evolution of fractional population difference N as a function of time (thick black lines) for different rates R of increase of the potential gradient: (a) $R = 10^{-3}$ $(\hbar\omega_\perp^2/a_\perp)$ and (b) $R = 10^{-2}$ $(\hbar\omega_\perp^2/a_\perp)$. Grey (brown) lines plot corresponding evolution of the population difference for the case when the potential gradient is held constant after a time $t =$ (a) $100\ \omega_\perp^{-1}$ ($400\ \omega_\perp^{-1}$) and (b) $10\ \omega_\perp^{-1}$ ($40\ \omega_\perp^{-1}$). Other parameters used, as in Fig. 6.1.

6.3   Comparison to numerical results in one dimension

In this section we compare numerical results in three dimensions to the one dimensional solutions. The one dimensional time-dependent GPE is given by Eq. (2.19) with the potential,

$$V(z) = \frac{1}{2}\lambda^2 z^2 + h\exp(-z^2) + \delta z \,, \tag{6.2}$$

which describes a harmonic trap with a Gaussian barrier at the centre of the trap and a potential gradient. The one dimensional nonlinearity is given by Eq. (2.16) which matches the densities profiles in one dimension and along the z-direction in the three dimensional system. In Fig. 6.9 we show a comparison of the Josephson flow in one and three dimensions in the case of small nonlinearities for the same trap geometry, $\lambda = 1$ and $h = 4 \; \hbar\omega_{\perp}$. Fig. 6.9 shows that for small nonlinearities the results are in good agreement in both dimensions, thus the three dimensional dynamics can be accurately described by a one dimensional model which simplifies the numerical study. However the agreement becomes worse as the nonlinearity is increased, hence a three dimensional model is not always well described by a one dimensional problem.

6.4   Time-dependent Perturbation theory argument

In this section we present a first order time-dependent perturbation theory which explains the initial flow dynamics. However higher order perturbation theory is needed in order to accurately describe the dynamics for later times. Following the standard method presented in the textbooks of quantum mechanics we write the total Hamiltonian of the system as the sum of two parts: H_0 which is the unperturbed Hamiltonian that describes the confinement of bosons in a cylindrically symmetric potential in the presence of a Gaussian barrier and H_1 which is the perturbation on H_0. Thus the total Hamiltonian is written as

$$H = H_0 + H_1 \,, \tag{6.3}$$
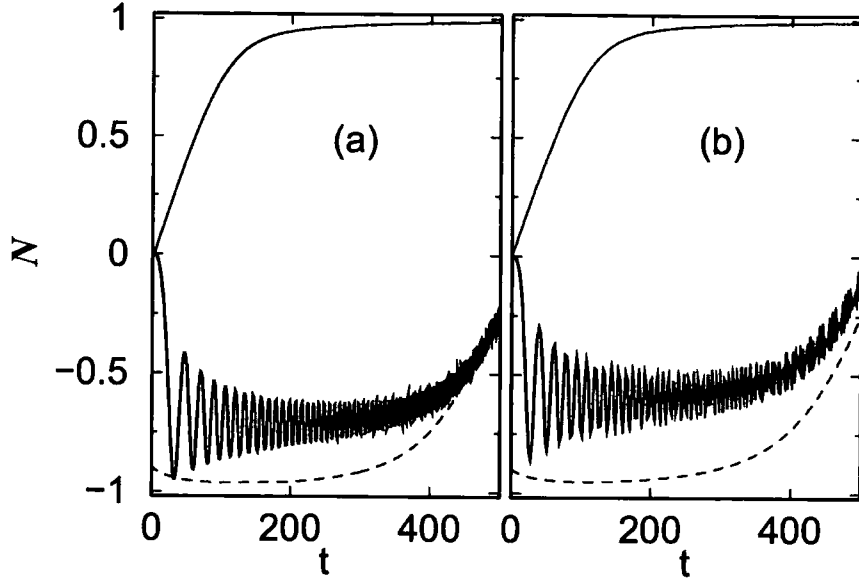
Figure 6.9: Comparison between the evolution of fractional population difference N (a) in three and (b) one dimension as a function of time $(\omega_\perp^{-1})$. In $g_{3D} = \pi$ and $\lambda = 1$ whereas in (b) $g_{1D} = 0.5$. Solid bold (dashed) lines indicate corresponding eigenstate populations for the ground (first excited) state. Other parameters same as in Fig. 6.1.

where

$$H_0 = -\tfrac{1}{2}\nabla^2 + \tfrac{1}{2}\left[(x^2 + y^2) + \lambda^2 z^2\right] + h\exp\left[-z^2\right] + g_{3D}|\psi(\mathbf{r})|^2 \qquad (6.4)$$

and

$$H_1(\mathbf{r}, t) = \delta(t)z \, , \qquad (6.5)$$

where $\delta(t) = Rt$. We denote by E_k^0 and ψ_k^0 the eigenvalues and the orthonormal eigenfunctions of the unperturbed Hamiltonian H_0. Thus,

$$H_0\psi_k^0 = E_k^0\psi_k^0 \, . \qquad (6.6)$$

The total wavefuntion of the system, is given by the solution of the time-dependent equation,

$$ i\hbar \frac{\partial \psi}{\partial t} = H\psi \ . \tag{6.7} $$

Let us consider the atoms are initially in the π-state. Because the wavefunctions ψ_k^0 form a complete set, the total wavefunction ψ which describes the evolution of the system can be written as a superposition of the initial state, ψ_a^0 and the ground state ψ_b^0 with certain probabilities if we neglect the mixing with higher order states and is given by equation,

$$ \psi(\mathbf{r}, t) = \psi_a^0(\mathbf{r}) \exp(-iE_a^0 t) + c_b \psi_b^0(\mathbf{r}) \exp(-iE_b^0 t) \ , \tag{6.8} $$

where c_b describes the transition probability for a system initially in state a, to be found at time t in state b,

$$ c_b = \tfrac{1}{i} \int_0^t \exp[i(E_b^0 - E_a^0)t']t' R V_{ba} \mathrm{d}t' \ , \tag{6.9} $$

with,

$$ V_{ba} = <\psi_a^0|z|\psi_b^0> \tag{6.10} $$

describes the mixing of states ψ_a and ψ_b. The wavefunctions of ψ_k^0 can be written in the basis of the stationary symmetric and antisymmetric solutions of the unperturbed Hamiltonian H_0 in each well:

$$ \psi_b^0 = \tfrac{1}{\sqrt{2}} \left(\psi_R^0 + \psi_L^0 \right) \ , \tag{6.11} $$

and

$$ \psi_a^0 = \tfrac{1}{\sqrt{2}} \left(\psi_R^0 - \psi_L^0 \right) \ . \tag{6.12} $$

Replacing the above expressions for the wavefunctions and calculating the matrix element Eq. (6.10), we obtain the following expression for the wavefunction,

$$\psi(t) = \frac{\exp(-iE_a^0 t)}{\sqrt{2}} C \left[(1 + K)\psi_R^0 - (1 - K)\psi_L^0 \right] , \qquad (6.13)$$

where K is given by,

$$K = RV_{ba} \left[\frac{t}{\Delta E} + \frac{1}{i\Delta E^2} - \frac{\exp(i\Delta Et)}{i\Delta E^2} \right] , \qquad (6.14)$$

$\Delta E = E_b^0 - E_a^0$ and C is the normalization factor given by equation,

$$
\begin{aligned}
C^2 &= \frac{2}{|1 + K|^2 + |1 - K|^2} \\
&= \frac{1}{1 + \frac{R^2 V_{ba}^2}{\Delta E^2} \left[t^2 + \frac{2}{\Delta E^2} - \frac{2}{\Delta E} \left(t\sin(\Delta Et) + \frac{\cos(\Delta Et)}{\Delta E} \right) \right]}
\end{aligned}
\qquad (6.15)
$$

The number of particles on the left and right well is given by,

$$
\begin{aligned}
N_L &= C^2(1 - K)(1 + K^*) = \\
&\quad C^2 \left\{ \left[1 - \frac{RV_{ba}}{\Delta E}(t - \frac{\sin(\Delta Et)}{\delta t}) \right]^2 + \frac{R^2 V_{fi}^2}{\Delta E^4}[1 - \cos(\Delta Et)] \right\}^2 \right\} \quad (6.16)
\end{aligned}
$$

and

$$
\begin{aligned}
N_R &= C^2(1 + K)(1 - K^*) = \\
&\quad C^2 \left\{ \left[1 + \frac{RV_{ba}}{\Delta E}(t - \frac{\sin(\Delta Et)}{\delta t}) \right]^2 + \frac{R^2 V_{ba}^2}{\Delta E^4}[1 - \cos(\Delta Et)] \right\}^2 \right\} , \quad (6.17)
\end{aligned}
$$

respectively. Substituting the above equations in the expression for the asymmetry parameter $N = (N_L - N_R)/(N_L + N_R)$ we obtain,

$$N = -2C^2 \frac{RV_{ba}}{\Delta E} \left(t - \frac{\sin(\Delta Et)}{\Delta E} \right) . \qquad (6.18)$$

In order to find the evolution of N one should calculate ΔE and V_{ba} for a given trap geometry, asymmetry parameter g_{3D} and rate $R = 10^{-3} \, (\hbar\omega_\perp^2/a_\perp)$. For $h = 4 \, \hbar\omega_\perp$,
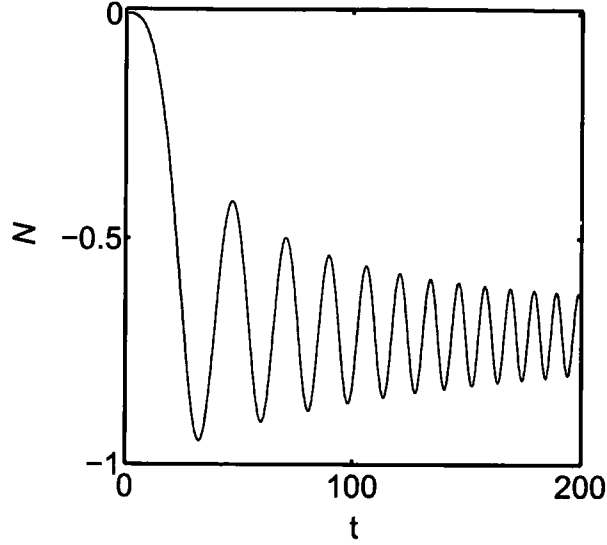
Figure 6.10: Comparison between the GPE (black) and the perturbation theory (light grey) evolution of the population difference N for a BEC with $g_{3D} = \pi$, $h = 4$ $\hbar\omega_\perp$ and $\lambda = 1$ as the potential gradient $\delta = Rt$ increases with constant rate $R = 10^{-3}$ $(\hbar\omega_\perp^2/a_\perp)$. The perturbation theory correctly describes the dynamics for small times.

$\lambda = 1$ and $g_{3D} = \pi$ we take $\Delta E = 0.10$ $\hbar\omega_\perp$ and $V_{ba} = 2.17$ $\hbar\omega_\perp$. In Fig. 6.10 we plot the evolution of the population difference as a function of time predicted by the time-independent perturbation theory (light grey) and by exact solution of the time-dependent GPE for with $R = 10^{-3}$ $(\hbar\omega_\perp^2/a_\perp)$. We observe that the time-dependent perturbation theory describes correctly the initial dynamics. However first-order perturbation theory is insufficient to describe the dynamics at later times and a higher-order theory is needed.

6.5 Experimental Considerations

We now discuss the feasibility of observing flow to the upper well using phase imprinting [124, 125, 126]. Starting from the condensate ground state in a symmetric double-well trap, population can be transferred to the excited states by applying a

light-induced potential of the form

$$V_r(z, t) = \alpha \sin(\pi t / \tau_0) \tanh(z) \qquad (6.19)$$

for $(t < \tau_0)$, where α and τ_0 are constants which we vary. At $t = \tau_0$, the potential V_r is suddenly switched off such that there is a π phase shift between the two wells. This simple phase-imprinting method does not distinguish between states with similar density and phase profiles such as Ψ_e, or $\Psi_{\pi\pm}$. Other more sophisticated methods of preparing the initial state such as 2-photon adiabatic passage [127] could also be explored.

Figure 6.11: Evolution of fractional population difference N as a function of time for initial states prepared by phase imprinting for different values of α ($\hbar\omega_\perp$) and τ_0 ($\omega_\perp^{-1}$). Top row: $\alpha = 0.5$ $\hbar\omega_\perp$ with $\tau_0 = 6.0, 7.0, 7.5$ $\omega_\perp^{-1}$ in (a)-(c) respectively. Bottom row: $\alpha = 1.0$ $\hbar\omega_\perp$ with $\tau_0 = 3.0, 3.2, 6.3$ $\omega_\perp^{-1}$ in (e)-(f) respectively. In (a) and (d) the oscillations are "self-trapped" with $\langle N(t) \rangle \neq 0$. Other parameters as in Fig. 6.1.

In Fig. 6.11, we show the evolution of the population difference for different values of α and τ_0. We observe that we can choose the phase imprinting parameters such

that the amplitude of the subsequent number oscillations between the wells in a symmetric double-well potential (i.e. in the absence of a potential gradient) are minimized. The time dynamics for this case are shown by the grey lines in Fig. 6.12, and essentially correspond to the π-oscillations with $\langle N(t) \rangle \neq 0$ discussed in [66, 64, 65, 67] and shown in Fig. 6.2(c). For an imprinted phase of π, the population oscillates with most of the condensate in the left well (grey line in Fig. 6.12(a)), while for an imprinted phase of $-\pi$, the population oscillations are contained within the right well (grey line in Fig. 6.12(b)).

In both cases, the addition of the potential gradient at a time indicated by the open circle in Fig. 6.12, induces a flow to the right or upper potential well (solid lines in Fig. 6.12). Even at the time in the π-oscillation cycle when most of the population is already on the right well and would subsequently flow back to the left, the addition of the gradient induces more flow to the right, as shown in Fig. 6.12(b). Note that, in this case, the population remains trapped in the right well until the influence of the second excited state becomes important. If the correct initial state parameters are obtained from the full GP calculation, then the results shown in Fig. 6.12 can be reproduced using the two-state model, except for the transition to the second excited state. However, a full potential calculation is required to correctly predict the initial state and the dynamics for larger potential gradients, where the two-state model breaks down.

Finally, we discuss typical experimental parameters required for the demonstration of Josephson flow to the upper potential well. The number of atoms is given by

$$\mathcal{N} = \frac{g_{3D}}{4\pi} \frac{a_\perp}{a} = \frac{g_{3D}}{4\pi a} \sqrt{\frac{\hbar}{m\omega_\perp}} \; . \tag{6.20}$$

The total atom number is independent of the trap aspect ratio, therefore, for given dimensionless nonlinearity g_{3D}, large atom numbers can be obtained for light, weakly-interacting, transversally weakly-confined systems. For a large number of atoms, one should preferably choose species with a small value of $a\sqrt{m}$. For example, taking $g_{3D} = 4\pi$ and $\omega_\perp = 2\pi \times 20$ Hz, we find: $\mathcal{N} = 1700$ (^{23}Na) and 500 (^{87}Rb). An enhancement of the atom number by a factor of 10 may be possible by tuning
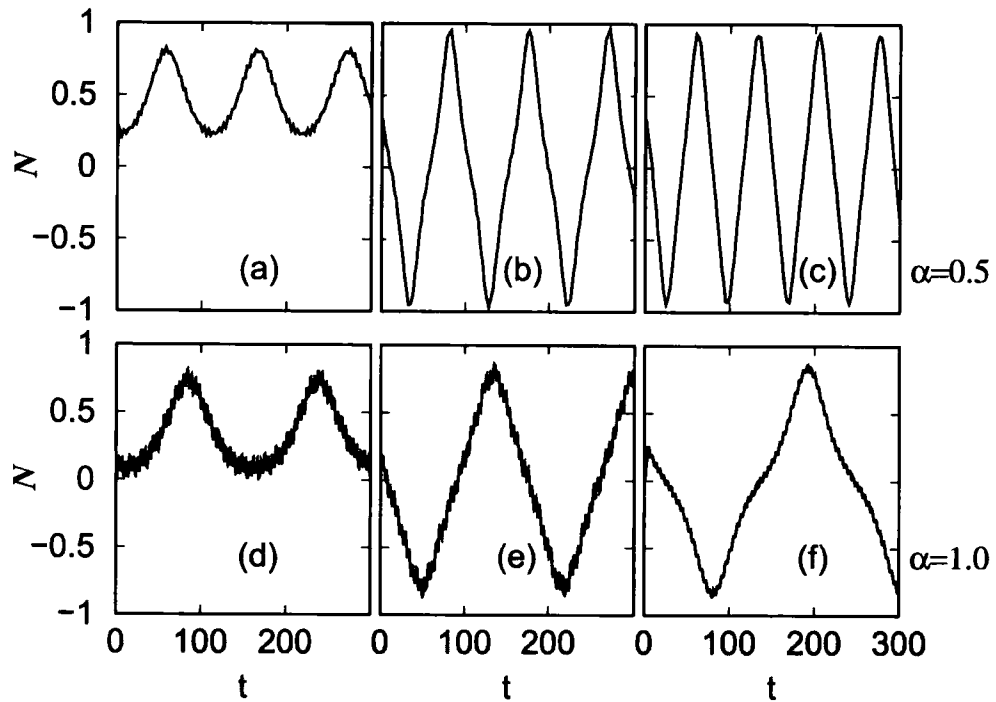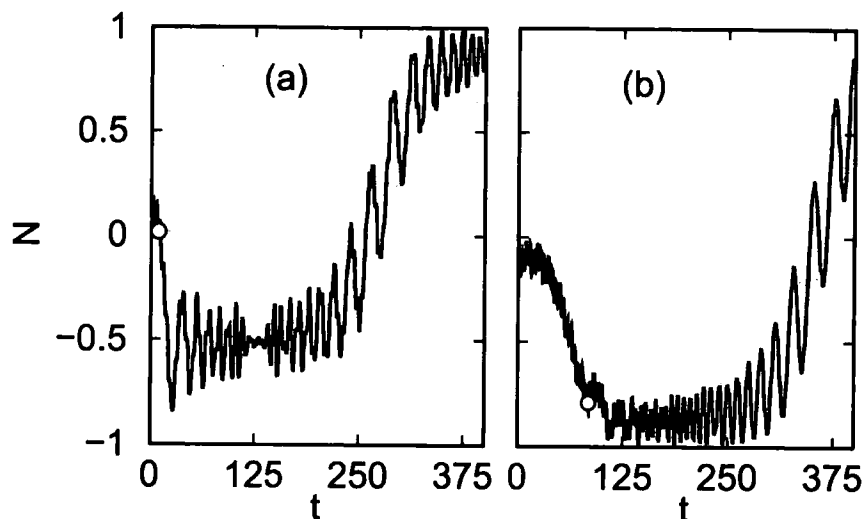
Figure 6.12: Evolution of fractional population difference N as a function of time for initial states prepared by phase imprinting ($|\alpha| = \hbar\omega_\perp$, $\tau_0 = 3\ \omega_\perp^{-1}$). The grey and black curves correspond respectively to the absence of a potential gradient (i.e. symmetric double well), and the addition of a potential gradient $\delta = R(t - \tau_1)$ increased linearly at rate $R = 2 \times 10^{-3}$ ($\hbar\omega_\perp^2/a_\perp$) from time τ_1, with this time indicated by the open circles. (a) $\alpha = \hbar\omega_\perp$, $\tau_1 = 10\ \omega_\perp^{-1}$ and (b) $\alpha = -\hbar\omega_\perp$ $\tau_1 = 85\omega_\perp^{-1}$. Other parameters as in Fig. 6.1.

around a Feshbach resonance (e.g. ^{23}Na, ^{85}Rb, ^{133}Cs) [23, 24, 25]. In the case of ^{7}Li and ^{85}Rb, the number of atoms needed to observe such Josephson flow is not likely to exceed the critical value [1, 15, 75, 76, 77, 78, 79] for collapse, see also next Chapter.

Note that for fixed, reasonably small, nonlinearity ($g_{3D} < 10\pi$), such that the effect can be clearly observed, one needs weak transverse confinement $\omega_\perp$ in order to obtain a reasonable number of atoms which can be imaged easily. However, small $\omega_\perp$ imply long timescales, such that the observation of this effect becomes limited by other factors (e.g. thermal damping [68, 71, 73, 123], atom losses [72], etc.). If we choose $\omega_\perp = 2\pi \times 20$ Hz and an applied field gradient $R = 2 \times 10^{-3}$ ($\hbar\omega_\perp^2/a_\perp$) the experimental realization requires a time $t_{\rm exp} \sim 2$ s.

In the next two Chapters we concentrate on the properties of dilute BECs with attractive interactions in a double-well potential. We begin Chapter 7 by considering

the static properties of a BEC in a single harmonic trap which has been extensively studied and we generalise to a double-well potential. Finally, in Chapter 8 we study the tunnelling dynamics.

Chapter 7

Stability of a BEC with attractive interactions

We study the stability of a condensate with attractive interactions by solving numerically the GPE. We begin by studying the stability of a dilute BEC in a single harmonic trap for which we compare our results with existing predictions and experimental results. We then study the stability of a dilute BEC in a double-well potential.

7.1   Introduction

One of the central questions in the field of Bose condensed gases concerns the influence of interparticle interactions on the character of BEC. In the mean field model described in Chapter 1, these interactions are described by a nonlinear term in the GPE that depends on the density of the condensate and the s-wave scattering length a. When $a > 0$ ($a < 0$), the interatomic interactions are repulsive (attractive). In addition one can control not only the strength of these interactions but also whether they are attractive ($a < 0$ e.g. ^{7}Li, ^{85}Rb, ^{133}Cs at low magnetic fields) or repulsive ($a > 0$) using magnetic-field induced Feshbach resonances [23, 24, 25]. Whereas a harmonically confined BEC with repulsive interactions is stable for any number of atoms, a condensate with attractive interactions is only stable if the atom number $\mathcal{N}$ is smaller than a critical value $\mathcal{N}_c$ [1, 15, 75, 76, 77, 78, 79]. As the number of atoms

exceeds the critical value the interaction energy becomes larger than the zero-point kinetic energy, determined by the confining potential and a collapse occurs.

In Ref. [75] it was shown numerically that a condensate with attractive interactions becomes unstable if $\mathcal{N}_c$ is reached. A dimensionless constant k_c relating the scattering length a with $\mathcal{N}_c$ and the properties of the confining trap, is defined by,

$$\frac{\mathcal{N}_c|a|}{a_0} = k_c , \qquad (7.1)$$

where $a_0 = \sqrt{\hbar/m\omega_0}$ and m is the mass of the atoms confined in the trap and $\omega_0 = \lambda^{1/3}\omega_\perp$ is the geometrically averaged trap frequency. The above parameter describes the ratio of the interparticle interaction to the kinetic energy, (see Chapter 2) and its importance will be discussed in the following Sections.

BEC with attractive interactions was first achieved with [7]Li [15, 128, 129, 130] and more recently with [85]Rb atoms [131, 132] using a Feshbach resonance [17]. In experiments on [7]Li, the magnetic field is held fixed and the number of condensate atoms grows up to $\mathcal{N}_c$ whereas for [85]Rb, a Feshbach resonance [17, 131] has been used to switch the scattering length from positive to negative values, producing a condensate with $\mathcal{N} \gg \mathcal{N}_c$. There have been many theoretical estimates for $\mathcal{N}_c$ both numerically using mean-field calculations [75, 79, 133, 134] and using variational methods [1, 76, 135]. In the case of [7]Li, the GPE correctly predicts $\mathcal{N}_c$ whereas for [85]Rb atoms, there is disagreement between the experimental value and theoretical estimates derived using the GPE.

Although much work has been done to study the collapse properties of dilute BECs in a single-harmonic trap, an interesting subject is to study the behaviour of a condensate with attractive interactions in a double-well potential. Magnetic [32, 48] and optical [49, 50] double-well potentials have been created in recent experiments and a proposal for a magnetic double-well trap has been reported [51]. Although condensates with $a > 0$ in a double-well system has received considerable theoretical attention (see previous Chapters), only Adhikari [136] and Coullet *et al.* [137] have studied the $a < 0$ case.

We begin this Chapter by studying the stability of a BEC with attractive interactions in a three-dimensional harmonic trap, in Section 7.2. Our study is based on the numerical solution of the three-dimensional GPE for different trap geometries and we compare our results with existing work. We also study the stability of a dilute BEC in the presence of vortex states. Finally, in Section 7.3, we study the stability in a double-well. In this case the barrier expels atoms from the centre of the trap and the competition between the attractive interaction and the kinetic term modifies the stability.

7.2 Stability of a BEC in a harmonic trap

In this Section we study the stability of a BEC with attractive interactions in a three dimensional harmonic trap. We solve numerically the GPE (2.31) using the Newton method [96], described in Appendix A. We consider ground state solutions ($\kappa = 0$) as well as vortex states ($\kappa \neq 0$). In Appendix C we also present a variational calculation to study the stability, in the case of a spherical and axially symmetric trap, by minimizing the energy functional and we compare the solutions derived by the numerical solution of the GPE and the variational method.

7.2.1 Ground state solutions

In Chapter 2 we presented typical density plots for a BEC with attractive interactions and we saw that attractive interactions increase the central density and decrease the spatial extension of the condensate. This is also shown in Fig. 7.1 by presenting surface plots of the density distribution for positive and negative nonlinearity g_{3D} for the case of a condensate confined in a spherical trap ($\lambda = 1$). We note that as the nonlinearity is decreased the condensate density becomes narrow and sharply peaked, increasing the interaction energy, and at a critical value g_{3D}^c which is related to $\mathcal{N}_c$ from Eq. (2.8), the condensate collapses.

We begin our study for the stability of a condensate with attractive interactions by showing in Fig. 7.2 the variation of the eigenenergy for the ground state μ, as
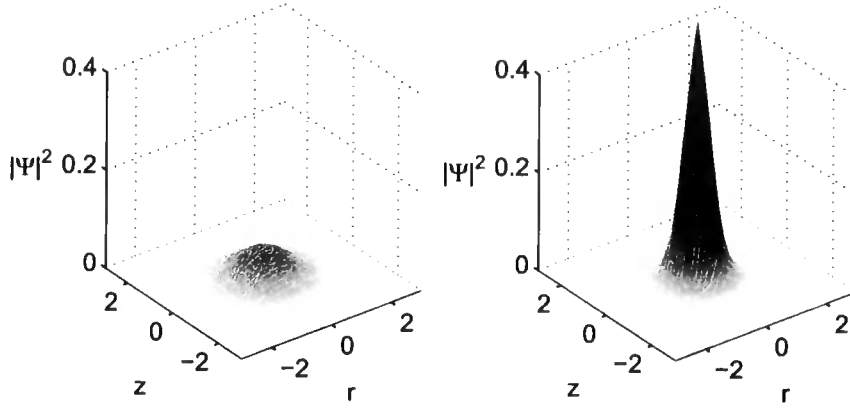
Figure 7.1: Surface plots of the condensate density for a BEC confined in a spherical trap for $g_{3D} := 13$ (left) and -13 (right).

a function of the parameters (a) g_{3D} and (b) $k = \mathcal{N}|a|/a_0$ for different types of geometries. The choice of these parameters will be more apparent in the following paragraphs. In both cases, there is a critical value g_{3D}^c or k_c beyond which there are no stable solutions of the GPE, and a collapse occurs. Substituting the value of g_{3D}^c in Eq. (7.1) we obtain a critical value $k_c = 0.54,\ 0.57,\ 0.54$ for $\lambda^2 = 1/8,\ 1,\ 8$, respectively. For $\lambda = 1$ our simulations give $k_c = 0.57$ which is in excellent agreement with Refs. [1, 75, 77, 78, 79, 133, 134]. Taking values used in the ^{7}Li experiments at Rice University [128] with an almost symmetric trap, $\lambda = 1$, $a = -14.5$ Å, $\omega_0 \sim 2\pi \times 160$ Hz we obtain $\mathcal{N}_c \approx 1250$. The experiments with ^{7}Li predict a value of $\mathcal{N}_c = 1400$ atoms, [128, 129], which is consistent with the theoretical value and provide a good test of the GPE.

We also study the instability in the case of a "cigar-shape" trap ($\lambda < 1$) using the value of λ from experiments with ^{85}Rb of JILA [131, 132]. The frequencies of the trap were $17.24 \times 17.47 \times 6.80$ Hz and the critical constant was found to be $k_c = 0.46$ experimentally. Using the above values for the trap geometry we obtain $\omega_\perp = \sqrt{\omega_x \omega_y} = 2\pi \times 17.35$ Hz and $\lambda = \omega_z/\omega_\perp = 0.39$ which gives $k_c = 0.55$ which
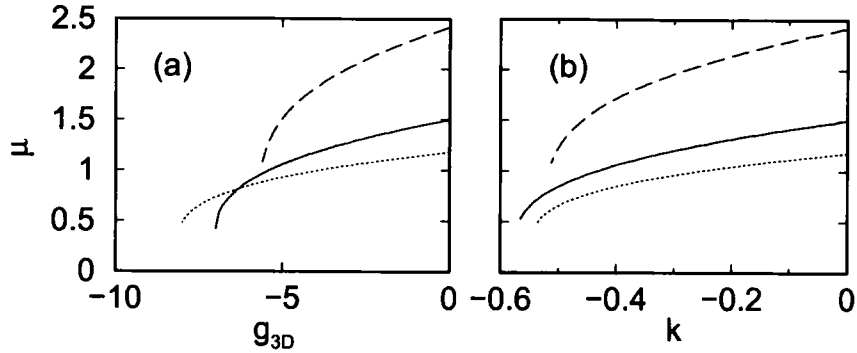
Figure 7.2: Eigenenergy value μ, for the ground state for a spherical, $\lambda = 1$ (solid), a "pancake", $\lambda^2 = 8$ (dashed) and "cigar" trap, $\lambda^2 = 1/8$ (dotted line) as a function of: (a) the nonlinear parameter g_{3D} and (b) the parameter $k = \mathcal{N}|a|/a_0$.

is in excellent agreement with previous numerical calculations [79, 133, 134]. We note that there is a disagreement with the experimental result $k_c = 0.46$ [132]. This discrepancy might be resolved by including higher order terms in the GPE (2.31) [79, 133]. Substituting the values of $\omega_\perp$ and k_c in Eq. (7.1) we find $\mathcal{N}_c = 84$ for ^{85}Rb atoms. Higher number of atoms can be obtained by means of a Feshbach resonance [17].

By exchanging the radial and axial frequencies of the trap, we study the stability of a "pancake-shape" trap ($\lambda > 1$) with $\omega_z = 2\pi \times 17.35$ Hz, $\omega_\perp = 2\pi \times 6.80$ Hz, and $\lambda = 1/0.39 = 2.55$. In this case, $k_c = 0.55$, which corresponds to $\mathcal{N}_c = 98$ from Eq. (7.1). Comparing with the previous values of k_c for $\lambda^2 = 8$ and $1/8$ we note that $k_c(\lambda) = k_c(1/\lambda)$ but the number of atoms in a "pancake-shape" trap is larger than the corresponding number for a "cigar-shape" trap, because,

$$\mathcal{N}_c(\lambda) = k_c(\lambda)\frac{a_0}{|a|} = k_c(\lambda)\frac{a_\perp}{|a|}\lambda^{-1/6} \ . \tag{7.2}$$

Substituting $a_\perp = \lambda^{1/2}a_z$, we obtain a new expression for the critical number of atoms,

$$\mathcal{N}_c(\lambda) = k_c(\lambda)\frac{a_z}{|a|}\lambda^{1/3} \ . \tag{7.3}$$

By exchanging the frequencies $\omega_\perp \to \omega_z$ we have $a_\perp \to a_z$, and $\lambda \to 1/\lambda$, thus taking

the ratio $\mathcal{N}_c(\lambda)/\mathcal{N}_c(1/\lambda)$ we obtain [133],

$$\frac{\mathcal{N}_c(\lambda)}{\mathcal{N}_c(1/\lambda)} = \frac{k_c(\lambda)}{k_c(1/\lambda)}\lambda^{1/6} , \tag{7.4}$$

yielding $\mathcal{N}_c(\lambda) > \mathcal{N}_c(1/\lambda)$ for $k_c(\lambda) \approx k_c(1/\lambda)$ and $\lambda > 1$.

We summarise our main results by plotting the stability curves for the parameters g_{3D}^c and k_c for different trap geometries (different values of λ), and the corresponding critical number $\mathcal{N}_c$ for ^{85}Rb atoms, in Fig. 7.3. We note that the maximum number of atoms in the condensate depends on the trap frequencies as pointed in [134]. If we fix two equal frequencies, for example $\omega_x = \omega_y = \omega_\perp$, corresponding to the choice of units that have been considered in this Thesis, then $\mathcal{N}_c$ is maximized for $\lambda < 1$ since g_{3D} is proportional to $\mathcal{N}$. However considering previous calculations we note that if we fix only one of the frequencies then $\mathcal{N}_c$ is maximized for $\lambda > 1$. Finally, if a_0 is fixed, and therefore the product $\omega_\perp^2 \omega_z$, then $\mathcal{N}_c$ is maximized for $\lambda = 1$ corresponding to a spherical trap in agreement with the variational method presented in Appendix C.
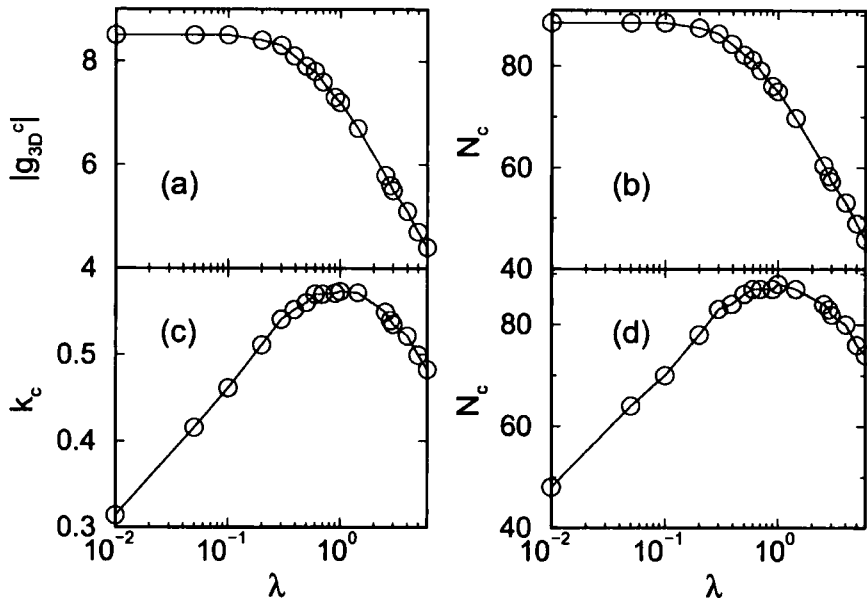
Figure 7.3: Plots of the critical parameters, (a) nonlinear constant g_{3D}^c and (c) k_c, Eq. (7.1) and the corresponding $\mathcal{N}_c$ in (b) and (d) as a function of λ.

An interesting question is how the stability is modified by changing the trap frequency. We solve the GPE (2.31), for $\kappa = 0$ using a harmonic trap,

$$V_{\text{trap}}\left(r, z\right) = \frac{1}{2}\omega_{\perp}^2 \left(r^2 + \lambda^2 z^2\right) , \tag{7.5}$$

where $\omega_{\perp}$ is the angular frequency of the potential in the radial direction. By increasing $\omega_{\perp}$ the trap becomes tighter in all directions and the condensate is confined in a smaller volume. In Fig. 7.4(a) we plot the three dimensional trap, Eq. (7.5) for $\lambda = 1$ for two values of $\omega_{\perp}$ and in Fig. 7.4(b) we plot the critical parameter k_c as a function of $\omega_{\perp}$. We observe that by squeezing the condensate in all directions the stability is decreased.

7.2.2 Vortex States

In the previous subsection we saw that the attractive interactions increase the central density leading to instability and collapse. In the case of axial confinement, this increase is along the axis of the trap. However in the presence of vortex states ($\kappa \neq 0$), due to the centrifugal force the atoms are pushed away from the z-axis and the atoms have more space to stabilize. Thus BECs with vortices are more stable than in the absence of vorticity ($\kappa = 0$) [79, 81, 98].

We repeat the previous calculations for low values of vorticity. In Fig. 7.5(a) and (b), and (c) and (d) we plot the eigenenergy value μ for $\kappa = 1$ and $\kappa = 2$, respectively, for $\lambda^2 = 1/8$, (dot-dashed), $\lambda^2 = 1$, (solid) and $\lambda^2 = 8$ (dashed line) as a function of the parameters g_{3D} and $k = \mathcal{N}|a|/a_0$. For $\kappa = 1$ we obtain $k_c = 1{,}67$, 1.87, 1.91 for $\lambda^2 = 1/8$, 1, 8, respectively, whereas for $\kappa = 2$ we obtain that $k_c = 2.56$, 2.94, 3.11, respectively. Our calculations are in excellent agreement with [79] and small differences between the results are due to numerical precision. We note that for the same type of geometry, k_c increases with increasing κ and that in the presence of vorticity, k_c increases with increasing λ from $\sqrt{1/8}$ to $\sqrt{8}$. We note that $k_c(\lambda) \neq k_c(1/\lambda)$ for states with $\kappa \neq 0$.
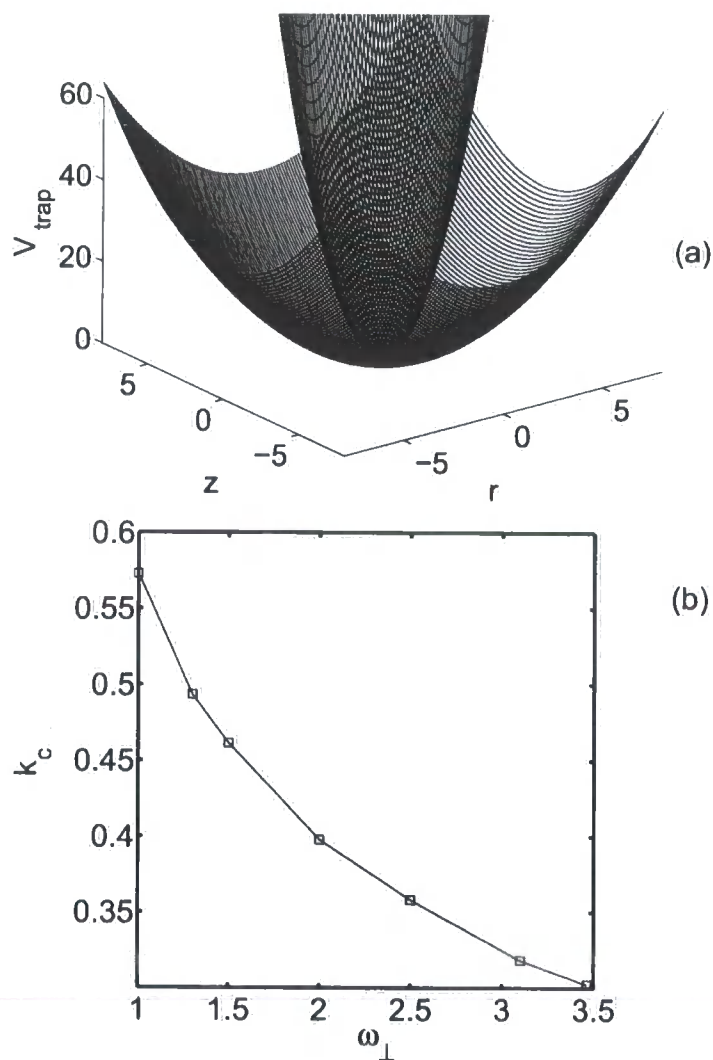
Figure 7.4: (a) Plots of the three dimensional harmonic trap, Eq. (7.5), for two frequencies, $\omega_\perp = 1$ (outer trap) and $\omega_\perp = 3.1$ (inner trap). (b) Stability parameter k_c as a function of $\omega_\perp$. In both cases we assume $\lambda = 1$.
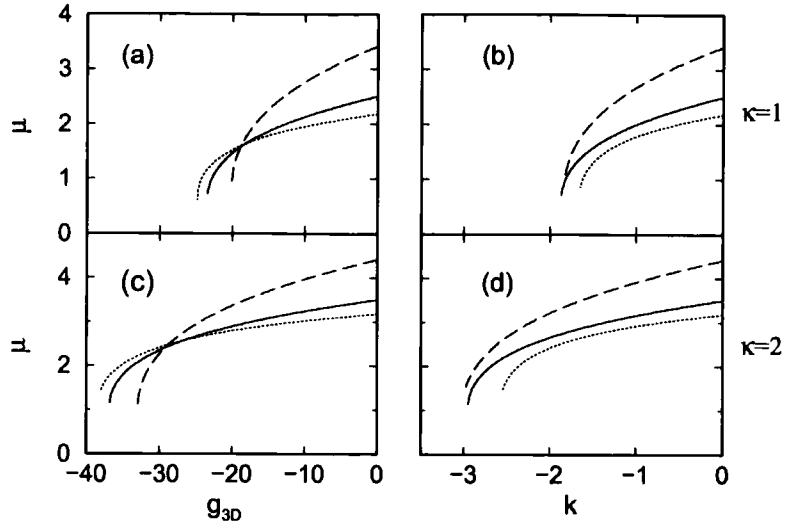
Figure 7.5: Eigenenergy value μ, for (a) and (b) $\kappa = 1$ and (c) and (d) $\kappa = 2$, as a function of the nonlinear parameter g_{3D} (left column) and the parameter, $k = \mathcal{N}|a|/a_0$, (right column). Other parameters as in Fig. 7.2.

7.3 Stability of a BEC with attractive interactions in a double-well potential

Next we consider the stability of a dilute BEC with attractive interactions in a double-well potential which is created by superimposing a harmonic trap and a Gaussian barrier of height h in the z-direction located at $z = 0$. In addition, a linear potential δz of gradient δ is pivoted about the centre of the trap. In order to study the stability we solve the stationary GPE (3.3) in the presence of the total confining potential Eq. (3.4). We also consider the one dimensional limit (Eq. (3.1)), which accurately takes into account the transverse dynamics of "cigar-shape" condensates with a total confining potential in the axial direction given by,

$$V_{1D}(z) = \tfrac{1}{2}z^2 + h\exp\left(-z^2\right) + \delta z . \tag{7.6}$$

We present the eigenenergy curves and the eigenstates of a dilute BEC with attractive interactions in one and three dimensional double-well configuration and address the issue of the stability.

7.3.1 Stationary solutions

The eigenstates of the double-well condensate in one and three dimensions are calculated as discussed in Chapter 3. For small nonlinearities there are only two levels and at $\delta = 0$ the eigenstates are (in order of increasing energy): (i) a symmetric ground state Ψ_g and (ii) an antisymmetric first excited state, Ψ_e, with equal population in both wells, as shown in Fig. 7.6(a). Sufficiently large attractive interactions lead to the appearance of a loop structure in the ground state, [115, 116, 117, 118] and asymmetric states at $\delta = 0$, as shown in Fig. 7.6(b). The corresponding wavefunctions at $\delta = 0$ are: (iii) two low energy, asymmetric ground state solutions with most of the particles in either the left (dashed) or the right (dotted) well (the so-called "self-trapped" states [60, 63, 64, 65]), (iv) a higher energy symmetric ground state Ψ_g with equal population in both wells, and (v) an antisymmetric first excited state Ψ_e with equal population in both wells.

Under certain conditions the eigenenergies μ can also be reproduced by the two-state model approximation (see Chapter 3) using Eq. (3.34) where the values of E_C, E_J, and $\Delta = \alpha\delta$ are determined from the GP solution. The energy splittings E_C and E_J are indicated in Fig. 7.6 for a noninteracting system ($E_C = 0$) and in the presence of attractive interactions ($E_C < 0$). In Fig. 7.7 we plot the two-state model and the GP solutions for g_{1D}. We note that the two-state model correctly reproduces the eigenenergy curves for small values of the nonlinearity.

The picture for the eigenenergy levels as a function of δ shown in Figs. 7.6 and 7.7, is only valid in one and three dimensions for a limited range of nonlinearities. To illustrate the behaviour for the complete range of nonlinearities we plot the value of splittings $|E_C|$ and E_J as a function of g_{1D} and g_{3D} in Figs. 7.8 and 7.11 for the one and three dimensional cases, respectively.

First we discuss the one dimensional case. In Fig. 7.8(a) we plot the two-state model parameters $|E_C|$ and E_J at $\delta = 0$ (symmetric double-well) as a function of g_{1D}. For $g_{1D} < 0$, increasing the magnitude of the nonlinearity leads to the appearance of a loop structure in the ground state at a critical point $|E_C| = E_J$. As a one dimensional
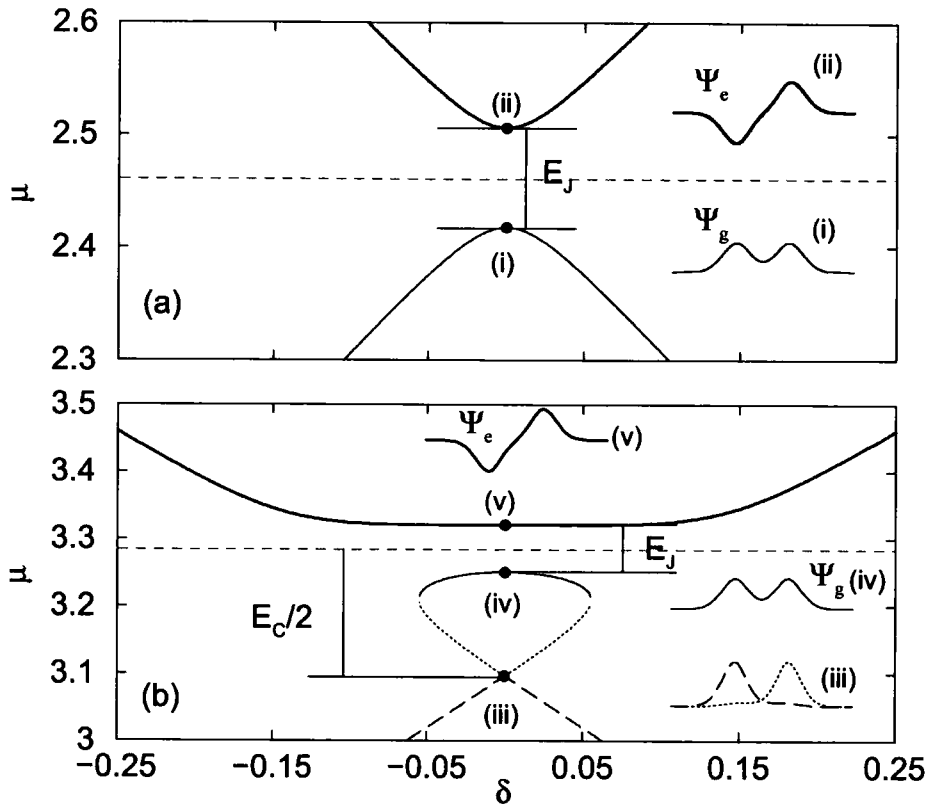
Figure 7.6: Eigenenergies for the double-well for (a) a noninteracting and (b) attractive Bose gas as a function of the potential gradient δ indicating the self-interaction energy, E_C, and the Josephson coupling energy, E_J in each case. The horizontal dotted grey line corresponds to the zero energy of the two-state model. The values of the nonlinearity used here are (a) $g_{3D} = 0$ and (b) $g_{3D} = -\pi$ corresponding to (a) $E_J = 0.089\ \hbar\omega_\perp$ and $E_C = 0$ and (b) $E_J = 0.071\ \hbar\omega_\perp$ and $E_C = -0.379\ \hbar\omega_\perp$. The eigenstates at the centre of the trap are also shown in each case. We assume a spherical trap geometry ($\lambda = 1$), and a Gaussian barrier of height $h = 4\ \hbar\omega_\perp$ located at the centre of the trap.

Figure 7.7: Comparison between the GP solutions (solid) and the two-state model (dashed) eigenenergies, μ, as a function of the potential gradient δ for $g_{1D} = -0.5$ and for the one dimensional confining trap (Eq. 7.6), with $h = 4\ \hbar\omega_\perp$. Black (grey) lines correspond to the ground (first excited) states. The parameters of the two-state model used here are: $E_J = 0.074\ \hbar\omega_\perp$, $E_C = -0.268\ \hbar\omega_\perp$ and $\alpha = 2.695$.

condensate is stable against collapse, (see Chapter 2 and Appendix C), $|E_C|$ remains finite and a loop structure is always observed. Note that for a nonlinearity less than a critical value (indicated by I_1 in Fig. 7.8(a)) the splitting E_J becomes negative signifying an inversion of the lowest two energy eigenvalues.

In Fig. 7.8(b) we show typical eigenenergy levels for the ground and the first excited states as a function of the potential gradient for different values of the nonlinearity both negative and positive. Note that decreasing the nonlinearity ($g_{1D} < 0$), the first excited state has lower eigenenergy than the symmetric ground state for small values of δ (Figs. 7.8(b)I_1 and 7.9(a)). However, the initial inversion of the eigenenergy levels is absent when considering the energy levels, where we find that the first

Figure 7.8: (a) The self-interaction energy $|E_C|$ (dashed) and the Josephson energy E_J (solid) lines at $\delta = 0$ as a function of the nonlinearity g_{1D} for the one dimensional confining trap (Eq. 7.6), with $h = 4\ \hbar\omega_\perp$. (b) Typical eigenenergies μ as a function of the potential gradient δ for various nonlinearities (from left to right) $g_{1D} = -4, -0.5, 0$ and 0.5. The horizontal solid line corresponds to $E = 0$.

excited state has higher energy than the ground state, shown in Fig. 7.9(b). This can be explained using $\mu = E_{tot} - 1/2|g| \int |\Psi|^4 dr = E_{tot} - |E_{int}|$. Although E_{tot} is larger for the first excited state than for the ground state, the first excited state has more negative interaction energy (shown in Fig. 7.9(c)) as its peak density is higher thereby reducing μ below the ground state value. In Fig. 7.10 we compare the two-state model (dashed) and the GPE solutions (solid lines) for the same value of nonlinearity as in Figs. 7.8(b)I_1 and 7.9(a). We observe that the two-state model cannot reproduce the inversion of the eigenenergy levels.

In Fig. 7.11 we consider the three dimensional case. In Fig. 7.11(a) we plot the splittings $|E_C|$ and E_J at $\delta = 0$ as a function of g_{3D}. In contrast to the one dimensional case, for $g_{3D} < 0$ the condensate collapses when the atom number or magnitude of
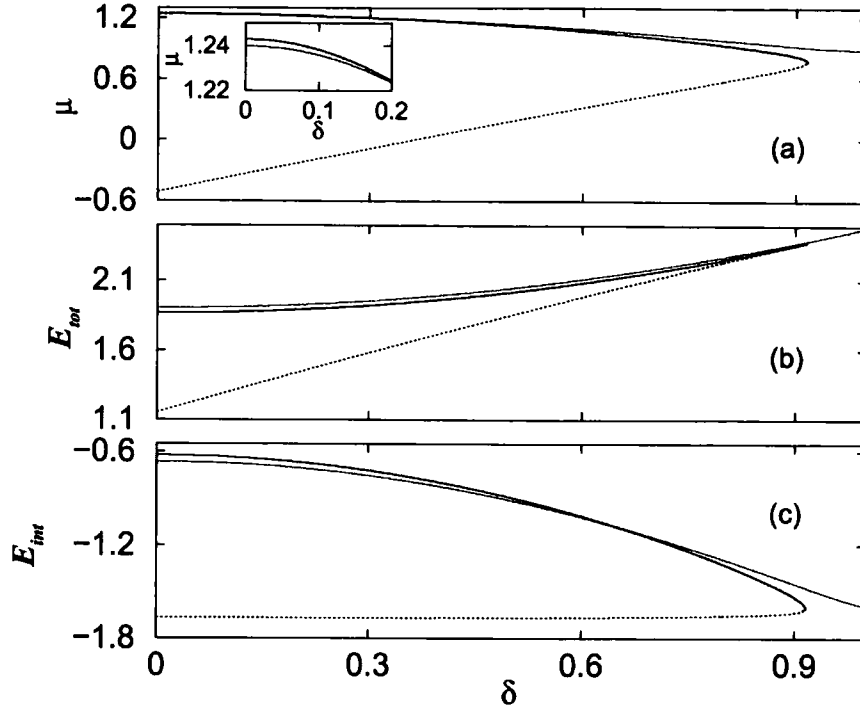
Figure 7.9: (a) The eigenstates μ, (b) the total energy E_{tot} and (c) the interaction energy E_{int} as a function of the potential gradient δ for the Ψ_g (solid black), the Ψ_e (grey) and the "self-trapped" ground (dotted lines) states. Inset in (a) we plot the eigenstates μ for small δ. Other parameters: $g_{1D} = -4$ and $h = 4\ \hbar\omega_\perp$.

the nonlinearity g_{3D} exceeds a critical value. The collapse appears first in the "self-trapping" states. In Fig. 7.11(a) this corresponds to the point where the curve for $|E_C|$ terminates at the boundary between region I and II (indicated by the vertical dotted line in Fig. 11(a)). At larger negative nonlinearities (region I in Fig. 7.11(a)) the lowest eigenstates invert (as in the one dimensional case) and at $\delta = 0$ the symmetric states also become unstable at $g_{3D} = -11.6$. In Fig. 7.11(b) we plot typical eigenenergy levels as a function of δ. The curves are similar to the one dimensional case except in the limit of large negative nonlinearities (region I) where a completely different structure is found. In this region there is no longer a loop structure as the "self-trapped" states are unstable. This parameter region is of interest for investigating tunnelling induced collapse where one begins with a stable symmetric state and adds a gradient and induce a collapse. This region is not described by the two-
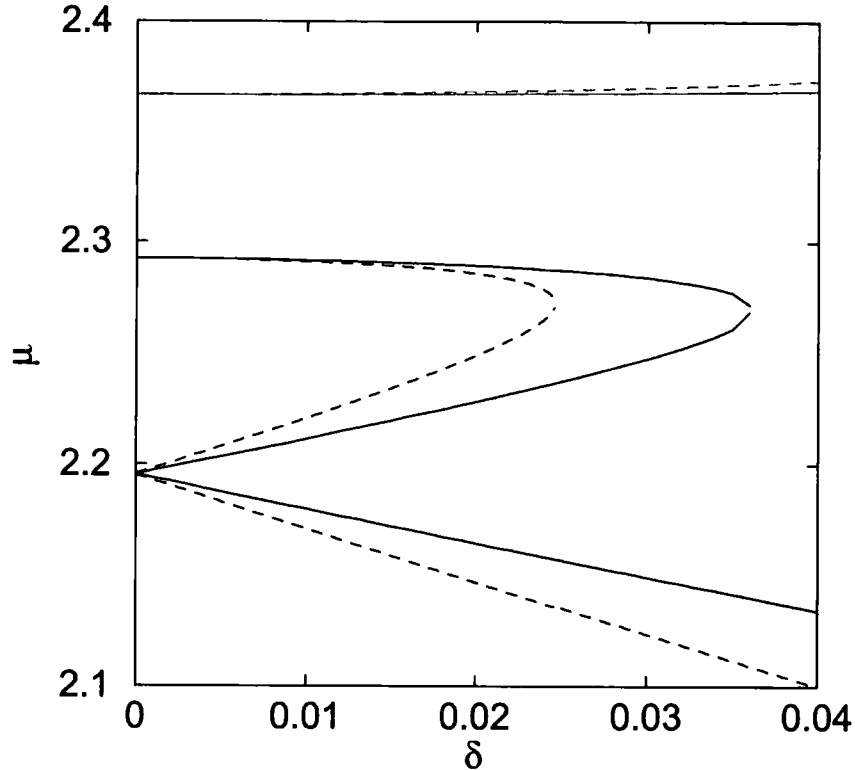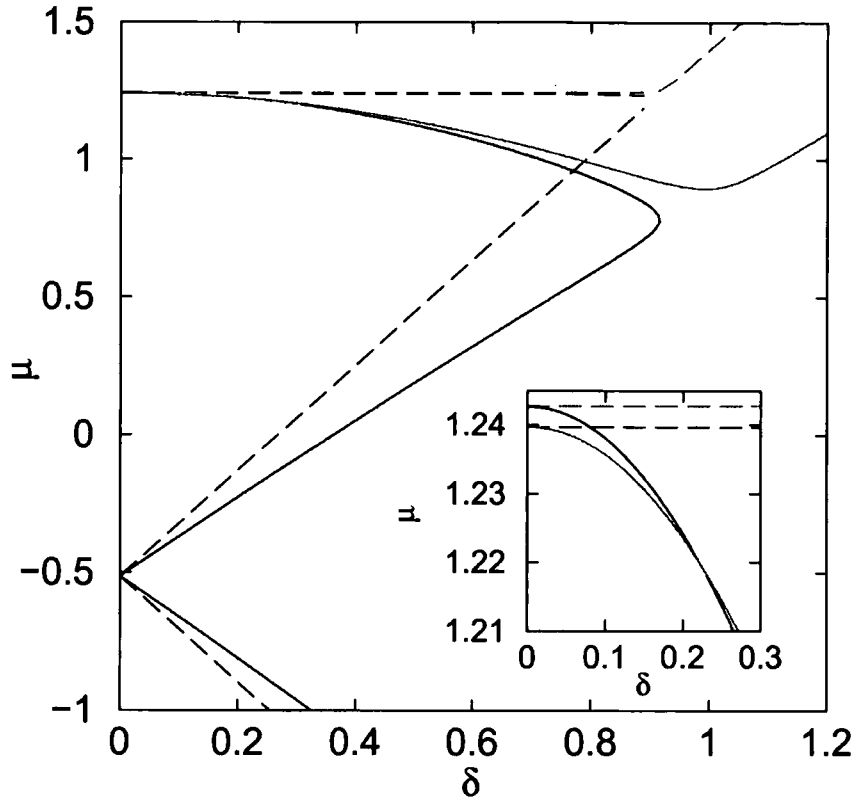
Figure 7.10: Comparison between the GP solutions (solid) and the two-state model (dashed) eigenenergies, μ, as a function of the potential gradient δ for $g_{1D} = -4$ and for the one dimensional confining trap (Eq. 7.6), with $h = 4\ \hbar\omega_\perp$. Black (grey) lines correspond to the ground (first excited) states. Inset are shown the eigenenergies for small δ. The parameters of the two-state model used here are: $E_J = 0.003\ \hbar\omega_\perp$, $E_C = -3.509\ \hbar\omega_\perp$ and $\alpha = 3.832$.

state model. However, before discussing the dynamical behaviour we consider the stability in the symmetric double-well as function of the barrier height.

7.4 Stability of a BEC in a double-well potential

In this Section we study the stability of a BEC with attractive interactions in a three dimensional symmetric double-well trap. In Fig. 7.12(a) we plot the critical constant k_c as a function of h for the case of a symmetric double-well trap with $\lambda = 1$ for the ground and first excited states. We find that at a critical value of the barrier
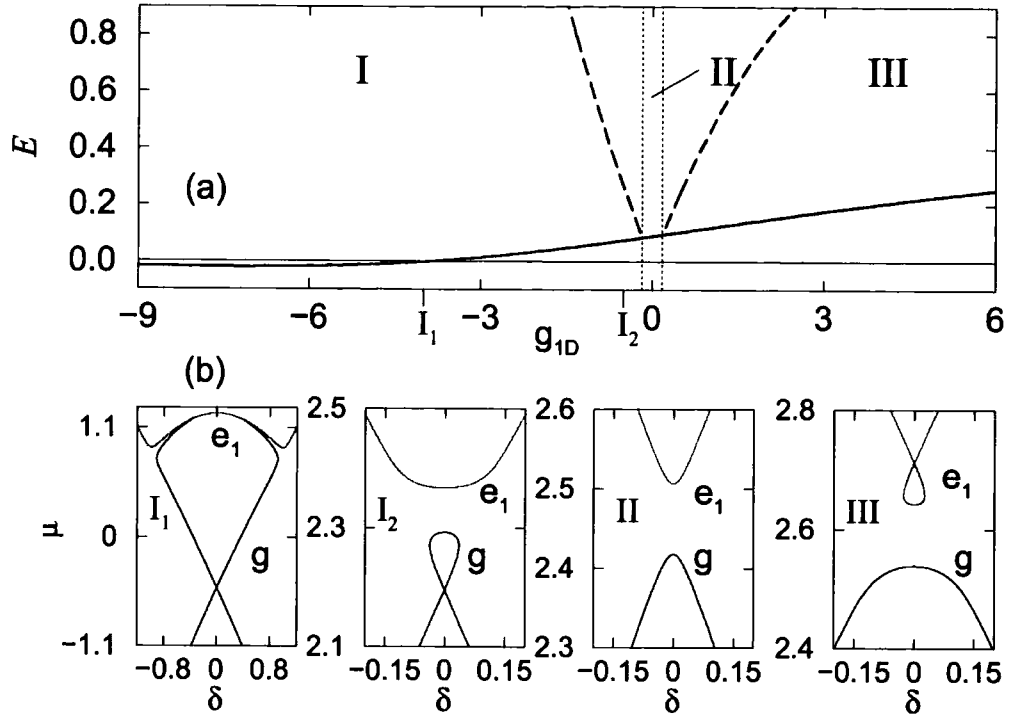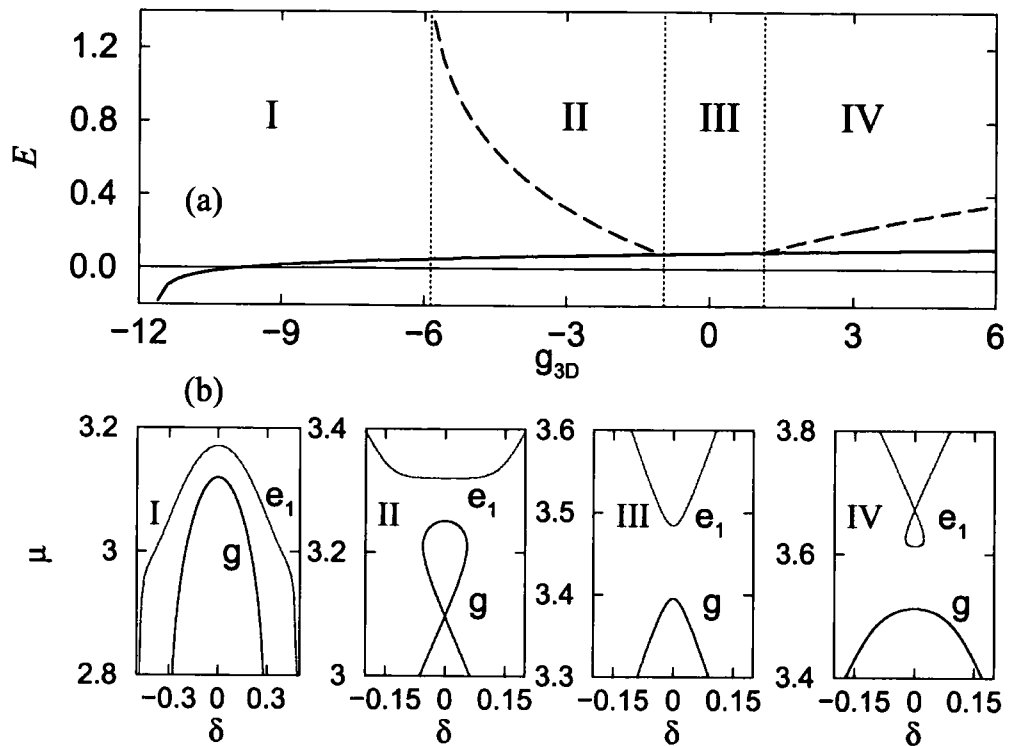
Figure 7.11: (a) The self-interaction energy $|E_C|$ (dashed) and the Josephson energy E_J (solid) lines at $\delta = 0$ as a function of the nonlinearity g_{3D} for the three dimensional confining trap (Eq. 3.4), with $\lambda = 1$, $w = a_\perp$ and $h = 4\ \hbar\omega_\perp$. (b) Typical eigenenergies μ as a function of the potential gradient δ for various nonlinearities (from left to right) $g_{3D} = -6, -\pi, 0$ and π. Compared to the one dimensional case (Fig. 7.8), in three dimensions there is an additional region (I) corresponding to the case where the "self-trapped" states become unstable. The horizontal solid line corresponds to $E = 0$.

height, h_c, there are two branches to the stability curve for the ground state. The upper and lower branches correspond to the symmetric (Fig. 7.6(b), curve (iv)) and asymmetric (Fig. 7.6(b), curve (iii)) eigensolutions respectively, (plotted by circles and squares in Fig. 7.12(a)). Note also that k_c reaches the maximum value at a height just above that corresponding to the appearance of the second branch. This maximum can be explained by a minimum in the peak density which is plotted in Fig. 7.12(b). As the barrier is raised the condensate is split in two, thus reducing the maximum density. However, as the trap splits to form two separate condensates, the condensates in each well become compressed and the peak density increases again.
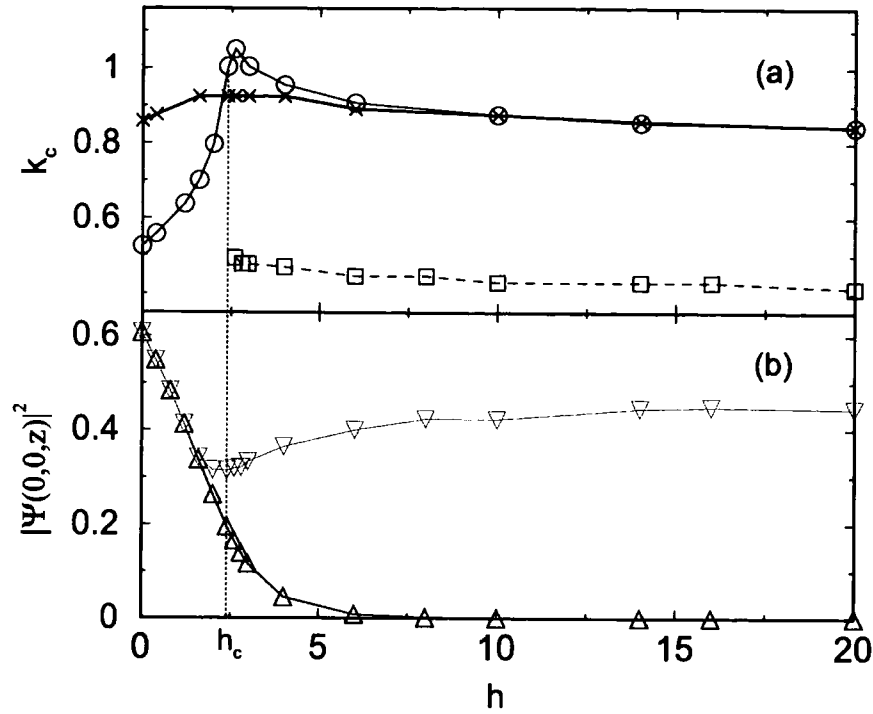
Figure 7.12: (a) Critical parameter k_c as a function of h for a spherical geometry ($\lambda = 1$). Stability curves of the symmetric Ψ_g, (curve (iv) in Fig. 7.6(b)), first excited Ψ_e (curve (v)) and asymmetric ground states (curve (iii)) are shown as circles, crosses and squares respectively. (b) Condensate density $|\Psi(0,0,z)|^2$ along the z axis as a function of h for the state Ψ_g. Shown are the central $|\Psi(0,0,0)|^2$ (black) and peak $|\Psi(0,0,z_m)|^2$ (grey lines) densities, where z_m is the longitudinal position of maximum density in the double-well configuration (i.e. centre of each well). Vertical dotted line highlights the critical value h_c, above which the stability curve consists of two branches.

This result is similar to that of Adhikari [136], except for large h, where he finds that k_c increases again. Our results for different values of λ, are similar to Fig. 7.12. As anticipated, we find that, for $h > h_c$, when the system is essentially composed of two separate condensates, the value of k_c in each well tends towards the value in a single harmonic trap containing the same number of atoms as each half of the double-well.

Finally, the critical constant k_c as a function of h, for the first excited state, Ψ_e (black line in Fig. 7.12(a)) first increases, reaches a peak value, and then decreases approaching the value for the symmetric ground state for large h. This is expected,
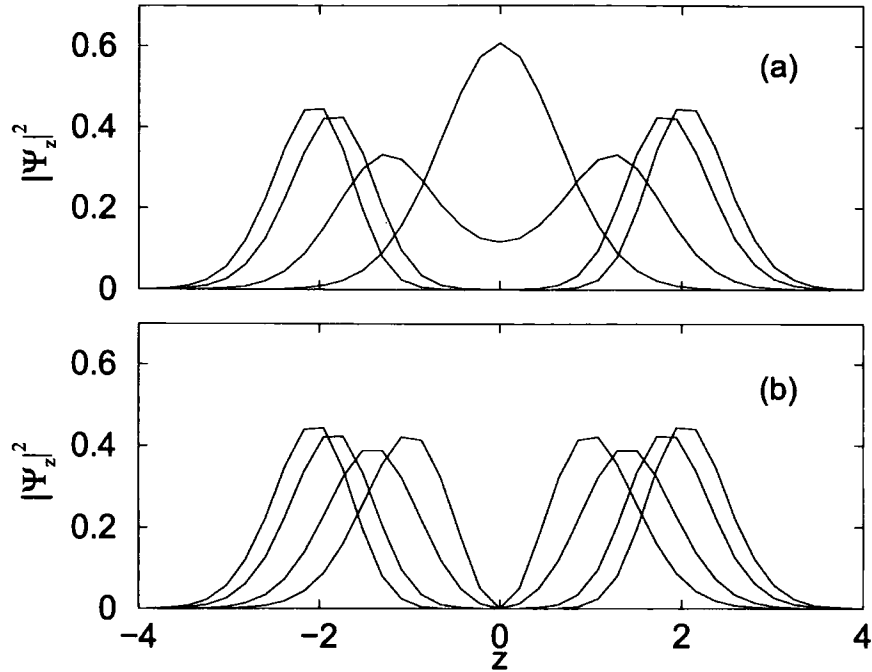
Figure 7.13: Density distributions $|\Psi_z|^2$ along the z-axis for (a) the Ψ_g and (b) the Ψ_e states for various barrier heights. In both cases we consider a spherical geometry, $g_{3D} = -2$ and $h = 0, 3, 10, 20$ $\hbar\omega_\perp$, in terms of increasing width.

as in the limit of large h, the densities distributions of Ψ_g and Ψ_e become very similar, as shown in Fig. 7.13.

In the next Chapter we consider the tunnelling dynamics in the case of a BEC with attractive interactions in a one and three dimensional double-well potential under a time-dependent potential gradient. We will focus on small nonlinearities (regions I and II in Fig. 7.8 and 7.11 for the one and three dimensionals cases) and large negative nonlinearities (region I in Fig. 7.11). In the latter case, and for a three dimensional trap, the condensate is shown to collapse at a critical potential gradient determined by the eigenstates. We will also consider the more complex case of tunnelling in an optical lattice potential.

Chapter 8

Josephson dynamics of an atomic BEC with attractive interactions

The Josephson tunnelling of a low temperature Bose-Einstein condensate with attractive interactions in one and three dimensional double-well potentials is discussed. In particular, the tunnelling dynamics of a condensate under the influence of a time-dependent potential gradient is investigated. The condensate is shown to collapse at a critical potential gradient which corresponds to a critical number of atoms in one of the two wells. We also show that by creating a lattice we can stabilise a condensate at a nonlinearity larger than the critical value for collapse, and we investigate the dynamics.

8.1   Introduction

The successful realization of BECs in trapped atomic gases of ^{7}Li and ^{85}Rb atoms has motivated the study of dynamical effects such as the condensate collapse if the number of condensate atoms exceeds a critical value $\mathcal{N}_c$ [1, 15, 75, 76, 77, 78, 79]. For ^{7}Li, when the number of atoms is increased beyond $\mathcal{N}_c$, the condensate collapses, ejecting atoms until the number of atoms is reduced below $\mathcal{N}_c$ and a stable configuration is reached. Elastic collisions rethermalize the gas, and the condensate

grows again and thus a series of growth and collapse cycles can take place until there are not enough atoms left to completely fill the condensate. In experiments on ^{7}Li, the magnetic field is held fixed and the number of condensate atoms grows up to $\mathcal{N}_{cr}$ where a partial collapse occurs [138, 139]. In this system, it should be noted that the attractive interactions can lead to the formation of bright matter-wave soliton trains in elongated optical traps [140]. In ^{85}Rb experiments, a Feshbach resonance [17] has been used to switch the scattering length from positive to negative values, producing a condensate with $\mathcal{N} \gg \mathcal{N}_{cr}$ which subsequently collapses [131], as modelled in [141, 142, 144, 145, 146, 147, 148].

In this Chapter, we investigate the tunnelling dynamics of a low temperature atomic condensate with attractive interactions. We consider the case of a double-well trap as well as an optical lattice potential and show how tunnelling between two or multiple wells can lead to collapse. We do not, however, intend to describe the *collapse dynamics*, for which, one should additionally incorporate a suitable 3-body loss term [145, 149].

This Chapter is organised as follows. First in Section 8.2, we consider the simplest case of a BJJ, that is a double-well. We calculate the fractional population difference of the ground and first excited eigenstates of an atomic BEC with attractive interactions in an asymmetric one and three dimensional double-well potential. In Section 8.3 we investigate the Josephson dynamics induced by the addition of a time-dependent potential gradient. We study the time-dependent evolution of the system as the gradient is increased at a constant rate for small attractive nonlinear-ities. In Section 8.4 we consider the case of large nonlinearities of an atomic BEC in a three dimensional double-well and we find that collapse occurs as the gradient is increased above a critical value, which can be predicted by the eigenstate curves. Finally in Section 8.5 we consider the case of multiple well potential, and we study the interesting question the possibility of creation of stable condensates for values of the nonlinearity larger than the critical value [1, 15, 75, 76, 77, 78, 79]. For an axially symmetric trap this is achieved by adding an optical lattice along the axis. However, tunnelling dynamics in this case are rather complex and further work needs to be

done.

8.2 Fractional population difference in a double-well potential

We present typical plots of the fractional population difference N, for the ground and the first excited states for the case of an atomic BEC with attractive interactions in a one and three dimensional double-well. Our study is based on the eigenenergy levels shown in the previous Chapter. We vary the nonlinearity at fixed barrier height, but it should be noted that similar results will be obtained in the opposite limit of variable barrier height at fixed nonlinearity. Our study is based on numerical solutions of the time-independent one and three dimensional GPEs (3.1) and (3.3), using the Newton method presented in Appendix A. Our studies explicitly consider the $\delta > 0$ limit, however, for completeness, we also plot the $\delta < 0$ values, which are produced by projecting the $\delta > 0$ solutions about the origin.

Fig. 8.1 shows the fractional population difference for the ground state in one and three dimensional double-wells. In Figs. 8.1(a) and (b) typical eigenenergy levels for various nonlinearites are plotted. In both cases, for zero nonlinearities there is no loop structure in the eigenstates and the fractional population difference is single valued at $\delta = 0$, (zero at $\delta = 0$), as shown in Figs. 8.1(i) and (iv). However, for sufficiently large negative nonlinearities, loop structure appears in the eigenenergy levels which is related to the existence of "self-trapped" states that have nonzero fractional population difference at $\delta = 0$ (see discussion in the previous Chapter). Therefore the ground state is degenerate and the fractional population difference acquires three values at $\delta = 0$, shown in Figs. 8.1(ii)-(iii) and (v). These values correspond to a state with the population balanced in both wells at the centre of the trap, thus $(N(0) = 0)$ and two other nonzero values that correspond to "self-trapped" states that have most particles trapped on the left $(N(0) > 0)$ and right well $(N(0) < 0)$, see the wavefunctions plotted in Fig. 7.6. In contrast to one dimension, for large $g_{3D} < 0$ the "self-trapped" states become unstable, thus there is no loop structure. Therefore, there is only one eigenenergy level for the ground
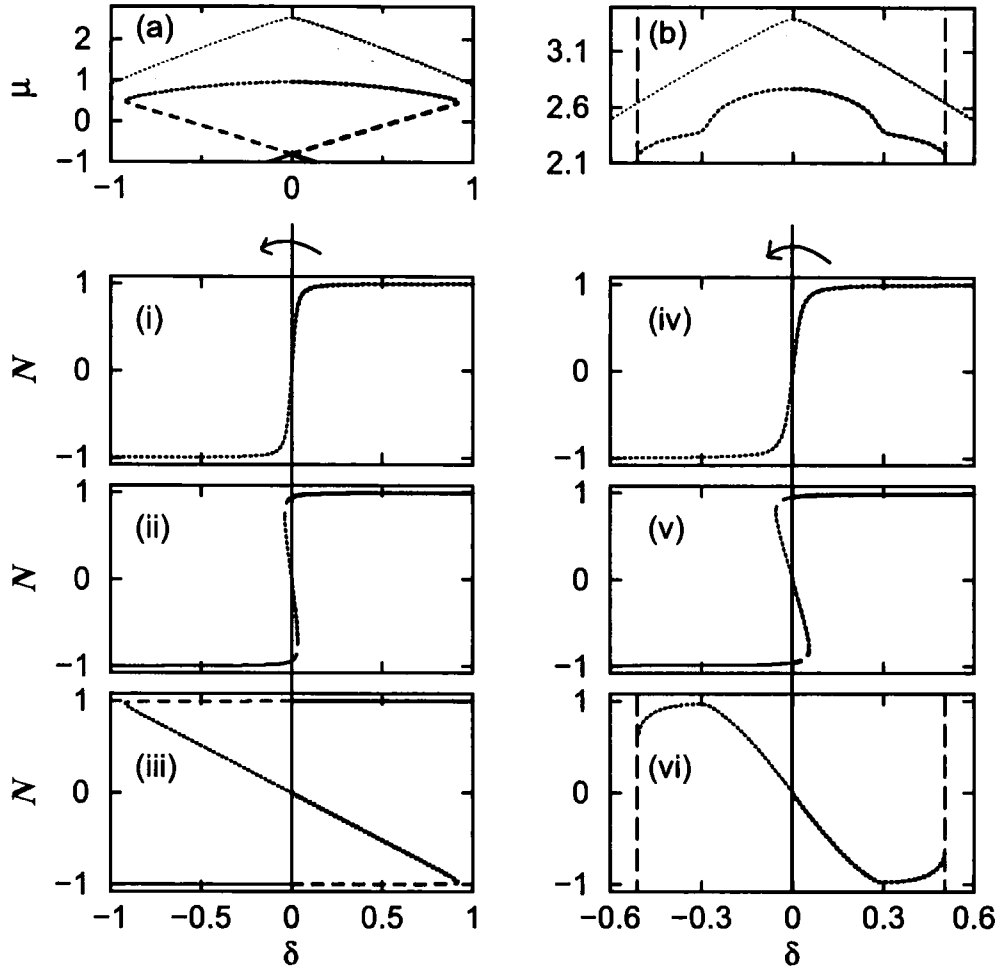
Figure 8.1: The eigenenergies μ for the ground state in (a) one and (b) three dimensional double-well potential as a function of the potential gradient δ for $g_{1D} :=$ 0, (dark grey), -0.5, (light grey) and -4 (black lines) and $g_{3D} := 0$, (dark grey), $-\pi$, (light grey) and -6 (black lines) (from top to bottom). The eigenenergies for $g_{1D} = 0, -4$ and $g_{3D} = -6$ have been shifted along the μ-axis by $(\hbar\omega_{\perp})$: $+0.1, -0.3$ and -0.4 respectively. The fractional population difference N in a one (i)-(iii) and three dimensional double-well (iv)-(vi) respectively as a function of δ. The values of the nonlinearities used here are: $g_{1D} = 0, -0.5, -4$ from (i)-(iii) and $g_{3D} = 0, -\pi, -6$. Bold lines correspond to stationary solutions of the GPE and black lines are the symmetric projections in the $-\delta$-axis. In all cases we consider $h = 4$ $\hbar\omega_{\perp}$.

state (black line in Fig. 8.1(b)) and the fractional population difference (Fig. 8.1(iv)) becomes single valued again. In addition, the ground eigenstate solutions become unstable beyond a critical value of the potential gradient (vertical dashed lines in Figs. 8.1(b) and (iv)). Finally, Figs. 8.1(i)-(vi) show that increasing the interactions, the fractional population difference curves are sheared along the δ axis.

We also consider the fractional population difference for the first excited state. Fig. 8.2(a) and (b) show the eigenenergy levels for the first excited eigenstates for a range of nonlinearities in a one and three dimensional double-well. Typical corresponding fractional population differences are shown in Figs. 8.2(i)-(vi). For attractive interactions, there is no loop structure thus there is one eigenenergy level and one curve for the fractional population difference. Therefore, in contrast to the repulsive limit discussed in Chapter 5, there are no "self-trapped" states, and the fractional population difference has only one value at $\delta = 0$. In all cases (i)-(v), the fractional population difference as a function of δ oscillates and is zero at the level crossings $\delta = 0$ ((i)-(vi)) for the ground state and $\delta \sim 0.5$ ((i)-(ii) and (iv)-(v)) for the second excited state. However, for large negative nonlinearities, the second level crossing for the one dimensional case occurs at $\delta > 0.5$ (Fig. 8.2(iii)), whereas for the three dimensional case, the eigenenergy and the corresponding population difference curve become unstable and therefore terminate at a critical δ_c (Fig. 8.2(vi)). Moreover Fig. 8.2(v) shows that the derivative $dN/d\delta$ diverges at $\delta \sim 0.5$ which is related to a cusp-like structure in the eigenenergy curve at that point, (grey line in Fig. 8.2(b)). Finally, Figs. 8.2(i)-(v) show that increasing the nonlinearity, the fractional population difference curves shear along the δ axis.

8.3 Tunnelling Dynamics under a time-dependent magnetic field gradient

We now apply the eigenstate level picture to analyse the population dynamics when the potential gradient is increased at a constant rate, ($\delta = Rt$) by solving numerically the time-dependent one and three dimensional GPEs (3.1) and (3.3) respectively. At $t < 0$ we produce a stable condensate, in a symmetric double-well, for a value for
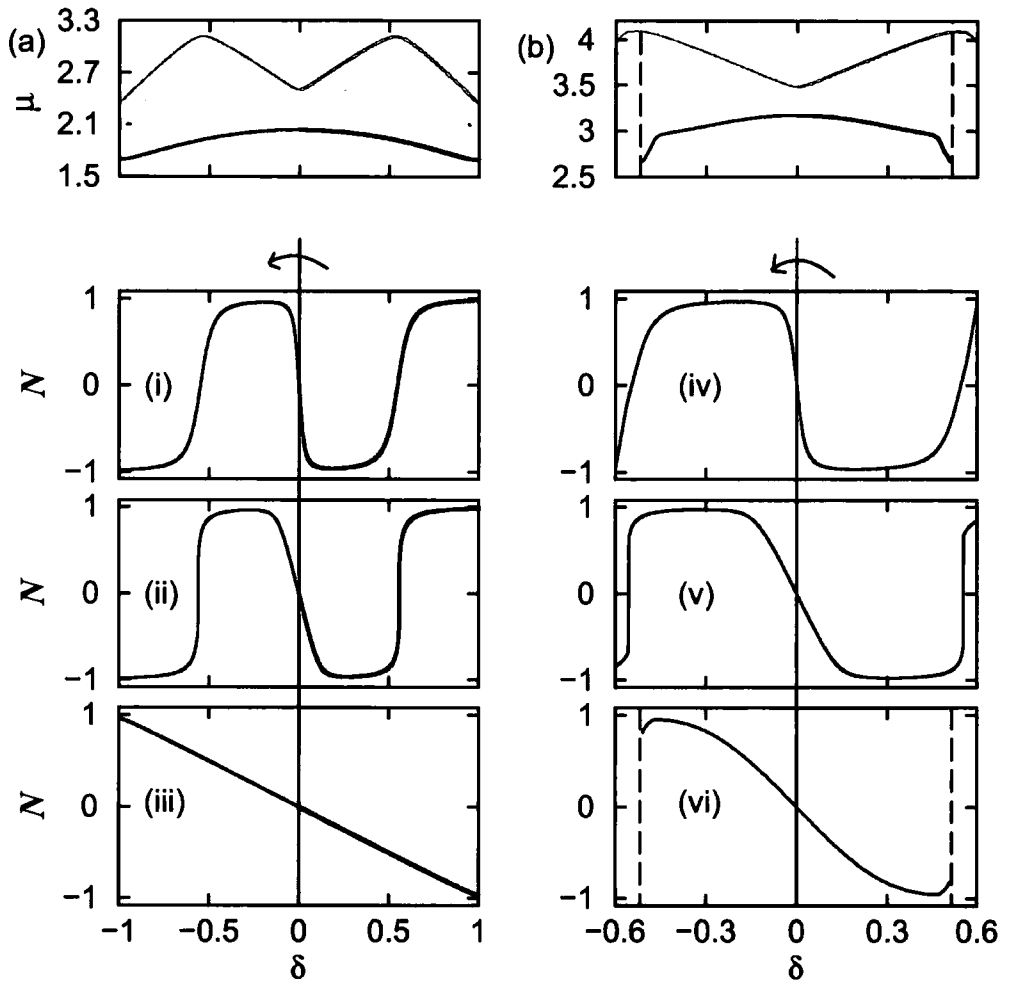
Figure 8.2: The eigenenergies μ for (a) the first and (b) the second excited states for large (black) and low interactions (grey) lines as a function of δ for the first excited state and (i)-(vi) the corresponding fractional population difference N. Other values same as Fig. 8.1.

the nonlinearity. The potential gradient is at $t = 0$, i.e., $\delta = Rt$ for $t > 0$, such that the right well has higher potential energy than the left.

In this Section we discuss the time evolution for the states Ψ_g and Ψ_e for a spherical trap and fixed $h = 4\ \hbar\omega_\perp$ shown in Fig. 8.3, for small nonlinearities (regions I and II in Fig. 7.8 and 7.11 for the one and three dimensional cases). For attractive interactions, the population difference for the ground state induced by the addition of the gradient does not follow that of the eigenstate, as shown in Fig. 8.3. The effect of the nonlinearity is that the ground state is immediately projected onto a superposition of states. In contrast, the population difference for the first excited state, for slow velocities, follows the eigenstate almost adiabatically. For Ψ_g, the potential gradient induces a Josephson current to the left (lower potential energy region), (black lines in Fig. 8.3) whereas for Ψ_e flow occurs to the right (higher potential energy) (bold black lines in Fig. 8.3).
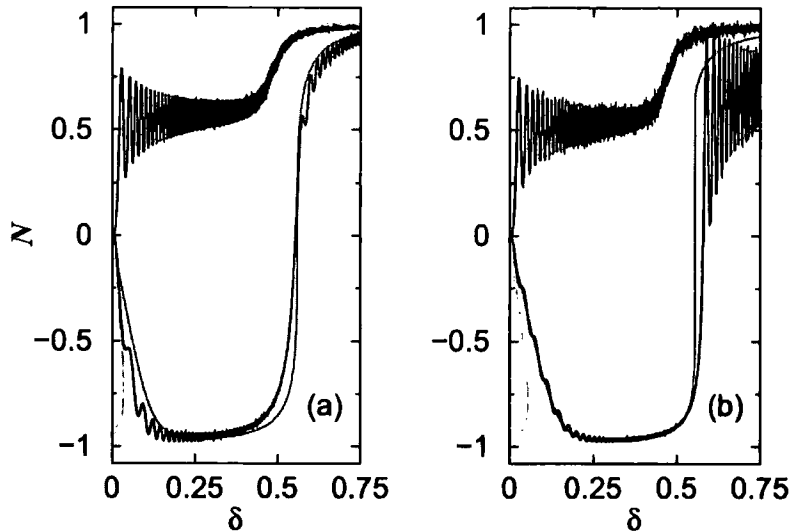
Figure 8.3: Evolution of fractional population difference N as a function of δ for a system initially prepared in state Ψ_g and Ψ_e (black lines) for an atomic BEC in (a) an one and (b) three dimensional double-well. The population difference for the eigenstates for the ground (first excited) states are also shown as solid light (dark) grey lines. Other parameters used here: $h = 4\ \hbar\omega_\perp$, $\lambda = 1$ and $R = 10^{-3}\ \hbar\omega_\perp^2/a_\perp$.

The initial dynamics discussed in Fig. 8.3 is also well described by the two-state model Eqs. (4.18) and (4.19), (see previous Chapters), for both Ψ_g and Ψ_e states,

as shown in Fig. 8.4. For comparison, we also consider the GP solutions. However, for larger gradients the two-state model does not predict the step in the evolution of the population difference for the ground and first excited states, (it suggests that the atoms remain in the lower (left) and upper (right) well for the ground and first excited states respectively). This breakdown of the two-state model occurs because it does not take higher lying modes into consideration [60] (see also the discussion in Chapter 5).
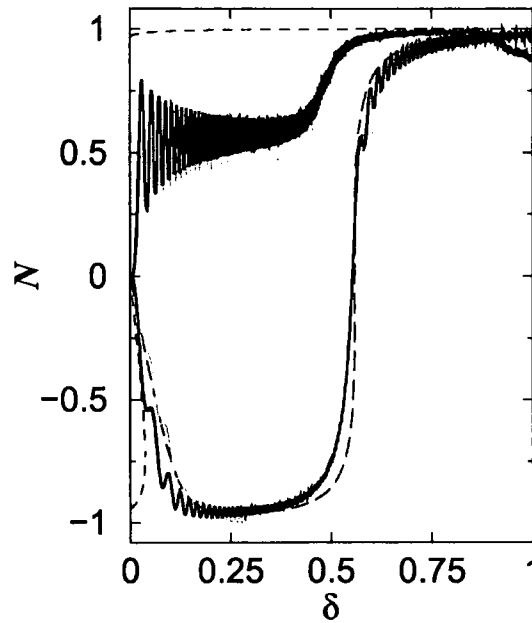
Figure 8.4: Comparison between the evolution of fractional population difference N as a function of δ for a system initially prepared in state Ψ_g ($N > 0$) and Ψ_e ($N < 0$) for an atomic BEC in an one dimensional double-well obtained by the numerical solution of the GPE (3.1) (bold black) and the two-state model (grey lines). The population difference for the eigenstates for the ground (first excited) states are also shown as dashed (long dashed lines). Other parameters used here: $g_{1D} = -0.5$, $h = 4\ \hbar\omega_\perp$ and $R = 10^{-3}\ \hbar\omega_\perp^2/a_\perp$. The parameters of the two-state model are shown in Fig. 7.7.

8.4 Tunnelling induced collapse

For large negative g_{3D} increasing the potential gradient, $\delta = Rt$, leads to an increase of the number of particles in one well and there is a critical gradient δ_c above which

a collapse occurs. We investigate the possibility of observing a tunnelling induced collapse. We study the dynamics leading to the onset of collapse but not the collapse itself. Note that this qualitative picture should remain correct, even if 3-body terms are included in the treatment, although the latter may affect the precise value of the onset of the collapse.
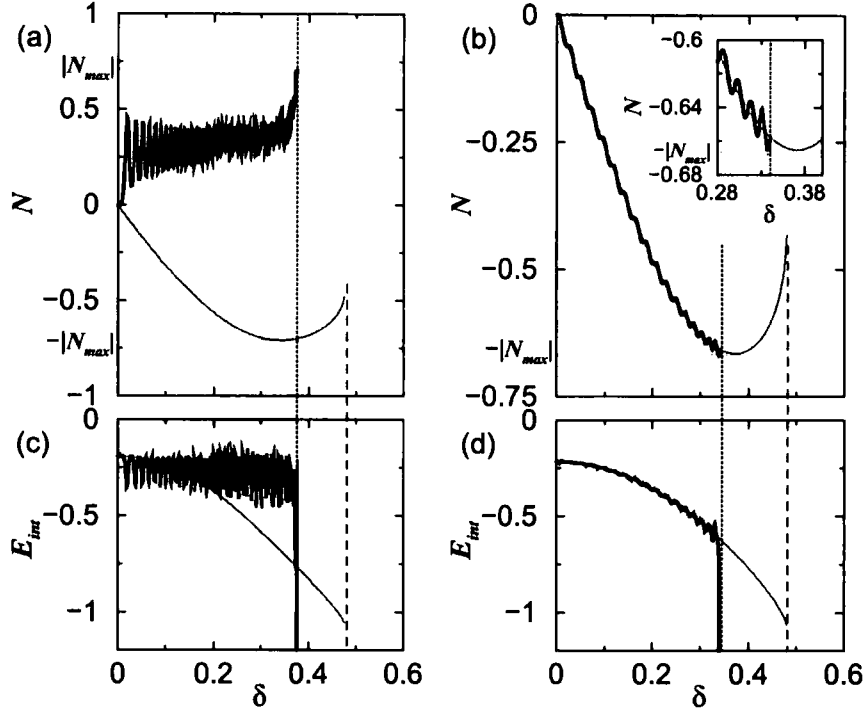
Figure 8.5: (a)-(b) Evolution of fractional population difference N as a function of δ for a system initially prepared in state (a) Ψ_g and (b) Ψ_e (black lines). The population difference for the eigenstates are also shown as solid grey lines. The vertical dashed lines mark the critical gradient at which the eigenstates become unstable ($\delta_0 = 0.475$ and $\delta_0' = 0.480$ for Ψ_g and Ψ_e respectively). The vertical dotted lines describe where the system collapses in the time-dependent simulation. The collapse occurs when N reaches the maximum value $|N_{max}|$ (indicated by horizontal grey lines in (a) and (b)) of the number asymmetry predicted by the eigenstates. (c)-(d) Evolution of the interaction energy E_{int} (thick black line) when the potential gradient $\delta = Rt$ is increased at a constant rate R for (c) Ψ_g and (d) Ψ_e, with corresponding eigenenergies shown by grey lines. Other parameters used here: $g_{3D} = -7$, $h = 4\ \hbar\omega_\perp$, $\lambda = 1$ and $R = 10^{-3}\ \hbar\omega_\perp^2/a_\perp$.

For attractive interactions, the ground state population difference induced by the

addition of the gradient does not follow that of the eigenstate, as shown in Fig. 8.5(a) and also discussed in the previous Section. The critical gradient corresponding to the collapse, shown by the dotted vertical line in Fig. 8.5(a), is identified as the point where the interaction energy ($|E_{int}| = 1/2|g_{3D}| \int |\Psi|^4 dr$) diverges, see Fig. 8.5(b). Note that the critical value of the number asymmetry N for which the time-dependent collapse occurs is close to the maximum value of $|N_{max}|$ found for the eigensolution (grey horizontal line in Fig. 8.5(a)).

This prediction becomes clearer if we consider a condensate prepared in the first excited state Ψ_e, where the time evolution closely follows the eigensolution, see Fig. 8.5(b). In this case the collapse occurs at exactly the point where the number asymmetry exceeds $|N_{max}|$, see inset of Fig. 8.5(b). The critical gradient at which the collapse is observed is found to be essentially independent of the rate R at which the gradient is increased.

One can also compare the critical number needed in one well before collapse occurs with the prediction for the symmetric potential shown in Fig. 7.12. By defining $K_{cr} = \mathcal{N}'_{cr}|a|/a_0$, where $\mathcal{N}'$ is the number of atoms in the well which collapses we find that $K_{cr} = 0.471$ and 0.467 for ground and excited states in Fig. 8.5, which is close to the value of $k_{cr} = 0.470$ predicted by the lower branch of Fig. 7.12.

8.4.1 Experimental realization

Finally, we discuss typical experimental parameters required for the demonstration of the tunnelling induced collapse. In the harmonic oscillator units discussed in Section 2, the number of atoms is given by,

$$\mathcal{N} = \frac{g_{3D}}{4\pi} \frac{a_\perp}{a} = \frac{g_{3D}}{4\pi a} \sqrt{\frac{\hbar}{m\omega_\perp}} . \tag{8.1}$$

For ^{7}Li atoms and taking $g_{3D} = -6$ and $\omega_\perp = 2\pi \times 100$ Hz, we find $\mathcal{N} = 1200$ which is below the critical value for collapse. For an applied field gradient $R = (10^{-3}) (\hbar\omega_\perp/a_\perp)$ the collapse occurs at $t_{exp} \sim 0.6$ s. The collapse is illustrated by the density plots shown in Fig. 8.6. We have confirmed that the collapse can be
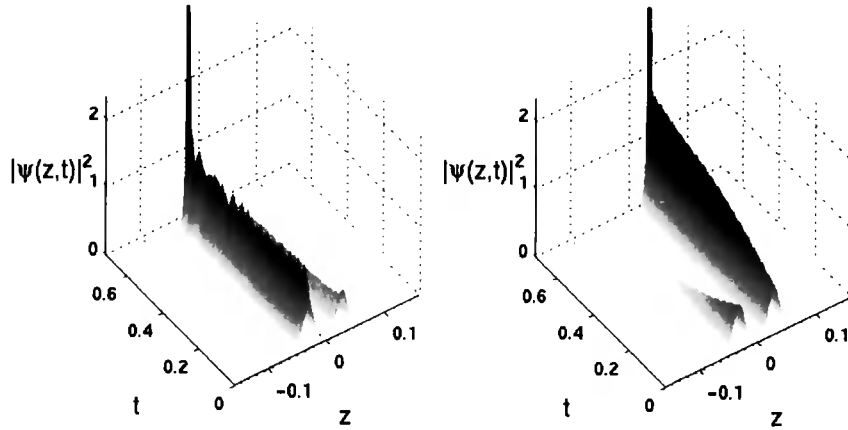
Figure 8.6: Surface plot of the evolution of the density distribution ($|\psi(z,t)|^2 \times 10^{10}\text{cm}^{-3}$) along the z-axis (mm) as a function of time (s) for a BEC initially prepared in the Ψ_g (left) and Ψ_e (right) states with $g_{3D} = -6$. Due to the potential gradient, tunnelling is induced to the left ($z < 0$) well for the Ψ_g state and to the right well for Ψ_e. The condensate instability occurs at $t = 0.65$ s for Ψ_g and $t = 0.67$ s for Ψ_e state. Other parameters as in Fig. 8.5.

avoided if the potential gradient is ramped up to a gradient smaller than the critical value and then held constant. This would not hold if the system were very close to the critical region, in which case number fluctuations [69] could enhance tunnelling and hence induce the collapse at a slightly smaller gradient than that predicted by our simple model.

Finally, in the following Section we address the interesting question of the stability in an optical lattice potential and discuss tunnelling effects in a multi-well system.

8.5   Three dimensional Optical lattice

The basic idea of stabilisation in an optical lattice is that by confining the condensate in smaller regions we increase the kinetic energy and thus can counterbalance the attractive interaction, thereby stabilising the condensate. In this way we can produce stable condensates for values of g_{3D} larger than predicted in the previous Chapter. If the number of condensed atoms in any individual well is larger than a critical value then the collapse still occurs, but is restricted to certain lattice sites, and the

collapse of the whole condensate is avoided. Next we describe the model we used to produce the lattice.

8.5.1 Numerical method-results

We consider the case of a "cigar" trap with $\lambda = 0.1$. At $t < 0$ we find a stable ground state solution, for a value for the nonlinear constant $g_{3D} = 18$. In Section 7.2.1 (Fig. 7.3), we saw that for this negative value of the nonlinearity and the trap geometry, the condensate collapses. At $t > 0$ we add a lattice potential along the z-axis of the form,

$$V_L = a_L t_L \sin^2(\frac{2\pi z}{\lambda_L}) \tag{8.2}$$

where $a_L = 50\ \hbar\omega_\perp^2$ is a constant, $\lambda_L = 4\ a_\perp$ is the wavelength, and

$$t_L = \begin{cases} t/t_{ramp}, & t \leq t_{ramp} \\ 1, & t > t_{ramp} \end{cases}$$

where $t_{ramp} = 50\ \omega_\perp^{-1}$ and $t_{max} = 1550\ \omega_\perp^{-1}$. For $0 \leq t \leq t_{ramp}$ the lattice cuts the cigar-shaped atomic cloud into spatially separated parts. For $t_{ramp} \leq t \leq t_{cr}$ the condensate stabilizes, Fig. 8.7(a).

At $t = t_{cr} = 200\ \omega_\perp^{-1}$, we suddenly change from repulsive to attractive interactions by changing the sign of the nonlinear constant, $g_{3D} = -18$. We then study the response of the condensate to this sudden change. We observe motion of atoms between wells and the condensate remains stable for $g_{3D} = -18$, Fig. 8.7(b). In Fig. 8.8 we plot the number of atoms in each separated well as a function of time, while the last graph shows the distribution of the mean number of atoms in each well. The results are rather complex, we observe coupled Josephson oscillations in most wells, except for the outermost well. Further work is needed to completely understand the complex dynamics in the multi-well case.

Varying the value of g_{3D} we observed an interesting case at a value of $g_{3D} = -19.5$, where the condensate in the middle well collapses while the condensates in the other
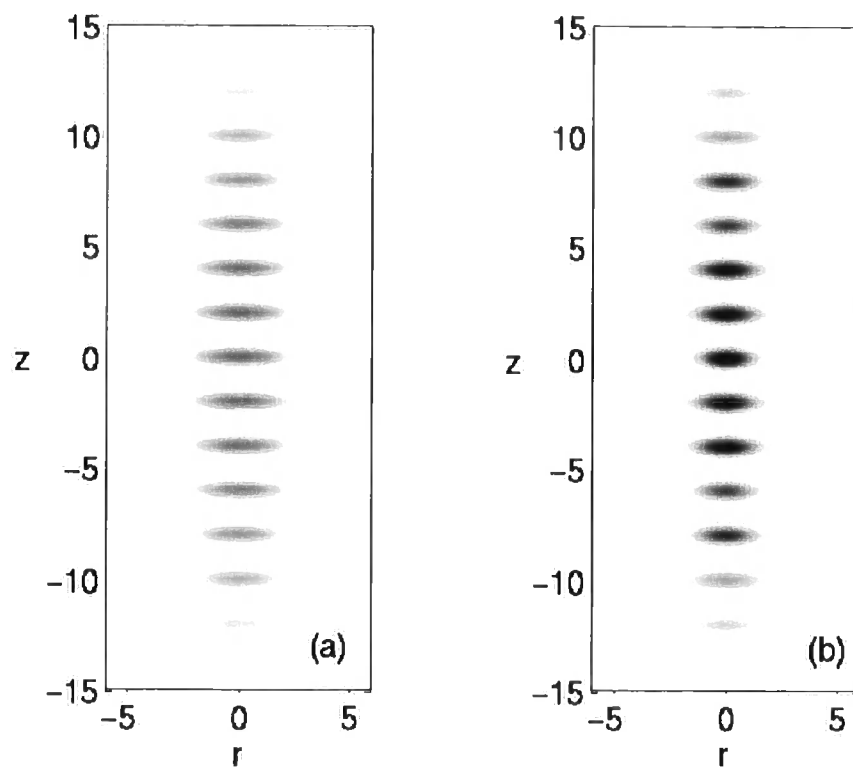
Figure 8.7: Images showing a cross-section of the condensate density at (a) $t = 175\ \omega_\perp^{-1}$ and (b) $t = 625\ \omega_\perp^{-1}$. (a) shows that the potential (Eq. (8.2)) creates lattice along the axial direction. (b) shows the response of the condensate to the sudden change to attractive interactions, $g_{3D} = -18$.

wells do not, Fig. 8.9. Beyond this value of the nonlinear constant and using the above parameters for the confining trap, the whole condensate collapses.
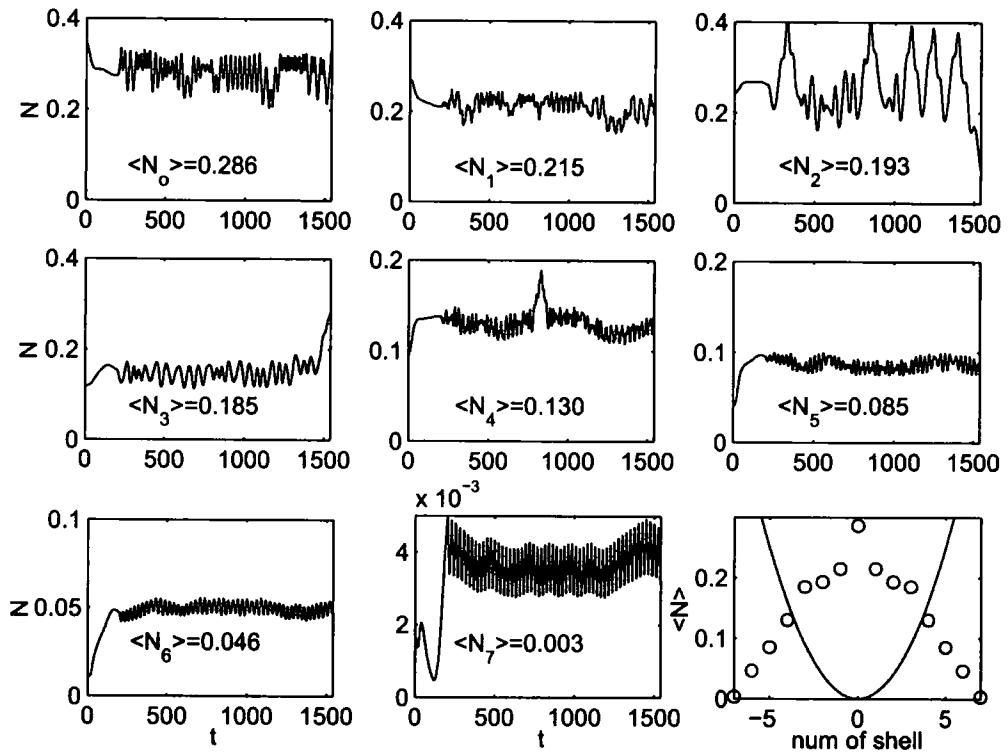
Figure 8.8: Number of particles in each well as a function of time. We observe oscillations as a result of Josephson tunnelling. On each plot we write the mean number of particles in that well. The last graph shows the mean value of the number of particles at each well over all time and the trapping potential, $V(z) = \frac{1}{2}\lambda z^2$, $\lambda = 0.1$. We notice that the majority of atoms occupy the centered well.
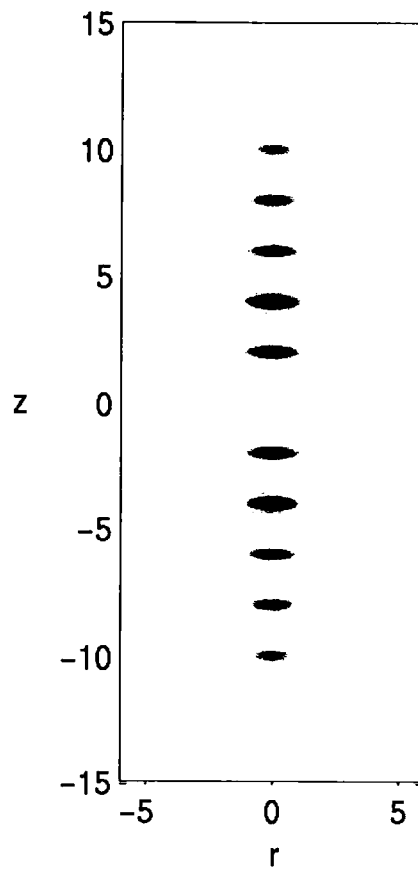
Figure 8.9: Image showing a cross section of the condensate density at $t = 363\ \omega_\perp^{-1}$ and $g_{3D} = -19.5$ (h.o.u). The centered well has already collapsed, but the remaining condensate remains stable. Dark gray corresponds to regions with higher density.

Conclusion

The main topic of this Thesis has been the study of properties of dilute BECs in one and three dimensional asymmetric double-well potential Josephson junction where the weak link is provided by a potential barrier. The Gross-Pitaevskii equations has provided the main theoretical tool. We induce an asymmetry in the double-well either by moving the barrier uniformly through the condensate or by adding a potential gradient that increases at a constant rate. Our studies reveal rich phenomena arising from the interplay between interactions (both repulsive and attractive) and the tunnelling (controlled by the barrier height). In particular we have highlighted three interesting topics:

- We identify tunnelling resonances associated with level crossings, and determine the critical velocity that characterises the resonance. Under certain conditions, the properties of a condensate in a double-well potential can be described by a nonlinear two-state model. We test the validity of the two-state model, and we show that for the experimentally interesting case, a two-state model is insufficient to completely describe the tunnelling dynamics.

- We discuss the feasibility of experimental control of the flow direction by phase-imprinting. We show that phase-imprinting can lead to significant change in the flow direction for condensates of up to a few thousand atoms. The phase-imprinting technique provides a clear signature of macroscopic quantum tunnelling.

- We also address the stability of an atomic BEC with attractive interactions. We emphasise a regime of parameters where the condensate is stable if the

population in both wells is approximately equal, but becomes unstable if there is sufficient tunnelling from one well to the other. We show that a collapse occurs at a critical gradient predicted by the eigenstates.

Further work is need to study the influence terms not included in the GPE model and the possible applications of double-well systems in atom interferometry and precision measurement.

Appendix A

Numerical methods

We describe the numerical methods that have been used in this Thesis, to solve the Gross-Pitaevskii equation. The Crank-Nicholson and the Newton-Raphson methods can both be applied to find time-independent solutions, whereas Crank-Nicholson method has also been applied to find solutions in the time-dependent domain.

A.1 Crank-Nicholson method

The basic task in this Thesis is how one solves the Gross-Pitaevskii equation (GPE) which has the same form as the Schrödinger equation plus an extra nonlinear term,

$$i\hbar \frac{\partial}{\partial t} \psi(z,t) = \left(-\frac{\partial^2}{2\partial z^2} + V(z) + g|\psi(z,t)|^2 \right) \psi(z,t) = H\psi(z,t) \ . \qquad \text{(A.1)}$$

As in any differential equation we are given the initial wavefunction $\psi(z, t = 0)$ together with boundary conditions that $\psi(z,t) \to 0$ at $z \to \pm\infty$ with the wavefunction normalised to unity,

$$\int_{-\infty}^{+\infty} |\psi(z,t)|^2 \, dz = 1 \ . \qquad \text{(A.2)}$$

In this Section, we present a scheme to solve the GPE, originally proposed by Crank and Nicholson.

It is known from quantum mechanics that the solution of Eq. (A.1) has the form,

$$\psi(z,t) = e^{-iHt}\Psi(z,0) \ . \tag{A.3}$$

It is clearly an advantage to formulate a numerical scheme that conserves the probability by keeping the evolution operator unitary even as it is discretized. This can be achieved by writing the evolution operator $\exp(-iH\Delta t)$ in the so-called *Cayley* form with

$$e^{-iH\Delta t} \simeq \frac{1 - \frac{1}{2}iH\Delta t}{1 + \frac{1}{2}iH\Delta t} \tag{A.4}$$

which is unitary, accurate to second-order in time $O(\Delta t^2)$. Thus the evolution is of the form,

$$\left(1 + \tfrac{1}{2}iH\Delta t\right)\psi^{t+\Delta t} = \left(1 - \tfrac{1}{2}iH\Delta t\right)\psi^t \ . \tag{A.5}$$

Replacing the second order derivative in the Hamiltonian operator with finite differences, one obtains,

$$\psi_j^{t+\Delta t} + \frac{i\Delta t}{2}\left(-\frac{\psi_{j+1}^{t+\Delta t} - 2\psi_j^{t+\Delta t} + \psi_{j-1}^{t+\Delta t}}{(\Delta z)^2} + U_j\psi_j^{t+\Delta t}\right) =$$
$$\psi_j^t - \frac{i\Delta t}{2}\left(-\frac{\psi_{j+1}^t - 2\psi_j^t + \psi_{j-1}^t}{(\Delta z)^2} + U_j\psi_j^t\right) \ , \tag{A.6}$$

where $U_j = V_j + g|\psi_j^t|^2$. The above equation can be represented by a matrix equation,

$$A \cdot \psi^{t+\Delta t} = B \cdot \psi^t \tag{A.7}$$

or more analytically,

$$\begin{pmatrix} \left[1 + \frac{i\Delta t}{(\Delta z)^2} + \frac{i\Delta t}{2}U\right] & -\frac{i\Delta t}{2(\Delta z)^2} & 0 & \cdots \\ -\frac{i\Delta t}{2(\Delta z)^2} & \ddots & \ddots & \\ 0 & \ddots & \ddots & \ddots \\ \vdots & & \ddots & \ddots \end{pmatrix} \cdot \begin{pmatrix} \vdots \\ \psi_{j-1}^{t+\Delta t} \\ \psi_j^{t+\Delta t} \\ \psi_{j+1}^{t+\Delta t} \\ \vdots \end{pmatrix} =$$

$$\begin{pmatrix} \left[1 - \frac{i\Delta t}{(\Delta z)^2} - \frac{i\Delta t}{2}U\right] & \frac{i\Delta t}{2(\Delta z)^2} & 0 & \cdots \\ \frac{i\Delta t}{2(\Delta z)^2} & \ddots & \ddots & \\ 0 & \ddots & \ddots & \ddots \\ \vdots & & \ddots & \ddots \end{pmatrix} \cdot \begin{pmatrix} \vdots \\ \psi_{j-1}^t \\ \psi_j^t \\ \psi_{j+1}^t \\ \vdots \end{pmatrix} . \qquad (A.8)$$

Thus the problem reduces solving a tridiagonal system, $A\psi^{t+\Delta t} = X$ where $X = B\psi^t$ using standard methods [96]. Note that the left hand side of Eq. (A.8) depends on the wavefunction at time $t + \Delta t$ whereas the right hand side depends on the previous time t. The wavefunction at the new time step is obtained using an iteration method.

The above method can be generalized to three dimensions. The Hamiltonian in cartesian coordinates has the form,

$$H = -\left(\frac{\partial^2}{2\partial x^2} - \frac{\partial^2}{2\partial y^2} - \frac{\partial^2}{2\partial z^2}\right) + V(x, y, z) + g\left|\psi(x, y, z, t)\right|^2 . \qquad (A.9)$$

The idea is to split the Hamiltonian into three one-dimensional operators H_x, H_y, H_z and divide each time step into three steps of size $\Delta t/3$. In each time step we solve for each dimension independently following the method described before for the one dimensional problem.

Finally the Crank-Nicholson method can be applied to find time-independent solutions by substituting $\Delta t \rightarrow -i\Delta t$ in the above equations. Propagating an initial wevefunction using negative imaginary time steps, the initial wavefunction relaxes after some time to the ground state solution.

A.2 Newton's method

Newton's method is used to find stationary solutions of Eq. (A.1) or generally to solve equations of the form

$$f(x) = 0 . \qquad (A.10)$$

For simplicity we consider first the case of a single equation and then generalize it to solve differential equations.

A.2.1 Single function

Let us suppose we are looking for solutions of the Eq. (A.10) on a given interval, then using Taylor's series expansion near x, the function is approximated by,

$$f(x + \delta x) \approx f(x) + f'(x)\delta x + O(\delta x^2) \ . \tag{A.11}$$

If we keep only the first order term, we are looking for small δx such as,

$$f(x + \delta x) = 0 \approx f(x) + f'(x)\delta x \ , \tag{A.12}$$

giving,

$$\delta x = -\frac{f(x)}{f'(x)} \quad \text{or} \quad x + \delta x = x - \frac{f(x)}{f'(x)} \ . \tag{A.13}$$

The Newton iteration is then given by the following procedure: start with an initial guess of the root z_0, evaluate the derivative $f'(x_0)$, extend the tangent line at a current point x_n until it crosses zero, and set the next guess x_{n+1} to the abscissa of that zero crossing, until find the limit of recurrence:

$$x_{n+1} = x_n - \frac{f(x_n)}{f'(x_n)} \ . \tag{A.14}$$

Fig. A.1 shows a geometrical interpretation of a single iteration of this formula. Unfortunately this iteration may not converge if for example the derivative is zero at the neighborhood of a root or the initial guess is so far from the true root, so as to let the search interval include a local extremum. To ensure convergence of the method, only a fraction of the calculated step (Eq. (A.13)) is taken to update the approximation of the root,

$$x_{n+1} = x_n + \lambda \, \delta x \ , \qquad 0 < \lambda \leq 1 \ . \tag{A.15}$$

Close to a root $\lambda \sim 1$ whereas far from the root i.e. first steps, $\lambda \sim 0.1$.
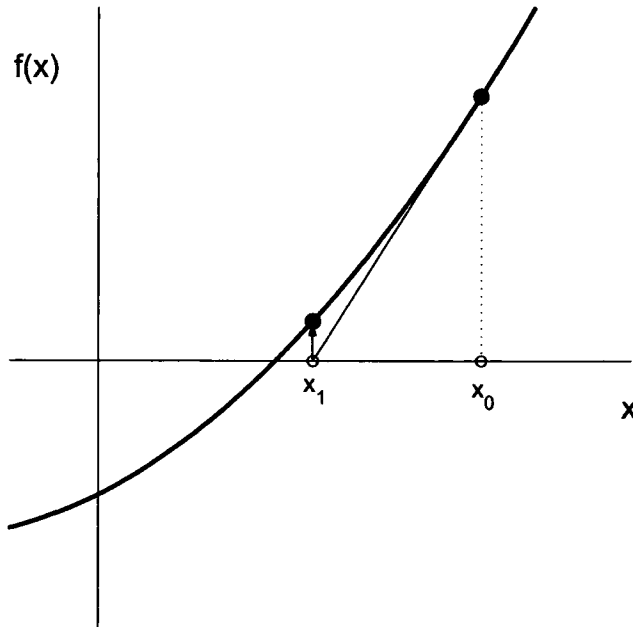
Figure A.1: Newton's method for finding root of an one dimensional function: start with an initial guess for the root at x_0 calculate the derivative at that point to find the next guess of the root.

A.2.2   Newton's method for systems of equations

Newton's method may also be used to find a root of a system of N-dimensions,

$$F(x) = 0 \ , \tag{A.16}$$

where $\mathbf{F}$ and $\mathbf{x}$ are vectors of N functions f_i and variables x_i where $i = 1, ..N$, written explicitly,

$$\mathbf{F} = \begin{pmatrix} f_1(x_1, ..., x_N) \\ \vdots \\ f_N(x_1, ..., x_N) \end{pmatrix} = 0 \ . \tag{A.17}$$

In the neighborhood of $\mathbf{x}$, each function f_i can be approximated by first order Taylor series,

$$f_i(x + \delta x) \approx f_i(x) + \sum_{j=1}^{N} \frac{\partial f_i}{\partial x_j} \delta x_j = 0 \ , \tag{A.18}$$

where the partial derivatives appearing in the equation are the elements of the Jacobian $(N \times N)$ matrix given by,

$$J_{ij} = \frac{\partial f_i}{\partial x_j} \; . \tag{A.19}$$

For each Newton step, the Jacobian $(N \times N)$ matrix has to be inverted. However the sparseness of the Jacobian matrix allows the computational scale within a reasonable time. The inversion is performed using the bi-conjugate gradient method [96]. This method is based on minimising the function,

$$g(\boldsymbol{x}) = \frac{1}{2}\Delta\boldsymbol{x}^T \cdot J \cdot \Delta\boldsymbol{x} + \boldsymbol{f} \cdot \Delta\boldsymbol{x} \; , \tag{A.20}$$

which requires that its gradient is zero, i.e.,

$$\nabla g = J \cdot \Delta\boldsymbol{x} - \boldsymbol{f} = 0 \tag{A.21}$$

which is equivalent to solving (A.18). The minimisation is performed by creating a succession of linearly independent search directions and improved minimizers. After N iterations, the algorithm converges at the solution of Eq. (A.21). The attractiveness of this method is that it references the Jacobian only through its multiplication of a vector or the multiplication of its transpose and a vector, and can be very efficient for a properly stored sparse matrix.

Let us consider for illustration a set of two functions,

$$f(x,y) \;\; = \;\; 0 \tag{A.22}$$

$$g(x,y) \;\; = \;\; 0 \; . \tag{A.23}$$

Using Taylor's expansion of the two functions near (x,y), at first order, we are looking for a couple $(\delta x, \delta y)$ such as,

$$f(x+\delta x, y+\delta y) = 0 \;\; \approx \;\; f(x,y) + \delta x \frac{\partial f}{\partial x} + \delta y \frac{\partial f}{\partial y} \tag{A.24}$$

$$g(x+\delta x, y+\delta y) = 0 \;\; \approx \;\; g(x,y) + \delta x \frac{\partial g}{\partial x} + \delta y \frac{\partial g}{\partial y} \; . \tag{A.25}$$

The previous system can be written in a matrix form,

$$
\begin{pmatrix} \frac{\partial f}{\partial x} & \frac{\partial f}{\partial y} \\ \frac{\partial g}{\partial x} & \frac{\partial g}{\partial x} \end{pmatrix} \cdot \begin{pmatrix} \delta x \\ \delta y \end{pmatrix} = - \begin{pmatrix} f(x,y) \\ g(x,y) \end{pmatrix} \tag{A.26}
$$

or equivalently

$$
J(x,y) \cdot \delta \mathbf{x} = -\mathbf{F}(x,y) \ , \tag{A.27}
$$

where $J(x,y)$ is the (2×2) Jacobian matrix. The analogue of the iteration process Eq. (A.14) is,

$$
\begin{pmatrix} x_{n+1} \\ y_{n+1} \end{pmatrix} = \begin{pmatrix} x_n \\ t_n \end{pmatrix} - J^{-1}(x_n, y_n) \cdot \begin{pmatrix} f(x_n, y_n) \\ g(x_n, y_n) \end{pmatrix} \ . \tag{A.28}
$$

Starting with an initial guess (x_0, y_0), this process converges to a root of the system provided a good initial guess. For each Newton step, the Jacobian $J(x,y)$ has to be inverted.

A.2.3 Newton's method for the GPE

One dimension

Stationary solutions of Eq. (A.1) can be obtained by substituting $\psi(z,t) = e^{-i\mu t}\Psi(z)$,

$$
\mu\Psi(z) = \left(-\frac{\partial^2}{2\partial z^2} + V(z) + g\left|\Psi(z)\right|^2 \right) \Psi(z) \ , \quad \text{or} \tag{A.29}
$$

$$
\left(-\frac{\partial^2}{2\partial z^2} + V(z) + g\left|\Psi(z)\right|^2 - \mu \right) \Psi(z) = 0 \ . \tag{A.30}
$$

We note the above equation is of the form $\mathbf{F}(x) = 0$, where $x = (\Psi, \mu)$ with Ψ a time-independent wavefunction normalised to unity and μ is the chemical potential. Using finite differences Eq. (A.30) can be written in an explicit form,

$$
\begin{array}{ll} i \neq N & f_i = \left(\frac{1}{\Delta z^2} + V(z) + g|\Psi|^2 \right) \Psi_i - \frac{1}{\Delta z^2}\Psi_{i+1} - \frac{1}{\Delta z^2}\Psi_{i-1} - \mu\Psi_i \\ i = N & f_N = \left(\Psi_1^2 + \Psi_2^2 + \ldots + \Psi_{N-1}^2 \right) dz - 1 \end{array} \tag{A.31}
$$

The Jacobian J_{ij} has the form,

$$
J(\Psi, \mu) = \begin{pmatrix}
\left[\frac{1}{\Delta z^2} + V(z) + 3g|\Psi|^2 - \mu\right] & -\frac{1}{\Delta z^2} & 0 & \cdots & -\Psi_1 \\
-\frac{1}{\Delta z^2} & \ddots & \ddots & \ddots & -\Psi_2 \\
0 & \ddots & \ddots & \ddots & \vdots \\
\vdots & \ddots & \ddots & \ddots & -\Psi_{N-1} \\
2\Psi_1 dz & 2\Psi_2 dz & \cdots & 2\Psi_{N-1}dz & 0
\end{pmatrix} \quad \text{(A.32)}
$$

whereas $\delta x = (\delta\Psi_1, \delta\Psi_2, \cdots, \delta\Psi_{N-1}, \delta\mu)^T$. Thus the solution is found using equation,

$$
f_i(\Psi_n) + \sum_j \left(\frac{\partial f_i}{\partial \Psi_j}_n (\Psi_{n+1}) - \Psi_n \right) = 0 \quad \text{(A.33)}
$$

and following the method described in previous sections.

Three dimensions

The time-independent three dimensional GPE has the form,

$$
\left(-\frac{\partial^2}{2\partial x^2} - \frac{\partial^2}{2\partial y^2} - \frac{\partial^2}{2\partial z^2} + V(x, y, z) + g_{3D}|\Psi(x, y, z)|^2 - \mu \right) \Psi(x, x, y) = 0 \text{ ,(A.34)}
$$

where μ, g_{3D} and $\Psi(x, y, z)$ are the three dimensional chemical potential, nonlinearity and wavefunction. As in the one dimensional case, the wavefunction is normalised to unity however in three dimensions, we separate the wavefunction into real and imaginary parts, defining, Ψ_{ijkr} where $r = 0, 1$ such that, $\Psi_{ijk0} = \text{Re}(\Psi(x_i, y_j, z_k))$ and $\Psi_{ijk1} = \text{Im}(\Psi(x_i, y_j, z_k))$. Discretising Eq. (A.34) on a three dimensional grid, yields,

$$
\begin{aligned}
f_{ijkr} \equiv \quad & - \left(\Psi_{i-1,j,k,r} - 2\Psi_{i,j,k,r} + \Psi_{i+1,j,k,r}\right)/2\Delta x^2 \\
& - \left(\Psi_{i,j-1,k,r} - 2\Psi_{i,j,k,r} + \Psi_{i,j+1,k,r}\right)/2\Delta y^2 \\
& - \left(\Psi_{i,j,k-1,r} - 2\Psi_{i,j,k,r} + \Psi_{i,j,k+1,r}\right)/2\Delta z^2 \\
& + \left(V_{i,j,k} + \Psi_{i,j,k,r}^2 + \Psi_{i,j,k,1-r}^2 - \mu\right)\Psi_{i,j,k,r} = 0 \text{ ,}
\end{aligned}
$$

where $\Delta x, \Delta y$ and Δz are the grid spacings in the x, y and z-directions respectively. The Jacobian has the same form as in the one dimensional case, however, there are more elements arising from the real and imaginary parts of $\Psi_{i,j,k,r}$ and new derivatives, for example $J_{i-1,j}^{1-r} = \partial f_{ijkr}/\partial \Psi_{i-1,j}^{1-r}$ and $J_{i+1,j}^{1-r} = \partial f_{ijkr}/\partial \Psi_{i+1,j}^{1-r}$. We solve the three dimensional problem following the steps described in the one dimensional case.

Appendix B

Analytic proof for the equation for the one dimensional energy functional

In this Appendix, we discuss in more details the derivation of the one dimensional energy functional. We start from the full three dimensional energy functional given by,

$$E_{3D}[\psi] = \int d\mathbf{r} \left[\tfrac{1}{2} |\nabla \psi|^2 + V_{ho} |\psi|^2 + \tfrac{1}{2} g_{3D} |\psi|^4 \right] , \tag{B.1}$$

with a harmonic trap,

$$V_{ho} = \frac{1}{2} \left(x^2 + y^2 + \lambda^2 z^2 \right) . \tag{B.2}$$

The total wavefunction is of the form

$$\psi(x, y, z, t) = \phi(x, y) \Phi(z, t) . \tag{B.3}$$

In Section 2.4 we saw that for weakly interacting condensates we assume a Gaussian ansazt for the $\phi(x, y)$ wavefunction,

$$\phi(x, y) = \frac{1}{\sqrt{\pi}} \exp[-(x^2 + y^2)/2] . \tag{B.4}$$

We substitute the above expression for the two dimensional wavefunction $\phi(x, y)$ in the expression for the total wavefunction Eq. (B.3) and we perform the integration in Eq. (B.1). We show the results for each term separately:

- The kinetic energy term

$$E_{\text{kin}} = \int \mathrm{dr} \frac{1}{2} |\nabla \psi|^2 = \frac{1}{2} \int \mathrm{d}z |\nabla \Phi|^2 + \frac{1}{2} \int \mathrm{d}z |\Phi|^2 , \qquad (B.5)$$

- the potential energy term,

$$E_{\text{pot}} = \int \mathrm{dr} V_{\text{ho}} |\psi|^2 = \frac{1}{2} \lambda^2 \int \mathrm{d}z (z^2 |\Phi|^2) + \frac{1}{2} \int \mathrm{d}z |\Phi|^2 , \qquad (B.6)$$

- and finally the mean-field interaction energy term,

$$E_{\text{int}} = \int \mathrm{dr} \frac{1}{2} g_{\text{3D}} |\psi|^4 = \frac{g_{\text{3D}}}{4\pi} \int \mathrm{d}z |\Phi|^4 . \qquad (B.7)$$

Adding all the above terms we find the equation of the one dimensional energy functional,

$$E_{\text{1D}}[\Phi] = \int \mathrm{d}z \left[\frac{1}{2} |\nabla \Phi|^2 + (V(z) + 1)|\Phi|^2 + \frac{1}{2} g_{1D} |\Phi|^4 \right] , \qquad (B.8)$$

where

$$g_{1D} = \frac{g_{\text{3D}}}{2\pi} \qquad (B.9)$$

and

$$V(z) = \frac{1}{2} \lambda^2 z^2 , \qquad (B.10)$$

since we have assumed a trap potential of the form Eq. (B.2). The constant 1 represents the energy of the transverse modes and comes from summing two one-halves from the kinetic and potential energy terms respectively. We drop this term since it is a constant energy shift and we derive the most common form of the one-dimensional energy functional,

$$E_{\text{1D}}[\psi] = \int \mathrm{d}z \left[\frac{1}{2} |\nabla \psi|^2 + V(z)|\psi|^2 + \frac{1}{2} g_{1D} |\psi|^4 \right] . \qquad (B.11)$$

Appendix C

Stability of a dilute BEC with attractive interactions

We review a variational method based on Gaussian trial functions to study the stability of a dilute Bose-Einstein condensate with attractive interactions in both one and three dimensions. We show that a one dimensional BEC is always stable in contrast to the three dimensional case.

C.1 Stability of a dilute BEC in one dimension

Let us first consider the case of N bosons confined in one dimensional harmonic potential,

$$V_{\text{trap}}(z) = \frac{1}{2}z^2 . \tag{C.1}$$

We assume that the interparticle interactions are attractive ($g_{1\text{D}} < 0$) where $g_{1\text{D}} = g_{3\text{D}}/2\pi$ is the one dimensional self-interaction parameter. The explicit form of the ground-state wavefunction is obtained by minimising the one dimensional energy functional (see Appendix B for derivation),

$$E[\Psi] = \langle H \rangle = \int dz \left[\frac{1}{2}|\nabla \psi(z)|^2 + V_{\text{trap}}(z)|\Psi(z)|^2 + \frac{1}{2}g_{1\text{D}}|\Psi(z)|^4 \right] \tag{C.2}$$

where $\Psi(z)$ is the one dimensional condensate wavefunction normalised to unity. We consider a trial wavefunction of the form,

$$\Psi(z,b) = \left(b^2/\pi\right)^{1/4} \exp(-b^2 z^2/2) \ ,$$ (C.3)

where b is a dimensionless variational parameter. Substituting into Eq. (C.2) yields,

$$E[b] = \frac{1}{4}b^2 + \frac{1}{4b^2} - \frac{|g_{1D}|b}{2\sqrt{2\pi}} \ .$$ (C.4)

This energy is plotted in Fig. C.1 as a function of the parameter b, for different values of the dimensionless constant $|g_{1D}| > 0$. We observe that we can always find a minimum and thus the condensate is always stable in one dimension. We can also prove the stability from the form of Eq. (C.4). For large values of b the term $b^2/4$ dominates whereas for small values of b the term $1/4b^2$ dominates thus we can always find a minimum of Eq. (C.4).
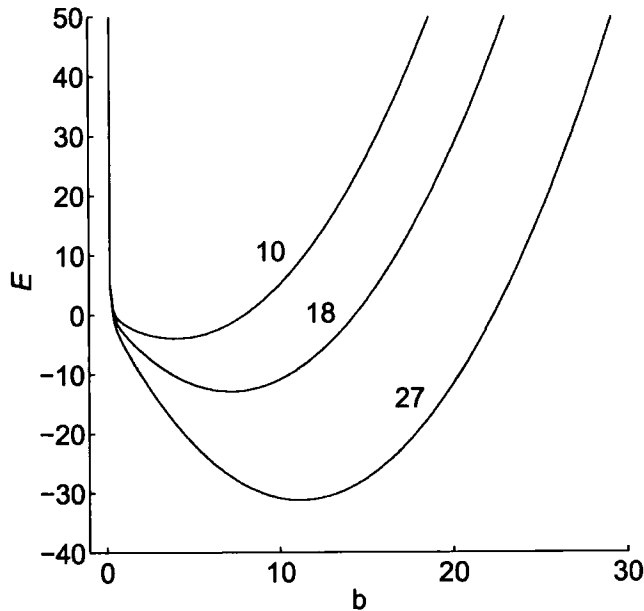

Figure C.1: Energy for bosons interacting with attractive forces, as a function of the condensate size b for different values of $|g_{1D}| = 10, 18, 27$. The energy functional has always minima and the condensate is always stable in one dimension.

C.2 Stability of a dilute BEC in three dimensions

We generalise the above results for atoms interacting with attractive forces, $g_{3D} < 0$, in three dimensions. We can find the ground state energy by minimising the energy functional,

$$
\begin{aligned}
E[b] = \langle H \rangle &= \int d\mathbf{r} \left[\frac{1}{2} |\nabla \Psi(\mathbf{r})|^2 + V_{\text{trap}}(\mathbf{r}) |\Psi(\mathbf{r})|^2 + \frac{1}{2} g_{3D} |\Psi(\mathbf{r})|^4 \right] \\
&= E_{\text{kin}} + E_{\text{pot}} + E_{\text{int}} ,
\end{aligned}
\tag{C.5}
$$

where E_{kin} is the kinetic, E_{pot} is the potential, E_{int} is the interaction energy and $g_{3D} = 4\pi \mathcal{N} a / a_\perp$ is the three dimensional nonlinear parameter. We begin by studying the simplest case of a spherical trap and then we extend our study for an axially symmetric trap.

C.2.1 Spherical trap

We consider an isotropic three-dimensional harmonic potential,

$$
V_{\text{trap}}(\mathbf{r}) = \frac{1}{2} r^2 ,
\tag{C.6}
$$

and a Gaussian trial function of the form (normalised to unity),

$$
\Psi(r, b) = \sqrt{b^3 / \pi^{3/2}} \exp(-b^2 r^2 / 2) ,
\tag{C.7}
$$

where b is a dimensionless variational parameter. Substitution into Eq. (C.5) yields an expression for the total energy,

$$
E[b] = \frac{3}{4} \left(b^2 + \frac{1}{b^2} \right) - \frac{|g_{3D}| b^3}{4\sqrt{2\pi^3}} .
\tag{C.8}
$$

In Fig. C.2 we plot equation Eq. (C.8) for different values values of g_{3D}, as a function of the Gaussian width b. For a metastable condensate to exist, the energy functional $E[b]$ must have a local minimum which is determined by the condition that the first

derivative must be zero. We observe that there is a critical value of g_{3D} beyond which the local minima disappear and the condensate becomes unstable, collapsing into a dense state. This critical value can be obtained by requiring that the first and second derivative of Eq. (C.8) must be zero at that critical point b_c. For a spherical trap, this happens at $b_c = 5^{1/4}$ and $g_{3D}^{cr} = -8\sqrt{2\pi^3}/5^{5/4} \simeq -8.45$ which is in agreement with previous results [1, 75]. Taking values from ^{7}Li experiment, [128], the variational method predicts a maximum condensate number $\mathcal{N} \approx 1460$. This result is somewhat larger to the value $g_{3D}^{cr} = -7.3$, or equivalently $\mathcal{N} = 1250$ obtained by solving numerically the GPE (2.27) for $g_{3D} < 0$ and using a spherical potential, Eq. (C.6). In the next Section we give more details on the comparison between the variational method and the exact solutions of the GPE.
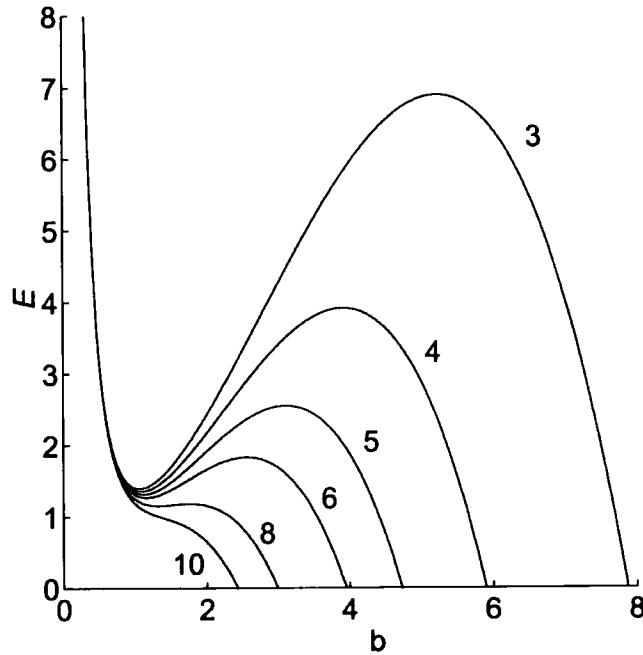

Figure C.2: Ground state energy, E (Eq. (C.8)) as a function of the variational parameter b for various values of the nonlinearity $|g_{3D}| = 3, 4, 5, 6, 8, 10$. At $|g_{3D}^{cr}| = 8.5$ the local minima disappear and the condensate collapses for $|g_{3D}| > |g_{3D}^{cr}|$.

C.2.2 Axially symmetric trap

We extend the variational method to an axially symmetric trap of the form,

$$V_{\text{trap}}(r) = \frac{1}{2}\left(r^2 + \lambda^2 z^2\right) . \tag{C.9}$$

In this case, the Gaussian trial wave function (normalised to unity) has the form,

$$\Psi(r, b_\perp, b_\parallel) = \sqrt{\frac{1}{\pi^{3/2} b_\perp^2 b_\parallel}} \exp\left(-\frac{r^2}{2b_\perp^2} - \frac{z^2}{2b_\parallel^2}\right) . \tag{C.10}$$

In this section we reproduce the calculations in [76]. However we are working in h.o.u. which are defined in section 2.2, and for comparison with reference [76] we convert our final equations in h.o.u. which are set by two harmonic oscillators lengths: $b_{\perp 0} = \sqrt{\hbar/m\omega_\perp}$ in the transverse direction(s) and $b_{\parallel 0} = \sqrt{\hbar/m\omega_\parallel}$ in the z-direction. We begin by calculating each term in the three dimensional energy functional Eq. (C.5), using the trial function Eq. (C.10). This yields:

$$\langle E_{\text{kin}} \rangle = \int dr \frac{1}{2} |\nabla\Psi|^2 = \frac{1}{2b_\perp^2} + \frac{1}{4b_\parallel^2} , \tag{C.11}$$

$$\langle E_{\text{pot}} \rangle = \int dr \frac{1}{2}\left(r^2 + \lambda^2 z^2\right) |\Psi|^2 = \frac{b_\perp^2}{2} + \frac{\lambda^2}{4} b_\parallel^2 \tag{C.12}$$

and

$$\langle E_{\text{int}} \rangle = \frac{g_{3D}}{4} \int dr |\Psi|^4 = \frac{1}{4} \frac{g_{3D}}{\sqrt{2\pi^3}} \frac{1}{b_\perp^2 b_\parallel} . \tag{C.13}$$

Thus the three dimensional energy functional is given by

$$E[b_\perp, b_\parallel] = \frac{1}{2b_\perp^2} + \frac{1}{4b_\parallel^2} + \frac{b_\perp^2}{2} + \frac{\lambda^2}{4} b_\parallel^2 - \frac{1}{4} \frac{|g_{3D}|}{\sqrt{2\pi^3}} \frac{1}{b_\perp^2 b_\parallel} \tag{C.14}$$

and it depends on the variational parameters $b_\perp$ and $b_\parallel$ and the nonlinearity. In Fig. C.3 we plot the above expression for the energy as a function of the variational
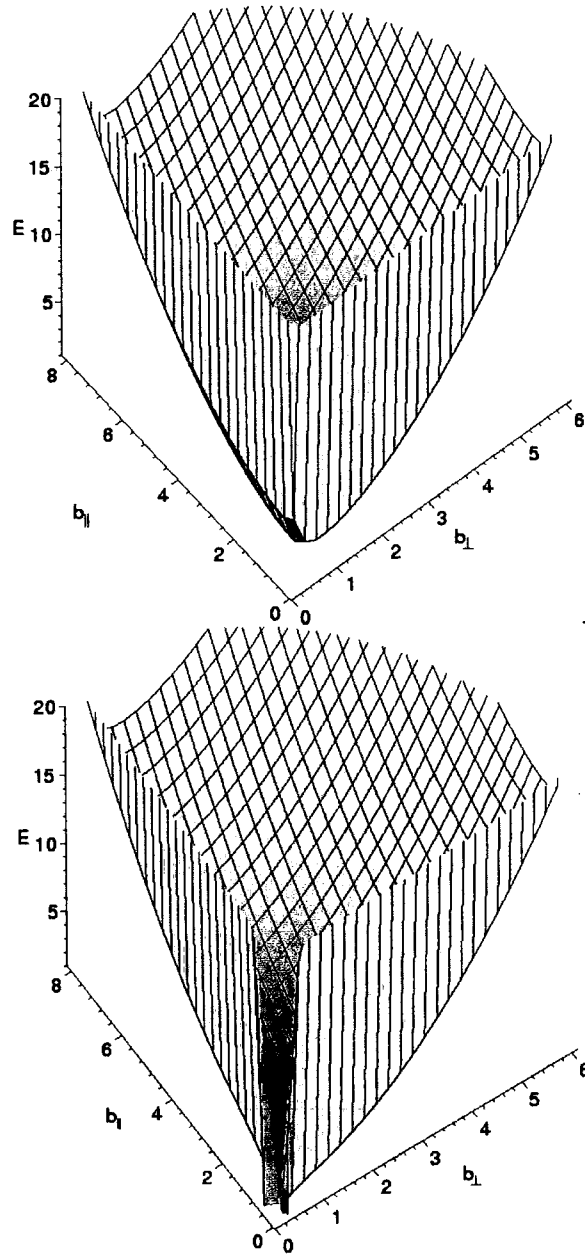
Figure C.3: Ground state energy E as a function of the variational parameters $b_\perp$ and $b_\parallel$ for two values of the nonlinearity $|g_{3D}| =: 4$ (top) and 8.5 (bottom). We note that there is a critical value $|g_{3D}^{cr}|$ for which the energy has no longer minima and the condensate collapses.

parameters, for two values of the nonlinearity $|g_{3D}|$. We observe that the energy functional has minima, however increasing $|g_{3D}|$, there is a critical value $|g_{3D}^{cr}|$ that the energy functional has no minima thus the condensate collapses. In order to study the collapse, we define a new dimensionless parameter

$$\Gamma = \frac{1}{4}\frac{|g_{3D}|}{\sqrt{2\pi^3}} = \frac{k\lambda^{-1/6}}{\sqrt{2\pi}} \tag{C.15}$$

where k is defined by (see also Chapter 7),

$$\frac{N|a|}{b_0} = k , \tag{C.16}$$

where $b_0 = (b_{\perp o} b_{\parallel o})^{1/3} = b_{\perp o}\lambda^{-1/3}$ and we minimize the energy functional Eq. (C.14) with respect to each of the variational parameters,

$$\frac{\partial E}{\partial b_\perp} = 0 \tag{C.17}$$

$$\frac{\partial E}{\partial b_\parallel} = 0, \tag{C.18}$$

yielding the following sets of equations,

$$b_\parallel = \frac{2\Gamma}{1 - b_\perp^4} \tag{C.19}$$

and

$$b_\perp^2 = \frac{2\Gamma b_\parallel}{1 - \lambda^2 b_\parallel^4} . \tag{C.20}$$

The solutions of the above equations give the points of possible maxima, minima or saddle points. The condition for a stable condensate to exist is that the energy functional $E[b_\perp, b_\parallel]$, always has minima, which means that at the local minimum the curvature is positive, that is,

$$D \equiv \frac{\partial^2 E}{\partial b_\perp^2}\frac{\partial^2 E}{\partial b_\parallel^2} - \left(\frac{\partial^2 E}{\partial b_\perp \partial b_\parallel}\right)^2 > 0 . \tag{C.21}$$

Calculating the partial derivatives we obtain,

$$\frac{\partial^2 E}{\partial b_\perp^2} = 4 > 0, \tag{C.22}$$

$$\frac{\partial^2 E}{\partial b_\parallel^2} = \frac{1}{2}(3\lambda^2 + \frac{1}{b_\parallel^4}) > 0 \tag{C.23}$$

and

$$\frac{\partial^2 E}{\partial b_\perp \partial b_\parallel} = -\frac{2\Gamma}{b_\parallel^2}\left(\frac{1 - \lambda^2 b_\parallel^4}{2\Gamma b_\parallel}\right)^{3/2} < 0 \,. \tag{C.24}$$

There must be a critical value of $\Gamma = \Gamma_c$ which the condition Eq. (C.21) is zero and for $\Gamma > \Gamma_c \to D < 0$ which means that the local minimum becomes a saddle point and the condensate collapses. This value is given by,

$$\Gamma_c = \frac{(1 - \lambda^2 b_{\parallel c}^4)^3}{4(3\lambda^2 b_{\parallel c}^4 + 1)b_{\parallel c}^3} \tag{C.25}$$

whereas substituting Eq. (C.25) into Eq. (C.20) we find,

$$b_{\perp c} = \frac{1 - \lambda^2 b_{\parallel c}^4}{\sqrt{2(3\lambda^2 b_{\parallel c}^4 + 1)b_{\parallel c}^2}} \,. \tag{C.26}$$

Substituting Eqs. (C.26) and (C.25) into Eq. (C.19) we obtain,

$$4(3\lambda^2 b_{\parallel c}^4 + 1)^2 b_{\parallel c}^4 = (1 - \lambda^2 b_{\parallel c}^4)^3(5\lambda^2 b_{\parallel c}^4 + 3) \,. \tag{C.27}$$

For a given asymmetry parameter λ, a real positive root of Eq. (C.27) gives $b_{\parallel c}$ and the corresponding values of Γ_c and $b_{\perp c}$. In order to compare the present equations with the corresponding ones in [76] we have to transform the characteristic parameters such as the variational parameters and the nonlinear coefficient in the units used in [76]. Thus by making the substitutions $r_{\parallel c} = b_{\parallel c}\lambda^{1/2}$ and $\gamma_c = \Gamma_c 4\lambda^{1/6}$ we

obtain the same equations as the ones in [76]. For example Eqs. (C.25), (C.26) and (C.27) become,

$$\gamma_c = \frac{4r_{\|c}(3r_{\|c}^4 + 1)}{\lambda^{1/3}(5r_{\|c}^4 + 3)} ,$$

(C.28)

$$b_{\perp c} = \frac{\lambda^{1/2}(1 - r_{\|c}^4)}{\sqrt{2r_{\|c}^2(1 + 3r_{\|c}^4)}}$$

(C.29)

and

$$\lambda^2 = \frac{4(3r_{\|c}^4 + 1)^2 r_{\|c}^4}{(1 - r_{\|c}^4)^3(5r_{\|c}^4 + 3)} .$$

(C.30)

In Fig. C.4 we plot the critical parameter γ_c as a function of the asymmetry parameter $\lambda = \omega_\| / \omega_\perp$.
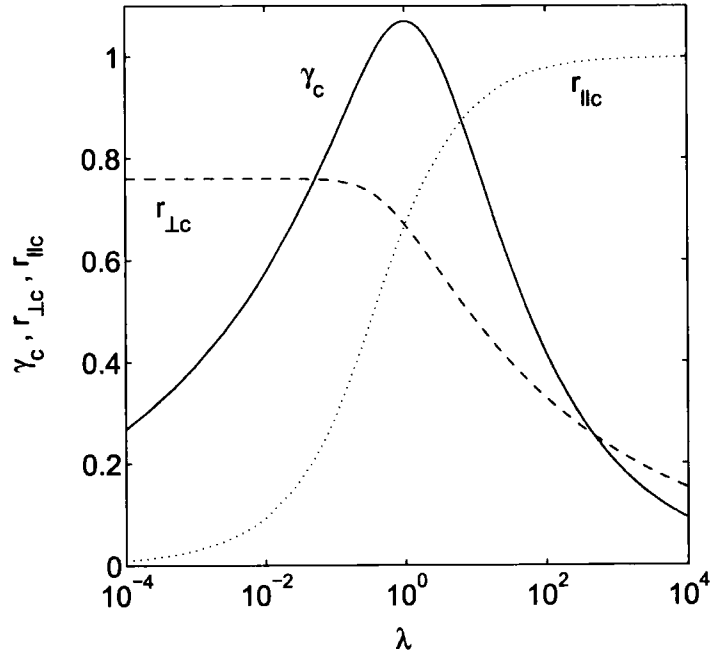
Figure C.4: Critical values of the nonlinear parameter γ_c (solid) and the lengths $r_{\|c}$ (dotted) and $r_{\perp c}$ (dashed lines) as a function of the asymmetry parameter λ (in units $\hbar\omega$) for bosons interacting with attractive forces in units defined by the two harmonic oscillator lengths $b_{\|0}$ and $b_{\perp 0}$. Those results are also presented in [76].

We note that the peak value is $\gamma_c = 1.07$ in agreement with [76] or the equivalent value $|g_{3D}| = 8.45$ obtained from previous derivation in subsection C.2.1. We also observe that the maximum value of γ_c is obtained for $\lambda = 1$ thus the optimum geometry for confining a BEC with attractive interactions is a spherical trap.

In Fig. C.5 we plot the parameter k_c, defined in Chapter 7 as a function of λ obtained by the variational method (solid line) presented here and by numerical solution of the GPE (2.27) (dashed line) presented in Chapter 7. Since the variational method gives an upper bound on the energy, the variational results are shifted compared to the exact values found numerically in Chapter 7.
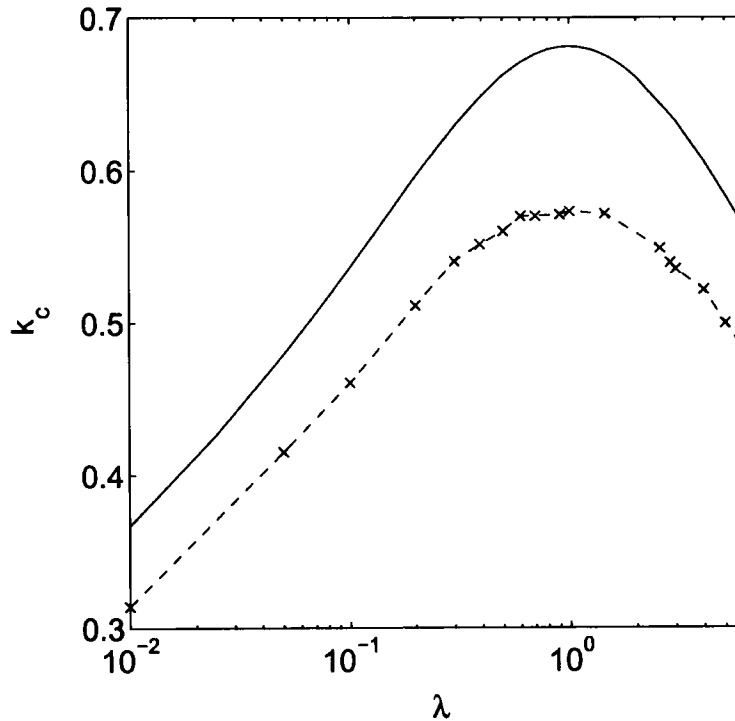
Figure C.5: Comparison of the critical parameter k_c defined in Eq. (C.16) as a function of the asymmetry parameter λ obtained by the variational method (solid line) presented in subsection C.2.2 and by numerical solution of the GPE (2.27) (dashed line) presented in Chapter 7.

Bibliography

[1] F. Dalfovo, S. Giorgini, L. P. Pitaevskii, and S. Stringari, *Theory of Bose-Einstein condensation in trapped gases*, Rev. Mod. Phys. **71**, 463 (1999).

[2] A. J. Leggett, *Bose-Einstein condensation in the alkali gases: Some fundamental concepts*, Rev. Mod. Phys. **73**, 307 (2001).

[3] D. S. Durfee and W. Ketterle, *Experimental studies of Bose-Einstein condensation*, Optics Express **2**, 299 (1998).

[4] J.R. Anglin and W. Ketterle, *Bose-Einstein condensation of atomic gases*, Nature **416**, 211 (2002).

[5] K. Huang, *Statistical Mechanics, 2nd Edition* (John Wiley and Sons, New York, 1987).

[6] C. C. Tannoudji, B. Diu, and F. Laloe, *Quantum Mechanics, 2nd Edition* (Hermann and John Wiley and Sons, Paris, 1997).

[7] F. London, *The λ- Phenomenon of Liquid Helium and the Bose-Einstein Degeneracy*, Nature **141**, 643 (1938).

[8] M. Y. Shen, T.Yokouchi, S. Koyama, and T. Goto, *Dynamics associated with Bose-Einstein statistics of orthoexcitons generated by resonant excitations in cuprous oxide*, Phys. Rev. B **56**, 13066 (1997).

[9] J. L. Lin and J. P. Wolfe, *Bose-Einstein condensation of paraexcitons in stressed Cu2O*, Phys. Rev. Lett. **71**, 1222 (1993).

[10] A. B. Migdal, , Nucl. Phys. **13**, 665 (1959);M. Hoffberg, A. E. Glassgold, R. W. Richardson, and M. Ruderman, *Anisotropic Superfluidity in Neutron Star Matter*, Phys. Rev. Lett. **24**, 775 (1970).

[11] J. Bardeen, L. N. Cooper, and J. R. Schrieffer, *Theory of Superconductivity*, Phys. Rev. **106**, 489 (1957).

[12] P. W. Anderson and P. Morel, *Generalized Bardeen-Cooper-Schrieffer States and the Proposed Low-Temperature Phase of Liquid ^3He*, Phys. Rev. **123**, 1911 (1961);R. Balian and N. R. Werthamer,*Superconductivity with Pairs in a Relative p Wave*, Phys. Rev. **131**, 1553 (1963);P. W. Anderson and W. F. Brinkman, *Anisotropic Superfluidity in 3He: A Possible Interpretation of Its Stability as a Spin-Fluctuation Effect*, Phys. Rev. Lett. **30**, 1108 (1973).

[13] M. H. Anderson, J. R. Ensher, M. R. Matthews, C. E. Wieman and E. A. Cornell, *Observation of Bose-Einstein Condensation in a Dilute Atomic Vapor*, Science **269**, 198 (1995).

[14] K. B. Davis, M.-O. Mewes, M. R. Anderson, N. J. van Druten, D. S. Durfee, D. M. Kurn, and W. Ketterle, *Bose-Einstein Condensation in a Gas of Sodium Atoms*, Phys. Rev. Lett. **75**, 3969 (1995).

[15] C. C. Bradley, C. A. Sackett, J.J. Tollett and R. G. Hulet, *Evidence of Bose-Einstein Condensation in an Atomic Gas with Attractive Interactions*, Phys. Rev. Lett. **75**, 1687 (1995).

[16] D. G. Fried, T. C. Killian, L. Willmann, D. Landhuis, S. C. Moss, D. Kleppner, and T. J. Greytak, *Bose-Einstein Condensation of Atomic Hydrogen*, Phys. Rev. Lett. **81**, 3811 (1998).

[17] S. L. Cornish, N. R. Claussen, J. L. Roberts, E. A. Cornell and C. E. Wieman, *Stable ^{85}Rb Bose-Einstein Condensates with Widely Tunable Interactions*, Phys. Rev. Lett. **85**, 1795 (2000).

[18] A. Robert, O. Sirjean, A. Browaeys, J. Poupard, S. Nowak, D. Boiron, C. I. Westbrook, A. Aspect, *A Bose-Einstein Condensate of Metastable Atoms*, Science **292**, 461 (2001).

[19] F. P. Dos Santos, J. Léonard, J. Wang, C. J. Barrelet, F. Perales, E. Rasel, C. S. Unnikrishnan, M. Leduc, and C. Cohen-Tannoudji, Bose-Einstein Condensation of Metastable Helium, Phys. Rev. Lett. **86**, 3459 (2001).

[20] G. Modugno, G. Ferrari, G. Roati, R. J. Brecha, A. Simoni, and M. Inguscio, *Bose-Einstein Conensation of Potassium Atoms by Sympathetic Cooling*, Science **294**, 1320 (2001).

[21] T. Weber, J. Herbig, M. Mark, H.-C. Nagerl, and R. Grimm, *Bose-Einstein Condensation of Cesium*, Science **299**, 232 (2003).

[22] T. Yosuke, K. Maki, K. Komori, T. Takano, K. Honda, M. Kumakura, T. Yabuzaki and Y. Takahashi, *Spin-Singlet Bose-Einstein Condensation of Two-Electron Atoms*, Phys. Rev. Lett. **91**, 040404 (2003).

[23] E. Tiesinga, B. J. Verhaar, and H. T. C. Stoof, *Threshold and resonance phenomena in ultracold ground-state collisions*, Phys. Rev. A **47**, 4114 (1993).

[24] S. Inouye, M. R. Andrews, J. Stenger, H.-J. Miesner, D. M. Stamper-Kurn and W. Ketterle, *Osbervation of Feshbach resonances in a Bose-Einstein condensate*, Nature **392**, 151 (1998).

[25] P. Courteille, R. S. Freeland, D. J. Heinzen, F. A. van Abeelen, and B. J. Verhaar, *Osbervation of a Feshbach Resonance in Cold Atom Scattering*, Phys. Rev. Lett. **81**, 69 (1998).

[26] S. Jochim, M. Bartenstein, A. Altmeyer, G. Hendl, S. Riedl, C. Chin, J. H. Denschlag, and R. Grimm, *Bose-Einstein Condensation of Molecules*, Science **302**, 2101 (2003).

[27] M. W. Zwierlein, C. A. Stan, C. H. Schunck, S. M. F. Raupach, S. Gupta, Z. Hadzibabic, and W. Ketterle, *Observation of Bose-Einstein Condensation of Molecules*, Phys. Rev. Lett. **91**, 250401 (2003).

[28] M. Greiner, C. A. Regal, and D. S. Jin, *Emergence of a molecular Bose-Einstein condensate from a Fermi gas*, Nature **426**, 537 (2003).

[29] A. E. Leanhardt, T. A. Pasquini, M. Saba, A. Schirotzek, Y. Shin, D. Kielpinski, D. E. Pritchard, and W. Ketterle, *Adiabatic and Evaporative Cooling of Bose-Einstein condensates below 500 Picokelvin*, Science **301**, 1513 (2003).

[30] B. D. Josephson, *Possible new effects in superconductive tunnelling*, Phys. Rev. Lett. **1**, 251 (1962).

[31] A. Barone and G. Paterno, *Physics and Applications of the Josephson Effect*, (Wiley, New York, 1982).

[32] M. R. Andrews, C. G. Townsend, H. J. Miesner, D. S. Durfee, D. M. Kurn and W. Ketterle, *Observation of Interference Between Two Bose Condensates*, Science **275**, 637 (1997).

[33] D. S. Hall, M. R. Matthews, J. R. Ensher, C. E. Wieman, and E. A. Cornell, *Dynamics of Component Separation in a Binary Mixture of Bose-Einstein Condensates*, Phys. Rev. Lett. **81**, 1539 (1998);D. S. Hall, M. R. Matthews, C. E. Wieman, and E. A. Cornell, *Measurements of Relative Phase in Two-Component Bose-Einstein Condensates*, Phys. Rev. Lett. **81**, 1543 (1998).

[34] P. W. Anderson, in *The Lesson of Quantum Theory*, J. D. Boer, E. Dall, O. Ulfbeck, Eds. (Elsevier, Amsterdam, 1986), pp.23-33.

[35] R. Feynman, *The Feynman lectures on Physics*, (Addison-Wesley Publ. Comp., (1965).

[36] V. B. Geshkenbeim, A. I. Larkin and A. Barone, *Vortices with half magnetic flux quanta in "heavy-fermion" superconductors*, Phys. Rev. B **36** 235 (1987).

[37] J. J. A. Baselmans, A. F. Morpurgo, B. J. van Wees and T. M. Klapwijk, *Reversing the direction of the supercurrent in a controllable Josephson junction*, Nature **397**, 43 (1999).

[38] S. Backhaus, S. V. Pereverzev, A. Loshak, J. C. Davis and R. E. Packard, *Direct Measurement of the Current-Phase Relation of a Superfluid ³He-B Weak link,* Science **278**, 1435 (1997).

[39] S. V. Pereverzev, A. Loshak, S. Backhaus, J. C. Davis and R. E. Packard, *Quantum oscillations between two weakly coupled reservoirs of superfluid ³He,* Nature **388**, 449 (1997).

[40] K. Sukhatme, Yu Mukharsky, T. Chui and D. Pearson, *Observation of the ideal Josephson effect in superfluid ⁴He,* Nature **411**, 280 (2001).

[41] S. Backhaus, S. Pereverzev, R. W. Simmonds, A. Loshak, J. C. Davis and R. E. Packard, *Discovery of a metastable π-state in a superfluid 3He weak link,* Nature **392** 687 (1998).

[42] B. P. Anderson and M. A. Kasevich, *Macroscopic Quantum Interference from Atomic Tunnel Arrays,* Science **282**, 1686 (1998);C. Orzel, A. K. Tuchman, M. L. Fenselau, M. Yasuda and M. A. Kasevich, *Squeezed States in a Bose-Einstein Condensate,* Science **291**, 2386 (2001).

[43] F. S. Cataliotti, S. Burger, C. Fort, P. Maddaloni, F. Minardi, A. Trombettoni, A. Smerzi, and M. Inguscio, *Josephson Junction Arrays with Bose-Einstein Condensates,* Science **293**, 843 (2001);

[44] F. S. Cataliotti, L. Fallani, F. Ferlaino, C. Fort, P. Maddaloni, and M. Inguscio, *Superfluid current disruption in a chain of weakly coupled Bose-Einstein condensates,* New J. Phys. **5**, 71 (2003).

[45] O. Morsch, J. H. Müller, M. Cristiani, D. Ciampini, and E. Arimondo, *Bloch Oscillations and Mean-Field Effects of Bose-Einstein Condensates in 1D Optical Lattices,* Phys. Rev. Lett. **87**, 140402 (2001).

[46] M. Greiner, O. Mandel, T. Esslinger, T. W. Hänsch and I. Bloch, *Quantum phase transition from a superfluid to a Mott insulator in a gas of ultracold atoms,* Nature **415**, 39 (2002).

[47] D. Jacksch, H.-J. Briegel, J. I. Cirac, C. W. Gardiner, and P. Zoller, *Entanglement of Atoms via Cold Controlled Collisions*, Phys. Rev. Lett. **82**, 1975 (1999).

[48] T. G. Tiecke, M. Kemmann, Ch. Buggle, I. Shvarchuck, W. von Klitzing and J. T. M. Walraven, *Bose-Einstein condensation in a magnetic double-well potential*, J. Opt. B:Quantum Semiclass. Opt. **5**, S119 (2003).

[49] Y. Shin, M. Saba, T. A. Pasquini, W. Ketterle, D. E. Pritchard, and A. E. Leanhardt, *Atom Interferometry with Bose-Einstein Condensates in a Double-Well Potential*, Phys. Rev. Lett. **92**, 050405 (2004).

[50] Y. Shin, M. Saba, A. Schirotzek, T. A. Pasquini, A. E. Leanhardt, D. E. Pritchard, and W. Ketterle, *Distillation of Bose-Einstein condensates in a double-well potential*, Phys. Rev. Lett. **92**, 150401 (2004).

[51] N. R. Thomas and A. C. Wilson, C. J. Foot, *Double-well magnetic trap for Bose-Einstein condensates*, Phys. Rev. A **65**, 063406 (2002).

[52] J. Williams, R. Walser, J. Cooper, E. Cornell, and M. Holland, *Nonlinear Josephson-type oscillations of a driven, two-component Bose-Einstein condensate*, Phys. Rev. A **59**, R31 (1999).

[53] R. A. Webb, R. L. Kleinberg, and J. C. Wheatley, *Experiments on Dynamic Parallel Magnetism in Superfluid ^3He*, Phys. Rev. Lett. **33**, 145 (1974);A. J. Leggett, *A theoretical description of the new phases of liquid ^3He*, Rev. Mod. Phys. **47**, 331 (1975).

[54] L. Salasnich, A. Parola and L. Reatto, *Bose condensate in a double-well trap: Ground state and elementary excitations*, Phys. Rev. A **60**, 4171 (1999).

[55] A. J. Leggett 1999, in *Proceedings of the 16th International Conference on Atomic Physics*, Windsor, Ontario, Canada, Aug. 1998, edited by W. E. Baylis and G. F. Drake, AIP Conf. Proc. No. 477 (AIP, Woodbury, New York), pp. 154-169

[56] O. Zobay, B. M. Garraway, *Time-dependent tunneling of Bose-Einstein condensates*, Phys. Rev. A **61**, 033603 (2000).

[57] J. E. Williams, *Optimal conditions for observing Josephson oscillations in a double-well Bose-Einstein condensate*, Phys. Rev. A **64**, 013610 (2001).

[58] S. Giovanazzi, A. Smerzi and S. Fantoni, *Josephson Effects in Dilute Bose-Einstein Condensates*, Phys. Rev. Lett. **84**, 4521 (2000).

[59] C. Menotti, J. R. Anglin, J. I. Cirac and P. Zoller, *Dynamic splitting of a Bose-Einstein condensate*, Phys. Rev. A **63**, 023601 (2001).

[60] E. Sakellari, M. Leadbeater, N. J. Kylstra and C. S. Adams, *Josephson spectroscopy of a dilute Bose-Einstein condensate in a double-well potential*, Phys. Rev. A **66**, 033612 (2002).

[61] E. Sakellari, N. P. Proukakis, M. Leadbeater and C. S. Adams *Josephson tunnelling of a phase-imprinted Bose-Einstein condensate in a time-dependent double-well potential*, New J. Phys. **6**, 42 (2004).

[62] M. W. Jack, M. J. Collett and D. F. Walls, *Coherent quantum tunneling between two Bose-Einstein condensates*, Phys. Rev. A **54**, R4625 (1996).

[63] G. J. Milburn, J. Corney, E. M. Wright and D. F. Walls, *Quantum dynamics of an atomic Bose-Einstein condensate in a double-well potential*, Phys. Rev. A **55**, 4318 (1997).

[64] A. Smerzi, S. Fantoni, S. Giovanazzi and S. R. Shenoy, *Quantum Coherent Atomic Tunneling between Two Trapped Bose-Einstein condensates*, Phys. Rev. Lett. **79**, 4950 (1997).

[65] S. Raghavan, A. Smerzi, S. Fantoni, S. Giovanazzi and S. R. Shenoy, *Coherent oscillations between two weakly coupled Bose-Eistein condensates: Josephson effects, π oscillations, and macroscopic quantum self-trapping*, Phys. Rev. A **59**, 620 (1999).

[66] I. Marino, S. Raghavan, S. Fantoni, S. R. Shenoy and A. Smerzi, *Bose-condensate tunneling dynamics: Momentum-shortened pendulum with damping*, Phys. Rev. A **60**, 487 (1999).

[67] S. Raghavan, A. Smerzi and V. M.Kenkre, *Transitions in coherent oscillations between two trapped Bose-Einstein condensates*, Phys. Rev. A **60**, R1787 (1999).

[68] I. Zapata, F. Sols and A. J. Leggett, *Josephson effect between trapped Bose-Einstein condensates*, Phys. Rev. A **57**, R28 (1998).

[69] J. Javanainen and M. Yu Ivanov, *Splitting a trap containing a Bose-Einstein condensate: Atom number fluctuations*, Phys. Rev. A **60**, 2351 (1999).

[70] B. Wu and Q. Niu, *Nonlinear Landau-Zener tunneling*, Phys. Rev. A **61**, 023402 (2000).

[71] J. Ruostekoski and D. F. Walls, *Bose-Einstein condensate in a double-well potential as an open system*, Phys. Rev. A **58**, R50 (1998).

[72] S. Kohler and F. Sols, *Oscillatory Decay of a Two-Component Bose-Einstein Condensate*, Phys. Rev. Lett. **89**, 60403 (2002).

[73] S. Kohler and F. Sols, *Chemical potential standard for atomic Bose-Einstein condensates*, New J. Phys. **5**, 94 (2003).

[74] A. Griffin 1999, in *Bose-Einstein Condensation in Atomic Gases*, Proceedings of the International School of Physics "Enrico Fermi", Course CXL, Varenna on Lake Como, July 1998, edited by M. Inguscio, S. Stringari and C. E. Wieman, (IOS Press Ohmsha), pp. 591-623

[75] P. A. Ruprecht, M. J. Holland, K. Burnett, and M. Edwards, *Time-dependent solution of the nonlinear Schrödinger equation for Bose-condensed trapped neutral atoms*, Phys. Rev. A **51**, 4704 (1995).

[76] M. Ueda and A. J. Leggett, *Macroscopic Quantum Tunneling of a Bose-Einstein Condensate with Attractive Interaction*, Phys. Rev. Lett. **80**, 1576 (1998).

[77] Yu. Kagan, A. E. Muryshev, and G. V. Shlyapnikov, *Collapse and Bose-Einstein Condensation in a Trapped Bose Gas with Negative Scattering Length*, Phys. Rev. Lett. **81**, 933 (1998).

[78] A. Eleftheriou and Kerson Huang, *Instability of a Bose-Einstein condensate with an attractive interaction*, Phys. Rev. A **61**, 043601 (2000).

[79] S. K. Adhikari, *Collapse of attractive Bose-Einstein condensed vortex states in a cylindrical trap*, Phys. Rev. E **65**, 016703 (2002).

[80] M. Edwards and K. Burnett, *Numerical solution of the nonlinear Schrödinger equation for small samples of trapped neutral atoms*, Phys. Rev. A **51**, 1382 (1995).

[81] F. Dalfovo and S. Stringari, *Bosons in anisotropic traps: Ground state and vortices*, Phys. Rev. A **53**, 2477 (1996).

[82] M. Edwards, R. J. Dodd, C. W. Clark, P. A. Ruprecht and K. Burnett, *Properties of a Bose-Einstein condensate in an anisotropic harmonic potential*, Phys. Rev. A **53**, R1950 (1996).

[83] B. I. Schneider and D. L. Feder, *Numerical approach to the ground and excited states of a Bose-Einstein condensed gas confined in a completely anisotropic trap*, Phys. Rev. A **59**, 2232 (1999).

[84] D. S. Jin, J. R. Ensher, M. R. Matthews, C. E. Wieman, and E. A. Cornell, *Collective Excitations of a Bose-Einstein Condensate in a Dilute Gas*, Phys. Rev. Lett. **77**, 420 (1996).

[85] M.-O. Mewes, M. R. Andrews, N. J. van Druten, D. M. Kurn, D. S. Durfee, C. G. Townsend, and W. Ketterle, *Collective Excitations of a Bose-Einstein Condensate in a Magnetic Trap*, Phys. Rev. Lett. **77**, 988 (1996).

[86] Y. Castin, in 'Coherent atomic matter waves', Lecture Notes of Les Houches Summer School, p.1-136, edited by R. Kaiser, C. Westbrook, and F. David, EDP Sciences and Springer-Verlag (2001)

[87] W. Bao and W. Tang, *Ground-state solution of Bose-Einstein condensate by directly minimizing the energy functional*, J. Comp. Phys., **187**, 230 (2003);W. Bao, D. Jaksch and P. A. Markowich, *Numerical solution of the Gross-Pitaevskii equation for Bose-Einstein condensation*, J. Comp. Phys., **187**, 318 (2003).

[88] D. S. Petrov, G. V. Shlyapnikov and J. T. M. Walraven, *Phase-Fluctuating 3D Bose-Einstein Condendates in Elongated Traps*, Phys. Rev. Lett. **85**, 050404 (2001).

[89] K. K. Das, *Highly anisotropic Bose-Einstein condensates: Crossover to lower dimensionality*, Phys. Rev. A **66**, 053612 (2002).

[90] K. K. Das, M. D. Girardeau and E. M. Wright, *Crossover from One to Three Dimensions for a Gas of Hard-Core Bosons*, Phys. Rev. Lett. **89**, 110402 (2002).

[91] L. Salasnich, A. Parola, and L. Reatto, *Dimensional reduction in Bose-Einstein-condensed alkali-metal vapors*, Phys. Rev. A **69**, 045601 (2004).

[92] A. Görlitz, J. M. Vogels, A. E. Leanhardt, C. Raman, T. L. Gustavson, J. R. Abo-Shaeer, A. P. Chikkatur, S. Gupta, S. Inouye, T. Rosenband and W. Ketterle, *Realization of Bose-Einstein Condensates in Lower Dimensions*, Phys. Rev. Lett. **87**, 130402 (2001).

[93] F. Schreck, L. Khaykovich, K. L. Corwin, G. Ferrari, T. Bourdel, J. Cubizolles and C. Salomon, *Quasipure Bose-Einstein Condensate Immersed in a Fermi Sea*, Phys. Rev. Lett. **87**, 080403 (2001).

[94] M. Greiner, I. Bloch, O. Mandel, T. W. Hänsch, and T. Esslinger, *Exploring Phase Coherence in a 2D Lattice of Bose-Einstein Condensates*, Phys. Rev. Lett. **87**, 160405 (2001).

[95] H. Moritz, T. Stferle, M. Khl, and T. Esslinger, *Exciting Collective Oscillations in a Trapped 1D Gas*, Phys. Rev. Lett. **91**, 250402 (2003).

[96] W. H. Press, S. A. Teukolsky, W. T. Vetterling, and B. P. Flannery, *Numerical Recipes in FORTRAN, 2nd Edition* (Cambridge University Press, Cambridge, 1992).

[97] B. Jackson, *Vortices in trapped Bose-Einstein Condensates, Ph.D. Thesis*, (2000).

[98] A. L. Fetter and A. A. Svidzinsky, *Vortices in a trapped dilute Bose-Einstein condensate*, J. Phys. Condens. Matter **13**, R135 (2001).

[99] S. Stringari, *Collective Excitations of a Trapped Bose-Condensed Gas*, Phys. Rev. Lett. **77**, 2360 (1996).

[100] F. Zambelli and S. Stringari, *Quantized Vortices and Collective Oscillations of a Trapped Bose-Einstein Condensate*, Phys. Rev. Lett. **81**, 1754 (1998).

[101] A. A. Svidzinsky and A. L. Fetter, *Normal modes of a vortex in a trapped Bose-Einstein condensate*, Phys. Rev. A **58**,3168 (1998).

[102] G. Baym and C. Pethick, *Ground state Properties of Magnetically Trapped Bose-Condensed Rubidium Gas*, Phys. Rev. Lett. **76**, 6 (1996).

[103] M. R. Matthews, B. P. Anderson, P. C. Haljan, D. S. Hall, C. E. Wieman and E. A.Cornell, *Vortices in a Bose-Einstein Condensate*, Phys. Rev. Lett. **83**, 2498 (1999).

[104] K. W. Madison, F. Chevy, W. Wohlleben and J. Dalibard, *Vortex Formation in a Stirred Bose-Einstein Condensate*, Phys. Rev. Lett. **84**, 806 (2000).

[105] J. R. Abo-Shaeer, C. Raman, J. M. Vogels and W. Ketterle, *Observation of Vortex Lattices in Bose-Einstein Condensates*, Science. **292**, 476 (2001).

[106] C. Raman, J. R. Abo-Shaeer, J. M. Vogels and W. Ketterle, *Vortex Nucleation in a Stirred Bose-Einstein Condensate*, Phys. Rev. Lett. **87**, 210402 (2001).

[107] P. Rosenbusch, V. Bretin and J. Dalibard, *Dynamics of a Single Vortex Line in a Bose-Einstein Condensate*, Phys. Rev. Lett. **89**, 200403 (2002).

[108] V. Bretin, P. Rosenbusch and J. Dalibard, *Dynamics of a single vortex line in a Bose-Einstein condensate*, J. Opt. B:*Quantum Semiclass. Opt.* **5**, S23 (2003).

[109] D. S. Rokhsar, *Vortex Stability and Persistent Currents in Trapped Bose Gases*, Phys. Rev. Lett. **79**, 2164 (1997).

[110] J. D. Jackson 1962, in *Classical Electrodynamics*, pp. 136-141

[111] K. K. Likharev, *Superconducting weak links*, Rev. Mod. Phys. **51**, 101 (1979).

[112] J. C. Davis and R. E. Packard, *Superfluid ^{3}He weak links*, Rev. Mod. Phys. **74**, 741 (2002).

[113] O. Avenel and E. Varoquaux, *Josephson effect and quantum phase slippage in superfluids*, Phys. Rev. Lett. **60**, 416 (1998).

[114] Z. P. Karkuszewski, K. Sacha, and A. Smerzi, *Mean field loops versus quantum anti-crossing in trapped Bose-Einstein condensates*, Eur. Phys. J. D **21**, 251 (2002).

[115] B. Wu and Q. Niu, *Nonlinear Landau-Zener tunneling*, Phys. Rev. A **61**, 023402 (2000).

[116] B. Wu, R. B. Diener and Q. Niu, *Bloch waves and bloch bands of Bose-Einstein condensates in optical lattices*, Phys. Rev. A **65**, 025601 (2002).

[117] D. Diakonov, L. M. Jensen, C. J. Pethick and H. Smith, *Loop structure of the lowest Bloch band for a Bose-Einstein condensate*, Phys. Rev. A **66**, 013604 (2002).

[118] E. J. Mueller, *Superfluidity and mean-energy loops: Hysteretic behaviour in Bose-Einstein condensates*, Phys. Rev. A **66**, 063603 (2002).

[119] J. Javaneinen, *Oscillatory Exchange of Atoms between Traps Containing Bose Condensates*, Phys. Rev. Lett. **57**, 3164 (1986).

[120] J. J. A. Baselmans, B. J. van Wees and T. M. Klapwijk, *Controllable π SQUID*, Appl. Phys. Lett. **79**, 2940 (2001).

[121] H. J. H. Smilde, Ariando, D. H. A. Blank, G. J. Gerritsma, H. Hilgenkamp and H. Rogalla, *d-Wave-Induced Josephson Current Counterflow in YBa2Cu3O7/Nb Zigzag Junctions*, Phys. Rev. Lett. **88**, 057004 (2002).

[122] H. Pu, L. O. Baksmaty, W. Zhang, N. P. Bigelow and P. Meystre, *Effective-mass analysis of Bose-Einstein condensates in optical lattices: Stabilization and levitation*, Phys. Rev. A **67**, 043605 (2003).

[123] F. Sols 1999, in *Bose-Einstein Condensation in Atomic Gases*, Proceedings of the International School of Physics "Enrico Fermi", Course CXL, Varenna on Lake Como, July 1998, edited by M. Inguscio, S. Stringari and C. E. Wieman, (IOS Press Ohmsha), pp. 453-468

[124] S. Burger, K. Bongs, S. Dettmer, W. Ertmer, and K. Sengstock, A. Sanpera, G. V. Shlyapnikov, and M. Lewenstein, *Dark Solitons in Bose-Einstein Condensates*, Phys. Rev. Lett. **83**, 5198 (1999).

[125] J. Denschlaget, J. E. Simsarian, D. L. Feder, Charles W. Clark, L. A. Collins, J. Cubizolles, L. Deng, E. W. Hagley, K. Helmerson, W. P. Reinhardt, S. L. Rolston, B. I. Schneider, and W. D. Phillips, *Generating Solitons by Phase Engineering of a Bose-Einstein Condensate*, Science **287**, 97 (2000).

[126] K. W. Mahmud, H. Perry and W. P. Reinhardt, *Phase engineering of controlled entagled number states in a single compontent Bose-Einstein condensate in a double-well potential*, J. Phys. B **36**, L265 (2003).

[127] J. E. Williams and M. J. Holland, *Preparing topological states of a Bose-Einstein condensate*, Nature **401**, 568 (1999).

[128] C. C. Bradley, C. A. Sackett and R. G. Hulet, *Bose-Einstein Condensation of Lithium: Observation of Limited Condensate Number*, Phys. Rev. Lett. **78**, 985 (1997).

[129] C. A. Sackett, C. C. Bradley, M. Welling and R. G. Hulet, *Bose-Einstein Condensation of Lithium*, Appl. Phys. B **65**, 433 (1997).

[130] J. M. Gerton, D. Strekalov, I. Prodan and R. G. Hulet, *Direct Observation of Growth and Collapse of a Bose-Einstein Condensate with Attractive Interactions*, Nature **408**, 692 (2000).

[131] E. A Donley, N. R. Claussen, S. L. Cornish, J. L. Roberts, E. A. Cornell and C. E. Wieman, *Dynamics of collapsing and exploding Bose-Einstein Condensates*, Nature **412**, 295 (2001).

[132] J. L. Roberts, N. R. Claussen, S. L. Cornish, E. A. Donley, E. A. Cornell and C. E. Wieman, *Controlled Collapse of a Bose-Einstein Condensate*, Phys. Rev. Lett. **86**, 4211 (2001).

[133] A. Gammal, T. Frederico and L. Tomio, *Critical number of atoms for attractive Bose-Einstein condensates with cylindrically symmetric traps*, Phys. Rev. A **64**, 055602 (2001).

[134] A. Gammal, L. Tomio and T. Frederico, *Critical numbers of attractive Bose-Einstein condensed atoms in asymmetric traps*, Phys. Rev. A **66**, 043619 (2002).

[135] A. L. Fetter, *Variational study of Dilute Bose Condensate in a Harmonic Trap*, J. Low Temp. Phys. **106**, 643 (1997).

[136] S. K. Adhikari, *The critical number of atoms in an attractive Bose-Einstein condensate on optical plus harmonic traps*, J. Phys. B:At. Mol. Opt. Phys. **36**, 2943 (2003).

[137] P. Coullet and N Vandenberghe, *Chaotic dynamics of a Bose-Einstein condensate in a double-well potential*, J. Phys. B:At. Mol. Opt. Phys. **35**, 1593 (2002).

[138] C. A. Sackett, H. T. C. Stoof and R. G. Hulet, *Growth and Collapse of a Bose-Einstein Condensate with Attractive Interactions*, Phys. Rev. Lett. **80**, 2031 (1998).

[139] C. A. Sackett, J. M. Gerton, M. Welling and R. G. Hulet, *Measurements of Collective Collapse in a Bose-Einstein Condensate with Attractive Interactions*, Phys. Rev. Lett. **82**, 876 (1999).

[140] K. E. Strecker, G. B. Partridge, A. G. Truscott, and R. G. Hulet, *Formation and propagation of matter-wave solitons Trains*, Nature 417, 150 (2002);U. Al Khawaja, H. T. C. Stoof, R. G. Hulet, K. E. Strecker, and G. B. Partridge, *Bright Solitons Trains of Trapped Bose-Einstein Condensates*, Phys. Rev. Lett. **89**, 200404 (2002).

[141] R. A. Duine and H. T. C. Stoof, *Explosion of a Collapsing Bose-Einstein Condensate*, Phys. Rev. Lett. **86**, 2204 (2001).

[142] S. K. Adhikari, *Dynamics of a collapsing and exploding Bose-Einstein Condensed vortex state*, Phys. Rev. A **66**, 043601 (2002).

[143] S. K. Adhikari, *Mean-field description of collapsing and exploding Bose-Einstein condensates*, Phys. Rev. A **66**, 013611 (2002).

[144] L. Santos and G. V. Shlyapnikov, *Collapse dynamics of trapped Bose-Einstein condensates*, Phys. Rev. A **66**, 011602 (2002).

[145] H. Saito and M. Ueda, *Mean-field analysis of collapsing and exploding Bose-Einstein condensates*, Phys. Rev. A **65**, 033624 (2002).

[146] C. M. Savage, N. P. Robins and J. J. Hope, *Bose-Einstein condensate collapse: A comparison between theory and experiment*, Phys. Rev. A **67**, 014304 (2003).

[147] J. N. Milstein, C. Menotti, and M. J. Holland, *Feshbach resonances and collapsing Bose-Einstein condensates*, New J. Phys. **5**, 52 (2003).

[148] S. K. Adhikari, *Mean-field model of jet formation in a collapsing Bose-Einstein condensate*, J. Phys. B: At. Mol. Opt. Phys. **37**, 1185 (2004).

[149] W. Bao, D. Jaksch, and P. A. Markowich, *Three-dimensional simulation of jet formation in colapsing condensates*, J. Phys. B: At. Mol. Opt. Phys. **37**, 329 (2004).